On Modelling for Domestic Energy Autonomy in the UK:

Understanding the Role of Traditional and Novel Technologies for Small-Scale Hydrogen Storage

Alex Marshall

School of Computing, Science and Engineering,

University of Salford, Manchester, UK

Submitted in Partial Fulfilment of the Requirements of the Degree of Doctor of Philosophy, March 2018

Contents

Acknowledgements

Thanks to the family and friends who supported me throughout this endeavour. I couldn't imagine doing it without you wonderful lot behind me.

Thanks to Dr Dan Bull for your supervision, guidance and friendship throughout my time at Salford.

Thanks to Dr Richard Fitton and Prof Will Swan. Your contribution to the development of my career has been more than I ever could have imagined. Your combined wisdom has sustained my appreciation for the work that we do.

A final thanks to Dr Nikos Savvas. More than a decade ago, you saw something in a young man and convinced him to try physics. You opened his eyes and inspired him. Without your kind persuasion, he wouldn't be where he is today.

Material Acknowledgement

Acknowledgement is made to Richard Fitton, Will Swan, David Farmer, David Johnston, Moaad Benjaber and Yingchun Ji for contributions to the publication referenced in Chapter 2 entitled: “Domestic building fabric performance: Closing the gap between the *in situ* measured and modelled performance”. This work was published by “Energy and Buildings”, which received funding from the School of the Built Environment.

List of Figures

Chapter 3

Chapter 4

Chapter 5

Chapter 7

List of Tables

Chapter 6

Chapter 7

List of Publications

Marshall, A., Francou, J., Fitton, R., Swan, W., Owen, J. and Benjaber, M., 2018. Variations in the U-Value Measurement of a Whole Dwelling Using Infrared Thermography under Controlled Conditions. Buildings, 8, 46, pp. 1-17. doi:10.33990/buildings8030046

Marshall, A., Fitton, R., Swan, W., Farmer, D., Johnston, D., Benjaber, M. and Ji, Y., 2017. Domestic building fabric performance: Closing the gap between the in situ measured and modelled performance. *Energy and Buildings*, 150, pp. 307-317.

Mahdjoubi, L., Hawas, S., Fitton, R., Dewidar, K., Nagy, G., Marshall, A., Alzaatreh, A. and Abdelhady, E., 2017. A guide for monitoring the effects of climate change on heritage building materials and elements.

Patil, N., Marshall, A., Fitton, R. and Waddington, D., 2017.Combined Imaging Technologies for Measuring the In-Situ Thermal and Acoustic Energy Efficiency of Retrofit Building Elements. IRC 2017, pp. 966.

Fitton, R., Marshall, A., Benjaber, M. and Swan, W., 2017. A study of the thermal performance of tweed curtains under controlled conditions. In PLEA 2017. pp. 1079-1087.

Abstract

The domestic sector is one of the largest consumers of energy in the UK. The poor energy performance of the existing housing stock within this sector has resulted in an ever-growing energy demand and an energy infrastructure that is struggling to cope. With an increasing drive towards decarbonisation comes the expansion of renewable generation across the UK, however with that comes the limitations of intermittency inherent in the technologies. Energy storage is considered as a solution to these limitations, though with this is the potential for redefining the UK's energy regime. Decentralised generation, storage and consumption of energy is proposed as an alternative regime as the core theme of this thesis.

A common type of British home (a pre-1920s Victorian end terrace building) has been modelled in the dynamic energy simulation software Designbuilder in order to explore how such buildings respond to decentralised energy management. The model was based upon a house of this type within the Energy House research facility at the University of Salford, constructed inside a climate controlled chamber and augmented with a photovoltaic installation. Intrinsic flaws in building modelling appear in the phenomenon known as the performance gap, which reduces the accuracy of models. The same flaws were found in the model created for this study. By applying a calibration procedure that replaced assumed performance parameters with those measured in-situ, the observed performance gap was reduced by a significant amount and therefore increasing the accuracy and predictive capacity of the model.

The Energy House model was conditioned to reflect a variety of scenarios suited to the UK, including scenarios under the categories of archetype, occupancy, location, climate and level of retrofit. Each of these were identified as having a significant influence over energy

consumption. Simulations under these scenarios revealed a high sensitivity to factors influencing the performance of the building's envelope, with much less sensitivity to external influences and the building's occupants themselves. A combination of best-case scenarios was found to deliver the greatest tendency towards energy autonomy, with a reduction of the grid demand by up to 70%. Trends identified in the modelling results indicated a need for energy storage to counter the offset between solar generation using photovoltaics and domestic consumption and the potential for closing the gap of energy autonomy.

The home battery was considered as an established storage solution, while the use of hydrogen as an energy vector was also considered, with the established technology of compression and the novel technologies of absorption in metal hydrides and adsorption in activated carbon. A model for the battery in Designbuilder was conditioned to reflect a typical home battery, however additional models for hydrogen storage were scripted in Matlab. These models included bulk storage of hydrogen under pressure for the compressed gas and activated carbon solutions, whereas a finite element approach was modelled for the metal hydride solution.

When comparing energy storage methods, simulations revealed that scenarios with variations to the average annual temperature had no impact on energy storage; in this case, as with the baseline model, the home battery outperformed other methods of storage. Under scenarios where modifications were made to the building's envelope, compressed gas was found to be the most suitable candidate for storage. By combining the best-case scenarios from simulations, energy autonomy was virtually achievable, reducing the grid energy demand of a baseline model by 99.6%; both metal hydride and compressed gas storage solutions proved superior in providing this. This considerable reduction in domestic grid

demand was only represented in a small number of homes in the UK however, with the benefits of integrated energy storage reserved for homes having high thermal performance, located at lower latitudes, and having lower occupancy densities.

Despite the application of an autonomous decentralised energy regime being limited to a small proportion of the UK's housing stock, this study realises the importance of energy storage in a future of renewables; it paves the way for further work in determining the role of small-scale energy storage as a solution to the challenges faced in the future of energy for the UK.

This work found that for domestic energy autonomy to be achievable in the UK, it is first necessary to vastly improve the energy performance of the existing housing stock.

Chapter 1

Introduction

Abbreviations

BEIS	The Department for Business, Energy and Industrial Strategy
DECC	The Department for Climate Change
DSBR	Demand Side Balancing Reserve
ESCO	Energy Service Company
FES	Future Energy Scenarios
GHG	Green House Gas (es)
IEA-EBC	International Energy Agency Energy in Buildings and Community
PV	Photovoltaics
SBR	Supplemental Balancing Reserve
WEC	World Energy Council

The UK's domestic sector is the second largest consumer of energy with 29% of the overall consumption; this is divided into heating (80%) and electricity (20%), (BEIS, 2017). The high proportion of energy for heating is recognised due to the poor thermal performance of UK homes, with almost 50% of UK homes are labelled as 'hard to treat' (BRE, 2008). This means that there are no practical or economic solutions to reduce the heating demand of those buildings. UK dwellings also have long physical lifetimes and slow replacement cycles, where the existing housing stock is expected to make up at least 70% of the total housing stock by

2050 (SDC, 2006). Given this, considerable effort has been made to improve the thermal efficiency of UK homes and subsequently reduce the overall consumption of the domestic sector. Karvonen (2013) demonstrates the scale of this effort by reviewing several schemes put in place by the UK government to facilitate installation of retrofit across the UK's housing stock. The Green Deal (DECC, 2010a) is an example of one of these schemes, designed to provide affordability of retrofit installations to occupants.

Analysis of building information (in-situ, measured) also plays a large role in parameterising the thermal performance of the housing stock; this is done to predict future energy performance and to identify opportunity for improving this future energy performance e.g. with retrofit. Performance prediction and building parameterisation are a core focus of the IEA-EBC's Annex 71 project (Roels et al., 2017), in which direction is taken from earlier works that carry out modelling tasks to that effect. Significant focus is placed on quantifying the performance of buildings so that poor performers can easily be identified and retrofit measures proposed.

The success of domestic retrofit lies with its passive nature. Once carried out, the occupant takes no ownership in maintaining an improved thermal performance. The adoption of retrofit in the UK is considered as well established (Chahal et al., 2012; Swan et al., 2013 & 2013 and Brown et al., 2014).

Efforts to implement savings in electricity consumption have not received the same attention as that of heating. Schemes looking to reduce domestic electricity consumption often identify as active, where to improve energy efficiency occupants would actively need to change their behaviour. With the objective to educate domestic occupants and make them aware of their behaviour concerning electrical consumption, the rollout of smart meters is a scheme that

has been introduced by the UK government and across Europe (DECC, 2012). The scheme is implemented by the supply side for distribution to the demand side. However, as Warren (2014) discusses in his review of demand side management policy, supply side options are favoured by the suppliers due to the 'increased certainty of response'. This suggests unreliability and unpredictability of occupants in responding to their own energy saving measures. Changing the electricity consumption of the UK then, would appear to be more problematic than changing gas consumption for heating, and the electricity infrastructure of the UK is not already without its own problems.

1.1 The UK Energy Trilemma

Electricity production and distribution can be considered as a balance of three core dimensions: security, equity and environmental impact. Security ensures that a constant supply of energy is available to meet the demand of the nation; equity delivers accessibility to the supply of energy, be it economic or physical; and environmental impact is the cost to the environment, largely accredited to greenhouse gas (GHG) emissions from the burning of fossil fuels. Together these three core dimensions are better known as the 'Energy Trilemma', (WEC, 2016). Three key stakeholders are responsible for maintaining an energy regime, and so a balance between these three dimensions: market operators (suppliers), end users (consumers), and the government (regulators). Each of these actors tends towards one of these dimensions, for example market operators rely on energy security to balance revenue with losses, equity ensures affordable fuel for consumers and low environmental impact benefits the government's obligation to act on climate change.

The World Energy Council (WEC) monitor the Energy Trilemma of the world's nations and provide rankings based on an index for balance. The WEC also observe a 'watch list' - positive for nations with improving indices, and negative for nations in decline or who are anticipated to have sudden disruption to their energy distribution functionality. While the UK ranked 11th globally in the WEC's 2016 review (WEC, 2016), it also made it into the watch list of nations suddenly expected to decline. The WEC's supporting arguments for this include:

- Political issues surrounding the UK's exit from the EU impacting on planned infrastructure transition and the cost of energy imports.
- Changes to regulations on ownership of energy infrastructure.
- A sharp decline in feed-in-tariffs for renewables.

Concern for the continuing functionality of the UK's energy infrastructure is reflected in a report delivered by Ofgem (2015); the report looked at the country's overall energy capacity and drew focus to the generation of electricity. The report stated that due to the growing demand for energy and the decommissioning of power stations, the reserve margin of the UK (designed to mitigate unexpected increases in demand) has shrunk and continues to shrink. This would lead to an imbalance of the energy trilemma dimensions, whereas environmental impact becomes rapidly more positive, the remaining factors go into decline to balance it out. Energy security suffers due to the reduced energy capacity of the electricity grid. Energy equity further suffers due to the increased cost for imported fuels, and the additional costs incurred for the initial investment of energy companies into renewable technologies.

Ofgem discussed how a decreasing reserve margin would be particularly problematic over the winters of 2015, 2016 and 2017 – without a contingency plan, problems would be encountered during extended periods of low temperatures due to unexpected high demand.

A solution was explored by means of a 'safety net' that provided supplementary balancing reserves (SBRs) and demand side balancing reserves (DSBRs) (Ofgem, 2015). The balancing services support increasing the longevity of power plants supply side, while on the demand side incentives were provided for consumers who reduced energy use during peak hours.

The UK's diminishing reserve margin was a casualty of the UK's ambitious decision in 2008 to achieve an 80% reduction in carbon emissions by 2050 (UK Parliament, 2008). With a vision of decarbonisation, it was decided that several power stations should be retired – namely coal and older nuclear stations – in favour of a younger, more diverse and carbon-free supply network. Kennedy (2007) reviewed the systematic decommissioning of UK power stations planned between 2016 and 2025. Figure 1.1 summarises the findings of this work – showing the large initial decommissioning of coal stations, progressive decommissioning of nuclear stations and the extent to which that decommissioning has been delayed (to increase longevity) in response to the challenges faced by a shrinking energy capacity. The predictions in Kennedy's work summarised in Figure 1.1 indicate that by 2026, the UK's existing energy capacity would actually decrease by more than a third.

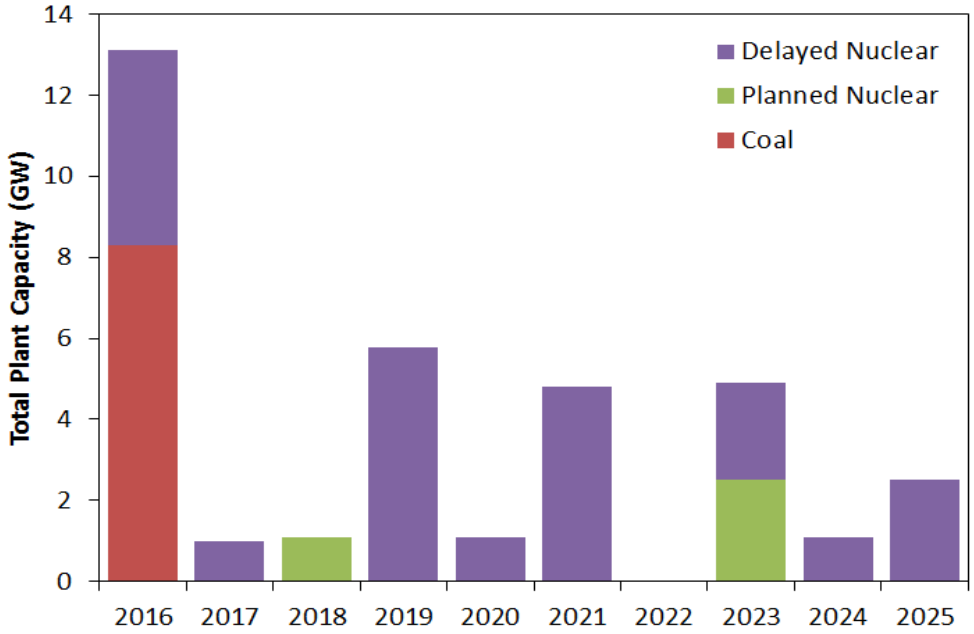

Figure 1.1 – Planned and delayed retirement of power stations in the UK between 2016 and 2025. Adapted from Kennedy (2007).

1.2 The Dynamic Growth of Renewables

The drive towards decarbonisation triggered in 2008, which has led to a shrinking energy reserve margin, has been met with dynamic growth of the UK's energy infrastructure. The Renewable Energy Roadmap (DECC, 2011) has instructed an increase in renewable energy consumption by at least 15% for 2020. Figure 1.2 demonstrates a significant shift in fuel consumption for electricity in the UK between 2008 and 2016, using data adapted from the BP Statistical Review of World Energy (BP, 2017).

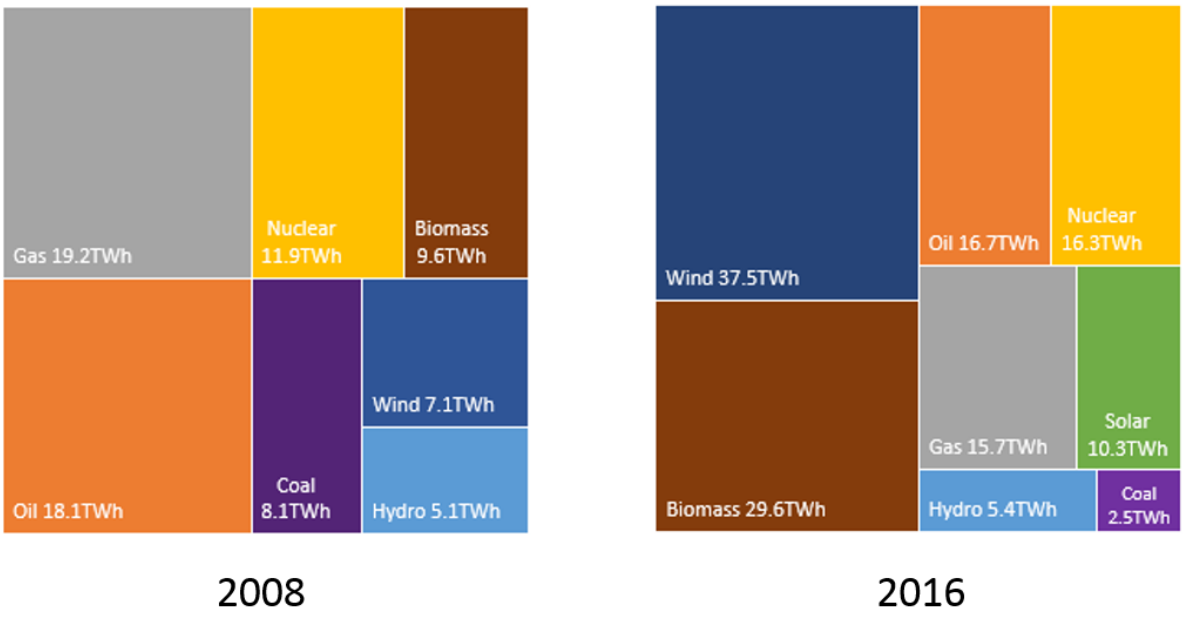

Figure 1.2 – Comparison of fuel consumptions for electricity in the UK in 2008 and 2016. Adapted from BP (2017).

Figure 1.2 shows that while four of the main fuels (gas, oil, nuclear and hydro) retain similar consumptions from 2008 to 2016, there was a significant shift in the remaining fuels. Coal consumption was reduced by more than 75%, while at the same time there was a growth of wind and biomass, and the emergence of solar generation.

The emergence and growth of renewables in response to decarbonisation has and is changing the very energy infrastructure of the UK. The established infrastructure operates under the principle that a base load can be provided to meet the minimum demand, with additional 'fast response' fuels to address peaks in that demand.

From an interview with experts on forecasting renewable energy from the US Energy Information Administration, Sovacool (2006) reports that:

"By and large, renewable energy resources are too rare, too diffuse, too distant, too uncertain and too ill-timed to provide significant supplies at the times and places of need".

This reflects on the intermittency of renewables, their inability to provide a constant supply of electricity, and their impracticality for providing a base load. The switch from fossil fuels to renewables completely changes the nature of the supply of electricity to end users. Fossil fuels have traditionally provided an energy vector that can be stored until needed. Complex statistical models (see Suganthi and Samuel, 2012) have then been used to determine when these energy vectors should be converted into electricity to meet demand. By having renewable energy sources, the ability to stockpile that energy source is not possible and so as electricity is generated using renewables it must be consumed to avoid waste. As it stands for renewable energy generation, there is a considerable misalignment between the generation of electricity using renewables and the consumption of that electricity by the end user.

1.3 A Solution to Renewable Intermittency

One solution to renewable intermittency would be to reintroduce the energy vector. Orecchini (2006) proposes the 'Era of Energy Vectors' in a period where renewables become a main source of energy. In this period, he states that for a 'closed energy system' consisting of sustainable energy cycles, energy vectors are a basic requirement. Orecchini summarises

that hydrogen is a suitable candidate for energy vector and despite the fact that inefficiencies may lie within its generation, it is feasible in terms of sustainability for that closed energy system. The use of hydrogen as an energy vector is also discussed by Krajačić et al. (2008), who identify the increase in penetration of renewables on island communities due to centralised energy storage.

Other methods of large scale energy storage, such as hydro power, are currently being used. By raising water up to a higher level, potential energy stored in that body of water can be accessed at any time by releasing it again. While this has proven to be an effective way to store energy on a large scale, the problem of estimating the supply side response to demand still exists.

Harvey et al. (2016) reviewed demonstration 'Power-to-Gas' projects in Germany and Canada, which look at penetration of renewables into energy grids using existing energy distribution infrastructure – notably that of gas. Each project considered large scale electrolysis of water to produce hydrogen as an energy storage medium. The fuel is mixed with natural gas and injected into the national gas grid. By doing this, energy from renewable sources has been used for heating and cooking, and has been proven to reduce the consumption of natural gas, delivering a positive impact on carbon emissions and the environment. The provision of electricity entirely from renewable sources is removed however, unless some method of extracting that electricity from the hybrid mixture can be found. The answer to this may be found in fuel cells.

Power-to-Gas projects are not the first time that hydrogen has been considered as an energy vector to meet domestic demand – in particular, electricity demand. Demonstration projects have been designed to show how hydrogen can be used to store renewable energy on a

domestic scale to bridge the gap between intermittent supply and demand. In these cases, the large-scale electrolysis of water seen in Power-to-Gas projects is brought down to the domestic scale, where it can be consumed by a fuel cell on demand. In these cases, the microgeneration of electricity is carried out using photovoltaics. At this smaller scale, the enduring problem of supply side response to demand is removed, and the overall system becomes less complex.

The 'Self Sufficient Solar House' in Freiburg (Germany) is one demonstration project looking at using localised hydrogen generation and consumption in a closed energy system (Goetzberger et al., 1994; Stahl et al., 1994; and Voss et al., 1996). Energy has been generated for the house using PV and thermal collectors, where it could be stored in batteries and as hydrogen through the use of an electrolyser; a fuel cell and burners were used to provide the house with electricity, heating and cooking. The building was designed to be as energy efficient as possible, with an energy demand of less than 10kWh/m^2/a. Throughout the lifetime of the project, energy demands were completely satisfied using solar energy with the support of hydrogen as a long-term energy store.

Another demonstration project is found in Zöllbruck, Switzerland (Hollmuller et al., 2000). This project used a similar means of generating hydrogen with electricity from PV via electrolysis of water. Hydrogen was stored in metal hydride tanks until its use with fuel cells to provide appliances with electricity. Surplus hydrogen was also used to fuel the family vehicle and a backup battery was used alongside hydrogen storage. The house continues to demonstrate self-sufficient operability since its construction in 1991.

The above demonstration projects are both examples of autonomous buildings using hydrogen as an energy storage medium. Autonomy in buildings is characterised by the

building's ability to function without support and services from public facilities (Vale and Vale, 1997). Chen et al. (2009) discuss the use of autonomous energy systems for domestic buildings and their implications. They synonymise the need for energy autonomy with self-sufficiency, offering a simple shift in the market-economy paradigm to reach self-sufficiency. This is in support of Orecchini's closed energy system (2006). Figure 1.3 shows the diagram provided by Chen et al., demonstrating this shift in energy systems.

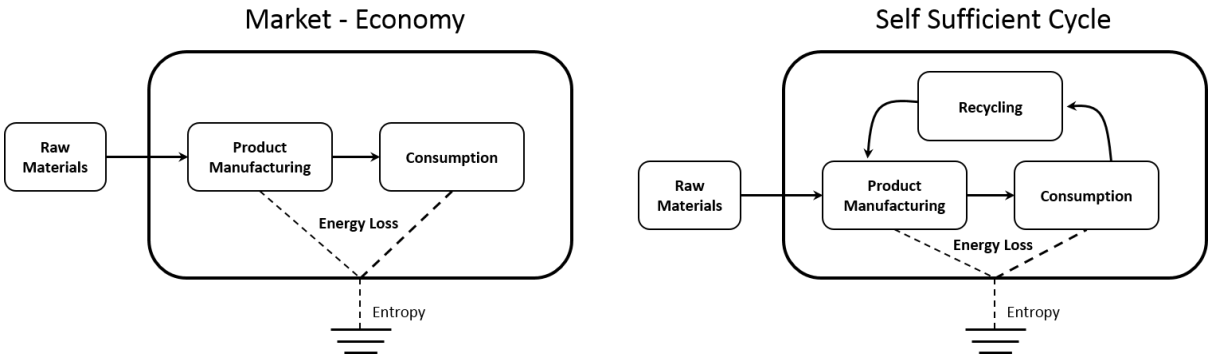

Figure 1.3 – Shifting energy systems between market economy and self-sufficient cycles.

Figure 1.4 shows how this shift in energy systems can be applied to the UK energy infrastructure. By using hydrogen as an energy storage medium, several different scenarios present themselves to take hydrogen generation and consumption away from a centralised energy system to a localised energy system.

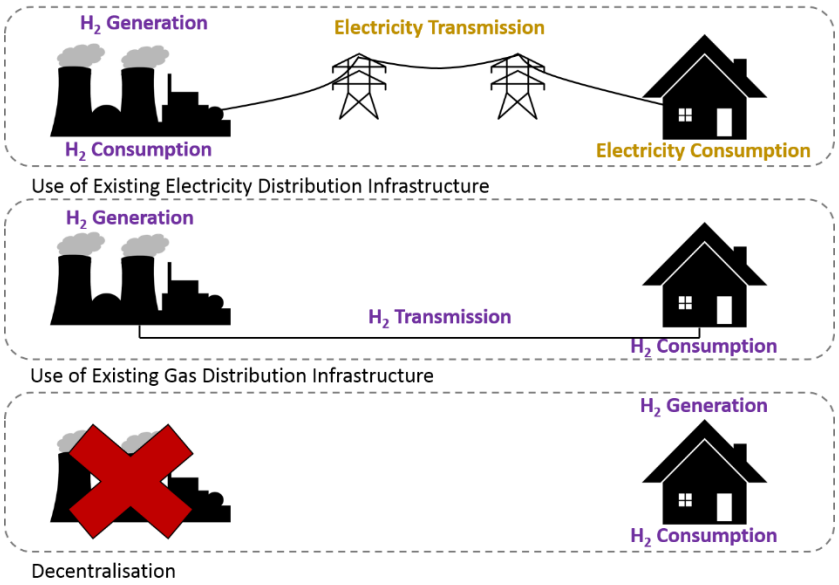

Figure 1.4 – Shifting energy systems in the UK, from centralised generation and consumption to localised generation and consumption.

As the overall energy system changes to accommodate the shift towards a self-sufficient cycle, there is an observed reduction in system complexity. This means that there are less processes involved and less reliability on distribution infrastructures. There are also big implications on the nature of energy distribution and the potential for energy savings with electrical consumption.

As discussed, there is difficulty when implementing significant reductions in electricity consumption due to the dependence on demand side behavioural change. Reliance falls upon the supply side to initiate savings on electricity consumption and its impact, where the challenge then is to close the gap between predicted and actual demand and minimise waste.

1.4 Decentralisation and Energy Autonomy

Energy saving measures for electrical generation and distribution can be discussed in the context of the Energy Trilemma. A shift of electricity generation and distribution as observed in the demonstration projects discussed in this chapter, and as investigated in Chen et al.'s work (Chan et al., 2009) could benefit each of the core dimensions. By implementing autonomous energy systems such as that of the self-sustaining solar house in Germany and the demonstration project in Switzerland, the following can be assumed:

- **Energy Security:** Increased on-site energy generation decreases grid demand, reducing the need for extending the life of power stations and increasing the overall reserve capacity of the network. This reserve can be used in the event of any shortfalls in domestic generation.
- With additional / renewed reserves of electricity supply, there would be increased support for growing electricity demand in the public sector e.g. the uptake and growth of the electric car industry.
- The existing renewable generation and distribution infrastructure could be used to extend the penetration of renewables as a whole, effectively 'topping up' domestic storage during periods of surplus generation and drawing electricity back into the grid during peak demand. This would see the domestic sector as a large energy 'cloud' storage.
- **Energy Equity:** On-site generation, storage and consumption allows greater control of energy use at the domestic level.
- With reduced dependency on electricity from the grid, overall energy costs are also reduced.

- **Environmental Impact:** The use of renewables decreases the demand for electricity originally supplied with the use of fossil fuels.
- Water vapour is the only output from hydrogen consumption.
- A reduced infrastructure dependency means a reduced carbon footprint in construction, maintenance and decommissioning of that infrastructure.

Decentralisation of electricity generation is already a key topic of works discussing transition pathways of the UK's energy infrastructure (see Foxon et al.,2009 & 2010; and Foxon 2008, 2011 & 2013). The transition is considered as a 'society-led' system over a 'market-based' or a 'government-led' system, and involved localised (individual dwelling or communal) energy generation and consumption with a focus on photovoltaics at the energy source. While decentralisation can be initially anticipated as bad for the market stakeholder of any energy sector, and thus discourage investment in such a transition, Foxon does in fact point out that a growing demand for energy service companies (ESCOs) would present the opportunity for suppliers to diversify their product in this field.

Also discussed in these works is uncertainty surrounding future transition pathways. The changing insights provided by Ofgem (Ofgem, 2016 & 2017) of future energy scenarios (FES) would also suggest uncertainty in the future of the UK's energy sector. With such uncertainty, there is potential to introduce a new energy regime within the market. And so, the key question of this thesis asks:

Is there potential for a transition towards hydrogen-based domestic energy autonomy?

The assumptions made surrounding energetically autonomous homes in the UK are made on the basis that the UK housing stock would perform in a similar way to the demonstration houses discussed earlier. With different archetypes, climates, thermal performance

characteristics and occupancy behaviour to consider, there is an uncertainty around whether this energy saving solution would be effective in the UK. With the benefits discussed in achieving the ultimate goal of a balance between the three dimensions of the energy trilemma, the opportunity to investigate this as a possibility presents itself. The modelling work discussed at the beginning of this chapter, which has been carried out to investigate the thermal performance of domestic buildings, provides a useful framework from which models investigating both electrical and thermal performance can be derived. The remaining questions are then:

- what (in terms of storage technology) will be modelled?
- what should (in terms of the building) should it be modelled on?
- and under what conditions should it be modelled?

To address these, it is appropriate to review the current energy storage environment. Batteries are an established form of energy storage in the home, so it would be beneficial to model this alongside hydrogen energy storage. The initial technology to be modelled for hydrogen storage is compressed gas. While not often used in a domestic setting, the technology is well understood. More novel technologies for hydrogen storage are metal hydrides and activated carbons, with the energy density of these materials proving to be promising for domestic use. The Zöllbruck demonstration house mentioned earlier does in fact use metal hydrides as a means of storage. Many complex materials are used to facilitate metal hydride storage (see Lotottskyy, 2014), and the Zöllbruck house does not fall short. For any modelling work, it is beneficial to use a more common alloy. Activated carbons have been used in modelling work for domestic hydrogen storage (Zini et al., 2010), however practical analysis of the material reveals that specifics surrounding material composition determine its

storage capacity, which can vary greatly (Wang et al., 2009). A simple activated carbon with known properties, as with metal hydrides, should be used to facilitate accurate modelling.

The Energy House research facility at the University of Salford has provided a test bed from which an accurate model of a typical UK home could be built (Marshall et al., 2017). An investigation into the modelling of buildings to determine energy performance was carried out. In finding a 'performance gap' could be attributed to such models, a calibration technique was applied to a model of the Energy House. The generation of this highly calibrated model for a traditional UK dwelling is covered as part of the work in this thesis, where the resulting model being used for all simulations.

The feasibility of the energy system in question must be determined by investigating the performance of that energy system in a number of different scenarios that reflect the diversity of similar dwellings across the UK. Within the scope of modelling the Energy House – a Victorian terrace building – there is the opportunity to vary particular conditions and analyse the sensitivity of those conditions to the performance of the energy system, thus mapping its suitability. The conditions considered for this sensitivity study are:

- Archetype – Mid terrace, end terrace / semi-detached, and detached.
- Occupancy – Typical working family, single worker, retired couple.
- Location – 45 different locations across the UK.
- Changing climates – 3 future predicted climates in 2030, 2050 and 2080.
- Retrofit – Modelled with deep retrofit and electric heating.

1.5 Aim and Objectives

The overall aim of this thesis is to investigate the feasibility of a decentralised domestic energy infrastructure in the UK, where photovoltaics and hydrogen storage promote autonomy at the local level through the use of energy vectors. Different permutations of a typical UK home will be used to model a range of energy systems and scenarios under which this infrastructure might be expected to operate. The following objectives were achieved:

- A model of a common UK home was built using dynamic simulation software.
- This model was calibrated to mitigate effects of the 'performance gap', so that it more accurately represents real building performance.
- The model was then modified to reflect each of the sensitivity factors listed above, and simulated to deliver an annual energy demand for gas and electricity.
- Models for energy storage were built to handle the outputs from the dynamic simulation software.
- Outputs from each simulation were introduced into these energy storage models for each method considered.
- Results from these simulations were then to be analysed to inform on the behaviour of energy storage systems, on the sensitivity of scenario conditions, and on whether or not domestic energy autonomy was feasible using these types of energy system.

1.6 Thesis Outline

Chapter 2: An introduction to the Energy House research facility, the modelling software used in developing models of this facility, and the process involved in that development.

Chapter 3: A discussion of the performance gap phenomenon, its prevalence in building energy modelling and the solutions available through calibration to reduce that gap.

Chapter 4: An explanation of how the Energy House model was calibrated using in-situ measurements. A discussion of how the model was conditioned for the baseline model, and subsequent models using a variation of scenarios befitting the UK.

Chapter 5: Results of initial dynamic energy simulations, undertaken without the integration of energy storage. An analysis of these results to investigate the sensitivity of domestic energy performance to varying scenarios.

Chapter 6: A description of the models used to represent energy storage, supplementary components, and the logic used to design each model.

Chapter 7: Results of further dynamic energy simulations, undertaken with the integration of energy storage modelling. An analysis of these results to investigate the impact of sensitivity scenarios on energy storage performance and the tendency for energy autonomy.

Chapter 8: A conclusion and final discussion of the findings in this thesis.

Chapter 9: A list of references used throughout the work.

Chapter 2

Domestic Building Modelling

Abbreviations

ABERG	Applied Buildings and Energy Research Group
ASHRAE	The American Society of Heating, Refrigerating and Air-Conditioning Engineers
BRE	Building Research Establishment
BS/EN	British Standard of European Standardisation
CEN	European Committee for Standardisation
CIBSE	Chartered Institution of Building Service Engineers
EH	Energy House
HVAC	Heating Ventilation and Air Conditioning
IES	Integrated Environmental Solutions
ISO	International Organization for Standardisation
NIHE	Northern Ireland Housing Executive
ONS	Office for National Statistics
SAP	Standard Assessment Procedure
TRNSYS	Transient Systems Simulator

Nomenclature

C_P	Specific heat capacity (J/kg K)	t	Time (s)
i	Distance Increment	T	Temperature (K)
j	Time Increment	x	Distance (m)
K	Thermal Conductivity (W/m K)	ρ	Density (kg/m^3)

The first objective of this thesis was to build a model of a typical UK home so that this model could be used to simulate the performance of such a building under any desired condition. To achieve this objective, the building needed to be representative of the current housing stock. Figure 2.1 gives the proportionality of building types within the UK, showing that the terraced house is the most common building type of the recent existing housing stock. These data were taken from housing stock reviews of England and Wales (ONS, 2011), Scotland (ONS, 2010) and Northern Ireland (NIHE, 2009), and are relevant for the year 2009.

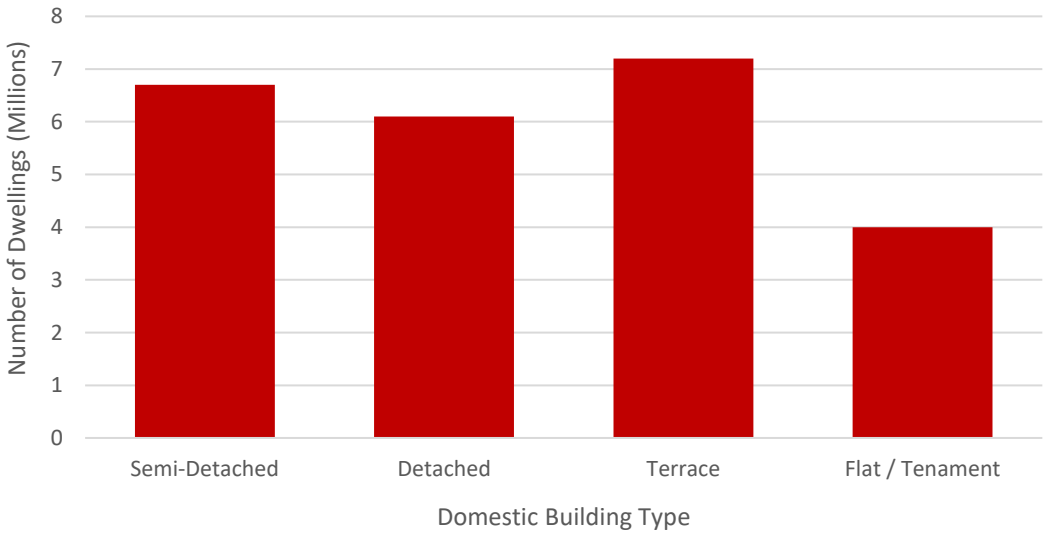

Figure 2.1 – Proportionality of domestic building types in the UK.

Although building type plays a part later on in the study, where the modelling of different archetypes was taken into consideration, it was decided that the basic model should be representative of a terrace house.

2.1 The Energy House Research Facility

The Energy House is a Research Facility belonging to the Applied Buildings and Energy Research Group (ABERG) at the University of Salford in Manchester. The facility, as described by Ji et al. (2014), is a pre-1920's Victorian terrace house built largely from reclaimed materials within an environmental chamber at the University. The house was constructed using traditional building methods to the periodic standard and keeps all of the original features. Figure 2.2 shows an image of the Energy House in the environmental chamber.

Figure 2.2 – The Energy House Research Facility at the University of Salford.

External walls of the building are a solid brick wall (222mm) with a lime mortar. Partition walls are single brick (111mm), and all internal faces are finished with a layer of plaster (13mm). The windows of the house are all single glazed sash (3mm) with wooden frames, all floors of

the building are suspended timber floors (20mm) and the roof of the house is at an angle of 32^{o}, using traditional slate tiles. The house is commonly known as a 'two up two down' house, with two main living areas downstairs (living room and kitchen), and two bedrooms upstairs. The only modification made to the house is an additional 100mm of mineral wool insulation in the roof. Figures 2.3 and 2.4 show the floor plans of the building, and figure 2.5 the elevation.

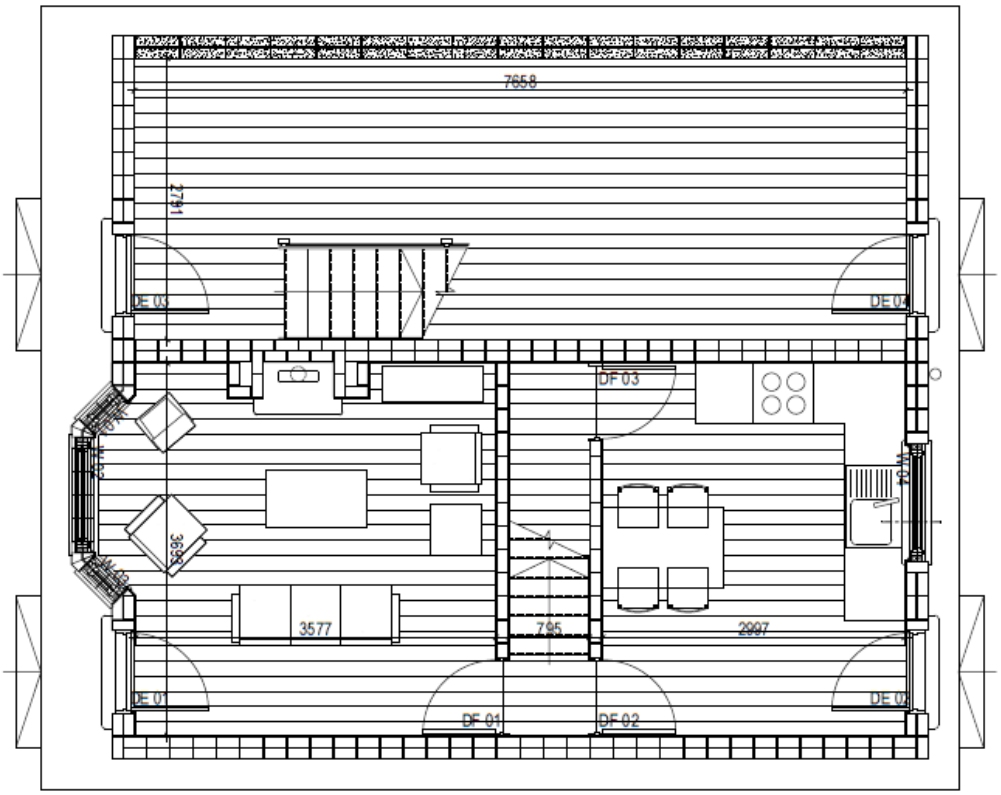

Figure 2.3 – Floor plan for the ground floor of the Energy House.

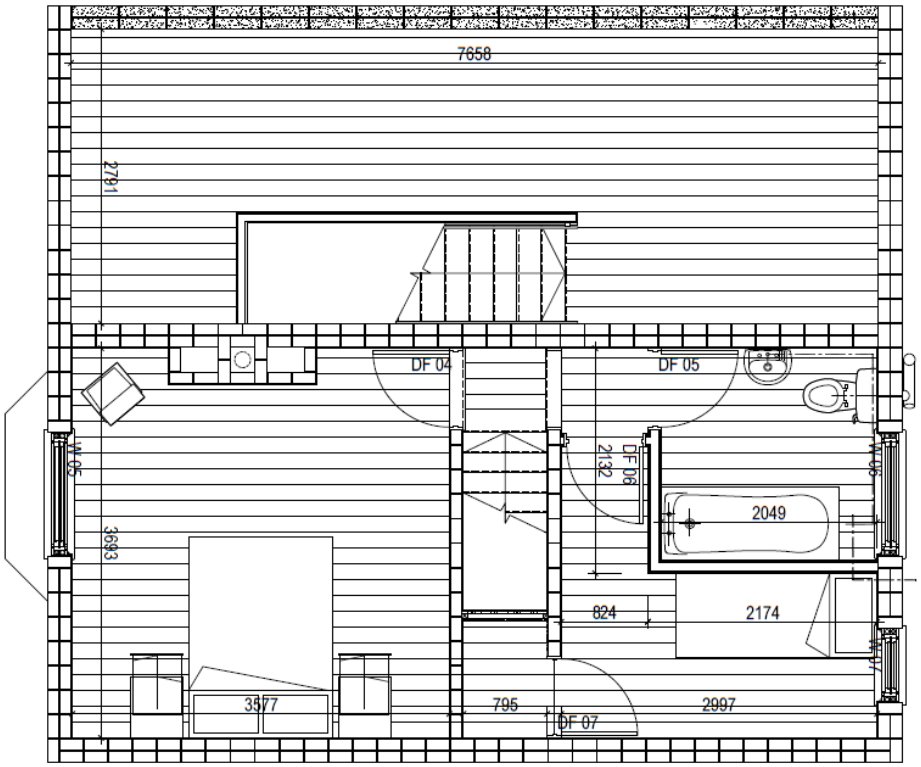

Figure 2.4 – Floor plan for the first floor of the Energy House.

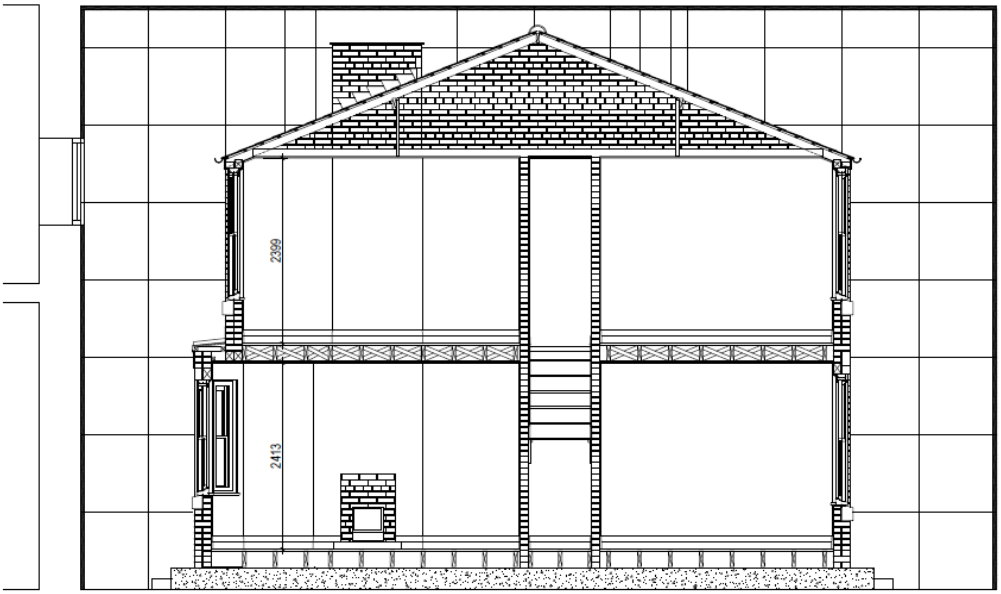

Figure 2.5 – Elevation of the Energy House.

The house is designed to be an end of terrace property, as can be seen on the plans there is an additional building adjacent to the house. This zone is reserved for conditioning the building and also houses plant services.

The chamber that contains the Energy House is designed in a way to allow customisable climate conditions. A sprinkler system generates wind driven rain, a series of fans varies the wind speed and direction, a mixture of pressurised air and cold water can be used to create snow, and a matrix of infra-red lamps can simulate solar radiation. The chamber also has a dedicated HVAC system to vary the temperature between -12^{o}C and +35^{o}C, while holding chosen temperatures constant to within ±0.5^{o}C.

A common requirement of research projects is the need for both steady state conditions and a mono-directional heat flow through the house's outer envelope. To facilitate this, the general operation of the house observes constant internal temperatures of 21^{o}C (Living Room) and 18^{o}C (Elsewhere), and a constant external chamber temperature of 4.4^{o}C. Internal temperatures are informed by the Standard Assessment Procedure (SAP), (BRE, 2010), which is used in determining the energy performance rating of homes in the UK. A wet central heating system is used to achieve these internal temperatures through the use of thermostatic radiator valves. The external temperature is held at the average winter temperature. To mimic the performance of a home in the field, the house has been fully kitted with furniture, appliances, carpets and curtains.

The facility has been fitted with a large quantity of sensors to capture variables as indicators of performance. The basic set of sensors measure relative humidity and temperature, radiative temperature, motion, carbon dioxide concentration, air velocity and heat flux. While data from these sensors can inform a wide variety of investigations, the common use of these

data is for identifying the building's thermal parameters, such as the U-values of specific building elements.

The general principle of the EH research facility is that real world conditions can be explored in a controlled environment. For that purpose, it has offered a platform upon which domestic based energy research can be performed. Examples of this is the work mentioned earlier by Ji et al. (2014): an investigation into overheating in existing UK dwellings, which covers the area of thermal comfort in homes. A majority of the work carried out at the facility however, do consider the thermal performance of materials – be it the existing fabric of the building or fabric introduced to the building to improve thermal performance – such as retrofit (see Pelsmakers et al., 2017; and Patil et al., 2017). Farmer et al. (2017) and Swan et al. (2017) presented substantial pieces of work concerning retrofit – where the gradual 'staged' installation of retrofit measures to a high level was monitored throughout. Thermal performance at each stage of the installation was recorded to determine the effectiveness at that stage. The research carried out at the Energy House to date has the dominant theme of thermal performance in domestic buildings. The idea discussed in the introduction that there is a general lack of attention given to domestic electricity consumption is simply reinforced by this dominance.

In having a familiarity with the structure of this building and by understanding how the building operates, it was possible to generate a model of the EH using dynamic modelling software.

2.2 Designbuilder: An Introduction

Dynamic modelling is used to simulate the performance of buildings under a set of predetermined conditions. Crawley et al. (2008) reviewed twenty modelling packages that have the ability to perform dynamic simulations on buildings. These packages included software such as Energy Plus (Crawley et al., 2004), TRNSYS (Klein et al., 2004), and IES-ve. Crawley et al.'s study conducted that of the software, Energy Plus had a superior performance.

Energy Plus is an authoritative modelling package that has been validated numerous times in literature (see Witte et al., 2001; Henninger et al., 2003; Henninger and Witte, 2011; and Shrestha and Maxwell, 2011), and using ASHRAE Standard 140-2010 (ASHRAE, 2010). It is the underlying engine behind the modelling tool Designbuilder – what is in essence a front-end user interface for Energy Plus – but with added features. In addition to the validation already received by Energy Plus, Designbuilder conforms to both BS EN ISO 13790:2008 (International Organisation for Standardisation, 2008), and EN 15265:2007 (CEN, 2007). These standards contain the methodology for determining building energy performance and for the calculation of energy for space heating and cooling. Each of the standards also support the modelling of domestic buildings. Figure 2.6 gives the flow diagram of the process involved in dynamic energy simulation as set out by BS EN ISO 13790:2008.

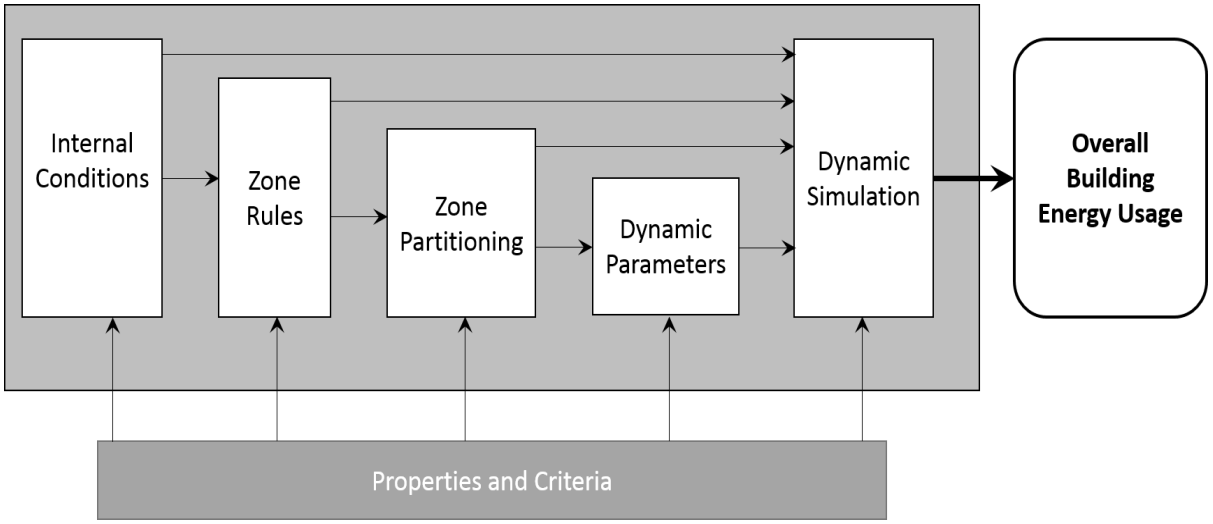

Figure 2.6 – Flow diagram for dynamic energy simulations in Energy Plus. Source: BS EN ISO 13790:2008.

A basic component of dynamic energy simulations is the ability to calculate heat balance. Heat balance within a building is determined using a finite difference model for each building element. Several calculations are carried out for each element, depending on the construction of that element, at each time step within the simulation. Figure 2.7 depicts the finite difference model used in this calculation.

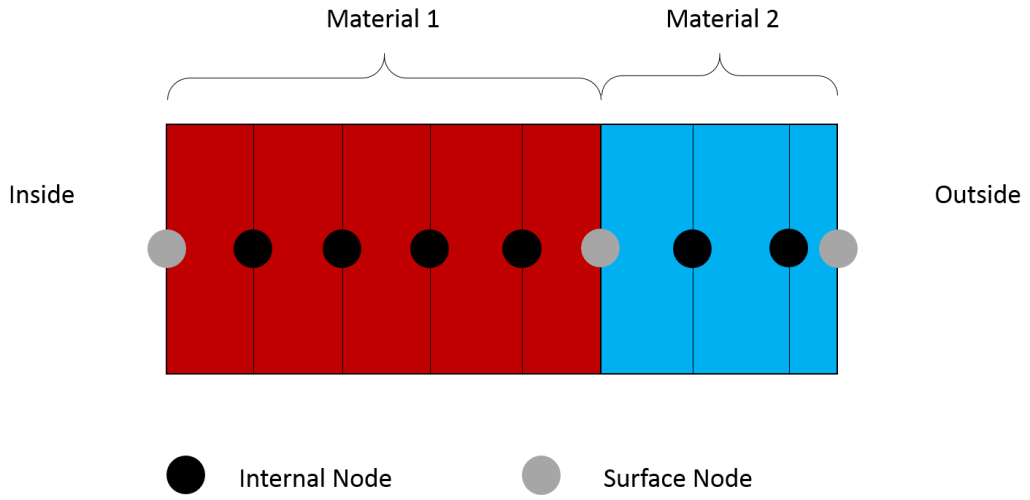

Figure 2.7 – Depiction of finite difference model used for calculating heat balance.

A series of nodes are distributed throughout the layers of material that make up a building element. These nodes represent discretised points at which heat transfer occurs. Internal nodes (found within the materials) and internal surface nodes (found between two layers of building material) are restricted to conductive heat transfer, while surface nodes in contact with the air consider the effects of convective and radiative heat transfer.

The equation for an internal node, which follows a Crank-Nicholson semi-implicit scheme, is given as:

$$c_P \rho \Delta x \frac{T_i^{j+1} - T_i^j}{\Delta t} = \frac{1}{2}\left(k_1 \frac{T_{i+1}^{j+1} - T_i^{j+1}}{\Delta x} + k_2 \frac{T_{i-1}^{j+1} - T_i^{j+1}}{\Delta x} + k_1 \frac{T_{i+1}^{j} - T_i^{j}}{\Delta x} + k_2 \frac{T_{i-1}^{j} - T_i^{j}}{\Delta x}\right),$$

where
- c_p is the specific heat of the material,
- ρ is the density of the material,
- Δx is the thickness of the finite layer,
- T is the temperature of the finite layer,
- Δt is the difference in time between each calculation,

$k_{1,2}$ is the thermal conductivity at the interface of the finite layer,

i signifies the current node,

i-1 the previous node,

i+1 the next node,

j the previous time step,

j-1 the new time step.

A series of equations representing each building element can be summated to give the overall heat balance for the entire building and thus inform an overall energy demand. The introduction of a quantity of heat to internal zones of the building (such as that of heating) determines the internal boundary condition of temperature at the surface of building elements. External temperatures determine the external boundary condition, and therefore the rate of heat transfer through the element at a single point in time. These equations can be used dynamically to determine the response of a building to varying environmental conditions, or in steady state to determine an overall heat loss given a fixed set of boundary conditions. The rate of heat transfer is in turn determined by the physical parameters and thermodynamic properties of the materials used for individual building elements.

Models are fully customisable in terms of both inputs and outputs, with inputs including these physical parameters and properties. This section now gives a brief overview of the model building process.

Figure 2.8 illustrates the modelling hierarchy used when creating any building model and the features that are contained at each level. This process was followed to create the model of the Energy House in Designbuilder, a process which is tracked in the next section.

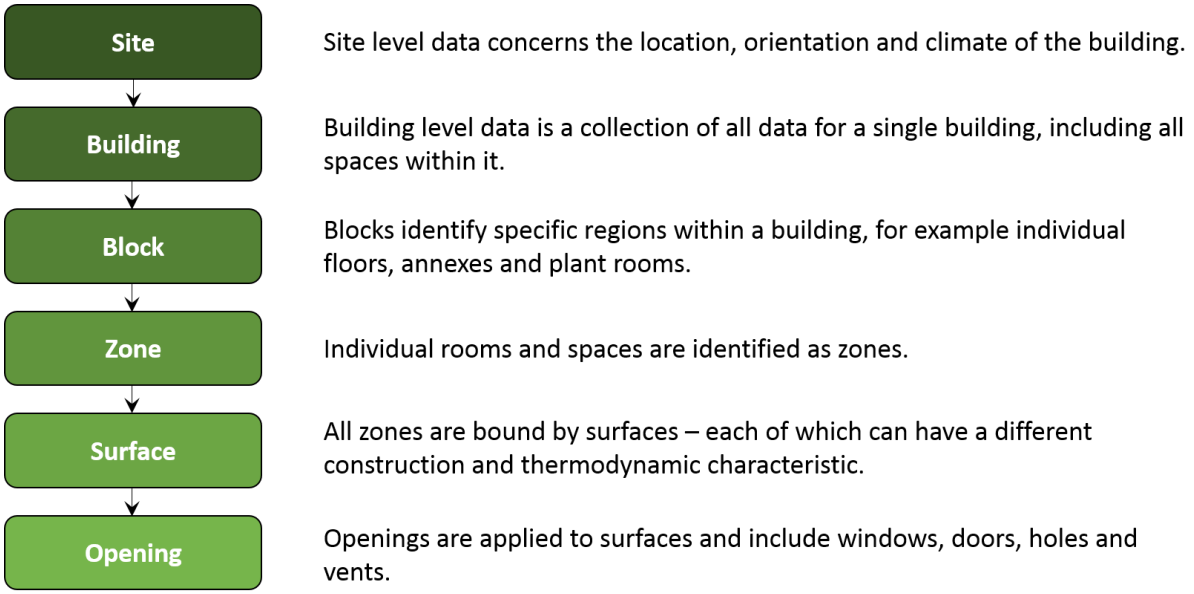

Figure 2.8 – Hierarchy used for building models in Designbuilder

2.3 The Energy House Model

This section follows each hierarchical step taken to build the model of the Energy House. Though multiples of each step exist, given there are multiple zones to the building that feed down into multiple zones and so on, only one example of each is given.

2.3.1 Site

The Site of the Energy House facility is difficult to recreate in Designbuilder, given that the house itself is in an environmental chamber, the dynamic weather generated within that chamber could place the building almost anywhere in the world. Since the house is located in Manchester in the UK, Site details for the house are set to mirror this location. Table 2.1 lists the features of the model at Site level, noting that since the weather station data comes from Manchester Airport, the data belonging to the building is based around this location.

Table 2.1 – Site level data assigned to the Energy House Model

Parameter	Value
Location Template	Manchester Airport
Latitude / Longitude	53.35 -2.28
Elevation above sea level	78m
Exposure to weather	Standard
Site Orientation	North Facing
Time	GMT
Weather Data	Manchester Ringway (CIBSE)

2.3.2 Building Level

This level simply collects all of lower hierarchy levels. From the building level, all settings can be modified for application at the lower levels. The main feature at this level is the HVAC setting, which can be customised for the building. As mentioned earlier, a wet central heating system serves the EH's heating needs. The HVAC system applied to the Designbuilder model reflects this and is shown in figure 2.9. The zone group attached to the heating system is the collection of radiators used in heated spaces. These spaces include the living room, kitchen, hall and stairs, bathroom, and both bedrooms.

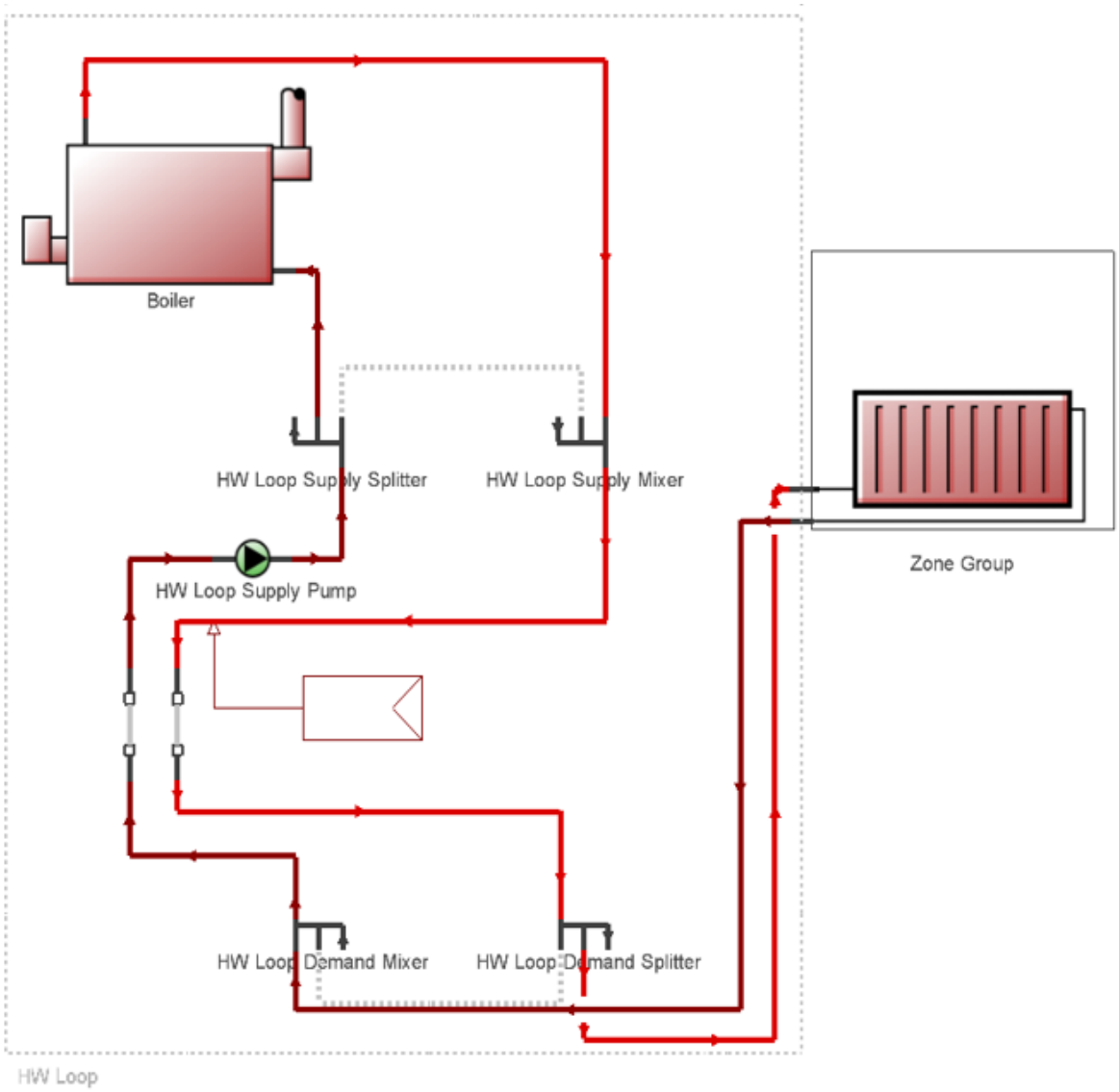

Figure 2.9 – HVAC system of the Energy House.

2.3.3 Block Level

This level manages the division of key building areas, typically reserved for individual floors, however it can specify particular areas such as staircases. The model of the energy house is broken into a number of different blocks, which make it easier to model given the internal features of each block. The living room and master bedroom for example have a chimney

featured within their space – so it is easier to have these rooms as an individual block so that this feature can be modelled appropriately. The staircase is a complex feature of the house which also required individual modelling as a separate block. The remainder of the upper floor (second bedroom and bathroom) however, remained grouped together. The base of the building is an example of how non-complex building levels can be grouped in a block. This block grouping is shown in figure 2.10.

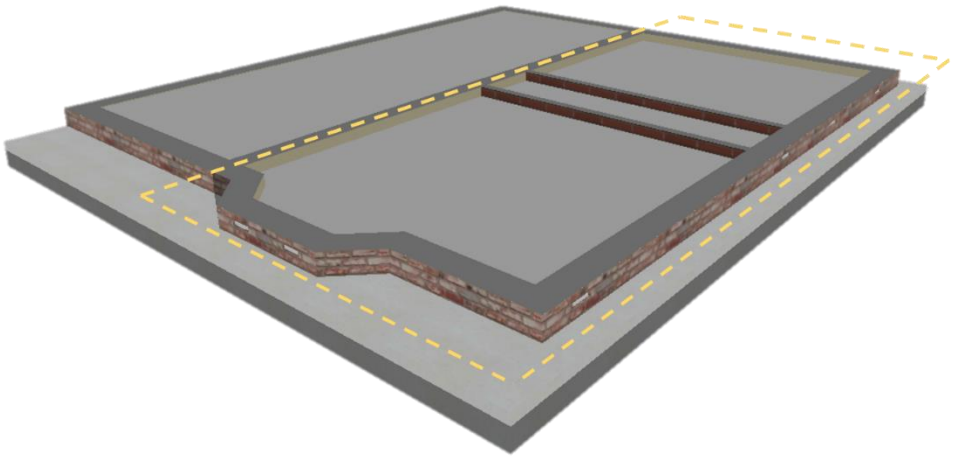

Figure 2.10 – Example of a building block (Building Base).

2.3.4 Zone Level

At this level, the data of a single room is captured. Each zone can be assigned with a particular parameter, depending on the type and use of that room. The individual zones of the Energy House are: the base, living room, kitchen, hall and stairs, kitchen store, master bedroom, second bedroom, bathroom and storage cupboard. The roof is also a zone, though this is considered unoccupied.

The following details groups of parameters for customisation:

- Layout
- Activity
- Construction
- Openings
- Electrical equipment
- Lighting
- HVAC

The **layout** of a zone gives a visualisation of the room plan; wall dimensions and positioning of openings can also be seen at this level.

The **Activity** in a zone is a general overview of occupant behaviour. While it informs simulations of the occupant density, metabolic rate due to activity and consumption of hot water, more importantly the activity in a zone defines the heating controls. Heating and cooling set points and set-backs can be allocated here. Schedules for occupancy are also set here, the UK NCM (National Calculation Methodology) (Department for Communities and Local Government, London) informs on these.

Construction allows the surface types (e.g. solid wall, cavity wall and partition wall) contained in the zone to be modified, for example all external walls, pitched roofs and floors. This group also contains data for the building's air permeability.

Openings contains data for all windows and doors of the zone.

The **Equipment** group identifies gains due to appliances within the zone. These can be pre-set for given activities or defined outright.

Lighting controls the type, thermal properties and control of lighting within the zone.

Finally, **HVAC** contains some of the more important data regarding space heating and cooling. At this part of the zone level, the type of HVAC system is identified, along with heating and cooling schedules, controls for natural ventilation and domestic hot water.

Figure 2.11 shows an example of this level by displaying the living room of the Energy House.

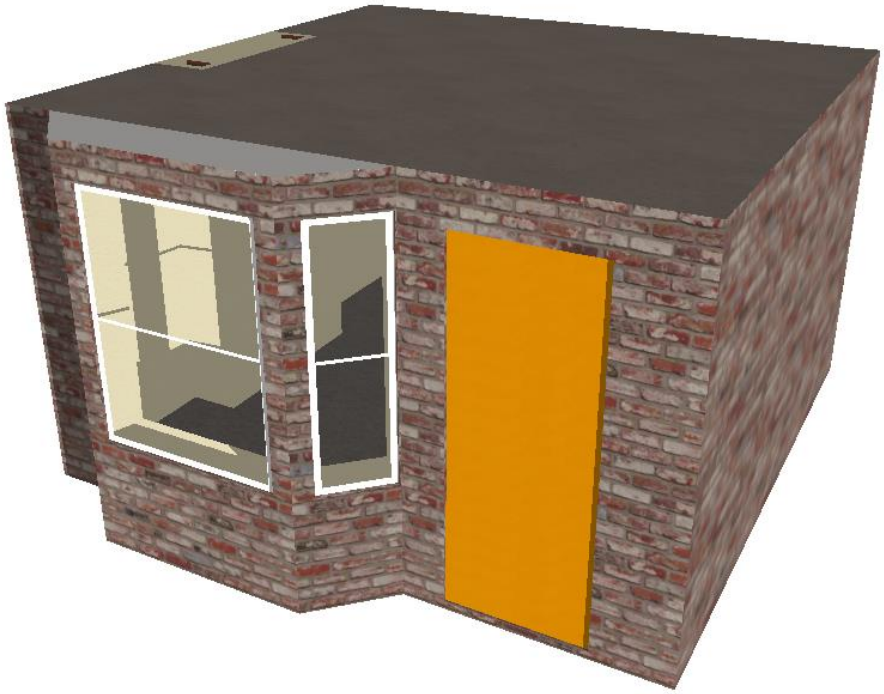

Figure 2.11 – Designbuilder representation of a single zone (the living room of the Energy House).

2.3.5 Surface Level

The individual properties of surfaces can be modified here and can be seen as one of the most important factors to consider within the modelling process. At this point, this is where

building elements are created – as they might be found in the real building. E.g. for a solid wall construction, the building element consists of 222mm brick to the outside, with 13mm of dense plaster at the internal finish. The thermodynamic properties of each material used, and the chosen thickness of those materials will ultimately determine the loss (or gain) of heat through that surface, and collectively through the entire building envelope. The materials chosen are pre-allocated with thermodynamic properties as per CIBSE Guide A (2006), and ISO 10456:2007 (International Standardisation Organisation, 2007).

Second to surface composition is the control of adjacency. This is important when considering surfaces that connect to external spaces – be it the air, the ground or an adjacent building. The behaviour at these different types of junctions can impact greatly on the heat transfer from that surface.

The model of the Energy House considers six different initial types of surface; figure 2.12 shows these types and displays the composition of each.

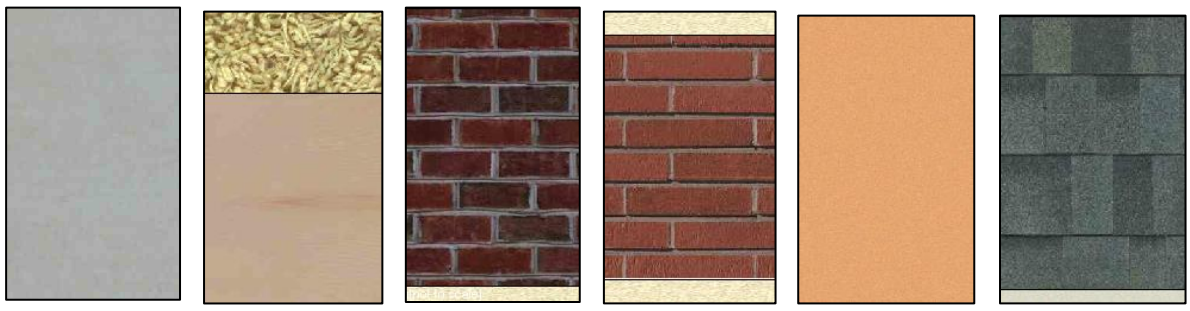

Concrete Base | **Suspended Timber Floor** | **Solid Wall** | **Partition Wall** | **Roof Insulation** | **Slate Roof**

Figure 2.12 – Surface type and composition in the Energy House model.

2.3.6 Openings

The final level to consider is openings. As with surfaces however, openings form an integral part of models as they are an essential feature of buildings, they also contribute considerably to the heating and cooling demand of a zone and to the building as a whole. While surfaces contribute some heat flow, openings contribute both heat and air flow, resulting in additional and significant transfers of heat. Examples of openings are windows, doors, holes and vents. Windows of the Energy House model are set to reflect the single glazed sash windows in-situ; doors of the house are chosen as standard timber doors; holes are used to provide airflow to the chimney; and vents are used in the base of the model to represent air bricks.

2.3.7 Outputs

While determining the content properties at each level of model building, it is important to keep in mind the outputs of both static outputs and dynamic simulations that can be delivered by Designbuilder.

Static outputs consider steady state properties of the building. This is important in determining the heating and cooling system of a building. Although HVAC type and conditions are informed while building the model, the size of that HVAC system is decided automatically by the software. To do this, typical winter (for heating systems) and summer (for cooling systems) temperatures are used to calculate the heat required given a fixed internal temperature. Figure 2.13 shows the output for the Energy House's heating system design, where each contribution to heat balance is quantified. The external temperature used for this calculation was -4.4^{o}C, and the internal temperature 18^{o}C.

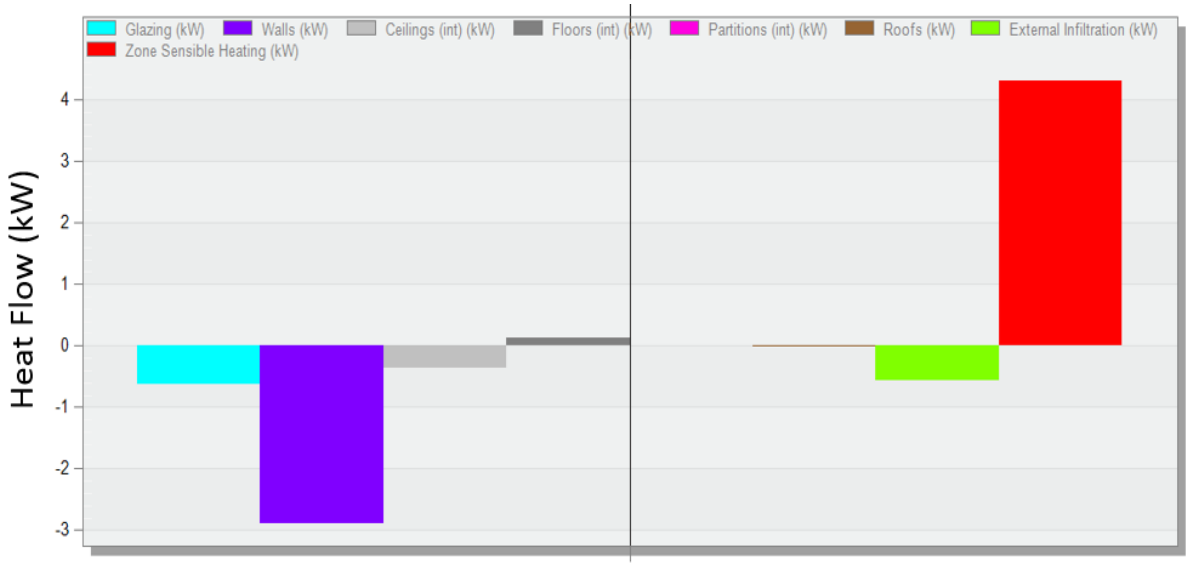

Figure 2.13 – Balance of heat gains and losses under steady state conditions for the Energy House model.

By assuming steady state conditions with fixed internal and external temperatures, Designbuilder calculates the required heat input into zones to balance the losses accumulated through each component. Quantities presented in figure 2.13 reveal that the greatest predicted heat loss from the Energy House is through the external walls. Designbuilder calculates the size of the heating system to be 5.37kW. Note that cooling requirements are unnecessary for this building at this time.

Dynamic outputs from Designbuilder cover a wide range of areas, from energy consumption to environmental conditions, temperature distributions, heat fluxes and air flows through to calculations thermal comfort. Outputs can be assigned depending on the level at which results are accessed. For example, surface temperature or heat flux is an output at the surface level; airflow and thermal comfort requires zone level outputs as a minimum; while some outputs can be summarised for the entire building.

Figures 2.14a, 2.14b and 2.14c show the typical heat gains, heat losses, and resulting zone temperature for the master bedroom of the Energy House, when simulated using Manchester weather for a weekday in June.

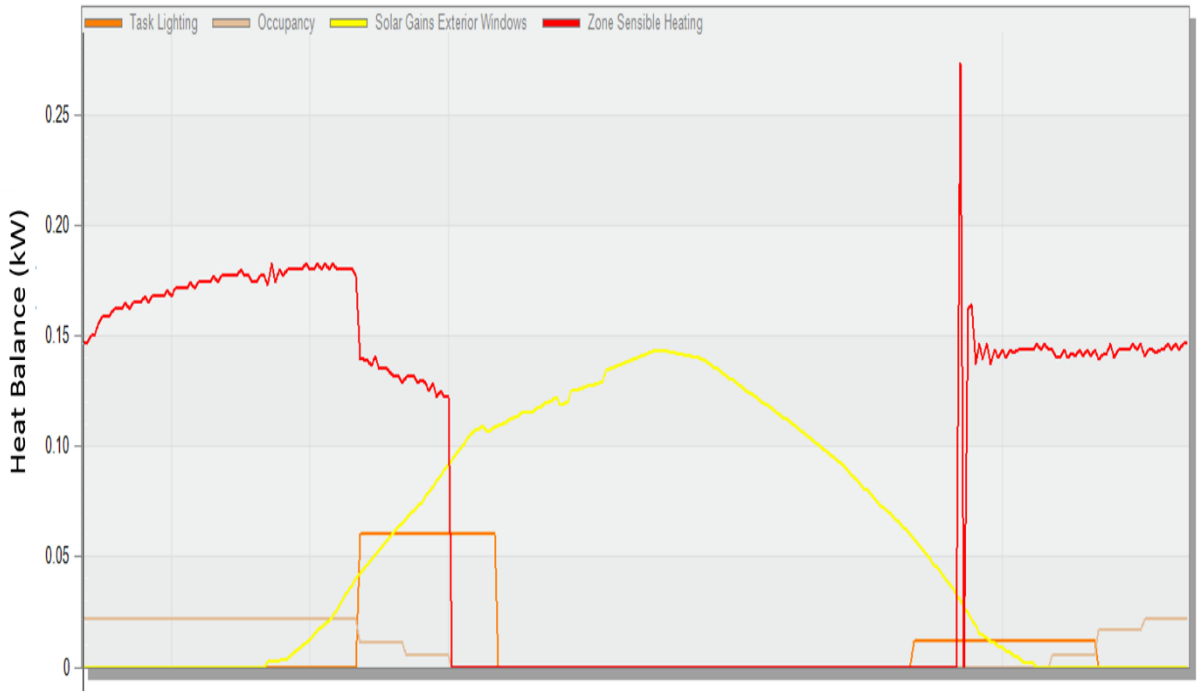

Figure 2.14a – Typical June weekday heat gains for the master bedroom of the Energy House.

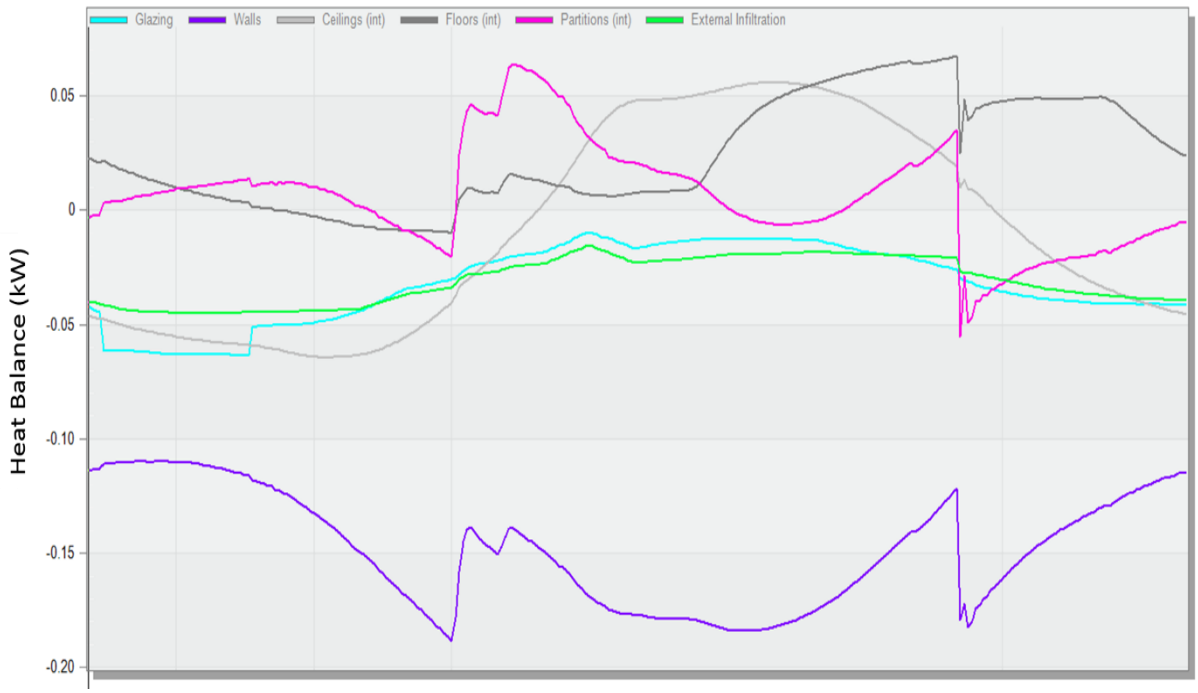

Figure 2.14b - Typical June weekday heat losses for the master bedroom of the Energy House.

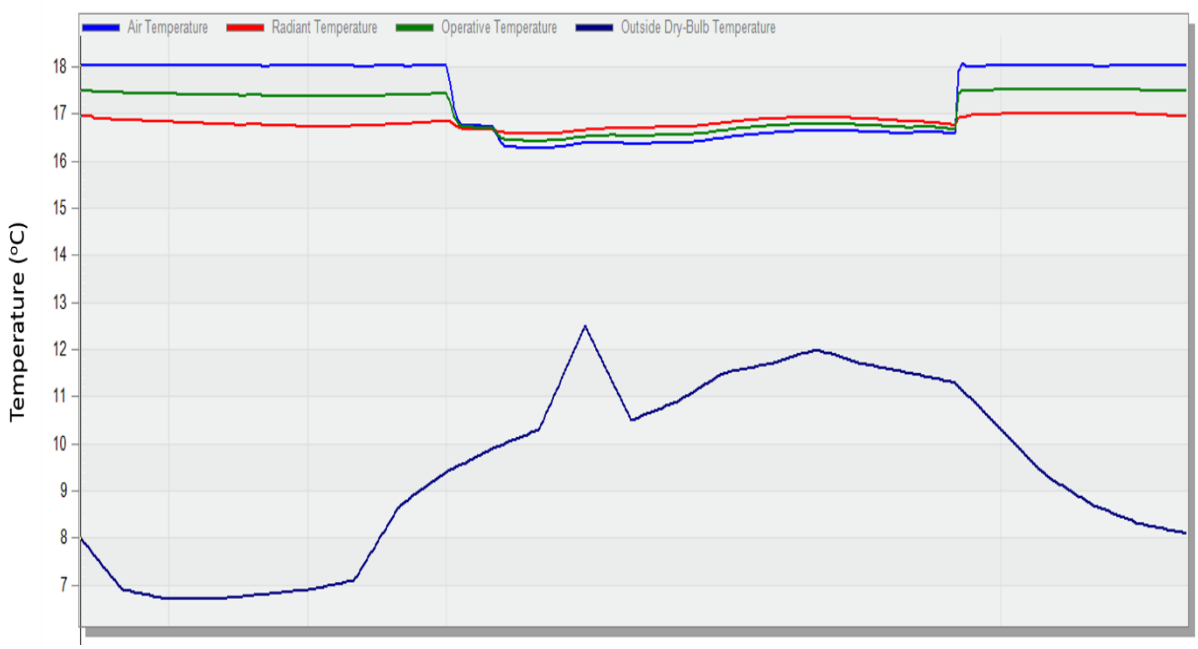

Figure 2.14c - Typical June weekday temperatures for the master bedroom of the Energy House.

These arbitrary results demonstrate how occupancy patterns play a key role in the heating cycle of a zone (active during the night and inactive during the day), and also how fabric and ventilation gains and losses of heat contribute to the variation of temperature within that zone throughout the day.

With all of the considerations made for both inputs and outputs from Designbuilder, a model of the Energy House was built to reflect the realistic dimensions, building element composition and operability of the actual building. Figure 2.15 shows the final model as built in Designbuilder.

Figure 2.15 – Final rendered model of the Energy House in Designbuilder.

This model demonstrated a good representation of the geometry and building element distribution of the Energy House facility, however a model's suitability is found in its ability to accurately predict the performance of the building in question. The next chapter moves on to discuss how the thermodynamic parameters assumed by the model actually obstructed the model's functionality.

Chapter 3

The Performance Gap and Model Calibration

Abbreviations

BREEAM – Building Research Establishment Environmental Assessment Method

DEAP – Dwelling Energy Assessment Procedure

DEC – Display Energy Certificate

EPC – Energy Performance Certificate

PSTAR – Primary and Secondary Terms Analysis and Renormalisation

RIBA – Royal Institute of British Architects

SEAI – Sustainable Energy Authority of Ireland

Nomenclature

y	The measured output from a set of conditions
δ	Discrepancy between measured and modelled outputs
ε	Uncertainty of measured values
μ	The modelled output from a set of conditions
θ	A series of uncertainties

"Essentially, all models are wrong, some are useful."

- George Box (1987).

Box's work on statistical models encouraged him to comment on the validity of models, suggesting that all models are wrong, and yet by excessive elaboration no model will ever be "correct". Instead, Box insists that in modelling, there should be an "economical description of natural phenomenon", which lends insight and usefulness. This chapter examines the model generated in the previous chapter for its usefulness in predicting the energy performance of the Energy House. The performance gap is first introduced as a concept, before the root causes and implications are discussed. Established calibration methods used in closing the performance gap are then explored, before moving onto the author's work on closing the performance gap in the next chapter, by calibrating the model of the Energy House.

3.1 The Performance Gap

Any model whose predictive capacity demonstrates discrepancy between the predicted performance of a building and the actual performance of that building experiences a phenomenon known as the 'performance gap', the implications of which can be far reaching and will be discussed in due course.

De Wilde (2014) highlighted the growing body of concern for this phenomenon and the significant impact the performance gap can have on predictive modelling. Possible sources of the gap have been identified at design level, construction level and with post occupancy, each of these are now explored.

3.1.1 Design, Construction and Post Occupancy

At design level, performance gap issues arise due to a mismatch between the design of the building at that stage, and the future operability of that building. Performance gaps manifest here in a number of different ways, the simplest of which can be found in the design of the building itself. Complex buildings, favoured for their aesthetics result in a great deal of problems due to a potential abundance of thermal bridging, which results in higher than normal heat loss from a building. The design of complex buildings, whose components require unfamiliar building techniques or materials also leave room for poor performance (Dronkelaar et al., 2016).

A lack of expertise from a limited design team can often lead to building design and aesthetics taking precedence over the requirement of appropriate energy systems. Installation of apparently suitable components would then lead to under or overperformance in the building's future operations (Zero Carbon Hub, 2013).

Communication is key to the propagation of appropriate design requirements from the start to the end of a construction project. Often, different groups from the occupant, to the designers, to the builders and even energy performance inspectors will be involved in the commissioning of new builds. With each involved party however, comes greater risk of

miscommunication of the function of that building, and therefore greater chance that building systems will either under or over perform (Dronkelaar et al., 2016).

Several issues arise at the construction level (Zero Carbon Hub, 2014). The theme of knowledge and skills within the construction industry plays a large part in inducing the performance gap. General poor fabric installation is a major source of heat loss that is not predicted in the design of the building; the same can be said about the installation of energy systems and services. An overall shortage of both awareness and understanding of construction teams on energy performance and the impact of build quality on that performance is also an issue. The lack of knowledge in construction becomes an even greater issue when considering the introduction of restrictive legislation around building standards. Other issues such as fabric substitutions can also arise on site and lead to problems when later identifying materials for performance analysis.

Post-occupancy evaluation of building energy performance has revealed that the behaviour of occupants themselves can cause a significant deviation in the energy performance of a building. Revealed more specifically for electricity consumption in office buildings, the behaviour of occupants has demonstrated discrepancy between design energy use and actual energy use of up to 69% (Martani et al., 2012). A study performed by Hong and Lin (2013) in which an office space was modelled, by varying the working pattern of office occupants a variation of between -50% and +90% in energy consumption was found.

In-use occupancy patterns also present problems during the modelling of buildings for energy performance analysis, where assumed occupancy patterns are used (Zero Carbon Hub, 2014). In reality, occupants are unpredictable and will not behave in a manner consistent with predictive models, resulting in an impassable uncertainty over whether occupancy schedules

for a building are inaccurate, or whether occupants simply introduce unexpected demand into energy models (i.e. leaving equipment switched on), (Dronkelaar et al., 2016). In later post-occupancy, the degradation of systems and poor maintenance of energy systems and building infrastructure then has a further impact on the performance gap, given models are designed with optimal system operating conditions in mind.

The propagation of factors impacting the performance gap can be reviewed from the initial design stages, right the way through to post occupancy. A useful way to visualise this linear progression, and to review further causes of the performance gap, is to identify its sources throughout the lifecycle of a building. Figure 3.1 shows a comparison between the RIBA Plan of Work (RIBA, 2013), a UK framework for the design and construction process; and the performance S-curve as developed by Bunn and Burman (2015), which observes the causes for variation in performance at the different stages of the design and construction process, from the original design performance.

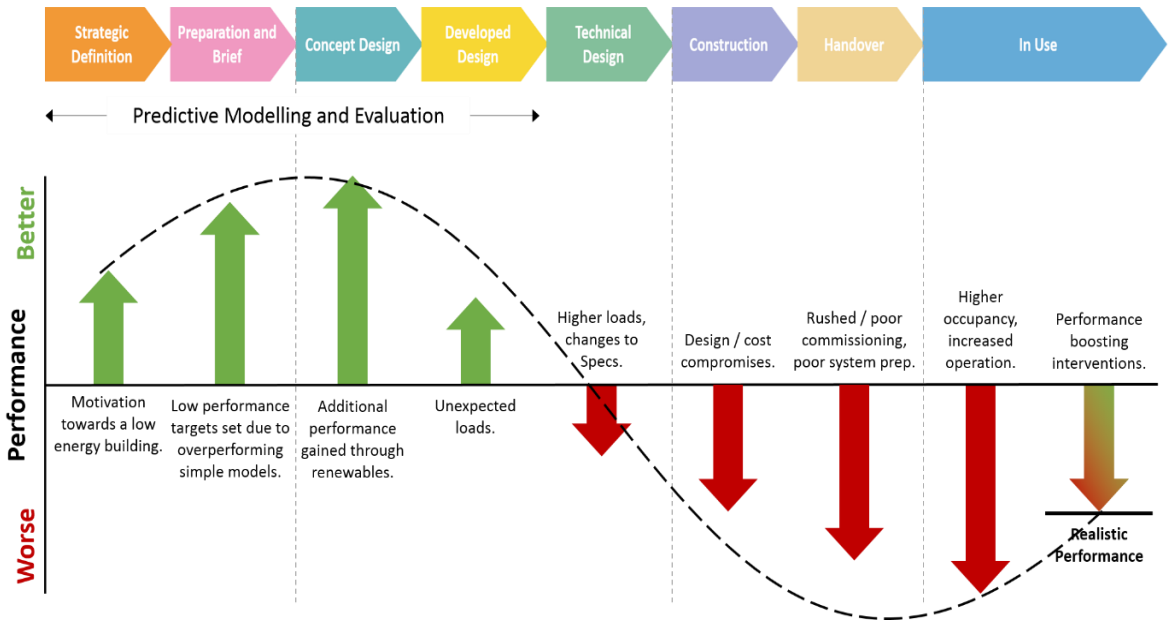

Figure 3.1 – Causes of variation in performance at different stages of the RIBA Plan of Work. Adapted from RIBA (2013) and Bunn and Burman (2015).

While the variation in performance throughout the stages of design, construction and post-occupancy all contribute to the performance gap, contributions from the process behind predictive modelling must also be taken into consideration. During this process, modellers have at their disposal their own modelling skills and information on each level of the building as described in figure 2.7 of the previous chapter. Although contributions to the performance gap from human error while modelling is a possibility, greater concern surrounds the information used to parameterise predictive models.

3.1.2 Predictive Modelling

One of the more important building levels visited in the previous chapter was that of the surface – collectively acknowledged as the building envelope – and the openings applied at

this surface level. The thermodynamic properties of a building's envelope determine the overall heat loss from that building and so the energy demand for heating; ensuring accurate parameterisation of building fabric is an important factor to consider in achieving accurate predictions of building performance. A great deal of works have identified a discrepancy between information supplied to modellers concerning this fabric parameterisation.

Work carried out by Doran (2001) as part of an investigation into the thermal performance of construction elements as built, for example, compares the calculated U-value of some 29 building elements to the U-value found through in-situ measurement. The calculation of U-values was carried out according to ISO 6946:2007 (International Organisation for Standardisation, 2007), while the U-value measurement was carried out to ISO 9869-1:1994 (International Organisation for Standardisation, 1994). Measured elements of Doran's investigation consisted of a mixture of empty and filled cavity walls, frame walls and ceilings. Figure 3.2 gives summarises the data gathered for each building element.

The line plotted against the data of figure 3.2 shows where the data would lie, were they equal. What figure 3.2 demonstrates is that for a majority of cases (74% of the overall results), the measured U-value was higher than the predicted U-value. When carrying out predictive modelling of buildings, it is often common practice to use U-values sourced using standardised methods, such as ISO 6946. As demonstrated by the data gathered by Doran, standardised U-values, more often than not, don't reflect the true parameter of building elements. Predictions made by models using these standardised parameters would then not reflect the true performance of the building, giving rise to contributions towards a performance gap. In the case of Doran's results, predictions based on calculated U-values would tend to be an over performance of the true building's performance.

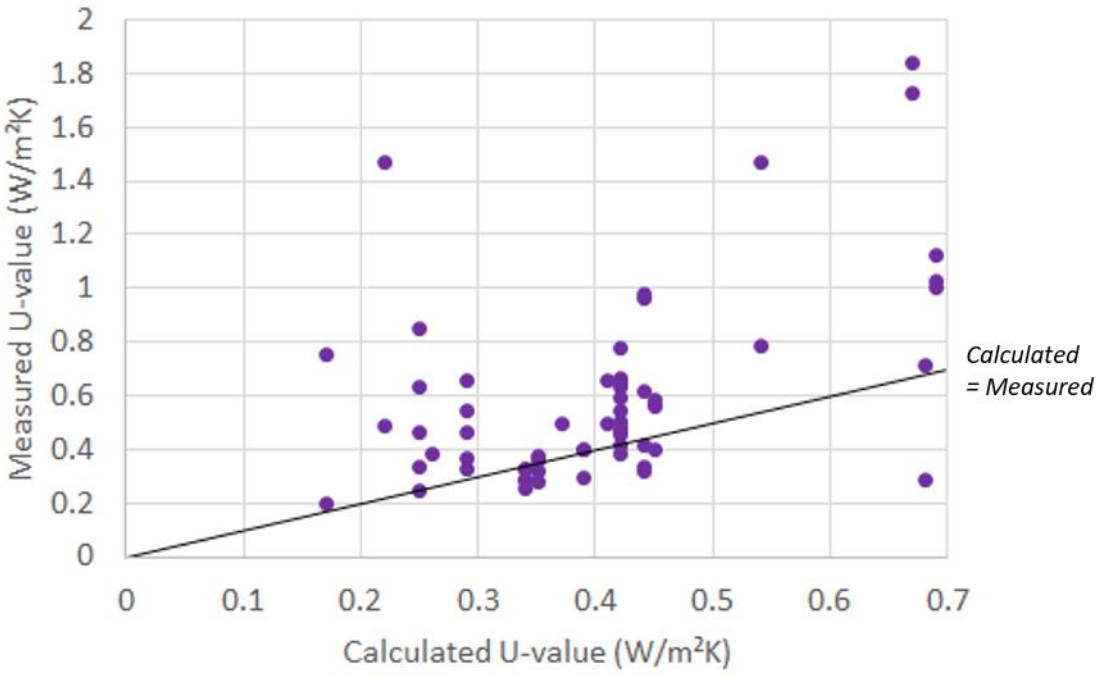

Figure 3.2 – Comparison of calculated and measured U-values for domestic building elements (Brickwork). Adapted from Doran (2001).

A similar investigation by Doran and Carr (2008) compared calculated and measured U-values under the context of retrofit installation. A mixture of archetypes (detached, semi-detached, bungalow) was considered for the investigation, each with a cavity wall. Seventy dwellings were assessed both before and after the application of cavity wall insulation, and the benefits of that insulation examined. This took into account the predicted retrofit benefit and the actual retrofit benefit.

Contrary to Doran's previous work, the building elements that were measured pre-retrofit are divided almost by half, with half of the U-values being overestimated and half being underestimated. In only one of the cases did the measured U-value equal the calculated U-value. Given this divide, predictive models would both overestimate and underestimate the

thermal performance of buildings such as these. This is particularly unfortunate in the context of the investigation, as incorrect applications of retrofit measures may arise from inaccurate calculations of building performance, this impacting on any anticipated variation in energy consumption or thermal comfort as a result of this structural modification. Figure 3.3 displays a comparison of the data obtained by Doran and Carr.

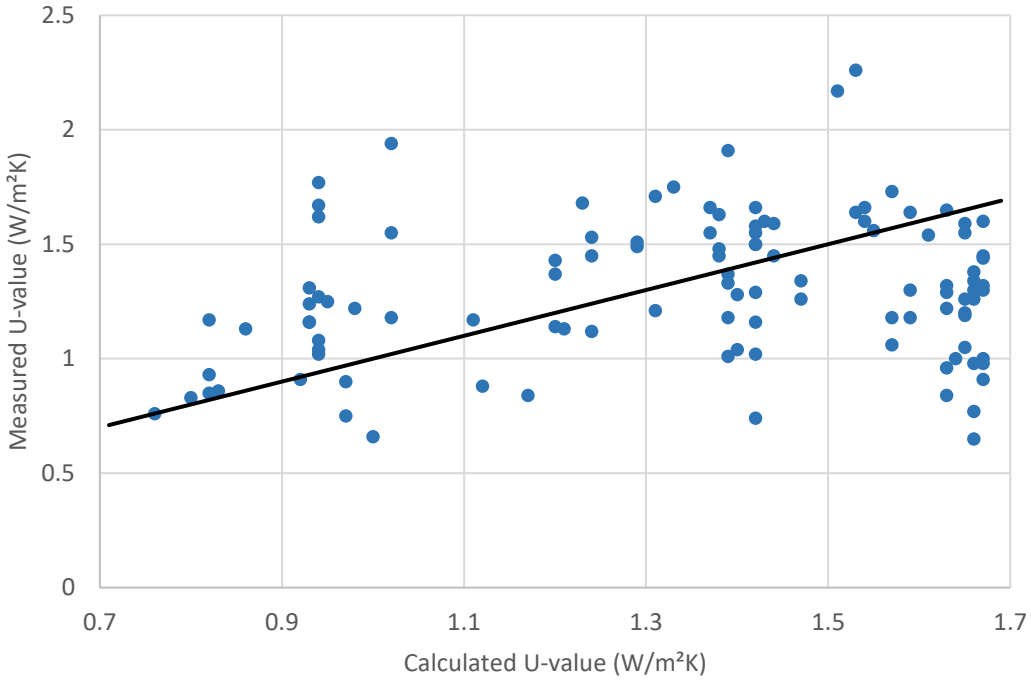

Figure 3.3 – Comparison of calculated and measured U-values for domestic building elements pre-retrofit. Adapted from Doran and Carr (2008).

Post-retrofit comparisons of calculated vs measured U-values told a different story however, with a majority of measured U-values (84%) being higher than the calculated U-value. This means that of the building elements under investigation, a majority of them did not meet the expected target thermal performance. In reality, these buildings would then underperform in

comparison to any models populated with standardised U-values. Figure 3.4 shows the comparison of measured and calculated U-values post-retrofit.

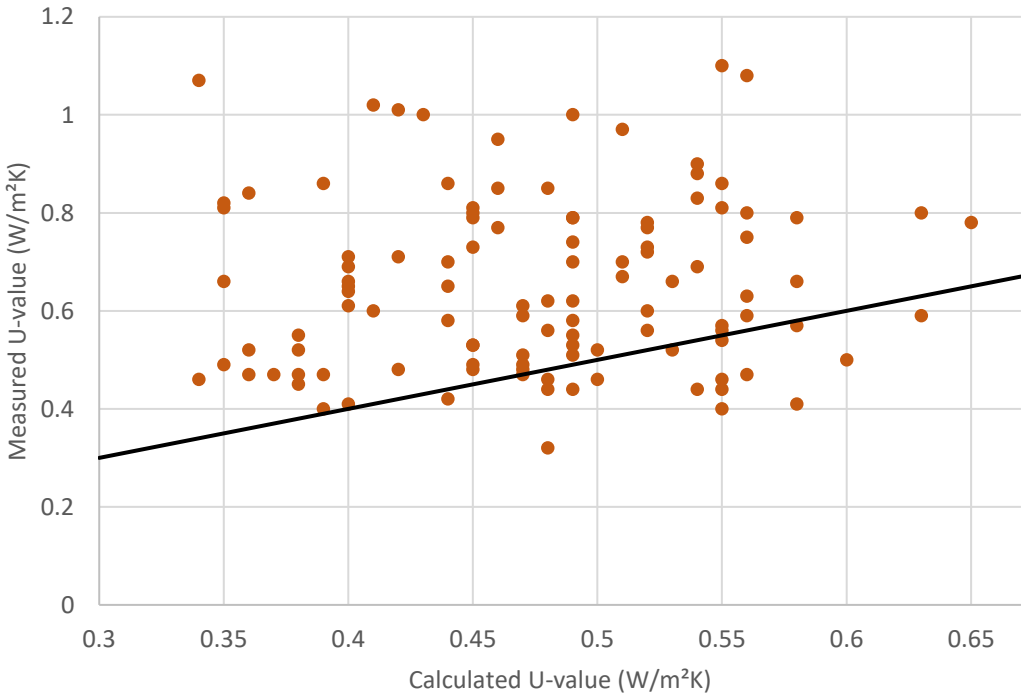

Figure 3.4 – Comparison of calculated and measured U-values for domestic building elements post-retrofit. Adapted from Doran and Carr (2008).

The effectiveness of insulation can be determined by comparing the measured increase in thermal resistance against the calculated increase in thermal resistance. Figure 3.5 shows this comparison for the walls measured in Doran and Carr's investigation.

What figure 3.5 demonstrates is that the real benefit of the installed retrofit is much lower than anticipated, in this case it is true for 85% of the measured building elements. Two

significant consequences occur because of this: higher than expected energy consumption and overall reduced thermal comfort.

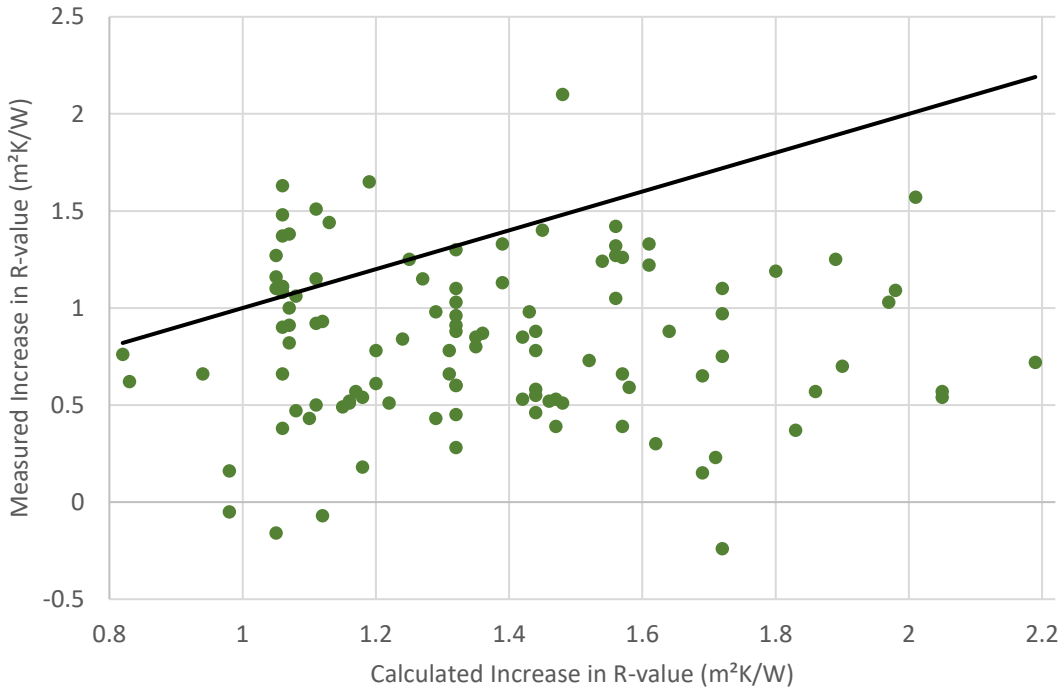

Figure 3.5 – Comparison of calculated and measured increase in thermal resistance of domestic building elements. Adapted from Doran and Carr (2008).

Baker (2011) too carried out a study on numerous dwellings in Scotland in an investigation aimed at solid wall buildings with a lime-and-stone core. The intention of this was to investigate the validity of standardised U-values for this type of building element, since the structure is entirely heterogeneous. Baker discusses that these structures are often assigned a range within which the U-value sits, even so these ranges are often conservative and overestimate the true performance of the structures.

Sixty-seven measurements were made on uninsulated solid walls and then compared to the calculated U-values for that composition of solid wall. Baker found discrepancies in all but two of the building elements measured, with a 67% majority of calculated U-values underestimating the thermal performance of the walls. This is reflected in figure 3.6, with positive differences between calculated and measured U-values demonstrating an overall better performance of buildings than their calculated performance might suggest.

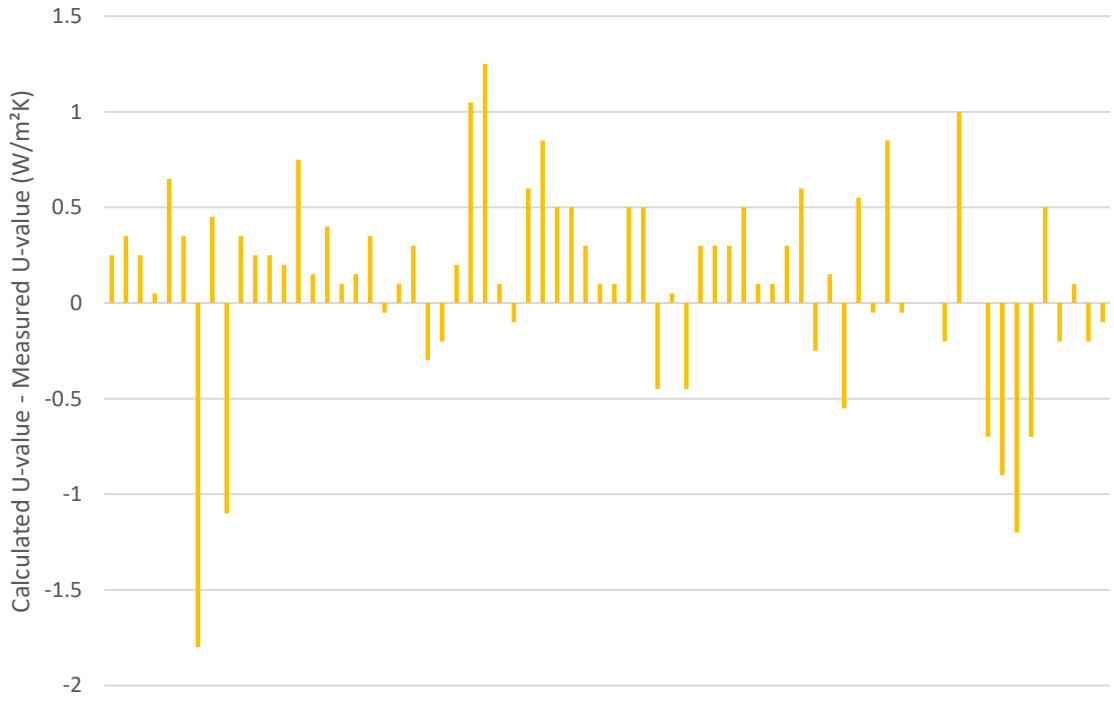

Figure 3.6 – Discrepancy between calculated and measured U-values of lime-and-stone core solid walls. Adapted from Baker (2011).

The findings of Baker support the conclusions of Doran and Doran and Carr's work, at least for uninsulated building elements, that standardised U-values tend to be overestimated. Discussions within these investigations points to conservatism in assigning standardised U-

values to building elements, allowing for the possibility of material performance degradation over time and the exposure to conditions that increase U-value.

Further evidence of this is provided by Rye and Scott (2012), who by investigating the discrepancy between calculated and measured U-values, found that of a mixture of homogeneous and heterogeneous building structures, overestimation of U-value occurred in 77% of all cases.

The impact of using inaccurate fabric parameters in predictive models is that predicted energy consumption and building behaviour due to dynamic conditions is misrepresented. Connotations of this have already been seen in Doran and Carr's work with retrofit, where application of performance improvement measures largely fail to meet the desired targets.

The discrepancy presented by the performance gap can have significant impact, considering discrepancies of up to 153% have been found (Evangelisti et al., 2015), some rectifying solution must be sought. Ahern et al., (2016) discuss how the performance gap impacts on predictions of energy performance to qualify energy ratings of buildings. It was determined that more often than not, buildings are assigned much lower energy ratings than they deserve – likely due to an overestimation of the U-values used in rating determination. Ahern et al. look at buildings in Ireland using the Dwelling Energy Assessment Procedure (DEAP), (SEAI, 2012) and determine that the underestimation of a building's energy performance has led to misinformed installations of retrofit and so the validity of the method used is scrutinised.

The authority of procedures that determine building energy ratings is no stranger to scrutiny. The work by de Wilde discussed initially in this chapter as a key reviewer of the performance gap investigates discrepancies between two procedures used in determining energy ratings. The Energy Performance Certificate (EPC), which can be provided using the Standard

Assessment Procedure (SAP), is an estimation of the energy performance of an existing building and shows how energy efficient the building *should* be; alternatively, a Display Energy Certificate (DEC) can be produced to show the operational performance of a building, and how energy efficient the building *actually* is compared to a benchmark building of the same type. Figure 3.7 shows a comparison between 20 buildings investigated by de Wilde.

This discrepancy wholly encapsulates the problem with assuming building fabric performance, given that both EPCs and DECs are legislative requirements for domestic buildings, and are the primary source of information for a building's energy performance despite the fact that inaccurate assumptions are made in its determination.

Building #	Building Type	Credentials	EPC Rating	DEC Rating
1	Court	BREEAM Excellent	B	D
2	Court	BREEAM Excellent	B	E
3	Data Centre	BREEAM Excellent	A	F
4	Education	BREEAM Excellent	B	F
5	Education	BREEAM Excellent	B	D
6	Education	BREEAM Excellent	B	D
7	Education	BREEAM Excellent	B	C
8	Office	BREEAM Excellent	A+	E
9	Office	BREEAM Outstanding	B	G
10	Education	BREEAM Excellent	D	D
11	Court	BREEAM Excellent	C	C
12	Education	BREEAM Excellent	B	C
13	Education	BREEAM Excellent	B	E
14	Education	Passivehouse	A+	B
15	Education	Concrete Centre Case	B	E
16	Education	Concrete Centre Case	B	F
17	Office	RIBA Prize	A	B
18	Office	RIBA Prize	B	C
19	Heathcare	RIBA Prize	B	E
20	Education	RIBA Prize	B	D

Figure 3.7 – Comparison of energy performance ratings of buildings using EPC and DEC procedures. Adapted from de Wilde (2014).

Without accurate models, there cannot be an accurate prediction of performance, and so the behaviour of modelled buildings cannot be fully understood. Viewing this in the context of the work for this thesis, where modelling has been used to inform on the behaviour of domestic buildings with novel energy systems, it is important that an accurate model can be used. While the focus of the thesis is aimed at covering electrical energy systems, the domestic energy system as a whole should be well understood as a representation of the global domestic energy system. For this to be the case, the benchmark model of the building in question should at least be as accurate as possible and able to deliver a good reflection on

the response of a building to the integration of such novel energy systems. Calibration techniques are a popular way in which predictive models can be treated to improve on the accuracy of their predictions; returning to the quote by George Box, all models are wrong, but when you introduce a certain level of accuracy, that's when they become useful.

3.2 Model Calibration

To improve on the accuracy of a model, and therefore improve its representation of the modelled building, several techniques can be employed to reduce the dissimilarities between the two. This in effect reduces the overall performance gap that occurs. As discussed by Heo et al. (2012):

"To get a good match between outcomes of the baseline model and monitored energy consumption, the analyst or the modeler calibrates the parameters of a simulation model to match their actual counterparts in the building."

Calibrating the parameters of the simulation model of the energy house was then key in providing an accurate model from which to base the simulations in this thesis. Model calibration can be carried out using a number of techniques; some of these are discussed before the chapter concludes with the technique used to calibrate the Energy House model.

3.2.1 Bayesian Calibration

The work carried out by Heo et al. (2012), as quoted above, uses a Bayesian calibration technique. The technique, as developed by Kennedy and O'Hagan (2001), defines a series of uncertainties in building simulation modelling:

- Uncertainty in the model outputs.
- Discrepancy between the model outputs and the measured data.

- Uncertainty in the measured data.

Since modelling approximates the overall heat transfer through a building's envelope, there will always be uncertainty in the output of a model. Sensor error when conducting measurements for energy consumption and heat loss gives rise to uncertainty in the measured data against which the model is compared and validated. Discrepancy between measured and modelled values then arise, however discrepancy with uncertainty of both over and underprediction ensures parameters aren't overestimated. Equation 3.1 shows how these terms can be applied:

$$y(x) = \mu(x, \theta) + \delta(x) + \varepsilon(x),$$

where

y(x)	is the measured output from a set of conditions x,
μ	is the modelled output from a set of conditions,
θ	is a series of uncertainties / calibration terms,
δ	is the discrepancy between measured and modelled terms,
ε	is the uncertainty in measured values.

The aim of Bayesian analysis is to produce a series of calibration terms that give the closest possible match between the measured and modelled outputs. The calibration process itself is probabilistic; calibration terms are primarily assigned with a distribution – which represents a likelihood that each term will deliver a match between measured and modelled. As both data are probed, the calculated calibration terms at each stage are used to update the distribution, eventually resulting in a final distribution that informs the most probable value for each term, and so the term that delivers the least uncertainty. Examples of calibration terms given by Heo et al. are: indoor temperature during heating, infiltration rate, discharge coefficient. This approach can also be used to determine the U-values (or most probabilistic U-value) of a building element, or indeed the 'global U-value' of the entire building envelope.

The Bayesian approach to calibrating building models for predicting energy performance has proven popular in a number of studies, such as that by Manfren et al. (2012), Tian et al. (2016),

Li et al. (2016) and Chong et al. (2017), each of which uses the technique to identify building performance parameters.

3.2.2 Deterministic Calibration

While probabilistic calibration seeks to actively use uncertainty in models to derive distributions for the most probable calibration terms for performance parameters, deterministic calibration instead targets the performance parameters themselves. The process involves varying these performance parameters and interpreting the resulting discrepancy between predicted and measured results. Parameters are varied until a minimum discrepancy is found. This method of calibration is supported in works by Sun and Reddy (2006), Pan et al. (2007), and Raftery et al. (2011) where it is seen as superior in reducing the uncertainty of models over Bayesian calibration, however the process is much more time consuming.

3.2.3 Alternative Calibration

Coakley (2014) reviewed publications that contained alternative calibration methods, such as those using neural networks, the PSTAR method, use of simplified models and system identification, all of which offer technically sound approaches to calibration. An alternative method in addition to these however, is calibration with the use of in-situ measured data.

An example of this method is found in work by Marini et al. (2016), who explore the calibration of their model of a real UK home in Loughborough, built in Designbuilder. By collecting in-situ data from the building over an extended period of time, Marini et al. were able to apply several stages of calibration to their model in an attempt to reduce the performance gap. These several stages of calibration included corrections for weather data, HVAC operation, rate of infiltration, and heat flow from the building. Energy consumption was

recorded during a posterior testing period, over which these calibration stages were applied. The technique demonstrated a reduction in the discrepancy between measured and modelled data by a significant amount (30% for gas consumption and 20% for electricity consumption). Residual errors were noted due to the responsiveness of the energy systems within the building. The work was carried out as a follow up to similar previous research (Marini et al., 2015a, b).

The process of calibration has demonstrated effectiveness in reducing the performance gap, significantly in some cases, which brings the modelled predictions of energy performance closer to the actual energy performance of a building. This delivers validation and accuracy of a model in its ability to represent the realistic behaviour of any given building. The following chapter takes the method of manual parameter adjustment using in-situ measured data and applies it to the model of the Energy House built for the work in this thesis.

Chapter 4

Calibrating and Conditioning the Energy House Model

Abbreviations

ATTMA	Air Tightness Testing and Measurement Association
HFP	Heat Flux Plates
HTC	Heat Transfer Coefficient
NCM	National Calculation Methodology
SBEM	Simplified Building Energy Model
UKCP	United Kingdom Climate Impact Program

Nomenclature

q	Power Input (W/m^2)	U	U-value (W/m^2 K)
T	Temperature (K)		
Subscript			
e	External	i	Internal
n	Number of data		

A model of the Energy House was built in Designbuilder, the process of which was set out in Chapter 2. In assigning the initial building fabric properties to the building, pre-set thermodynamic parameters provided by the modelling software (thermal conductivity, specific heat, density and calculated U-value) were assumed based upon the dimensions of each building element. As seen in the previous chapter, the use of assumed values in

simulations and prediction tools are simply not enough to provide an accurate reflection of a building's performance. Instead, some method of calibration should be applied to energy models to impart accuracy and to ensure the model can provide an appropriate level of behavioural representation. As the overall energy system of the house represented by the Energy House model is under investigation in this work, effort should be made to ensure the calibration of the Energy House model reduces the performance gap and its impact on predictability and delivering that required level of behavioural representation.

The Energy House test facility is rigged with a network of sensors for measuring the thermal performance of the building under controlled conditions and regularly undergoes testing to determine its performance parameters. There is, then, an abundance of data available that could be used to provide accurate performance parameters, used as an input. This chapter gives a breakdown of the tests performed on the Energy House, and how the results of the in-situ measurements taken from these tests were used to calibrate the model in Designbuilder.

4.1 Calibration Overview

Since the Energy House facility is kept under controlled conditions, a majority of the calibration factors explored in Marini et al.'s work (Marini et al., 2016) in the previous chapter do not apply. Two key energy performance parameters were chosen that could be measured accurately under those controlled conditions, the U-values of building elements and the air permeability of the building. Both of these parameters give rise to heat loss and in turn energy demand for the building, both can be used to quantify what is known as the global heat transfer coefficient (HTC). This global performance parameter can be used not only to

compare dissimilar buildings' energy performance, but as a target for predictive models to achieve and thus determine any existence of the performance gap.

The model built in Designbuilder underwent three stages of calibration using in-situ measured data – one with the application of corrections for air permeability, one with corrections for U-values and one with both air permeability and U-values. At each stage, the HTC of the model was determined and compared to the global HTC, a parameter also measured in-situ.

As mentioned in chapter 2, the HVAC system in Designbuilder is automatically sized and depends on the building parameters. Static analysis of the model can tap into this automatic sizing facility and deliver the HTC. To do this, Designbuilder assumes steady state conditions, with the internal temperature at a fixed high temperature (18^{o}C in all rooms, with 21^{o}C in the living room – as suggested by SAP), and the external temperature fixed at some extreme of the low winter temperature (the default for Designbuilder is -4.4^{o}C). The heat input required to maintain this temperature gradient is considered the 'design heating capacity', which is typically used to inform on heating system design, however here it can be used to inform the HTC by simply dividing this heat input by the temperature gradient. First of all, however, the performance parameters of the building required determination. Three tests were performed to determine building U-values, air permeability and HTC, these were:

- Air pressure tests.
- Heat Flux Density Tests.
- An electrical coheating test.

The calibration procedure carried out on the Energy House model can be viewed as part of the publication by Marshall et al. (2017). A list of equipment used in each of the tests is listed in table 4.1.

Table 4.1 – List of equipment used in the air pressure, heat flux density and electric coheating tests.

Equipment	Model	Tolerance
Blower door fan	Energy Conservatory Model 3 fan	-
Pressure / Flow Gauge	Energy Conservatory DG-700	± 1%
Temperature Sensor	Shielded 4-wire PT100 RTD	± 0.1^{o}C
kWh Meter	Elster A100C single phase meter	± 1%
Heat Flux Plate	Hukseflux HFP-01	± 3%
Data Logger	DataTaker DT80	± 0.1%

4.2 Air Permeability Test

A blower door test was used to measure the air permeability of the building to the standard set out in ATTMA's Technical Standard L1 (ATTMA, 2010). During the test, a pressure gradient was introduced within the building by positioning a powerful fan in an opening, causing large volumes of air to either enter (for a positive gradient) or exit (for a negative gradient) the building. A pressure difference of 50Pa was used as a standard target pressure difference, which was read using a pressure gauge. Both pressurisation and depressurisation tests were carried out on the Energy House to +50Pa and -50Pa. Further increments of ±5Pa were used up to ±80Pa in order to determine a series of air flow measurements. By plotting a graph of the pressure gradient against the air flow, it was possible to calculate an average air permeability for both pressurisation and depressurisation. An average of these two parameters was calculated for the overall air permeability as advised by CIBSE TM 23 (CIBSE, 2000), the details of which are given in table 4.2. The default value for air permeability in

Designbuilder is 16 m^3 h^{-1} m^{-2}. It should be noted that these tests were carried out with the house fully furnished, including carpets.

Table 4.2 – Results from the blower door test on the Salford Energy House

Air Permeability (m^3 h^{-1} m^{-2} @ 50Pa)		
Pressurisation	Depressurisation	Average
14.04	13.85	13.95

4.3 Heat Flux Density Measurements

The U-values of a number of building elements that make up the building envelope were considered for in-situ measurement and model calibration. These include external wall elements of different rooms, ceilings, windows and doors; specific details will be noted later on in this section. In order to determine the U-values of these elements, heat flux density measurements were carried out on each element. Hukseflux HFP-01 heat flux plates (HFPs) were attached to each of the surfaces to measure the heat flux through the building element. The internal and external air temperature were also measured using thermocouples. With these measured variables, the U-value of individual elements could be calculated according to ISO 9869-1:2014 (International Organisation for Standardisation).

Three heat flux panels were used to measure the heat flux through each building element, and an average used in the calculation of the U-value for that element. The equation used for this calculation is given as:

$$U = \frac{\sum_{j=1}^{n} q_j}{\sum_{j=1}^{n} (T_{i,j} - T_{e,j})},$$

where n is the number of data recorded,

j is the datum at a particular time,

q is the heat flux (W/m^2),

$T_{i,e}$ are the internal and external air temperatures (^{o}C).

Equation 4.1 is taken from the average method contained within ISO 9869-1:2014, which requires certain conditions for the estimation of the U-value to be valid. Conditions specified in the standard insist on a data collection period of greater than 72 hours, with sensors placement informed using thermography using ISO 6781-3:2015 (International Organisation for Standardisation, 2015); i.e. sensors should not be placed within the vicinity of any thermal bridges or cracks. A relatively consistent U-value should be found over the test period, without more than a 5% deviation between each 24-hour data set. To achieve this consistency, it is advised that a significant temperature gradient (greater than 10K) be maintained across the measured element to ensure monodirectional heat flow. To ensure this during the measurements carried out in the Energy House, each room had a fixed internal temperature of 25^{o}C and the external temperature was maintained around 4.4^{o}C (with an error margin of ±0.5^{o}C). Outside of these condition requirements, ISO 9869-1:2014 specifies the use of a different method – the dynamic method – however, under the controlled conditions of the Energy House, the average method was easy to achieve.

Figure 4.1 shows the data captured during the measurement of an external wall of the living room in the house. From this data, it is clear that a reasonable temperature was maintained throughout the test and that a consistent U-value was calculated for a majority of the test.

Similar quality data was collected for the tests of each of the measured building elements considered for this calibration step.

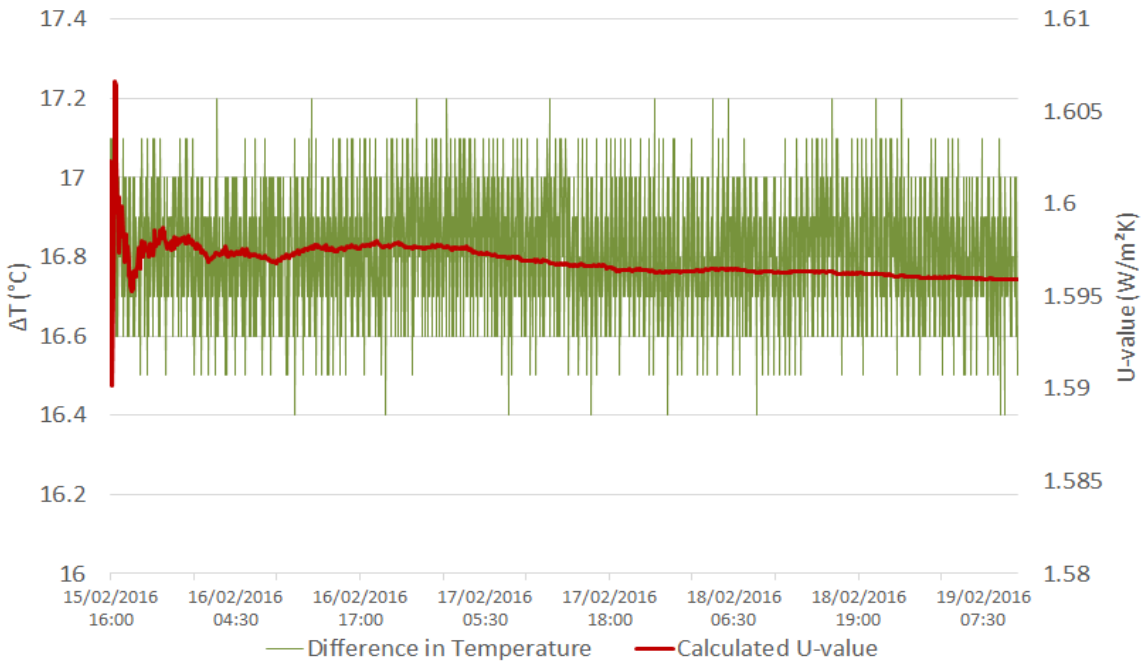

Figure 4.1 – Data collected for the U-value calculation of an external wall in the living room of the Energy House.

The fluctuations observed in the temperature difference of figure 4.1 are present due to the cyclic nature of the HVAC. It is important to note the increasing stability of the calculated U-value with a growing quantity of data.

Table 4.3 lists the results of the U-value measurements performed in the Energy House, along with the default U-values assigned by Designbuilder. These default values assigned by Designbuilder are determined provided by material properties provided by CIBSE Guide A (CIBSE, 2006), and calculated using BR 443 (BRE, 2006).

Table 4.3 – Default model and actual measured U-values for building elements of the Energy House. Marshall et al. (2017).

Room	Building Element Type	Model default U-value	Measured U-value
Living Room	External Wall	2.243	1.596 (± 0.086)
Kitchen	External Wall	2.243	1.530 (± 0.087)
Second Bedroom	External Wall	2.243	1.567 (± 0.091)
Main Bedroom	Ceiling	0.400	0.462 (± 0.026)
Living Room	Window	3.746	3.835 (± 0.257)
Kitchen	Window	3.746	3.670 (± 0.246)
Living Room	External Door	2.995	2.697 (± 0.178)

The results of these tests show that the greatest discrepancy between assumed and measured U-values lies with the external walls – up to 32%. This raises a significant concern over the accuracy of the baseline model, particularly since the proportion of the building envelope represented by the external walls is much higher than the other building elements; the window to wall ratio of the Energy House was measured to be 0.13. These results mirror the findings and concerns expressed in the previous chapter concerning overestimations of U-values for building elements. By introducing these measured parameters into a building model then, the size and impact of the performance gap, apparent due to this overestimation, should be reduced considerably.

4.4 An Electric Coheating Test

An electric coheating test is a test method that is able to calculate a building's HTC under quasi-steady-state conditions (Johnston et al., 2013). In order to carry out the test in the Energy House and quantify this energy performance parameter, a series of electric heaters were used to artificially heat the entire building to a fixed temperature to establish quasi-steady-state conditions. Circulation fans were also used to mix the air and reduce stratification. The test required a measurement period of between 7 and 21 days, once equilibrium had been reached and any thermal mass charged. The measured variables throughout test period were the internal air and external air temperatures, and the power input into the electric heaters; thermocouples and kWh meters were used to achieve this. By maintaining a regular temperature difference and power input, the HTC (W/K) can be calculated using:

$$HTC_{global} = \frac{Q_{avg}}{(\Delta T_{avg})},$$

where Q_{avg} is the average power input (W),

ΔT_{avg} is the average temperature difference across the envelope (K).

Note that the global HTC value groups together the component of HTC belonging to the building fabric and the component belonging to air leakage.

The coheating test for the Energy House was conducted using three temperature differences, under the notion that despite variance in that temperature difference the HTC should remain the same – error permitting. While the internal temperature of the house was held constant with the setpoint of 25^{o}C used with each thermostat, the external temperature of the

chamber was gradually reduced to extend this temperature difference. Figure 4.2 shows the data collected during the electric coheating test. Note that a drop in Energy House temperature was observed due to a loss of power.

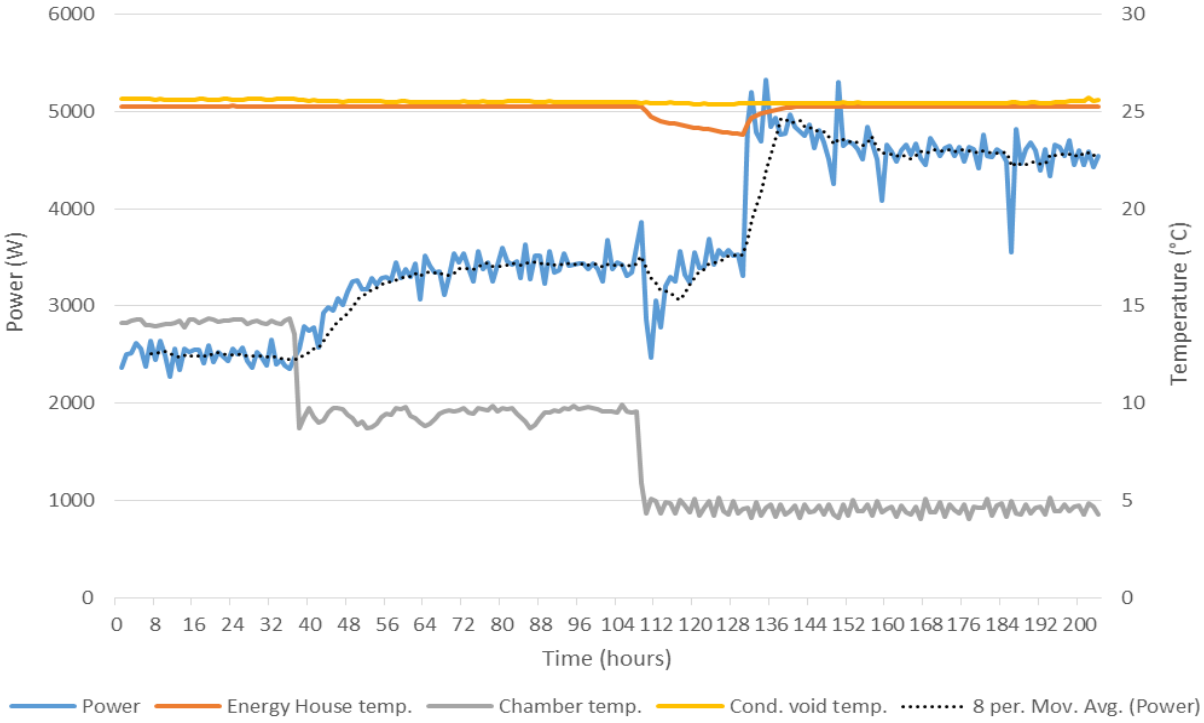

Figure 4.2 – Measured data from the electric coheating test. Marshall et al. (2017).

A list of the average temperature differences used in the coheating test, the average heating power determined for each difference in temperature, and the HTC calculated from this data are shown in table 4.4. Note that power input into the house due to auxiliary power systems (such as fans and dataloggers) of ~ 25W was removed from the final reading of power input.

Table 4.4 – Results from the electric coheating test.

Average Temperature Difference (K)	Average Power Input (W)	HTC (W/K)
11.2	2447	219.5 (± 3.3)
15.6	3432	219.5 (± 3.3)
20.7	4538	219.7 (± 1.8)
Mean		**219.6 (± 0.4)**

The last 4 hours of data for each temperature difference were used to ensure steady state conditions had been reached.

To ensure no excessive residual terms, such as unexpected energy losses and inputs, impact these results, graphical analysis of the results were considered and shown in figure 4.4.

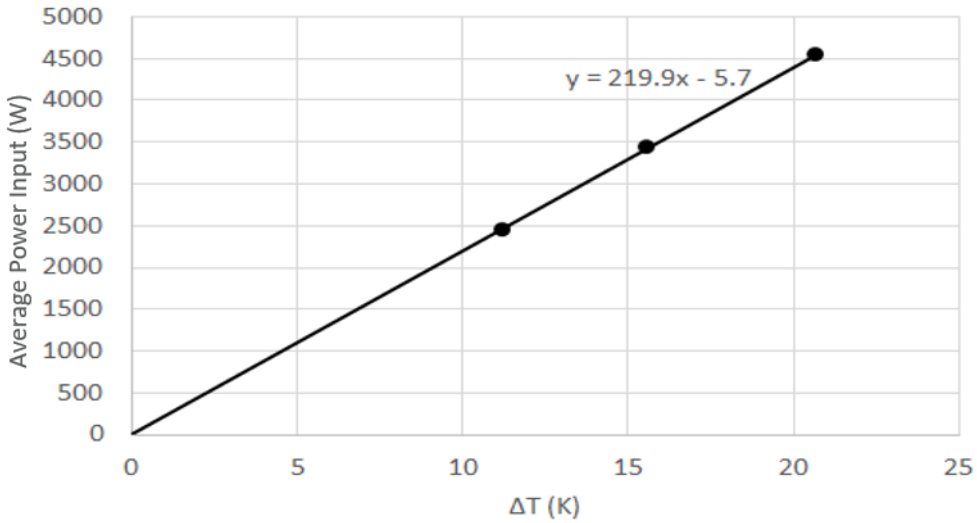

Figure 4.3 – Average power input for average temperature differences (ΔT) across the building envelope. A measure of HTC from an electric coheating test. Marshall et al. (2017).

A line of best fit was placed through the data, which showed the HTC from this graphical interpretation to be 219.9 ± 0.4 W/K. Minute discrepancy from the HTC measured with each difference in temperature can be attributed to the small residual of 5.7 W, which can be explained by unexpected loads of electrical systems (monitoring hardware, circulation fans etc.). Regardless of this residual, the line of best fit delivers an R^2 of 1.0, meaning this value of 219.9 W/K can be used as the global HTC for the Energy House, and as a target for the model calibration exercise.

4.5 Model Calibration

After the required performance parameters were measured for the modelled building, calibration could take place in several stages. This was done to see how the measurements of air permeability, and a combination of both air permeability and U-value, impact on the performance gap assumed to be present in the model. Simulations used at each stage of the calibration reflected the conditions of the coheating test – an internal temperature of 25°C was used, with external temperatures of 13.8°C, 9.4°C and 4.3°C. Table 4.5 gives the HTC calculated at each stage of calibration, including the baseline model, and indicates the difference between average modelled and measured HTCs.

Table 4.5 – A comparison between modelled and measured Heat Transfer Coefficients. Marshall et al. (2017), using corrected values.

ΔT (K)	HTC (W/K) **Baseline Model**	HTC (W/K) **Air Permeability**	HTC (W/K) **Air Permeability + U-value**	HTC (W/K) **Measured**
11.2	274.1	271.4	238.4	**219.5**
15.6	257.7	254.5	222.4	**219.5**
20.7	248.8	244.9	214.0	**219.7**
AVG	**260.2**	**256.9**	**224.9**	**219.6**
Difference	↑18.9%	↑17.1%	↑2.5%	-

Analysis of the results obtained from the baseline model revealed an average difference between modelled and measured HTC, and so a performance gap, of 18.9%. This can be attributed to an overestimation of both air permeability and U-value. These results reveal that correcting the building model for air permeability has much less of an impact on the performance gap than when corrections for U-values are applied. This calibration exercise has demonstrated that it was possible to reduce the overall average performance gap from 18.9% to 2.5%, and produce a model which is a more accurate representation of the true facility's thermal energy performance. In calibrating the Energy House model, the second objective of this work was completed.

The overall energy performance of the building was determined by consumption of both thermal and electrical energy. By calibrating the Energy House model, it has been possible to develop a model that can deliver realistic outputs of the actual building with regards to thermal energy consumption. Electrical energy consumption was 'calibrated' by conditioning the model for occupancy. This chapter continues on to discuss the full conditioning process for the Energy House model, and includes those conditioning factors which impact on the consumption of electricity. Conditioning the model for this purpose requires foresight of the conditions that are used to investigate the sensitivity of the model under different scenarios.

4.6 Model Conditioning

The third objective of this work was to modify / condition the model to reflect the scenarios for sensitivity analysis that have been determined. This section discusses how the model was conditioned to deliver a 'calibrated baseline' model – representative of a generic house based on the Energy House, located in Manchester. This model was used as a starting point from which the sensitivity factors were used to recondition the model for an investigation into the impact of these factors on the overall energy performance of the energy system. This was so that later on, these energy consumption data can be used to determine the performance of energy storage systems given each sensitivity scenario.

Conditioning factors are discussed in terms of the calibrated baseline Energy House model, with supplementary information on how these factors were changed to investigate each sensitivity factor.

4.6.1 Energy Generation

The domestic energy system for the Energy House model, as discussed in the introduction to this work, considers the use of photovoltaics as a means of generating on-site energy and to promote autonomous operation. The model was changed to include this, with table 4.6 displaying the specifications for the photovoltaics used in the model. These photovoltaic properties were chosen to reflect the panels present at the research facility.

Table 4.6 – Photovoltaic Properties

Parameter	**Value**
Maximum Power Rating	246 W
Tolerance	± 3 W
Maximum Voltage	1000 V
Short Circuit Current Rating	8.4 A
Open Circuit Voltage Rating	34.7 V
Cell Efficiency	15 %

While it is common practice to install photovoltaics to the south of the building to allow the optimal catchment area for solar radiation, initial simulations indicate that by having

photovoltaics both north and south facing, the annual energy generation can be almost doubled. Table 4.7 gives the simulation results for photovoltaic energy generation, obtained using the Energy House model with annual weather data for Manchester, sourced from the predicted weather files of the Prometheus Project at the University of Exeter (Eames et al., 2011). The information contained within individual weather files and the process involved in predicting this information is discussed in section 4.6.3. Note that a difference exists between the north and south facing roof; this is due to the presence of a chimney.

Table 4.7 – Primary results of annual simulations for photovoltaic energy generation.

PV location	**Roof Area**	**Annual Energy Generation**
South Facing Only	17.6 m^2	2570 kWh
North and South Facing	33.1 m^2	4151 kWh

4.6.2 Location

As the Energy House is located in Manchester in the UK, the baseline calibrated model has this as its default location throughout the study. Location, and the subsequent climatic variation however, was anticipated to have a large impact on both thermal and electrical performance of the building. To offer models the variation in climate found throughout the UK, forty-two locations of major towns and cities spanning the length and breadth of the country were selected. The chosen locations were decided upon due to the availability of weather files, as is discussed in the following section, and reflect major towns and cities of the UK with high population densities. Table 4.8 lists these locations and their geographical details. The distribution of these locations is shown on a map of the UK in figure 4.4.

Table 4.8 – Location details of the cities used when investigating location sensitivity

Town / City Name	Latitude (°N)	Longitude (°W)	Elevation (m)
Aberdeen	57.15	2.09	29
Aberystwyth	52.42	4.08	9
Bangor	53.23	4.14	16
Barnstaple	51.08	4.06	70
Belfast	54.6	5.93	56
Bicester	51.9	1.15	74
Birmingham	52.49	1.89	140
Bodmin	50.47	4.72	198
Bradford	53.8	1.76	134
Brighton	50.82	0.14	19
Bristol	51.45	2.59	11
Camborne	50.21	5.29	106
Cambridge	52.21	0.12	6
Cardiff	51.48	3.18	19
Carlisle	54.89	2.93	29
Dover	51.13	1.31	0
Dundee	56.46	2.97	18
Ebbw Vale	51.78	3.21	324
Edinburgh	55.57	3.11	47
Exeter	50.72	3.53	7
Fort William	56.82	5.1	10
Glasgow	55.86	4.25	39
Heathrow	51.47	0.45	65
Hull	53.75	0.34	2
Islington	51.55	0.11	13
Lancaster	54.05	2.8	79
Leeds	53.8	1.55	49

Leek	53.11	2.02	173
Leicester	52.64	1.14	66
Liverpool	53.41	2.99	21
Londonderry	55	7.31	7
Manchester	53.48	2.24	49
Newcastle	54.98	1.62	38
Nottingham	52.95	1.16	28
Oxford	51.75	1.26	69
Penryn	50.17	5.11	36
Plymouth	50.38	4.14	29
Portsmouth	50.82	1.09	3
Sheffield	53.38	1.47	88
Southampton	50.91	1.4	4
Swindon	51.56	1.78	147
Truro	50.26	5.05	6

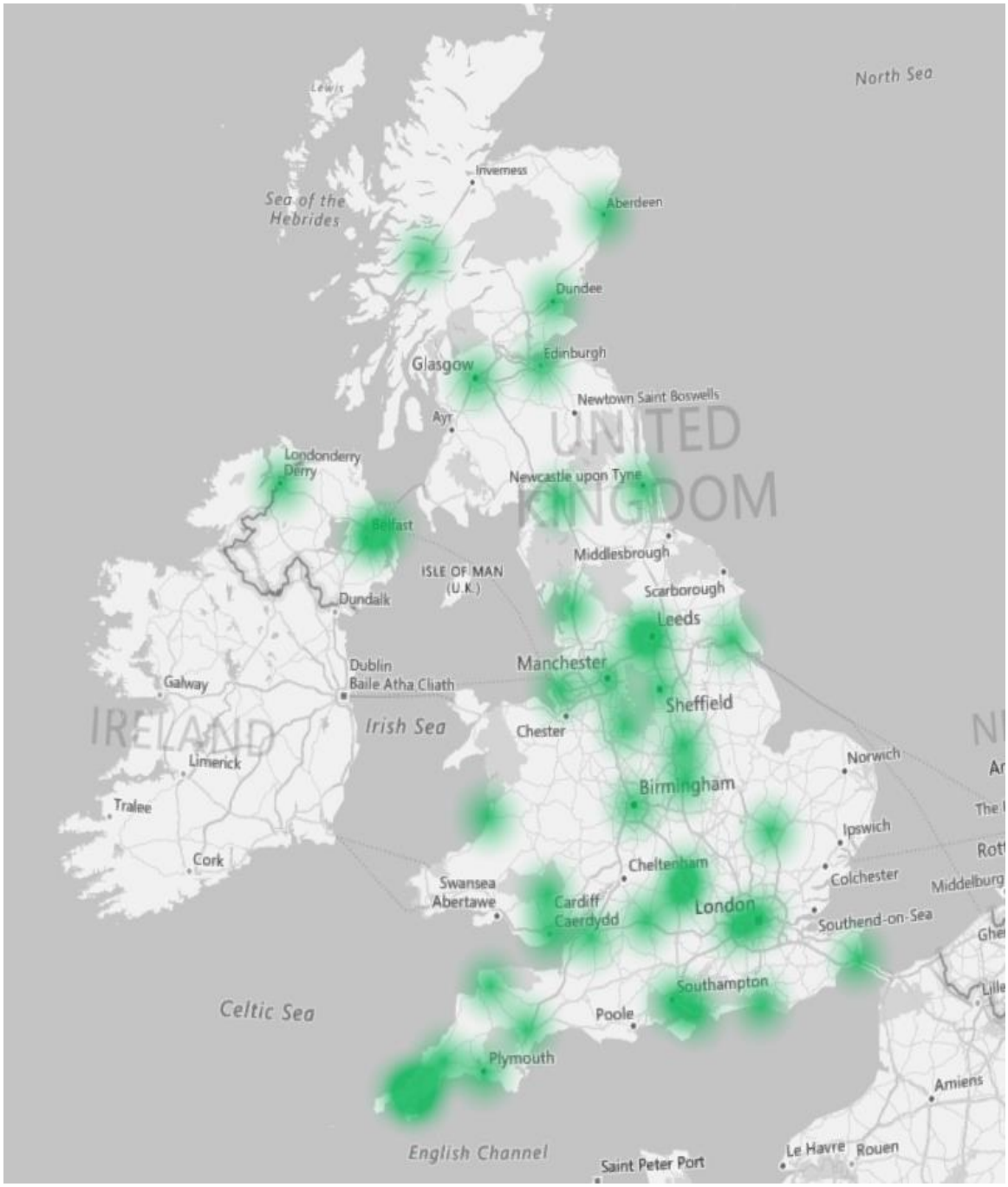

Figure 4.4 – Map of the UK showing the distribution of forty-two locations chosen for sensitivity analysis.

With the application of each location to the site level of the Energy House model, a suitable weather file must also be applied.

4.6.3 Weather

The model was assigned an individual weather file for each location for use during each simulation. Weather files were sourced from a research project undertaken out at the University of Exeter, designed to investigate the impact of climate change; a weather generator was developed in the United Kingdom Climate Impacts Program (UKCP09) to generate probabilistic weather files – see Eames et al. (2011) and Mylona (2012). Each weather file contains hourly data for each of the following variables: dry-bulb and dew-point temperatures, wind speed and direction, solar altitude and azimuth, atmospheric pressure, and direct and diffuse solar radiation.

Weather files were generated by taking precipitation as the predominant variable, all other variables are successively calculated based on this factor using statistical and mathematical relationships. These calculations allowed the prediction of the above variables at hourly intervals. See Eames et al. (2011) for a list of techniques used to accomplish these predictions. Current weather data used for baseline simulations and location sensitivity simulations were created using historic weather data from a baseline 1961 – 1990 time period. Additional weather files were sourced from this project and occur at future years of 2030, 2050 and 2080. These future climate data were used for the sensitivity analysis of the domestic energy system and take climate change into account. With climate change, as the average ambient temperature increases the demand for heating is reduced; it is also possible to investigate any variation in solar radiation and the subsequent impact on energy generation.

Figure 4.5shows the number of degree days for the current and future predicted weather files for Manchester. Degree days measure the frequency of days where the average temperature falls below 15.5^{o}C, indicating energy use for space heating. The figure demonstrates how the total number of degree days is reduced considerably over time.

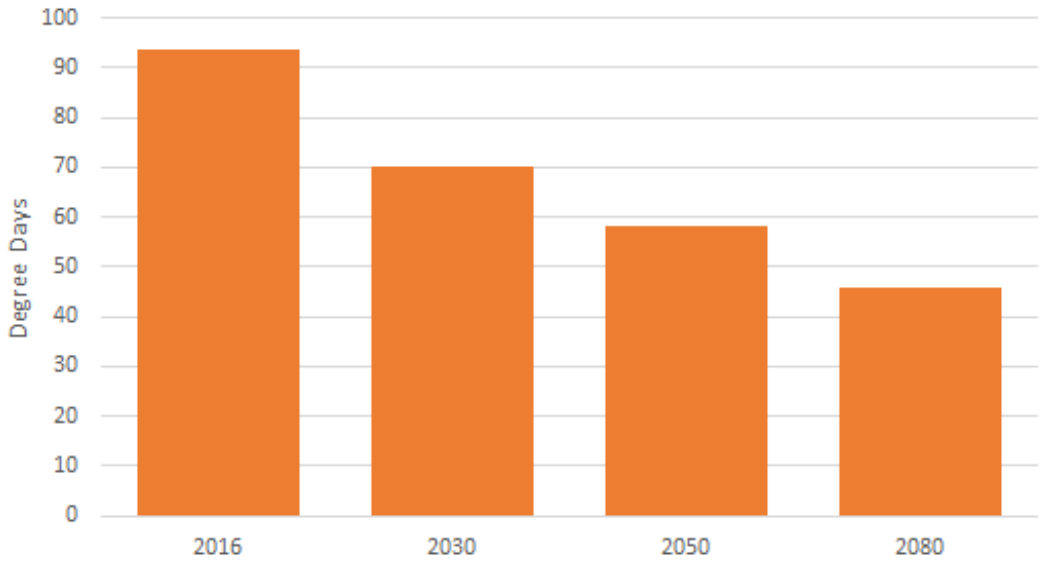

Figure 4.5 – Total number of degree days in Manchester for current and future weather scenarios

A slight variation in the solar radiation found in the successive years is also observed from these weather profiles. Figure 4.6 shows the increase in solar radiation at 2030, 2050 and 2080 from the total predicted annual figure.

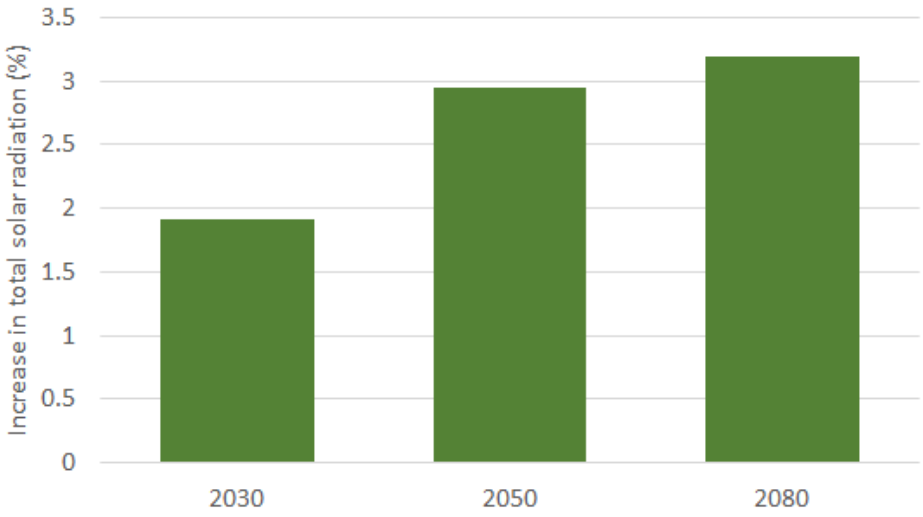

Figure 4.6 – Increase in total annual solar radiation for current and future weather files.

4.6.4 Archetype

The type of building – whether detached, end-terrace/semi-detached or mid terrace plays a huge role in the energy performance of a building in that entire facades of the building are exposed to excessive heat loss with the move from mid terrace to detached. Figure 4.7 and 4.8 show a representation of the mid-terrace and semi-detached/end-terrace type respectively, with their situation among others identified in black; the detached type is simply a solitary single house with exposure to all facades.

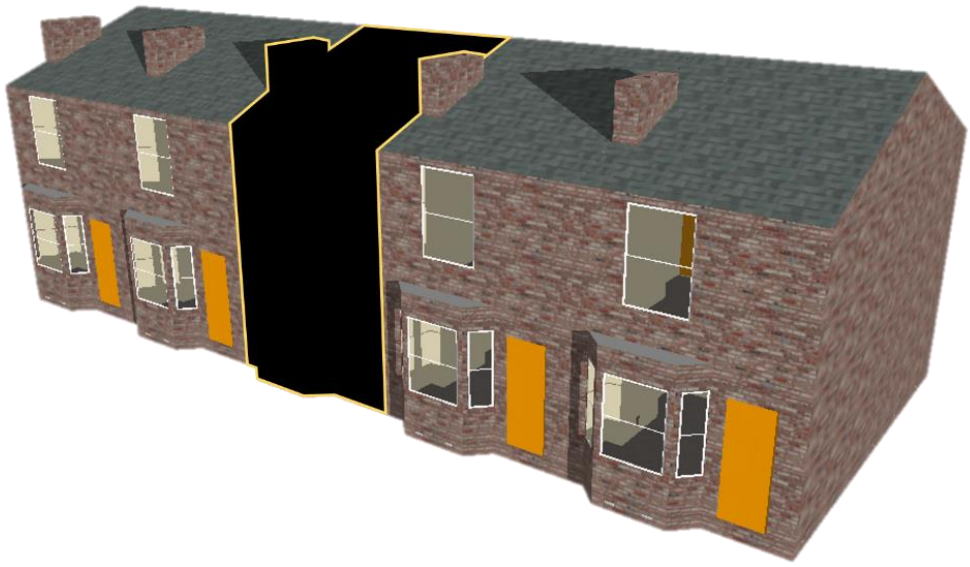

Figure 4.7 – Representation of a typical mid-terrace house situation.

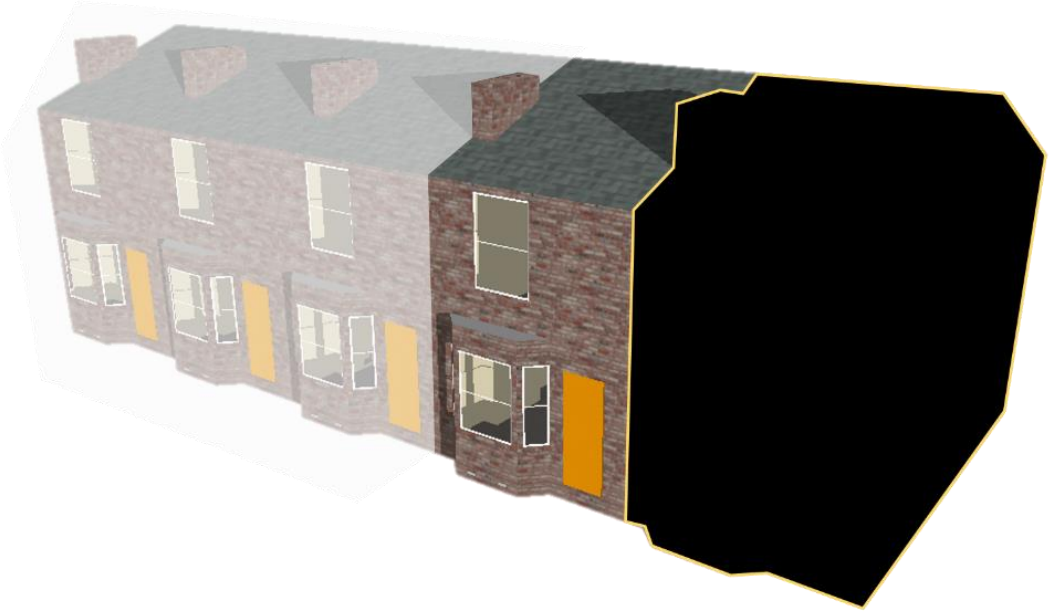

Figure 4.8 – Representation of a typical end-terrace / semi-detached house situation.

As discussed in chapter 2 of this thesis, for partition walls with adjacency to other buildings, as is the case for both end-terrace/semi-detached and mid-terrace, the heat flow through these surfaces is considered negligible and so is set to zero. This assumption is made on the basis that adjacent zones have similar occupancy, similar heating requirements and so similar temperatures at the same time. The boundary between adjacent buildings is modified between typical heat flow (to an external space) and adiabatic conditions (to neighbouring buildings) to reflect each of the modelled archetypes in order to investigate the sensitivity of each type on the energy performance of the building.

4.5 Occupancy Activity and Scheduling

The behaviour of occupants is difficult to predict – as discussed in the introduction it is one of the core reasons why demand side solutions to energy efficiency are side-stepped. Defining

occupancy and the behaviour of those occupants with regards their interaction with heating systems and electrical equipment is necessary in producing a reliable model. Occupancy has a dominant impact on the operation of both heating and electrical energy systems within the model, and so the scheduling of this occupancy is one of the more important factors of modelling. Sensitivity analysis of this occupancy is then of interest in this study.

Designbuilder uses the UK National Calculation Methodology (UK NCM) to determine both occupant and heating schedules based on SBEM (Simplified Building Energy Modelling), (BRE, 2017), which is used as a compliance procedure for UK buildings. Scheduling is initially based around a typical UK home. Time use data (Gershuny & Sullivan, 2017) informs that the most common UK homes consists of, in order of commonality, 2 working adults, 1 retired adult, 1 working adult and 2 retired adults. This is based on the collection of information over time on households fitting a wide variety of locations and household backgrounds. Figure 4.9 shows how these occupancy categories were determined by reviewing the proportionality of occupancy scenario from this time use data.

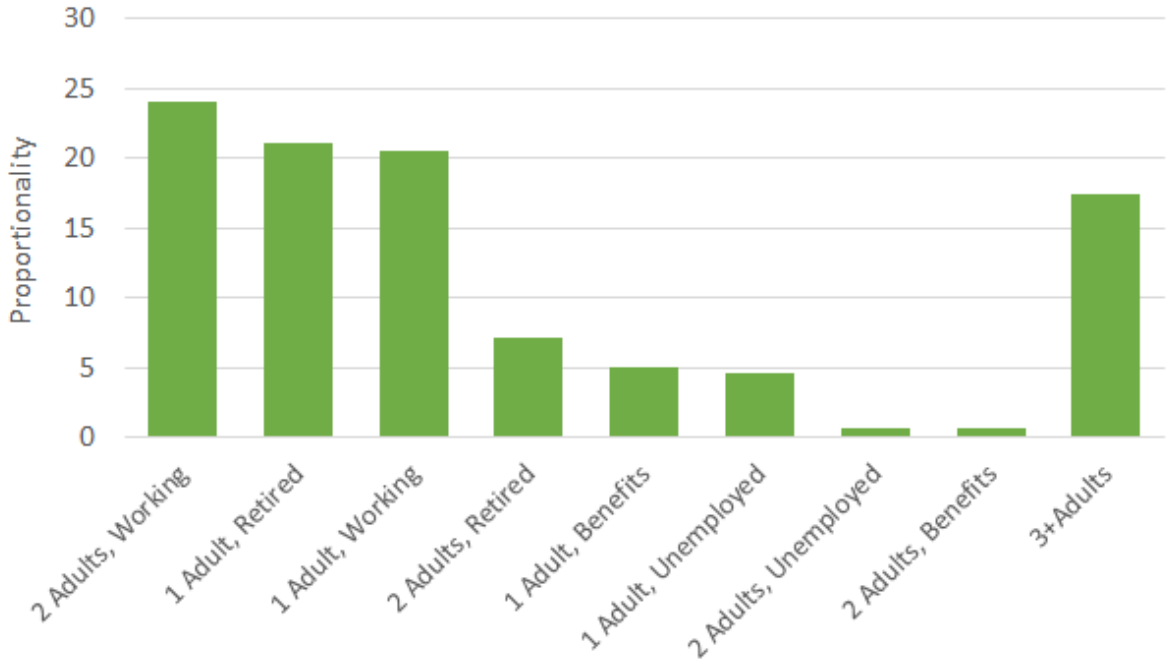

Figure 4.9 – Proportionality of occupancy profiles from UK time use data. (Gershuny & Sullivan, 2017).

Each occupancy category is reflected as a proportional of the overall number of people surveyed, note that the final category of 3+ adults is a grouping of all of the remaining categories and are no higher than 2 retired adults.

Occupancy is defined in two senses. A global occupancy where the home is inhabited and a local occupancy, which considers the habitation of individual spaces.

The default global occupancy used in Designbuilder accounts for an occupation density of 2 adults; the schedule attached to this is based on the BRE recommended working week as found in SAP (BRE, 2014); this is 07:00 – 09:00 and 16:00 – 23:00 during the week, and 07:00 – 23:00 at the weekend. Note that occupancy is only considered when the inhabitants are

awake. Global heating and electrical equipment schedules mirror this, but with a 30-minute lead time on each heating period.

For one adult, the occupancy density is simply halved, while the occupancy schedule for retired persons is modified to remove working hours from the SAP working week and heating schedules, resulting in a schedule for both as 07:00 – 23:00 for the entire week.

Local occupancy triggers both heating, when the room temperature is lower than the heating setpoint, and the electrical equipment used in each room. Table 4.9 lists occupancy schedules for the individual rooms of the model. Note that for any overlap, the occupation density is simply distributed between the spaces. The assumption is also made that due to limited occupancy, the second bedroom of the property is treated as a common circulation space.

Table 4.9 – Occupancy Schedules for each room of the Energy House model.

	Schedule (Hour)																							
Room	1	2	3	4	5	6	7	8	9	10	11	12	13	14	15	16	17	18	29	20	21	22	23	24
Living Room																								
Kitchen																								
Hall / Stairs																								
Bedroom																								
Bathroom																								

Equipment assigned to the model replicates the electrical appliances found in the Energy House test facility; these are listed in table 4.10.

Table 4.10 – List of electrical appliances in the Energy House

Equipment	Type	Brand / Model	Power Rating (W)
Oven / Hob	White Goods	Lamona HJA3320	2400
Kettle	Kitchen Appliance	Russell Hobbs 15217	2200
Toaster	Kitchen Appliance	Micromark MM52176	1750
Microwave	Kitchen Appliance	Russell Hobbs RHM1712	1200
Fridge Freezer	White Goods	Iceking IK5051C	100
Washer Dryer	White Goods	Indesit IWDC6105	1850
Laptop	Entertainment	HP Pavillion G50	90

Television	Entertainment	Sony KDL32EX301	94
Blu-ray Player	Entertainment	Panasonic DMPBDT260	14

4.6 Retrofit

The application of retrofit, discussed in the introduction, is well adopted in the UK. A 'deep retrofit' as described by Ji et al. (2014) includes modifications to the outer envelope of the building's conditioned space and internal energy systems to improve on the energy efficiency of a building. Table 4.11 lists the improvements considered for changes made to the Energy House model in order to investigate the sensitivity of energy systems to this type of variation. To maximise on energy system utilisation, the heating system for this retrofitted home was changed to electrical heating – this also reduced the necessity for gas consumption, further reducing the carbon footprint of that energy system.

Table 4.11 – Deep retrofit applications for sensitivity analysis.

Building Element	Modification
External Wall	100mm polystyrene added to the outside of all external walls.
Glazing	All windows changed to be double glazed.
Loft	Increase mineral wool insulation from 100mm to 250mm.
Infiltration	Air permeability reduced by 70%.
Boiler Efficiency	Improved to be 88% over 80%.

This chapter has explored the process of model calibration and the application of that process to the Energy House model, where in-situ measurements have demonstrated a reduction in the performance gap of the model from 18.9% to 2.5%. This closure of the performance gap attests to model accuracy in performing predictive simulations of the Energy House under given scenarios.

Several categories have been proposed, containing the scenarios under which the Energy House model should be simulated. These were discussed in terms of a conditioning exercise for the model – where baseline conditions were established and the scenarios of these categories explored. Table 4.12 gives a final matrix of these proposed scenarios, which will eventually investigate the sensitivity of the overall domestic energy system to understand the role of storage under these scenarios.

Table 4.12 – Simulation scenario matrix.

Category	**Scenario**
Archetype	Mid-Terrace: Adiabatic heat flow to two adjacent buildings.
	End-Terrace / Semi-Detached: Adiabatic heat flow to one adjacent building.
	Detached: No adiabatic heat flow, all facades are exposed.
Occupancy	Two working adults: Standard SAP schedule, full occupant density.
	One retired adult: Weekly 07:00 – 23:00 schedule, half occupant density.

	One working adult: Standard SAP schedule, half occupant density.
	Two retired adults: Weekly 07:00 – 23:00 schedule, full occupant density.
Location	Weather files for each of the forty-two locations listed in Table 4.8.
Future Climates	Manchester weather prediction for 2030.
	Manchester weather prediction for 2050.
	Manchester weather prediction for 2080.
Retrofit	Deep retrofit of the external fabric, change to electric heating system.

In calibrating the model and modifying/conditioning the model ready for simulation under these scenarios, the third objective of this work was actualised. This work moves on to complete this objective detailed in the next chapter by carrying out the simulations, displaying the results of each scenario and discussing the significance of the results in terms of energy system response, sensitivity and the likely impact on the introduction of energy storage systems.

Chapter 5

Dynamic Energy Simulations:

Results of Modelling without Energy Storage

This chapter explores the results of dynamic energy simulations of the Energy House model under the scenarios proposed in Table 4.12 of the previous chapter. By carrying out simulations of these scenarios, the third objective of this thesis is completed. These results form a prelude to the latter modelling work in this thesis, which looks to use these results as an input into energy storage modelling. Annual simulations were carried out on each model and subsequent variations, incorporating the predicted performance across that period. This accounts for variation in outdoor temperature and solar incidence, the two key climate factors that influence the consumption and generation of energy within the localised energy system.

Results collected during each simulation include the following:

- A summary of energy consumption.
- A detailed summary of energy generation, including net generation after losses to inversion.
- A summary of energy drawn from and sent to the grid.
- Hourly and daily data for all energy processes.
- Fuel-specific data for grouped energy processes.

Summaries of energy consumption can be used to inform on the overall energy performance of the building, given its simulation scenario. These summaries were used for comparison of the baseline model to the subsequent results that consider sensitivity factors. Hourly and daily data on specific energy processes gives progressive energy consumptions throughout the entire year. These data were collected for use in the energy storage models in the coming chapters, where the summary of energy consumptions is revisited post-storage, and the impact due to storage compared.

5.1 Baseline Model

The baseline model was the calibrated Energy House model as described at the end of the last chapter. Table 5.1 lists the conditioned state of this baseline model, the results of which were used as a comparable base for the subsequent results.

Table 5.1 – Conditioned state of the calibrated baseline Energy House Model

Category	**Scenario Conditioned State**
Archetype	End Terrace
Occupancy	Two Working Adults
Location	Manchester (53.48^{o}N, 2.24^{o}W)
Climate	Current
Retrofit	No Retrofit, Original Heating System

Figures 5.1 and 5.2 display examples of the weather data (sourced from Eames et al., 2011) used in the simulation of the baseline model – monthly outdoor temperature and monthly direct normal solar radiation. These determine the heat loss – and so the energy required to maintain a comfortable temperature gradient; and also the energy generated using photovoltaics.

Figure 5.3 then displays the resulting energy consumption / generation data found as a result of these external conditions and the internal conditions determined by occupancy and the activity of those occupants. Note that energy generation in figure 5.3 is negative, indicating generation rather than consumption.

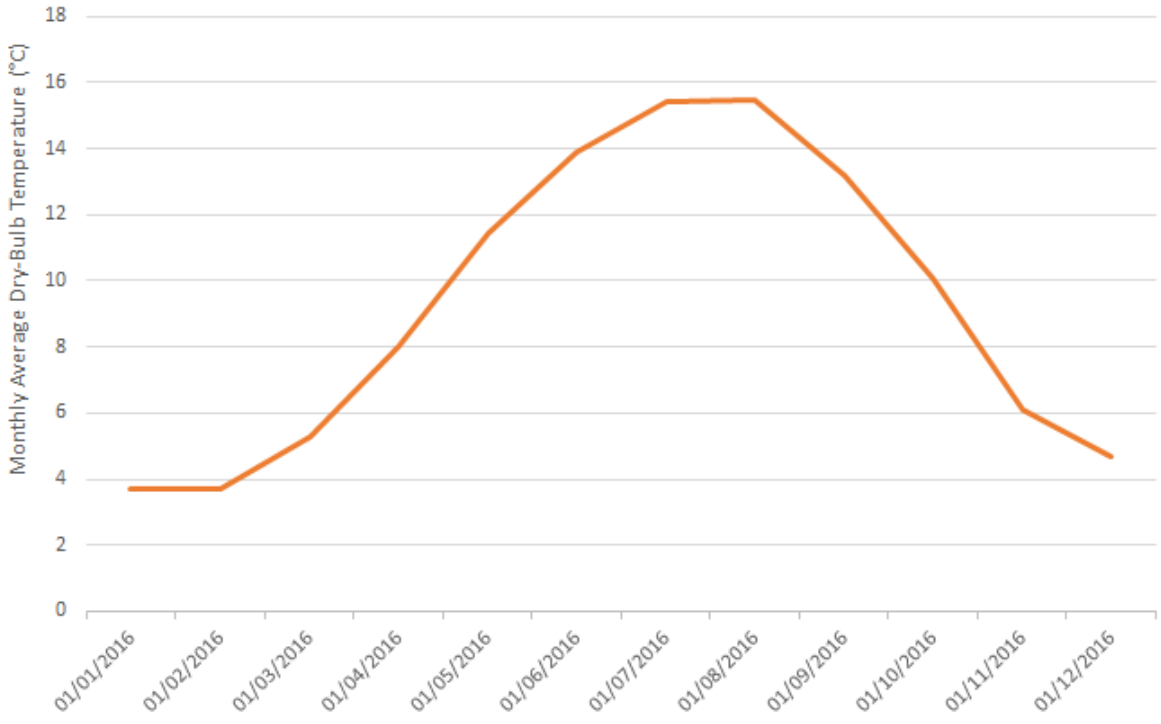

Figure 5.1 – Baseline Model: Monthly average outdoor dry-bulb air temperature

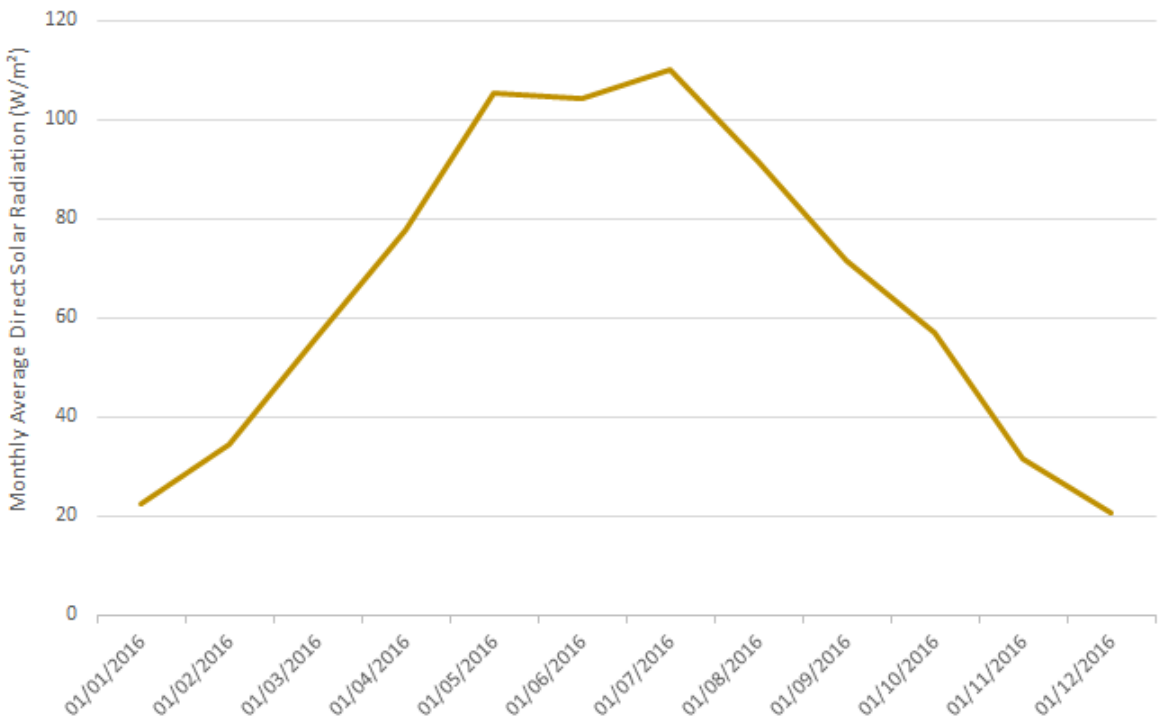

Figure 5.2 – Baseline Model: Monthly average direct normal solar radiation

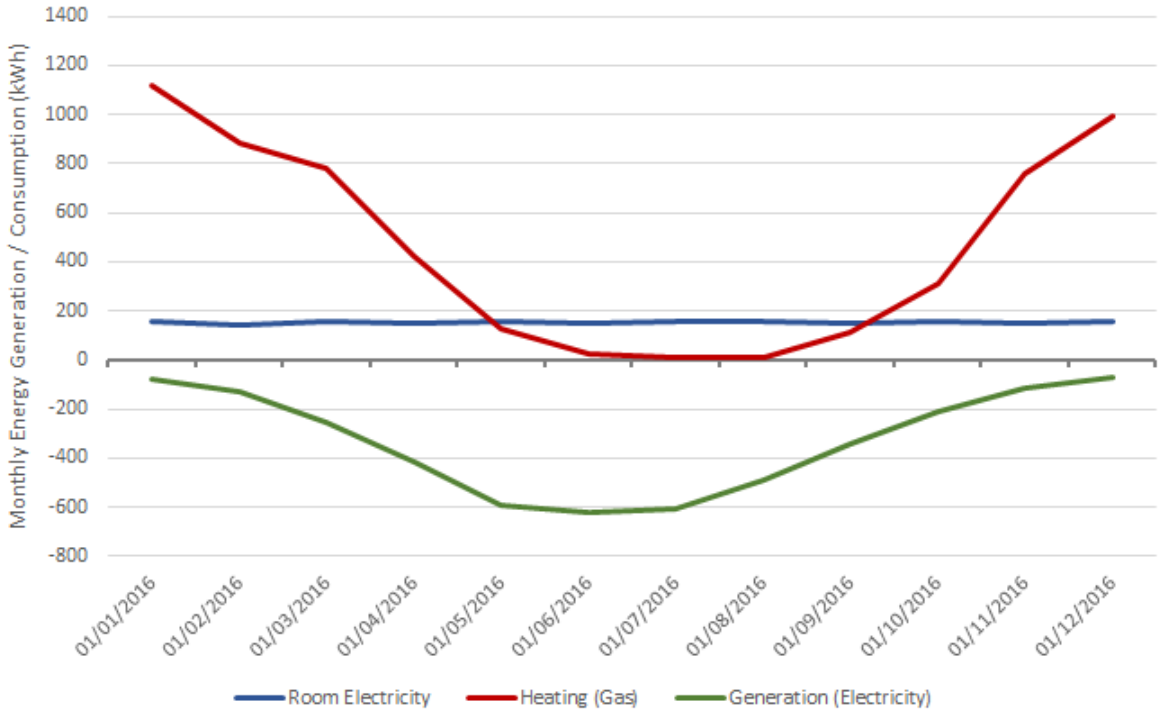

Figure 5.3 – Baseline Model: Monthly energy generation and consumption by fuel.

The results demonstrate how the domestic energy system of the Energy House model responds seasonally to the external conditions. Energy consumption for heating was typically active in the winter months (October – March), conversely energy generation at the photovoltaics was typically active in the summer months (April – September). Consumption of electricity cycles periodically throughout the year as it is directly dependent on occupancy, which has a repetitive cycle unaffected by external weather conditions.

A stark misalignment between domestic energy generation and energy consumption was apparent from this data. With the localised generation of energy from renewable sources, instant consumption of that energy was required or the surplus energy was redirected to the grid. Taking into consideration that solar incidence peaks not only throughout the summer months, but also during each day, the misalignment between energy generation and consumption was not just a seasonal issue, but occurs at the daily scale too. Figure 5.4 demonstrates how this is the case, by showing the hourly energy consumption and generation for the baseline model, during a day in June 2016.

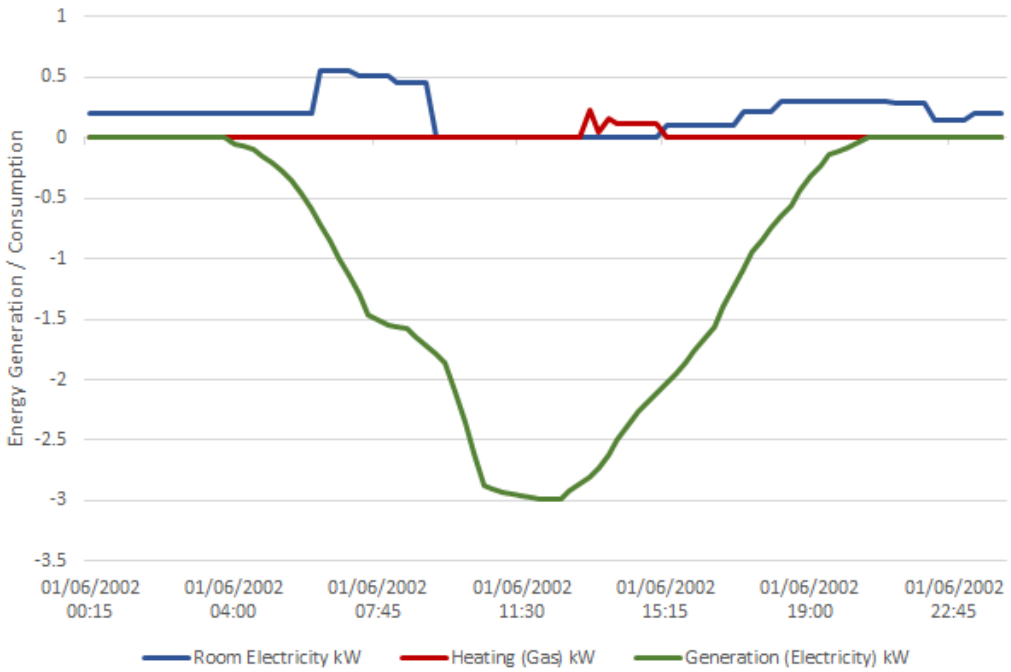

Figure 5.4 – Baseline Model: Hourly energy generation and consumption – an example day of data for a day in June 2016.

The information displayed in figure 5.4 shows two things. One, there is a misalignment in the timing of energy generation and consumption – meaning that energy generated throughout the day is not being consumed, since the building is unoccupied. Two, the quantity of energy is misaligned also – meaning that the generated quantity of energy is much higher for the entire day than the demand for energy for that same day. The summary of annual energy data provides more insight into this and is given in table 5.2.

Table 5.2 – Baseline Model: Summary of annual energy use.

Parameter	Annual Energy Use (kWh)
Electric Energy Consumption	2585 kWh
Gas Energy Consumption	5502 kWh
PV Energy Generation	4133 kWh
PV Losses	207 kWh
Net PV Generation	3926 kWh
Energy Drawn from the Grid	1812 kWh
Energy Sent to the Grid	3153 kWh

These results show that with the area of photovoltaics, as defined by the roof area of the Energy House, the energy generated on an annual basis is more than that required by the electrical demand of the building. When combining the energy demand of both fuels, gas and electricity, the photovoltaic output is able to cover almost half of the energy demand of the building.

What this baseline model points to is a necessity for energy storage in order to facilitate the use of photovoltaic generation outside of demand, reduce the misalignment between energy generation and energy consumption, and reduce the overall dependency of the building's energy systems on grid connection – thus promoting the autonomous localised domestic energy system targeted in the introduction to this thesis.

The need for energy storage is not expected to change despite variation to the modelled scenario. The next sections of this chapter describes how simulation results change due to variation of conditions, and how 'sensitive' the outputs of the domestic energy are to that variation.

To reflect on and compare against the results of the baseline model, a combined energy consumption of fuels from grid sources is quantified under each sensitivity scenario within each category (see table 4.12). The grid consumption of the baseline model was found to be 7314 kWh; a combination of both energy drawn from the grid and the gas consumed for heat energy.

Deviation from this baseline quantity demonstrates the impact of each sensitivity factor on the overall energy system performance from the viewpoint of system autonomy. This shows which scenarios within the sensitivity category offer favourability for the typical UK home. In chapter 6, energy storage is introduced into the localised energy system, these deviations are reproduced to show not only the change in sensitivity due to the introduction of storage, but the reanalysed favourability of energy systems with integrated storage.

5.2 Archetype

The archetype category is divided into three core scenarios: that of mid-terrace, end terrace and detached; the baseline condition for archetype was the end-terrace. This section then looks at how the results found for that baseline model vary when considering the mid-terrace and detached home instead.

By looking at the exposed façades of the building, the impact of archetype on annual energy consumption can be alluded to. Table 5.3 gives the exposed wall surface area for each archetype and the ratio of exposed wall to total wall surface area. The table also lists the predicted HTC determined by Designbuilder in its sizing of the appropriate heating system.

Table 5.3 – Exposed external wall surface area per archetype

Archetype	Exposed Surface Area	Ratio to Total Surface Area	Predicted HTC
End-Terrace	82.9 m^2	0.67	224.9 W/K
Mid-Terrace	41.9 m^2	0.34	133.5 W/K
Detached	124.0 m^2	1.00	288.8 W/K

Each of the models were simulated under the remaining baseline conditions; the data and summary for each simulation were recorded for analysis. The results, as would be expected, only revealed a variation in the domestic consumption of energy for space heating, since the variation in the model is demonstrative of a change to the fabric of the building by means of exposing and covering facades of the building. Figure 5.5 gives a comparison of daily heat energy consumption for the three different archetypes over the course of a year.

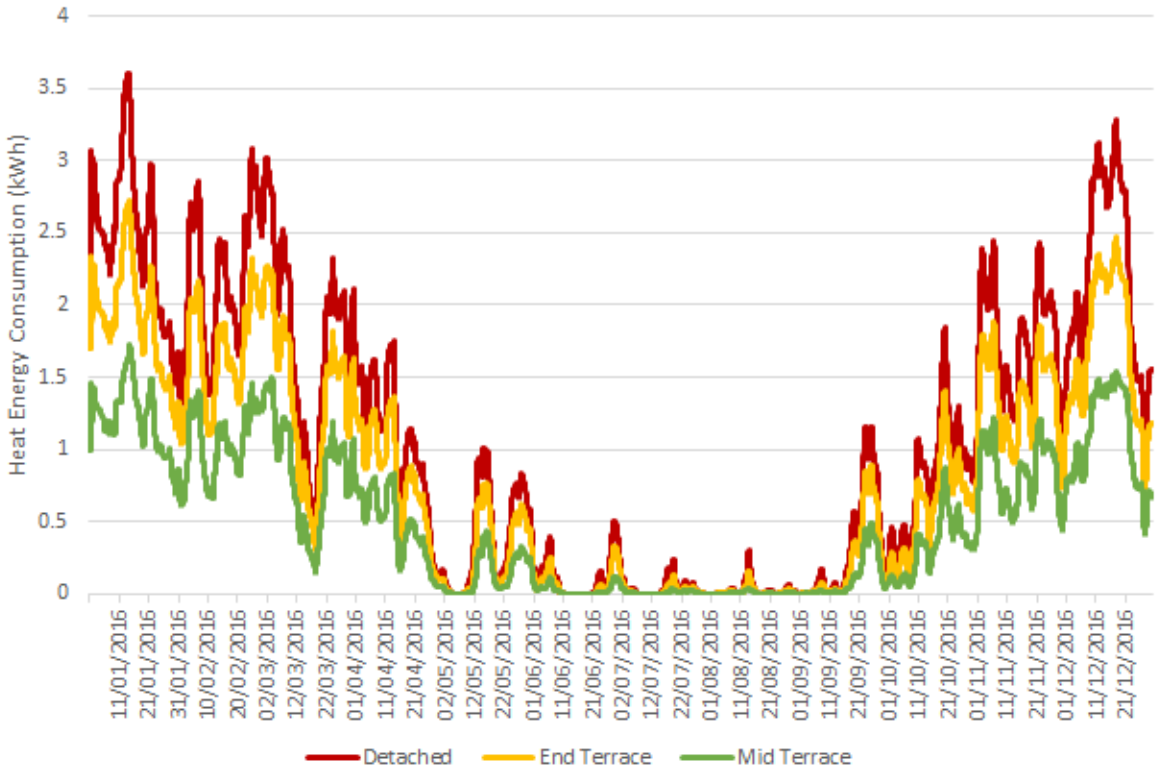

Figure 5.5 – Archetype Models: Daily averaged heat energy consumption comparison.

The data in figure 5.5 shows that trends in heat energy consumption are consistent throughout the year, with similar peaks appearing in each simulated data set. As would be expected, the variance in consumption is simply a shift depending on the archetype's exposed surface area. Table 5.4 lists the electricity energy summary for each building archetype.

Table 5.4 – Archetype Models: Summary of annual energy use.

Parameter	Detached	End Terrace [Baseline]	Mid Terrace
Total Gas Energy Consumption	7809 kWh	5502 kWh	3370 kWh

The linear relationship between each heat energy consumption and the exposed façade surface area further determined that around 1067 kWh per year is due to heat loss through the floor and roof, and through additional ventilation.

Although the variation of archetype scenario has no impact on the consumption of electricity in the home, when looking at the overall domestic energy systems as a whole, the sensitivity of that global energy system is significant. The detached archetype demonstrated an increased heat energy consumption by 38.8% over the end-terrace baseline model, while the mid-terrace archetype demonstrated a reduction in heat energy consumption by 29.5% from that baseline. A final comparison is made in figure 5.6 of the overall energy system's sensitivity to archetype in relation to the baseline performance. This figure expands to compare the sensitivity of all considered factors, as will become apparent as this chapter progresses.

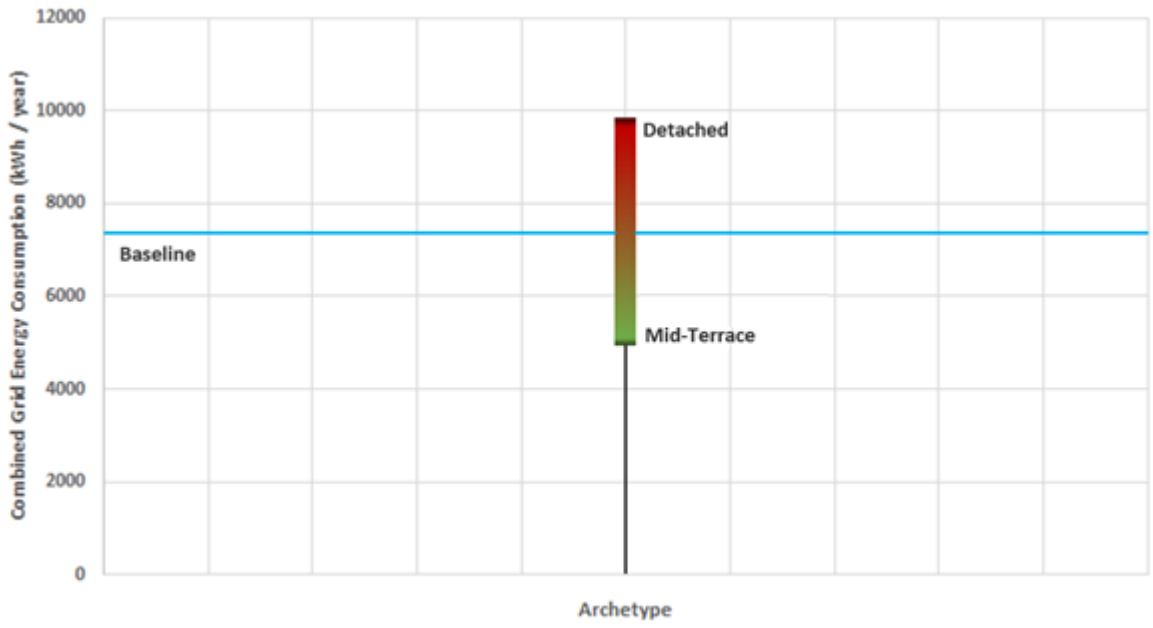

Figure 5.6 – Sensitivity of base energy system to archetype.

5.3 Occupancy

Four occupancies were considered for this sensitivity factor: the baseline of 2 working adults, 1 retired adult, 1 working adult and 2 retired adults. These were chosen as they made up the most common occupancy profiles for homes in the UK, as determined by time use data.

The variation in energy consumption from this factor has dependency on both period of occupation and occupation density. Table 5.5 gives the summary of energy use for each occupancy.

Table 5.5 – Occupancy: Summary of energy use.

Parameter	2 Working Adults	1 Retired Adult	1 Working Adult	2 Retired Adults
Electric Energy Consumption	2589 kWh	1797 kWh	1312 kWh	3550 kWh
Gas Energy Consumption	5502 kWh	6663 kWh	6317 kWh	5486 kWh
PV Energy Generation	4133 kWh	4133 kWh	4133 kWh	4133 kWh
PV Losses	207 kWh	207 kWh	207 kWh	207 kWh
Net PV Generation	3926 kWh	3926 kWh	3926 kWh	3926 kWh
Energy Drawn from the Grid	1883 kWh	991 kWh	840 kWh	2195 kWh
Energy Sent to the Grid	2982 kWh	3128 kWh	3243 kWh	2425 kWh

Consumptions of electricity follow a logical trend in this simulated data – for households with higher occupancy density (those with 2 adults) and for households with greater occupancy periods (retired occupants), consumption is higher. The same trend is not seen for heating demand however; while households with greater occupancy periods (retired occupants) do

still increase the heating demand, a much higher demand for heating is seen for households with lower occupancy density (1 adult).

The overall building energy system sensitivity to occupancy is finally shown in figure 5.7, and is compared to the previous sensitivity of archetype.

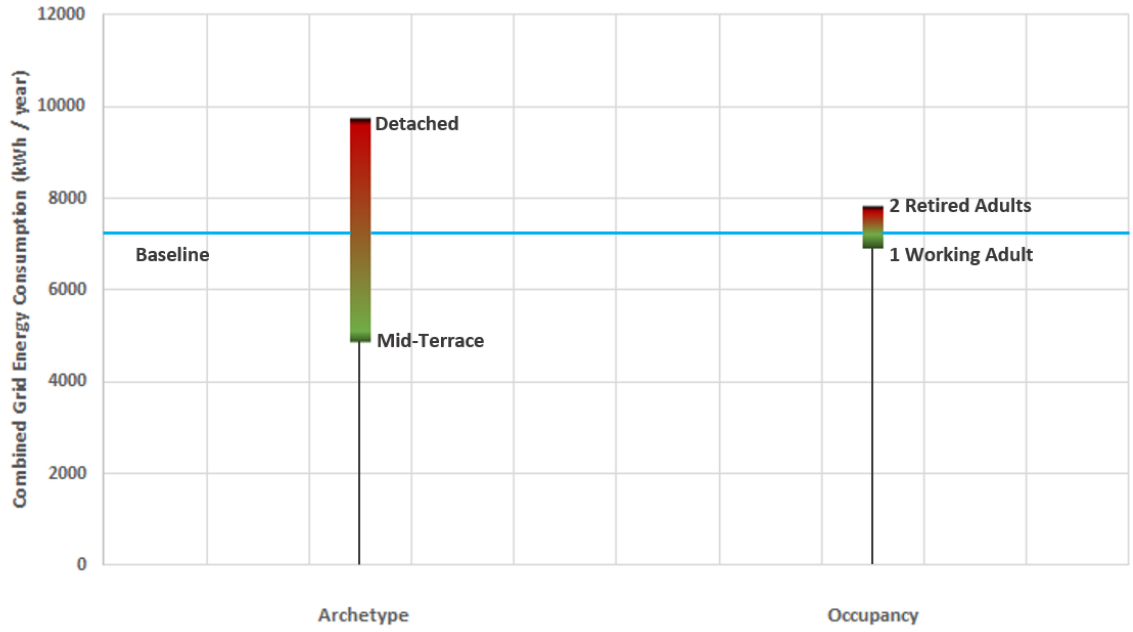

Figure 5.7 - Sensitivity of base energy system to archetype and occupancy.

Once again, the combined grid energy requirements are used for the comparison against each other and the baseline Energy House model. The comparison displayed in figure 5.7 shows that the domestic energy system represented by the Energy House model is much less sensitive to variations in occupancy than it is to archetype. The factors now tending towards system autonomy are mid-terrace homes with a single working adult.

Despite the increase in heating energy required by single occupant homes, the reduction in consumption of electrical energy works toward mitigation. Equally, the decrease in heating energy observed for homes with 2 occupants is countered by the subsequent increase in electrical energy consumption.

5.4 - Location

As with occupancy, the sensitivity factor of location was expected to impact on the energy consumption of both electricity and heat energy. This was due to the variations in solar radiation and average temperatures at different locations across the UK. Forty-two different locations (including the baseline location of Manchester) were considered, in order to quantify the impact of location on the performance of the domestic energy system.

Previous sections used tables to display the results of simulated scenarios, however given that there are forty-two different scenarios for this factor, a graphic of the key simulation results are:

- The Gas Consumption (Figure 5.8)
- The PV Generation (Figure 5.9)
- The Energy Drawn from the Grid (Figure 5.10)
- The Energy Sent to the Grid. (Figure 5.11)

The map used in figure 4.4 of the previous chapter was used in displaying these data. Each of the figures show the modelled distribution of the result for each of the location scenarios.

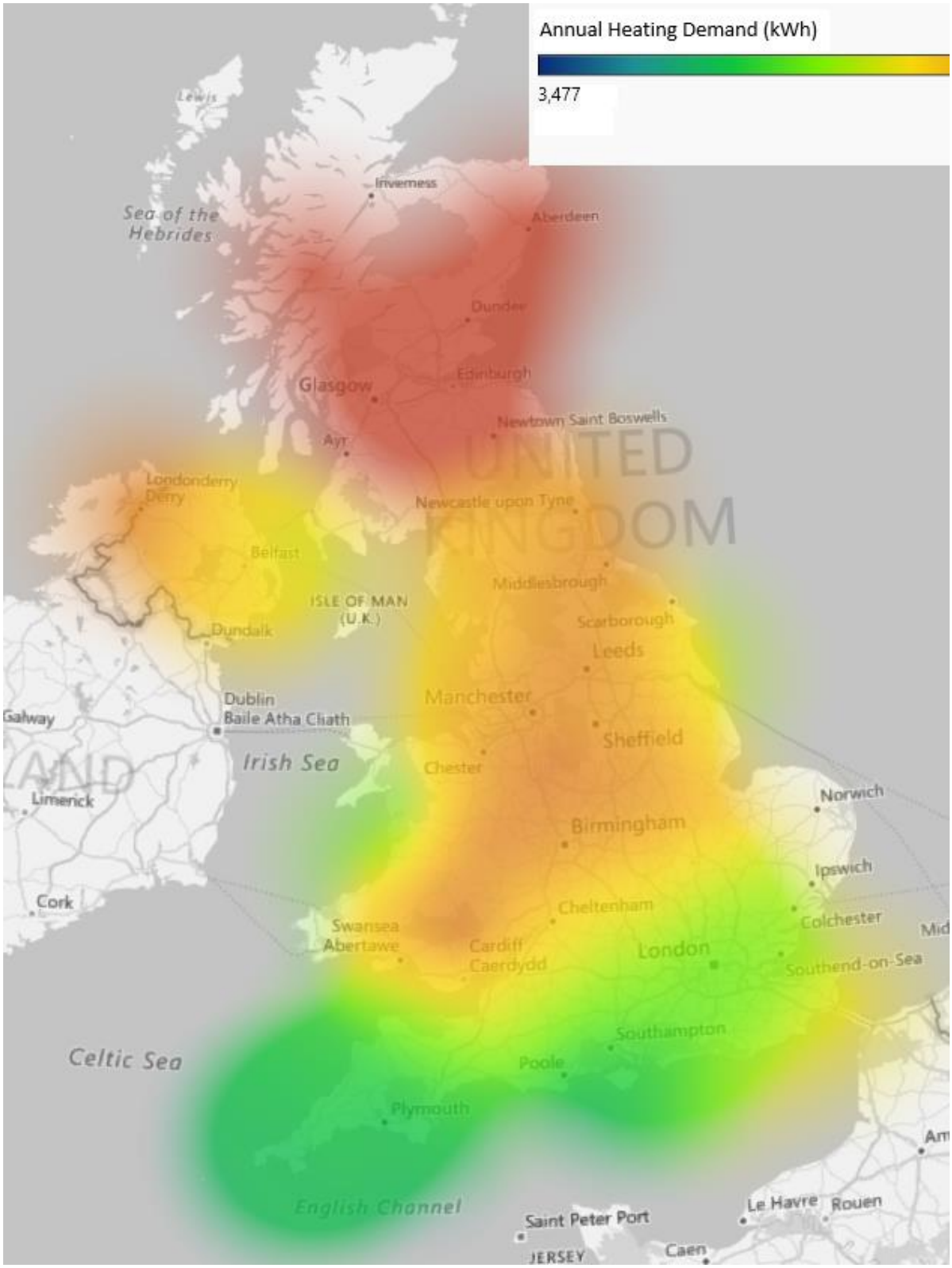

Figure 5.8 – Location: Distribution of annual heating demand.

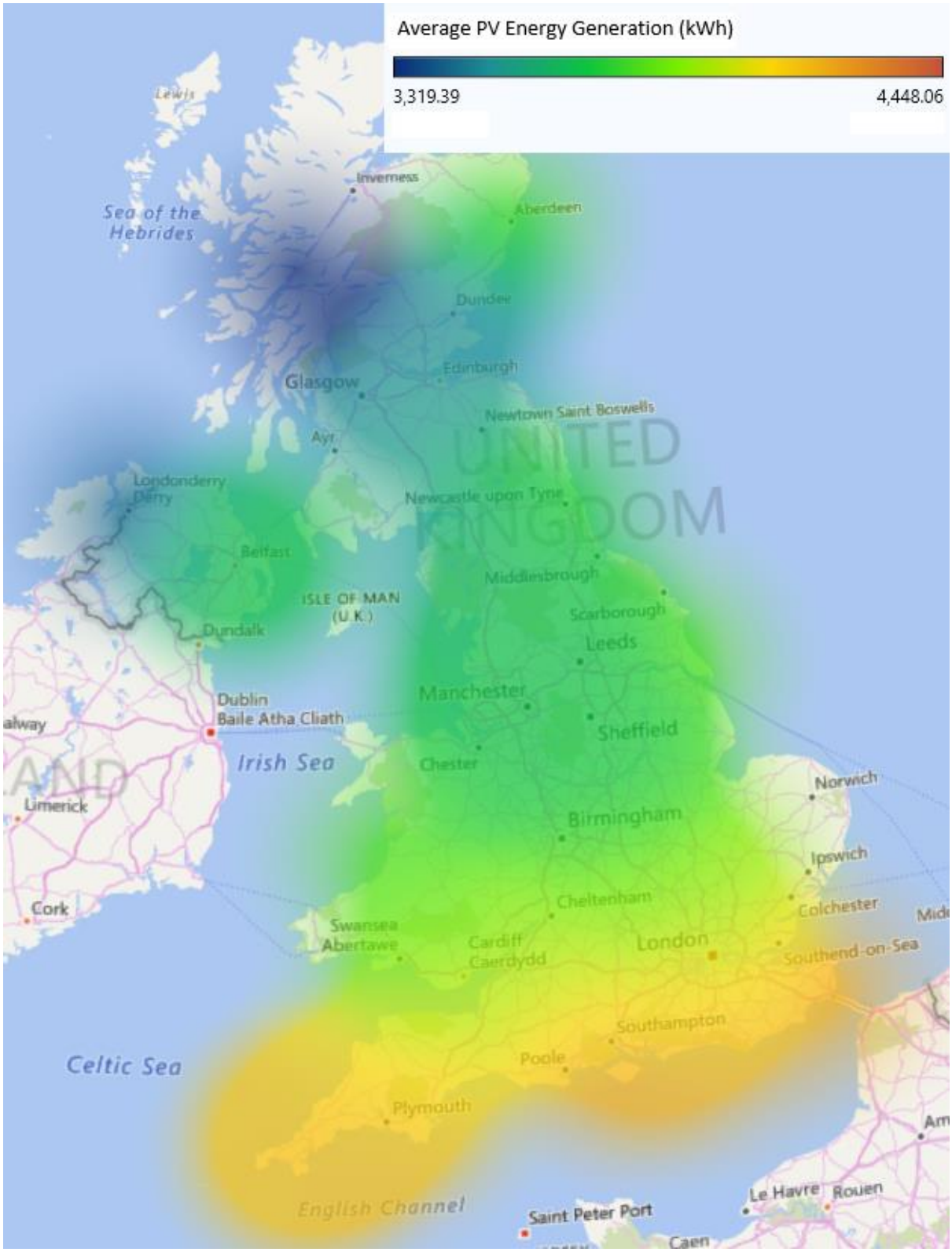

Figure 5.9 – Location: Distribution of annual PV energy generation.

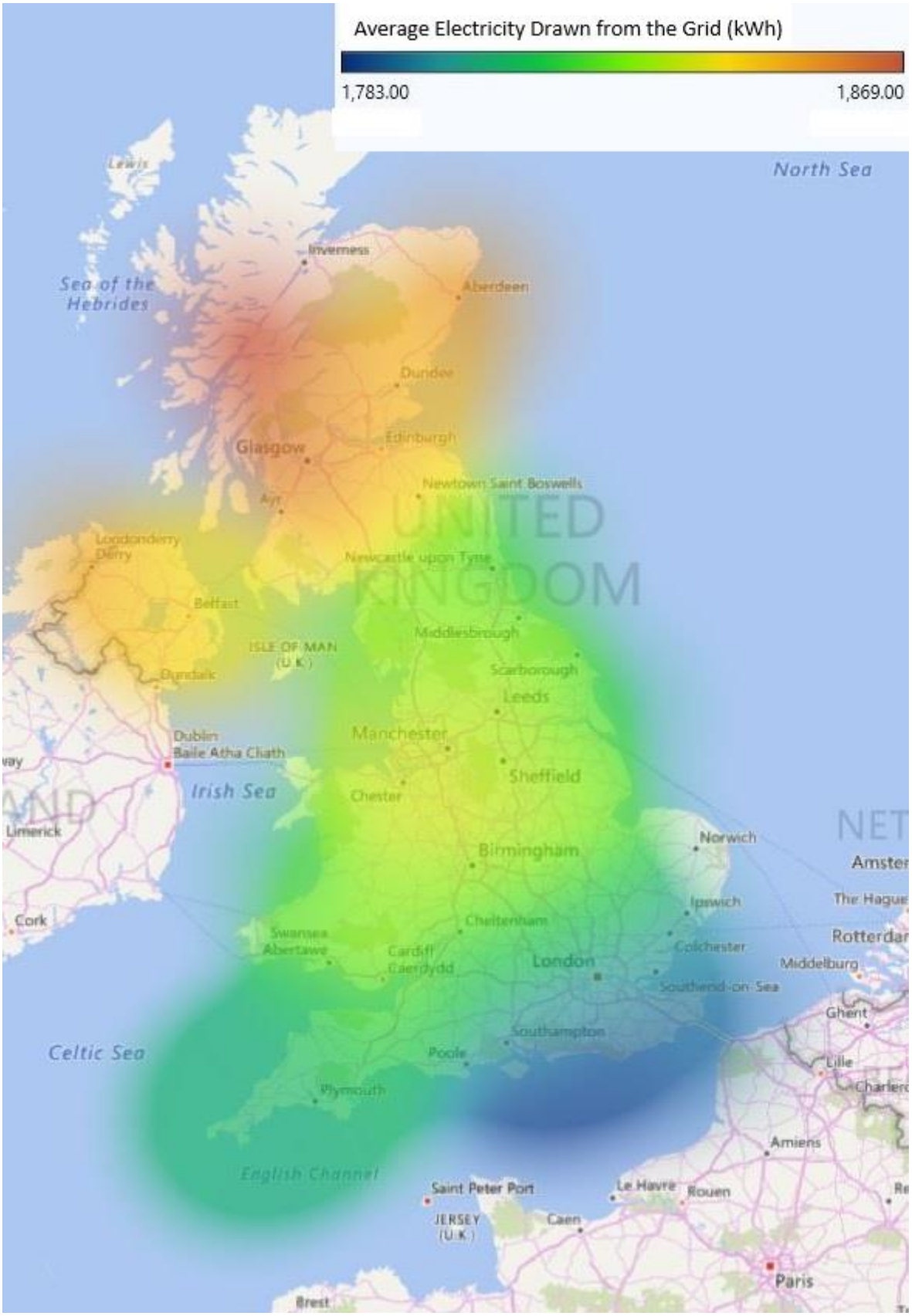

Figure 5.10 – Location: Distribution of annual grid electricity consumption.

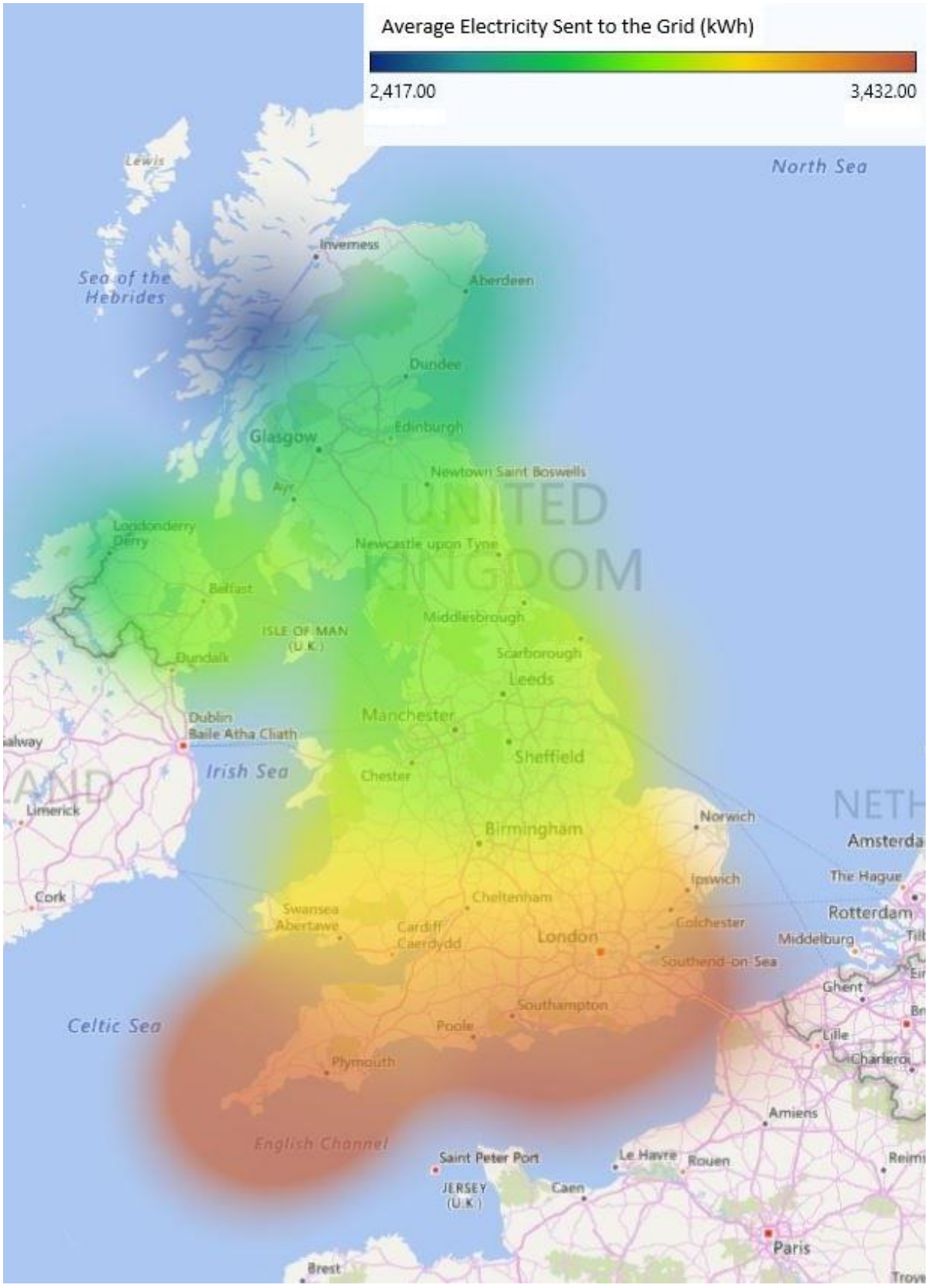

Figure 5.11 – Location: Distribution of annual electricity sent to the grid.

The distribution of heating demand across the UK, as shown in figure 5.8, reveals three important trends. The further north a location is, the greater the heating demand will be. This reflects typically colder climates at higher latitudes. Mountainous areas are the exception to this, where these locations are more exposed to climate conditions and experience greater heating demand than the surrounding areas. The lowest heating demands, which would benefit mostly from energy autonomy, are found in the south west and parts of the south east. Figure 5.9 shows that these regions also benefit the generation of PV.

The subsequent distributions of electricity drawn from the grid (figure 5.10) and electricity sent to the grid (5.11) follow the trend of the PV distribution (fig 5.9). Locations at lower latitudes requiring less energy from the grid, and also return more energy to the grid than those locations to the north.

It is important to note that large quantities of energy generated by PV are being redirected to the grid in, what was established in the previous chapter, is an inefficient use of the PV installations themselves. The baseline Energy House model demonstrated that only 24% of the photovoltaic output was being used within the local energy system – the remainder was released into the grid. Within the most southerly locations, useful photovoltaic output rose to 42%.

The combined grid energy consumption for each location is shown in relation to its latitude in figure 5.12.

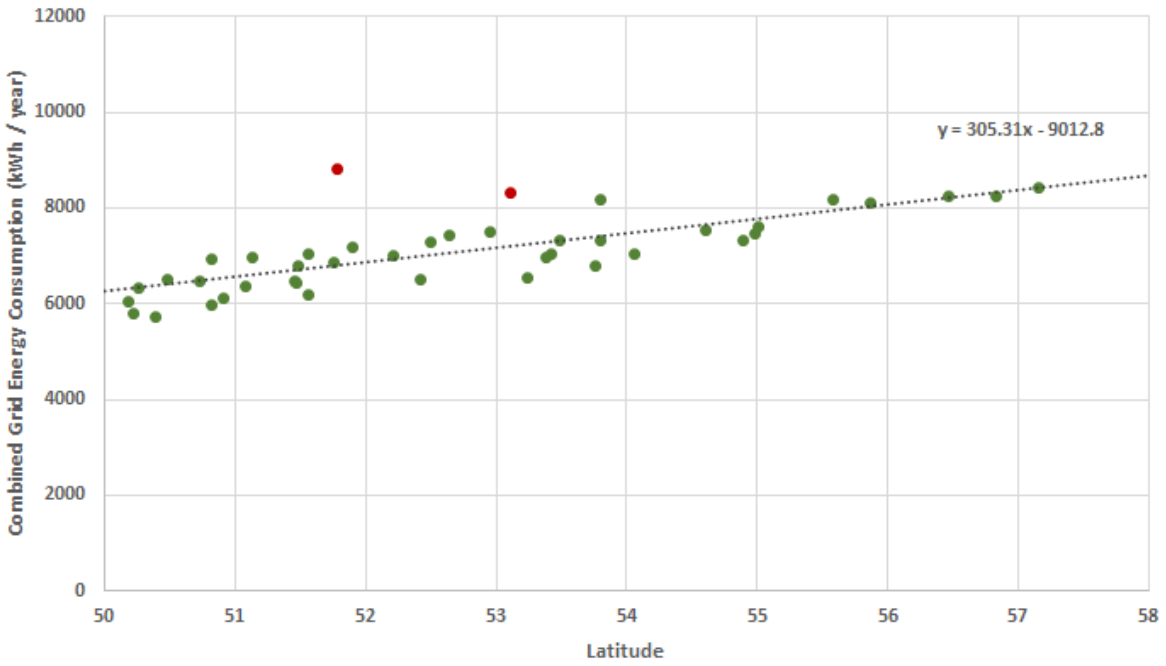

Figure 5.12 – Location: Combined grid energy consumption at each location latitude.

A linear trend appears in the relationship between the combined grid energy consumption and the latitude of each location. Two noticeable outliers to this are highlighted in red; these locations (Ebbw Vale and Leek) have two of the highest elevations of the forty-two, and so the exposure factor at these locations explains why the consumption is considerably high. Interestingly, were the relationship to remain linear, it would indicate that at a latitude of 30^{o}N the net energy demand of the building would reach zero.

These data provide an additional sensitivity factor to include in the ongoing comparison of this chapter. Figure 5.13 shows the comparison against the baseline consumption and the previous factors.

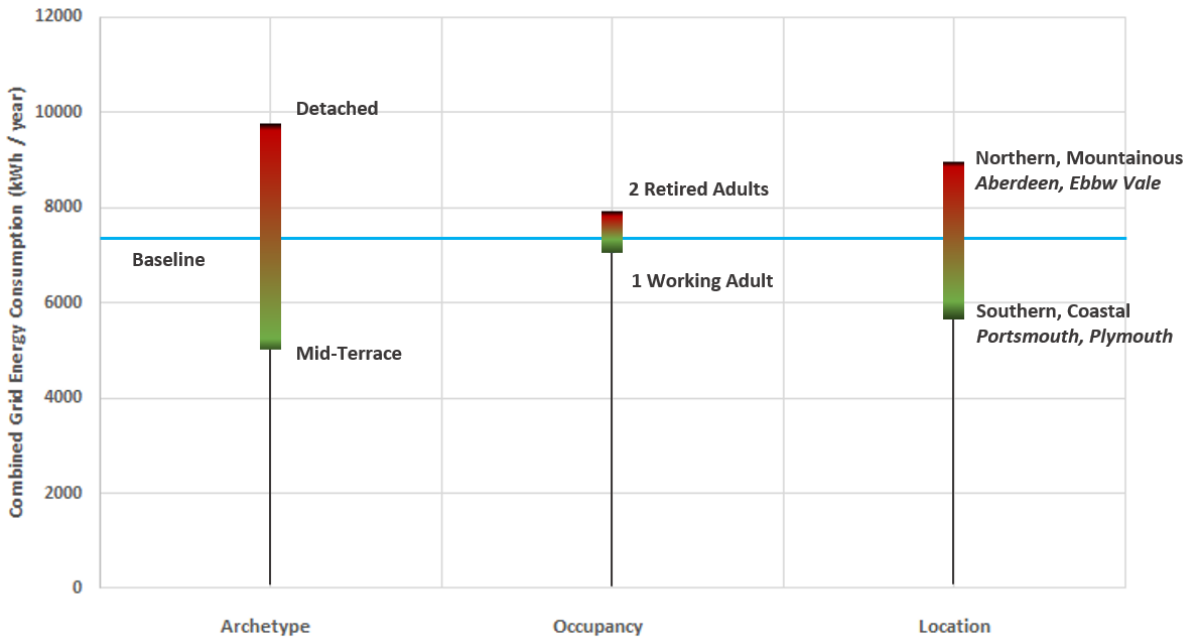

Figure 5.13 – Sensitivity of base energy system to archetype, occupancy, and location.

The comparison so far, as shown in figure 5.13, indicates that the sensitivity of the Energy House's energy system to location is more comparable to that of archetype. Variations in latitude dependent temperatures and solar incidence have led to a considerable variation in the combined domestic energy consumption, with more northerly and mountainous regions having much higher consumption and southern, more coastal regions having considerably lower consumptions. Tendency towards energy autonomy so far then rests on mid-terrace homes, occupied by one working adult, located towards southern coastal locales of the UK.

5.5 Future Climate

Variation in climate from current to future weather data was observed in the last chapter. With climate change comes a significant predicted increase in temperature and a slight

increase in the solar incidence. As seen in the results of sensitivity analysis for location, variations in both temperature and solar radiation have proven to deliver a sizeable variation in final combined grid energy consumption. This section now investigates whether this is the case for future climates. It is also important to check how energy systems such the baseline model respond to changing conditions, ensuring that performance isn't significantly hindered.

Table 5.7 lists the energy summary of energy use for each climate data. Note that the model used in this scenario was that of the baseline Energy House model – only the climate data file was changed to reflect each of the future years.

Table 5.7 – Future Climates: Summary of energy use. (Eames et al., 2011).

Parameter	2016	2030	2050	2080
Gas Energy Consumption	5520 kWh	4207 kWh	3725 kWh	3077 kWh
Electric Energy Consumption	2586 kWh	2579 kWh	2576 kWh	2572 kWh
PV Energy Generation	4132 kWh	4264 kWh	4433 kWh	4370 kWh
PV Losses	413 kWh	213 kWh	222 kWh	219 kWh
Net PV Generation	3719 kWh	4051 kWh	4212 kWh	4152 kWh
Energy Drawn from the Grid	1834 kWh	1802 kWh	1786 kWh	1790 kWh
Energy Sent to the Grid	2968 kWh	3274 kWh	3422 kWh	3369 kWh

A review of the weather data for future climates in the previous chapter revealed that the average air temperature increased, with the number of degree days (discussed in the previous chapter) decreasing. This is reflected in the data shown in table 5.7 – as the demand for heating is reduced by almost half. There is also a net increase in the quantity of electricity generated through PV, though this does not follow a linear trend. The drop in PV generation

observed in 2080 was traced to the increased cloud coverage, as predicted by Tham et al. (2011). The resulting impact of the decrease in heating demand and net increase in PV generation is a significant reduction in the overall grid energy demand. Figure 5.14 adds the sensitivity analysis of future climates to the overall comparison so far; note that as there is only a positive impact on the energy system in terms of autonomy, the baseline model is representative of the worst performance in this category.

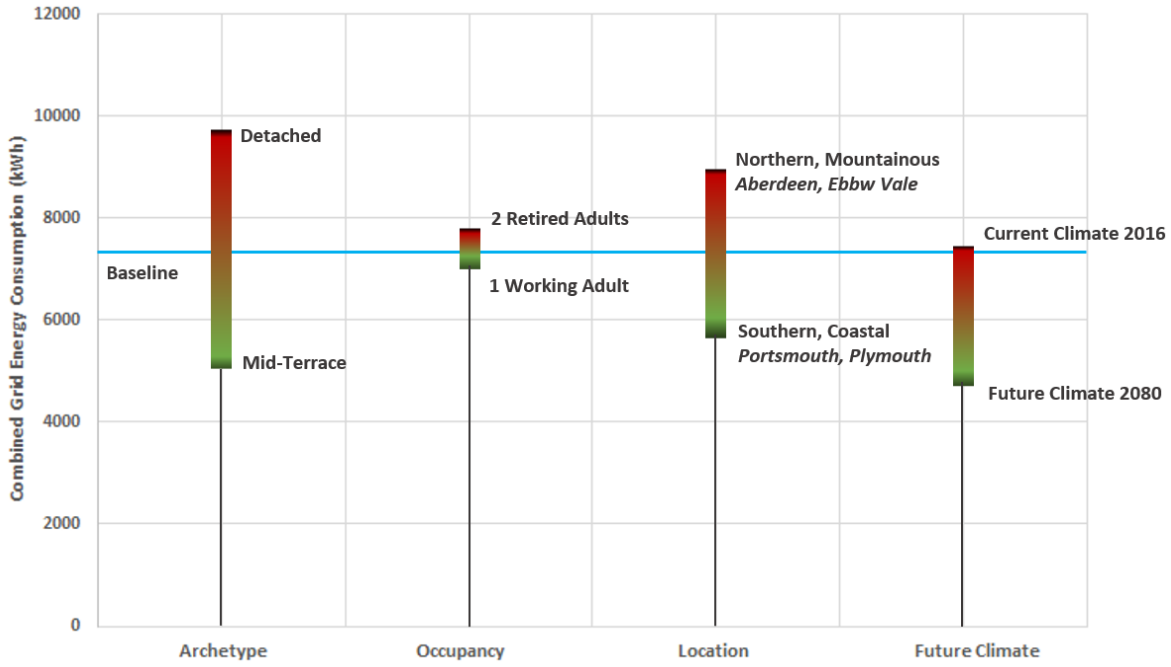

Figure 5.14 - Sensitivity of base energy system to archetype, occupancy, location and future climates.

Figure 5.14 shows that the sensitivity of the domestic energy system to future climates is comparable to that of the location in terms of magnitude, however as stated, all future scenarios fall under the baseline simulation due to the increase in overall temperature and

the increase in PV. This increase in PV generation is observed despite an increase in the overall temperature (and so a decrease in the performance of those photovoltaics could be assumed). Given the distribution of temperatures across the UK as indicated by figure 5.8, a similar shift across all climates is expected, meaning that locations in the south of the UK would receive the greatest reduction in overall energy demand as the climate varies in the future. Given that the climate changes are as predicted then, the domestic energy system considered in this study increases its tendency towards autonomy.

While efforts are made to curb the effects of climate change however, the predicted outcomes of future weather patterns are subject to change. Instead of waiting for these possible outcomes, the fabric of the building can instead be modified through retrofit, inducing better thermal performance of the building and reduce the demand for energy.

5.6 Retrofit

This section looks at retrofit as a solution for improving the energy performance of homes, and the impact it has on the overall energy system demand, i.e. on the sensitivity of domestic energy systems to the introduction of retrofit in the home. Deep retrofit was discussed in the last chapter (see table 4.11 for a list of possible solutions); this was applied to the model of the Energy House in stages so review the impact of each retrofit measure on the energy performance of the building. The overall retrofit application delivered the sensitivity analysis of this factor.

Although deep retrofit suggests a modification of the central heating system to an improved efficiency, initial investigations demonstrated that it would be practical to remove the gas

central heating system and replace it with an electric heating system, without affecting fuel costs.

Table 5.8 gives the summary of energy use for each of the retrofit measures considered in this modelling category. Note that the results show a cumulative addition of retrofit measures with each column.

Table 5.8 – Retrofit: Summary of energy use.

Parameter	No Retrofit	Electric Heating	+ Wall Insulation	+ Double Glazing	+ Roof Insulation	+ Reduced Infiltration
Gas Energy Consumption	5520 kWh	0 kWh				
Electric Consumption	2586 kWh	7588 kWh	4304 kWh	4098 kWh	3555 kWh	3153 kWh
PV Energy Generation	4132 kWh					
PV Losses	413 kWh					
Net PV Generation	3719 kWh					
Draw from the Grid	1834 kWh	6465 kWh	3361 kWh	3152 kWh	2868 kWh	2195 kWh
Energy Sent to the Grid	2968 kWh	2802 kWh	3029 kWh	3055 kWh	3062 kWh	3127 kWh
Net Transfer	1134 kWh	-3663 kWh	-332 kWh	-97 kWh	194 kWh	932 kWh

In removing the need for gas as a fuel, the total combined grid energy demand was then simply the energy drawn from the grid (highlighted in table 5.8). These data reveal an initial spike in the demand for electricity, due to the additional heating requirements, however this combined energy demand is reduced considerably with the application of retrofit. Figure 5.15 shows a breakdown of the contributions of each retrofit measure to the overall reduction in heating energy demand.

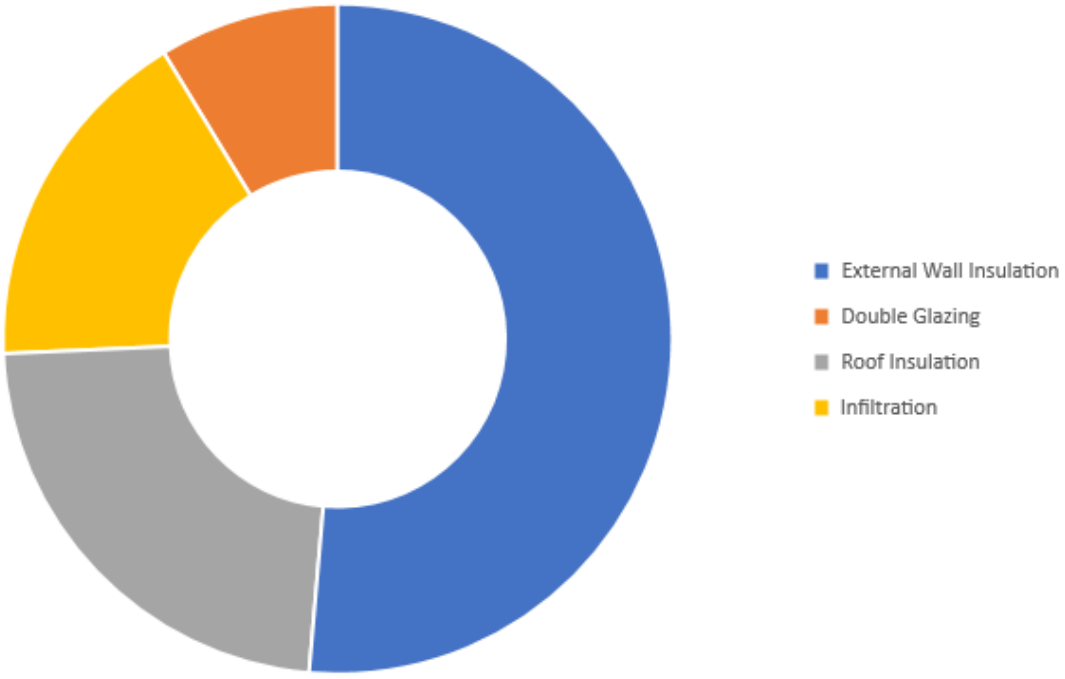

Figure 5.15 – Retrofit: Contribution of each retrofit measure to the overall reduction in heating energy demand.

The sensitivity of the domestic energy system to retrofit is shown in figure 5.16, in a final comparison of all sensitivity factors and the scenarios contained within.

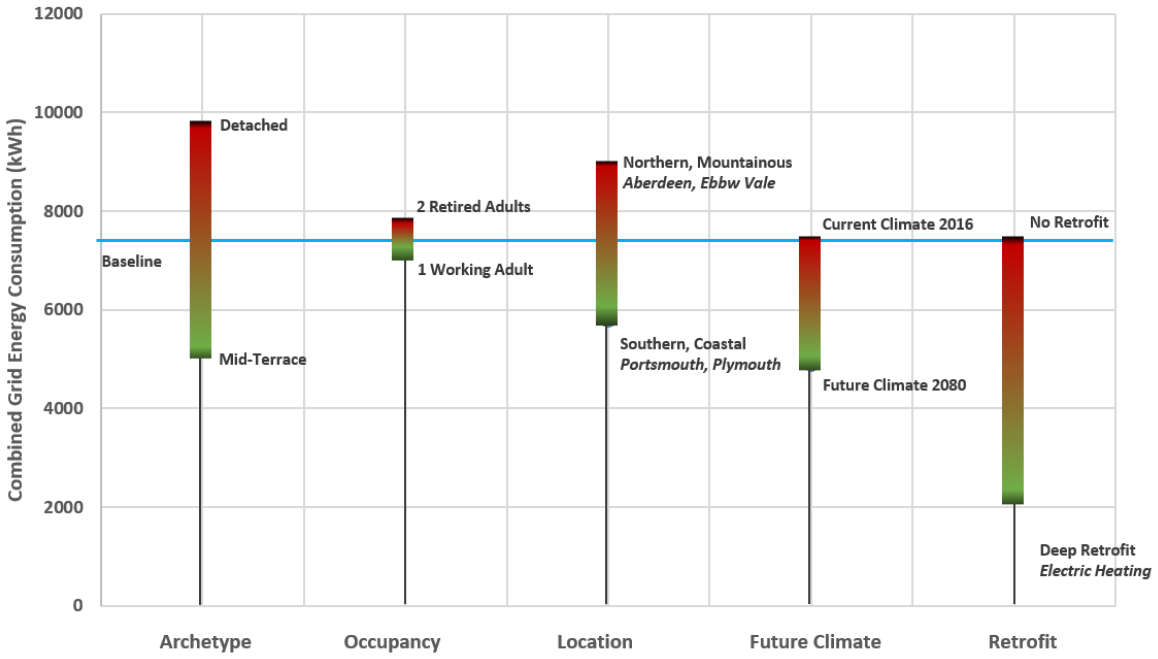

Figure 5.16 - Sensitivity of base energy system to archetype, occupancy, location, future climates and retrofit.

Figure 5.16 now compares the sensitivity of a PV-based domestic energy system to all factors considered in this part of the study. The final addition of retrofit to this figure shows that retrofit has the largest impact on the energy system, with reductions in the combined grid energy consumption per year of up to 70% (from the baseline grid consumption of 7314 kWh to a consumption of 2195 kWh.

The logical next step before considering energy storage, was to investigate whether or not a combination of the 'best-case scenarios' of these sensitivity factors supports further tendency toward energy autonomy.

5.7 The Best-Case Scenario

The Energy House model was modified for a final time to investigate how a combination of 'best-case scenarios' might impact on the overall energy system performance. The factors and scenarios considered for this model were:

- Archetype: Mid-Terrace
- Occupancy: 1 Adult, Working
- Location: Southern, Coastal, Plymouth
- Deep Retrofit

Note that the future climate data is not considered here. While it is important to understand how the system might be affected over time as the climate changes, predictions of the immediate system's performance are required at this stage.

Table 5.9 gives the summary data for the best-case scenario model, as compared to the original baseline model.

Table 5.9 – Best-case Scenario: Summary of energy use.

Parameter	Baseline Model	Best-Case Scenario Model
Gas Energy Consumption	5520 kWh	0 kWh*
Electric Energy Consumption	2586 kWh	1551 kWh
PV Energy Generation	4132 kWh	4634 kWh

PV Losses	413 kWh	232 kWh
Net PV Generation	3719 kWh	4402 kWh
Energy Drawn from the Grid	1834 kWh	1005 kWh
Energy Sent to the Grid	2968 kWh	3857 kWh

*Note that gas heating was removed from the model.

The data shown in table 5.9 demonstrates that a considerable reduction in the energy drawn from the grid of up to 86% is possible by using a combination of all the best-case scenarios found within the sensitivity analysis. Here, the energy demand from the grid is 26% of the quantity of surplus PV energy sent back to the grid. Given this finding, it is more than plausible that energy autonomy might be achieved with the use of some energy storage. While this result is positive and supports the aim of this study, it is restricted to the best-case scenario model.

The key restrictions, which prohibit energy autonomy from being applied to the entirety of the UK is the location and occupation requirements. Remaining factors of archetype and retrofit are achieved with modifications to the building fabric (though making variations to archetype may not be so simple). The 'worst-case scenarios' from both occupancy and location are reintroduced into the model in order to review whether the restriction on autonomy can be reduced across homes in all of the UK. The results from this simulation delivered a combined grid energy demand of 1981 kWh, with a return to the grid of 2427 kWh – a surplus energy 18% higher than the demand. This result reduces the impact of these

factors, demonstrating a positive argument for the use of energy storage methods at the domestic scale, with a tendency towards energy autonomy on a local scale.

This conclusion completes the third objective of this work, and suggests that it could be possible to integrate methods of energy storage for the purpose of energy autonomy, and that this integration may only be limited by the application of building fabric modifications. This thesis now continues to explore the techniques used to model energy storage, before using the inputs of the simulated scenarios of this chapter to investigate the impact on energy system sensitivity; to determine whether energy autonomy is achievable on the domestic scale; and to explore where restrictions lie in terms of both factors discussed in this chapter and of the storage methods themselves.

Chapter 6

Models for Energy Storage

Abbreviations

DoE	Department of Energy
EoS	Equation of State
KiBaM	Kinetic Battery Model
NIST	National Institute of Standards and Technology
PCT	Pressure Composition Temperature

Nomenclature

Battery Storage

a	Equation Constants	q	Battery Charge (Ah)
c	Charge Ratio	R	Resistance (Ω)
C_F	Cycles to Failure	R_{dis}	Fractional Depth of Discharge
E	Internal Voltage (V)	t	Time (s)
I	Current (A)	V	Voltage (V)
k	Rate Constant ($hour^{-1}$)	X	Internal Resistance (Ω)

Subscript

nom	Nominal	1	Available Charge
0	Initial Condition	2	Bound Charge

Compressed Hydrogen Storage

c	Shape Factor	Z	Compression Factor
$D_{m,n}$	BACK Constants	R*	Reduced Mean Curvature
k	Boltzmann Constant ($m^2kgs^{-1}K^{-1}$)	S*	Reduced Mean Surface Area

$k_{1,2}$	Constants	V*	Reduced Mean Volume
n	Number of moles (mol)	V^{00}	Close Packed Density
P	Pressure (Pa)	u_0/k	Energy Parameter
q	Shape Factor	ε	Square Well Depth (m^2kgs^{-1})
R	Gas Constant (Pa m^3/mol K)	η	Reduced Number Density
T	Temperature (K)	ρ	Number Density
V	Volume (m^3)	ω	Accentricity Factor
z	Constant		

Subscript

c	Critical	m	Molar

Metal Hydride Storage

C	Sorption Rate (s^{-1})	t	Time (s)
C_P	Specific Heat (J/kg K)	T	Temperature (K)
E	Sorption Energy (J/mol)	u	Gas Velocity Vector (m^3/s)
h	Thermal Conductance (W)	x	Distance (m)
ΔH	Enthalpy (kJ/mol)	α	Constant
P	Pressure (Pa)	β	Hysteresis Factor
R	Gas Constant (Pa m^3/mol K)	ρ	Density (kg/m^3)
ΔS	Entropy (kJ/mol kg)	φ	Flatness Factor

Subscript

a	Absorption	d	Desorption
Eq	Equilibrium	f	Fluid
g	Gas	s	Solid

Superscript

eff	Effective	s	Saturated
0	Initial		

Activated Carbon Storage

a	Total Adsorbed Quantity (mol/kg)	t	Time (s)
a_0	Saturation Quantity (mol/kg)	T	Temperature (K)
C_P	Specific Heat Capacity (J/kg K)	v	Darcy Velocity (m/s)
E	Characteristic Energy (J/mol)	X	ratio of absorbed quantity
k	Thermal Conductivity (W/m K)	α	Constant
K	constant	β	Constant
M	Molecular Mass (kg/mol)	γ	Volume Expansion Coefficient
n	Constant	ε	Adsorption Potential (J/mol)
P	Partial Pressure	ε_b	Porosity
R	Gas Constant (Pa m^3/mol K)	ρ	Density (kg/m^3)

subscript

g – Gas

H_2 – Hydrogen

s – Solid

Hydrogen Components

F	Faraday Constant (A/mol g)	N_c	Number of Cells
I	Current (A)	Z	Electron Number
$\dot{n}$	Molar Flow Rate (mol/s)	η_F	Faraday Efficiency

Subscript

E	Electrolyser	FC	Fuel Cell

This chapter explores the models developed and used to represent energy storage as part of an integrated energy system for the Energy House. Simulations so far have demonstrated that a considerable misalignment between energy generation using photovoltaics and energy consumed by the building was apparent. Initial simulations using the calibrated baseline model revealed that up to 76% of energy generated by photovoltaics would not be used for consumption in the home and that this energy would be redirected into the grid.

Further modelling showed that it was possible to significantly reduce the energy consumption of domestic buildings by applying modifications to the fabric of the building, while remaining relatively insensitive to the factors of occupancy and location.

It was determined that to realise the aim of domestic energy autonomy, some factor of energy storage would need to be introduced into the energy system. Since that in all cases, the amount of surplus energy provided by photovoltaics was greater than the energy demand of the home, the integration of energy storage media into the Energy House model can be assessed for the potential of reaching that desired level of autonomy.

Four types of storage method are considered within this thesis:

- Home Battery
- Hydrogen: Compressed Gas
- Hydrogen: Absorption in Metal Hydrides
- Hydrogen: Adsorption in Activated Carbon

The home battery was chosen as an established – yet newly penetrating method for energy storage. Several versions of the home battery are commercially available and actively promote integration with domestic PV systems (e.g. Tesla Powerwall, Powervault, Nissan

xStorage, etc.), see Rodriguez et al., 2016. As another established technology, the compression of gas is no stranger to the world of energy storage, however its use on the domestic scale has yet to take into effect. That being said, the technology is well modelled in publications that look into using compressed gas with hydrogen components within the home (see Griesshaber & Sick, 1991; Ulleberg & Morner, 1997; Pedrazzi et al., 2010; Shabani & Andrews, 2011; and Rahimi et al., 2014).

Novel storage methods are introduced in the way of metal hydrides and activated carbon. Metal hydrides are considered for their ability to absorb hydrogen under certain conditions; as will be discussed, the alloy of $LaNi_5$ has shown to readily absorb and desorb hydrogen around atmospheric conditions and so proving useful for everyday storage without adding a great deal of technical complexity or necessity for high pressures (Boser, 1976). While this is the case, the trade off with this technology is its expense. Activated carbon is able to physically adsorb hydrogen, the process of which is determined by its internal pore structure. Often cited as having a large hydrogen storage capacity, storage is typically performed at extremely low temperatures (77 K), however given a higher pressure, this material is capable of storing reasonably quantities of hydrogen for the purpose of home energy storage (Jordá-Beneyto et al., 2007). While high pressure is the trade-off with this novel storage method, the raw materials are comparatively inexpensive compared to metal hydrides.

The model used to represent the home battery is a component already available for use in Designbuilder, and so simulations were performed inclusively without the need for separate treatment. Models used in predicting hydrogen storage performance however, required the separate treatment of results from annual simulations. This chapter goes on to discuss the equations behind the models for each storage method. The equations listed for the home

battery are described to inform on the process used in the Designbuilder software, while those used in the three methods of hydrogen storage are described to inform on the modelling constructed for the purpose of this thesis.

The independent modelling of hydrogen storage in this thesis was carried out in **Matlab**, and was designed so that the outputs of Designbuilder simulations could be used as the input – indicating a hypothetical hydrogen storage throughout the annual simulation. An individual Matlab script was designed for each of the hydrogen storage methods and based upon earlier works with such modelling content. Each of the Matlab modelling processes are discussed, with a final discussion on the modelling of auxiliary hydrogen components – the electrolyser and the fuel cell – and the logical process considered within each model.

6.1 Battery Storage

The home battery model used in Designbuilder is based upon the Kinetic Battery Model (KiBaM), as developed by Manwell and McGowan (1991 & 1993b) and Manwell et al. (1995). The model is broken down into three main components: the capacitor model, the voltage model and the lifetime model.

6.1.1 Capacitor Model

Battery charge is assumed to exist under two conditions: available and bound, and are treated independently to give an overall charge:

$$q = q_1 + q_2, \tag{6.1}$$

Where q_1 is the available charge and q_2 is the bound charge. To find the available and bound charge after any given period of charge or discharge, the equations of flow for each are solved:

$$\frac{dq_1}{dt} = -I - k(1-c)q_1 + kcq_2, \tag{6.2}$$

$$\frac{dq_2}{dt} = +k(1-c)q_1 + kcq_2, \tag{6.3}$$

where

I	is the charge or discharge current (A),
k	is a rate constant (hours^{-1}),
c	is a ratio of available to total charge capacity.

Equations to calculate the available and bound charge at the end of any given time step are then given as:

$$q_1 = q_{1,0}e^{-k\Delta t} + \frac{(q_0kc - I)(1 - e^{-k\Delta t})}{k} - \frac{Ic(k\Delta t - 1 + e^{-k\Delta t})}{k}, \tag{6.4}$$

$$q_2 = q_{2,0}e^{-k\Delta t} + q_0(1-c)(1 - e^{-k\Delta t}) - \frac{I(1-c)(k\Delta t - 1 + e^{-k\Delta t})}{k}, \tag{6.5}$$

where

$q_{1,0/2,0}$	are available and bound charge at the beginning of the time step (Ah),

q_o is the total charge ($q_{1,0}$ + $q_{2,0}$) at the beginning of the time step (Ah),

Δt is the length of the time step (hours).

6.1.2 Voltage Model

The voltage model takes into consideration the four key observations made in previous battery modelling (Hyman 1986). These observations are a dependency of the terminal voltage on: a) whether the battery is charging or discharging; b) the battery's state of charge; c) internal resistance and d) the magnitude of charge or discharge current.

Beginning with the equation for terminal voltage, V:

$$V = E - IR_0, \tag{6.6}$$

where

E is the effective internal voltage (V),

R_0 is the internal resistance (Ω),

the effective internal voltage is broken down into the following components of voltage:

$$E = E_0 + AX + \frac{CX}{(D - X)}, \tag{6.7}$$

where

E_0 is the fully charged / discharged internal voltage (V),

X is the internal resistance (Ω),

A is a parameter representing the initial linear variation of internal voltage (V),

C is a parameter representing variation of voltage during progressive charging/discharging (V),

D is another parameter representing variation of voltage during progressive charging/discharging (V).

6.1.3 Lifetime, Charge Transfer and Losses

The materials which make up a battery undergo fatigue/damage as they are used; the lifetime of a battery given this damage can be calculated and is useful in the accurate modelling of batteries. Facinelli (1983) notes that the lifetime of a battery is dependent on the subjected depth of discharge and recharge. Primarily, the deeper the discharge cycles, the sooner the battery is likely to fail. The following equation calculates the number of cycles until battery failure:

$$C_F = a_1 + a_2 e^{a_3 R} + a_4 e^{a_5 R}, \quad (6.8)$$

where

a_i are equation constants,

R is the fractional depth of discharge.

Before charge is transferred, the maximum current must be calculated for both charge and discharge. The maximum discharge current is calculated using:

$$I_{d,max} = \frac{kq_{1,0}e^{-k\Delta t} + q_0 kc(1 - e^{-k\Delta t})}{1 - e^{-k\Delta t} + c(k\Delta t - 1 + e^{-k\Delta t})}, \quad (6.9)$$

while the maximum charging current is calculated using:

$$I_{c,max} = \frac{-kcq_{max} + kq_{1,0}e^{-k\Delta t} + q_0 kc(1 - e^{-k\Delta t})}{1 - e^{-k\Delta t} + c(k\Delta t - 1 + e^{-k\Delta t})}. \quad (6.10)$$

It is important to know the maximum charge and discharge rates to ensure the battery can facilitate the desired transfer. $I_{d,max}$ and $I_{c,max}$ are used when there is not enough charge left in the battery and when there is not enough space to accommodate additional charge respectively. In the case of there being both ample charge and space for charge, P/V is simply used in their place.

To calculate energy losses in battery cycles, the difference between the nominal voltage of the battery and its charging and discharging voltages are considered:

$$P_{loss} = I[V_{nom} - V(q, I)]. \quad (6.11)$$

These model components all combine to predict the performance of a battery at each timestep of the simulation, using outputs from the dynamic energy simulation as inputs into the battery model.

6.2 Compressed Hydrogen Storage

The behaviour of gas under different storage conditions is understood using the ideal gas equation:

$$PV = nRT. \quad (6.12)$$

While the equation is described as the ‘ideal’ gas law, the true behaviour of gases can fall far from this relationship, particularly when gases are held outside of ambient conditions. This led to a development of the ideal gas law in an effort to consider these other behaviours.

Each development of the equation typically involves an increase in the number of modelled parameters and the complexity of the equation and are considered as ‘Equations of State’. Table 6.1 lists earlier developments of the Equation of State in succession to the classical law. Note that nomenclature specific to this table is given for each model.

Table 6.1 – Early progression of gas laws from the ideal gas law.

Equation(s)	Parameters	Reference
$\left(P - \frac{a}{V_m^2}\right)(V_m - b) = RT,$ $a = \frac{27(RT_c)^2}{64P_c},$ $b = \frac{RT_c}{8P_C}.$	V_m is the molar volume, P_c is the critical pressure, T_c is the critical temperature.	Van der Waals, (1873) (6.13)
$P = \frac{RT}{V_m - b} - \frac{a\alpha}{V_m^2 + 2bV_m - b^2},$ $\alpha = \left(1 + \kappa\left(1 - \sqrt{\frac{T}{T_c}}\right)\right)^2,$ $\kappa = 0.37464 + 1.54226\omega + 0.26992\omega^2.$	ω is a factor for molecular accentricity.	Peng and Robinson, (1976) (6.14)
$\frac{RT}{V_m - b} = 1 + Z_{repulsive} + Z_{attractive},$ $Z_{rep} = \frac{4c\eta}{1 - 1.9\eta},$ $Z_{att} = -\frac{z_m q \eta Y}{1 + k_1 \eta Y},$ $Y = exp\left(\frac{\epsilon}{kT}\right) - k_2.$	c and q are shape factors, η is the reduced number density, z_m, k_1, and k_2 are constant parameters, ε is the square well potential depth, k is the Boltzmann constant.	Elliott, Suresh and Donohue (1990). (6.15)

With each development of the Equation of State there is an increase in the number of model parameters. From the inclusion of critical points in the van der Waals model, to factors of molecular shape, energy potentials and determined model constants, the level of complexity of these models simply increases over time.

Recent developments of the Equation of State have led to yet further model complexity, though each profess to better model the behaviour of gases over a broad range of pressures

and temperatures. Three of these later Equations of State are used to model the behaviour of gas over a large pressure range, in order to investigate the suitability of each for use in the modelling of pressurised storage of hydrogen within this work. The simulated data for each Equation of State is compared to measured experimental data, recorded over that same pressure range (NIST Chemistry Webbook, 2017).

6.2.1 Back Equation of State

Boublík (2005) presented the BACK Equation of State for Hydrogen, an EoS emerging from collaborative works by Boublík, Alder, Chen and Kreglewski (Chen & Kreglewski, 1977; Boublík, 1975 and Alder et al., 1972), with modifications to the EoS provided by Müller et al. (1996) and Wendland et al. (2004).

The approach is very much in the form of an 'augmented van der Waals Equation of State', where both repulsive and attractive components of the compressibility factor are considered for review. Scaled particle theory (SPT), as discussed by Boublík (1975) is used in the determination of the repulsive component, taking into consideration non-sphericity of the gas (α) along with its packing fraction (y):

$$Z_{rep} = \frac{1 + (3\alpha - 2)y + (3\alpha^2 - 3\alpha + 1)y^2 - a^2y^3}{(1-y)^3}. \qquad (6.16)$$

Here,

$$\alpha = \frac{R^* S^*}{3V^*},$$

$$y = \rho V^0 \left(\pi \frac{\sqrt{2}}{6}\right),$$

$$V^0 = V^{00}\left(1 - Cexp\left[\frac{-3u_0}{kT}\right]\right)^3,$$

where

R*, S*, V* are the reduced quantities of mean curvature integral, surface area and volume,

ρ is the number density,

V^{00} is the close packed density,

C is a shaping factor (0.12),

$\frac{u_0}{k}$ is the energy parameter.

Alder et al. (1972) deliver the attractive component of compressibility, which evolved from an evaluation of 'reciprocal temperature expansion of the Helmholtz free energy for the square well fluid':

$$Z_{att} = \sum_m \sum_n n D_{mn} \left(\frac{u}{kT}\right)^m \left(\frac{V^0}{V}\right)^n, \tag{6.17}$$

where

D_{mn} are constants of the BACK EoS,

and

$$\frac{u}{k} = \frac{u_0}{k}\left(1 + \frac{\eta}{kT}\right), \tag{6.18}$$

with $\frac{\eta}{k}$ representing electrostatic interactions of the gas.

Both terms combine to form an equation of compressibility for the BACK EoS:

$$Z = Z_{rep} + Z_{att}. \tag{6.19}$$

As with the previous Equations of State, the BACK EoS was compared to that of the ideal gas. NIST data was also used as a comparison from now on to assess how closely these Equations of State reflect the realistic behaviour of hydrogen. Figure 6.1 shows the comparison between plots of ideal gas and BACK EoS.

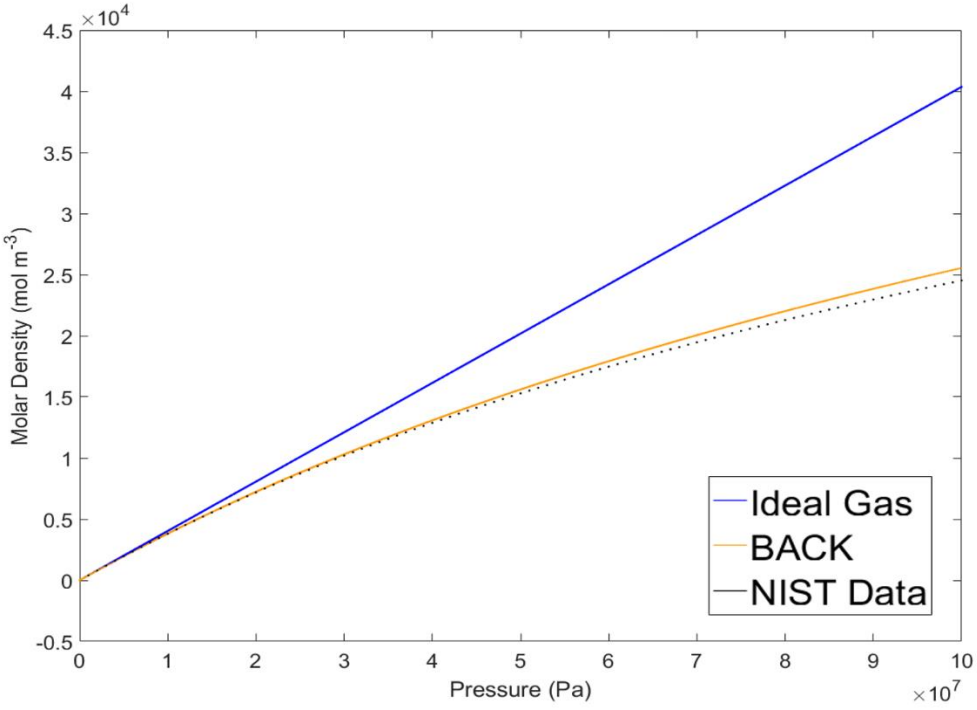

Figure 6.1 – Ideal and BACK Equation of State plots, with NIST data, for hydrogen at 298K up to 100MPa.

Similarity in the behaviour of hydrogen at low pressures of less than 1MPa appears as before. The BACK plot appears similar to the Peng-Robinson plot, however the BACK plot falls much closer to that of the NIST data.

6.2.2 Bender Equation of State

The Bender Equation of State (Bender, 1971) was a development of the Beattie-Bridgeman model (Beattie & Bridgeman, 1928):

$$P = \frac{RT}{V^2}\left(1 - \frac{c}{VT^3}\right)(V + B) - \frac{A}{V^2}, \tag{6.20}$$

where

$$A = A_0\left(1 - \frac{a}{V}\right),$$

$$B = B_0\left(1 - \frac{b}{V}\right).$$

The equation sports five equation constants: a, b, c, A_0 and B_0, which are independent to each gas / fluid. An intermediary model between this and the Bender EoS was introduced by Benedict, Webb and Rubin (1940). Well known for its precision outside of ambient conditions, the Beattie-Bridgeman EoS was expanded to incorporate a further three constants; thus increasing the range of applicability of the equation.

The BWR equation is given as:

$$P = \rho RT + \left(B_0 RT - A_0 - \frac{C_0}{T^2}\right)\rho^2 + (bRT - a)\rho^3 + \alpha a\rho^6 + \frac{c\rho^3}{T^2}(1 + \gamma\rho^2)exp(-\gamma\rho^2). \tag{6.21}$$

where

ρ is the molar density.

A total of eight equation constants are now considered: a, b, c, A_0, B_0, C_0, α and γ.

From this, Bender applies his own expansion to augment the Equation of State with an additional twelve constants, bringing the total to twenty ($a_{1\text{-}20}$). This eventual development of the Beattie Bridgeman EoS is given as:

$$P = \rho T[R + B\rho + C\rho^2 + D\rho^3 + E\rho^4 + F\rho^5 + (G + H\rho^2)\rho^2 exp(-a_{20}\rho^2)], \quad (6.22)$$

where

$$B = a_1 + \frac{a_2}{T} + \frac{a_3}{T^2} + \frac{a_4}{T^3} + \frac{a_5}{T^4},$$

$$C = a_6 + \frac{a_7}{T} + \frac{a_8}{T^2},$$

$$D = a_9 + \frac{a_{10}}{T},$$

$$E = a_{11} + \frac{a_{12}}{T},$$

$$F = \frac{a_{13}}{T},$$

$$G = \frac{a_{14}}{T^3} + \frac{a_{15}}{T^4} + \frac{a_{16}}{T^5},$$

$$H = \frac{a_{17}}{T^3} + \frac{a_{18}}{T^4} + \frac{a_{19}}{T^5}.$$

The increased accuracy of this Equation of State is witnessed in figure 6.2, where the plot is compared to that of the ideal gas and BACK EoS and NIST data; the plot now shows considerable closeness to the NIST data at both low and high pressures, surpassing the accuracy of the BACK EoS.

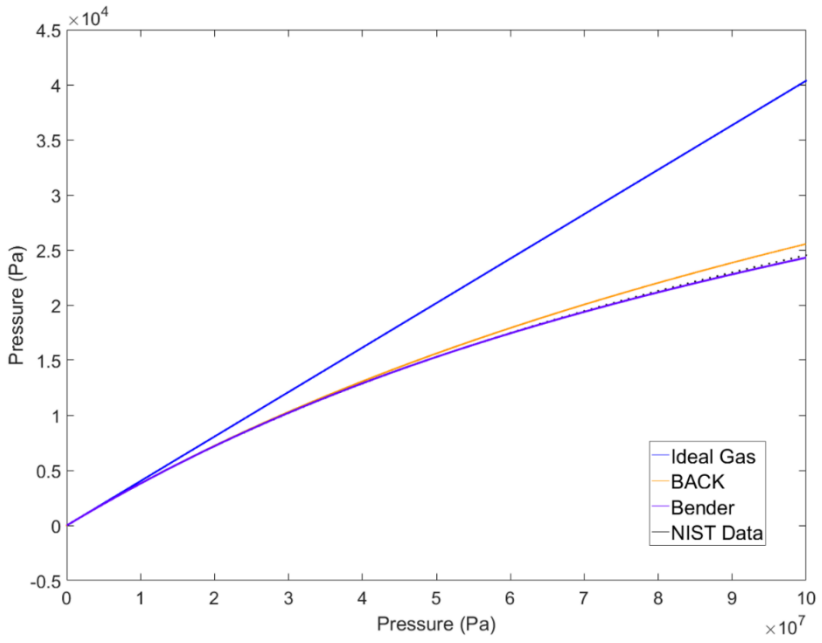

Figure 6.2 – Ideal, BACK and Bender Equation of State plots, with NIST data, for hydrogen at 298K up to 100MPa.

6.2.3 Lemmon Equation of State

Lemmon (2008) more recently offers his Equation of State, suggesting high accuracy particularly when compared to NIST data. It would suggest the highest accuracy of all EoS looked at so far, however there are limits in its operational range.

Lemmon's Equation of State is based on Leachman's equation for Helmholtz energy (Leachman, 2007), an equation which harbours 14 parameters:

$$\alpha^r(\delta,\tau) = \sum N_k \delta^{dk} \tau^{tk} + \sum N_k \delta^{dk} \tau^{tk} exp(-\delta^{lk}) + \sum N_k \delta^{dk} \tau^{tk} exp(\eta(\delta - \varepsilon_k)^2 + \beta(\tau - \gamma_k)^2), \quad (6.23)$$

where

α_r is the residual Helmholtz energy,

τ is $\frac{T_c}{T}$,

δ is $\frac{\rho}{\rho_c}$,

and all other parameters are fitted constants. Lemmon also calls upon the temperature-dependent virial equation, often used to calculate the density of gases by considering multi-particle interactions. This equation is given in terms of compressibility as:

$$Z(P,T) = 1 + \sum_{i=2}^{n} B_i^*(T) P^{i-1}, \tag{6.24}$$

where

B_i^* are temperature dependent virial coefficients.

Combining the elements of equations 8.34 and 8.35, Lemmon developed his own Equation of State:

$$Z(P,T) = 1 + \sum_{i=1}^{9} a_i \left(\frac{100K}{T}\right)^{b_i} \left(\frac{P}{1MPa}\right)^{c_i}, \tag{6.25}$$

where

a_i, b_i, c_i are constants for hydrogen using this EoS.

Lemmon's Equation of State is more complex than those explored so far by having a grand total of 27 different parameters. Though it might prove useful given the established constant terms for hydrogen gas, the complexity of using so many parameters dissuades from practicality, especially for other species. Nonetheless, given the claims of accuracy offered by Lemmon and his Equation of State, figure 6.3 shows a comparison to that of the most accurate EoS so far – the Bender Equation of State – and the NIST data.

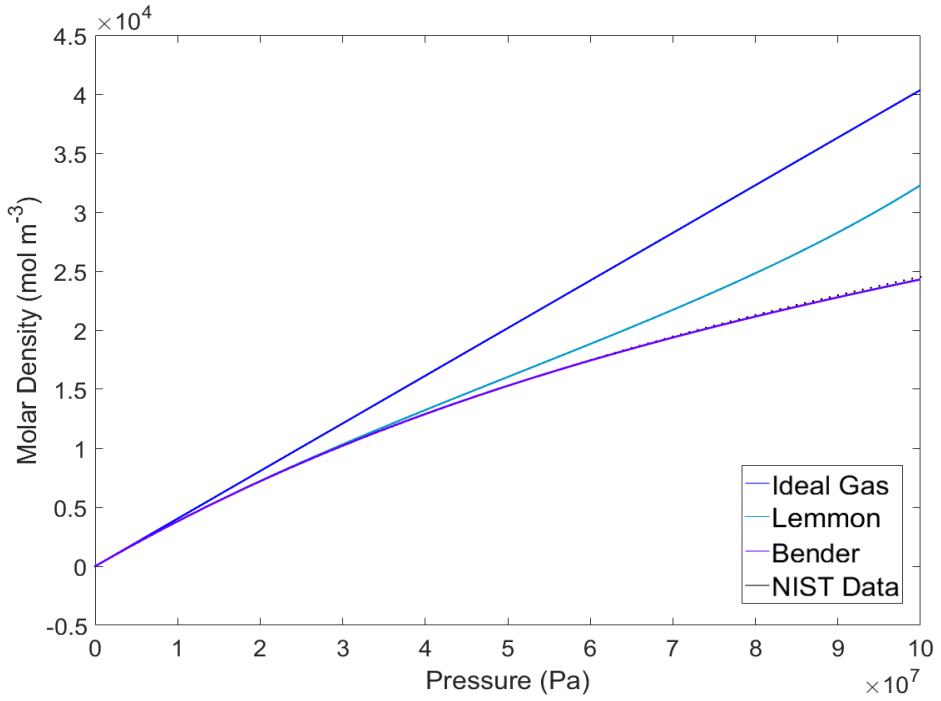

Figure 6.3 – Ideal, Bender and Lemmon Equation of State plots, with NIST data, for hydrogen at 298K up to 100MPa.

The Lemmon Equation of State performs well at lower pressures; however, this success is shared with both Bender and BACK equations. For higher pressures, the Bender Equation of State demonstrates the closest fit to the measured NIST data. Indeed, this validation is backed up in further works, with Puziy et al. (2003) describing it as 'one of the most sophisticated equations of state', with good prediction of behaviour over a wide range of temperatures and pressures, and varied application of the EoS by Cibulka et al., (2001), Ustinov et al., (2002), Ghazouani et al., (2005), Nagy & Símandi, (2008) and Schinder et al. (2011).

Given this likeness to the measured data, the Bender EoS was chosen to represent the behaviour of hydrogen compression within this work.

A final comment is made on the energy penalty of using a compressor within the system. To consider this penalty, the power required is calculated using:

$$P_{comp} = \frac{\dot{n}}{\eta}\frac{mRT_{in}}{m-1}\left[1 - \left(\frac{P_{out}}{P_{in}}\right)^{\frac{m-1}{m}}\right], \quad (6.26)$$

where $\dot{n}$ is the gas flow rate (mol/s),

η is the compressor's efficiency,

m is the polytropic coefficient,

P_{out} is the output pressure of gas (Pa),

P_{in} is the input pressure of gas (Pa),

T_{in} is the input temperature of gas,

R is the gas constant,

as is used by Zini and Tartarini (2010).

6.3 Metal Hydride Storage

Metal hydrides are so called because of the interaction between a metal and hydrogen gas. A process, comprising several stages, sees hydrogen absorbed into metals forming a number of different phases. The process is typically exothermic, with the quantity of heat produced proportional to the mass of the metal hydride that is formed. To understand the interaction process is to understand where the dominant rate-controlling stage which governs the behaviour of these metal hydrides comes from. Martin et al. (1996) visualises the stages

involved in absorption and desorption from metal alloys, using a concept which has been recognised and repeated by other authors (see Muthukumar et al., 2009 and Chou et al., 2005). A similar graphic is shown in figure 6.4, where the individual stages are highlighted.

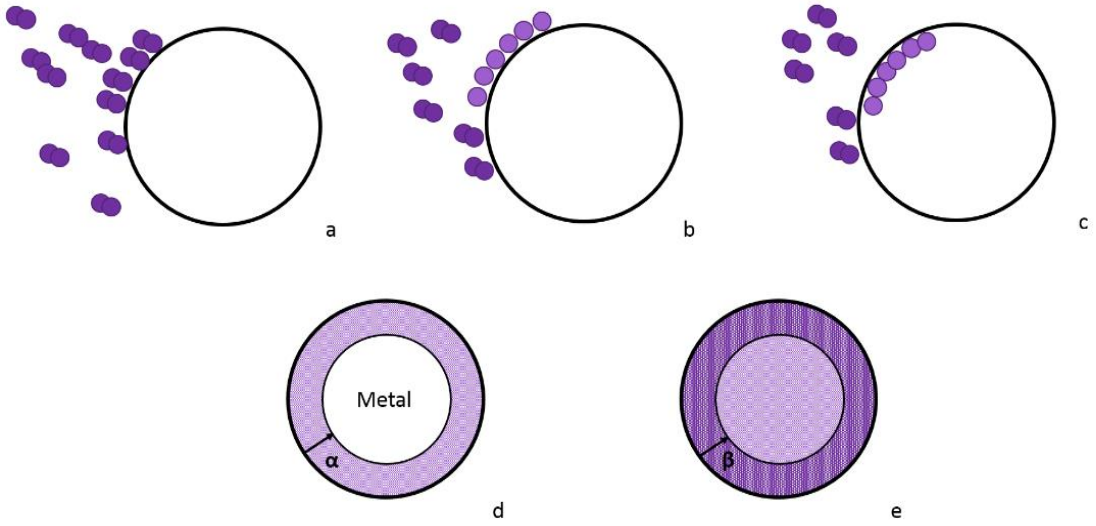

Figure 6.4 – Representation of the stages involved with hydrogen absorption kinetics of metal alloys.

Each partial stage makes up an overall reaction mechanic for absorption and are regarded as: a) **Physisorption** of hydrogen molecules onto the surface of the metal alloy due to van der Waals forces. b) **Dissociation and Chemisorption** occur when hydrogen molecules react with the metal alloy surface, resulting in hydrogen atoms. c) **Surface Penetration** of hydrogen atoms into the metal alloy lattice, where the hydrogen atoms occupy interstices. d) **Diffusion** of hydrogen atoms through the lattice, forming the α-phase of the metal hydride. Formation

of this phase occurs from the outside in. e) **Hydride Formation** occurs at nucleation sites within the lattice; growth of these sites then distributes the formation throughout the material forming the β-phase of the metal hydride. Again, this process is understood to occur from the outside in. With the formation of hydride material (often) comes lattice expansion, the stress of which typically disrupts the periodicity of the lattice with fractures, resulting in a fine powder. Desorption is essentially the reverse of this absorption process.

Dornheim (2011) discusses these individual processes in terms of energies for bonding hydrogen to a metal. Physisorption as commented above is due to van der Waals forces in the region of 6 kJ mol^{-1} H_2. In order to achieve dissociation and chemisorption, an activation energy of 20 – 150 kJ mol^{-1} H_2 must be overcome. Hydrogen atoms diffuse in bulk into the metal lattice, where hydride formation sees an alteration of the lattice structure. This alteration determines the energetic nature of the reaction, where an expansion of the lattice results in energy being expelled in an exothermic reaction, however lattice contractions are possible, making the reaction endothermic. The energy of this reaction depends on the metal alloy and its enthalpy of hydride formation. Figure 6.5 shows a rough energy schematic for distances from the surface of a metal alloy.

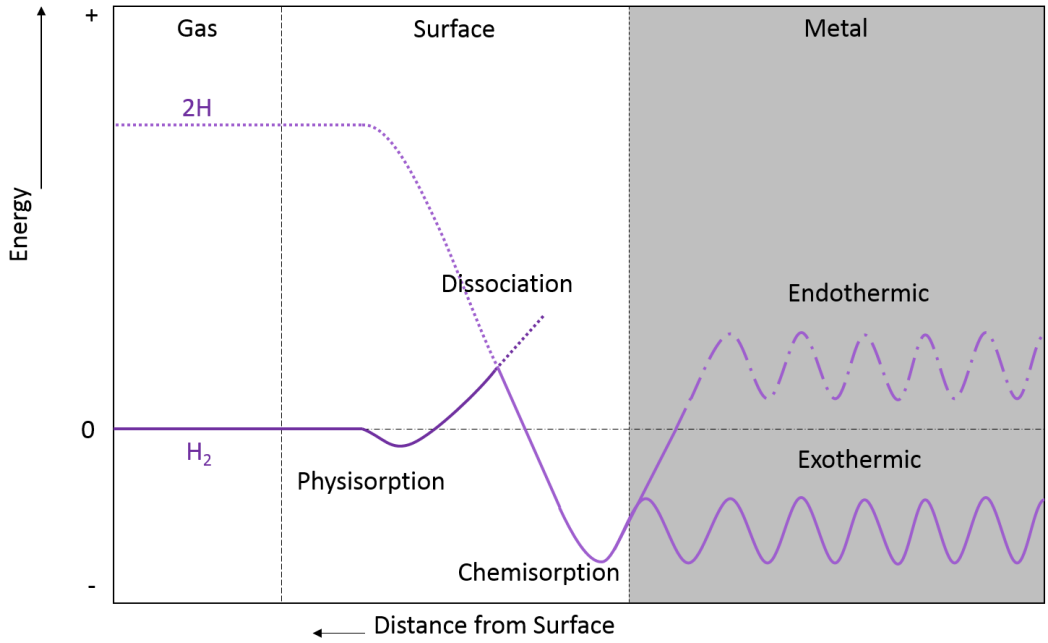

Figure 6.5 – Schematic of energy at distances from the surface of a metal, showing various stages of hydrogen absorption. Adapted from Dornheim (2011).

The main technique used to interpret and characterise the behaviour of metal hydrides during absorption and desorption is to evaluate the relationship between pressure and composition at a specific temperature. This information can be graphically analysed using a pressure-composition-isotherm. The incumbent thermodynamic constants, entropy and enthalpy of formation and deformation, control the relationship between temperature and pressure and can be demonstrated using the van't Hoff equation:

$$ln(P_{eq}) = -\frac{\Delta H}{RT} + \frac{\Delta S}{R}. \tag{6.27}$$

where

P_{eq} is the equilibrium / plateau pressure,

ΔH is the enthalpy of hydride formation,

ΔS is the entropy of hydride formation,

R is the gas constant,

T is temperature.

This equation works well to satisfy the relationship, however some works do use an expanded version of the equation (see Nishizaki et al., 1983):

$$ln(P_{eq}) = -\frac{\Delta H}{RT} + \frac{\Delta S}{R} + (\varphi \pm \varphi_0) tan\left\{\alpha_1 \pi \left[\frac{\rho_s - \rho_s^0}{\rho_s^s - \rho_s^0}\right] - \alpha_2\right\} \pm \frac{\beta}{2}, \qquad (6.28)$$

where

$\alpha_{1,2}$ are constants,

ϕ, ϕ_0 are flatness factors,

ρ_s is the metal hydride density,

ρ_s^s is the saturated metal hydride density,

ρ_s^0 is the original alloy density,

β is the hysteresis factor.

Within the equation are ± terms; positive terms are used during absorption, while negative ones are used for desorption.

When executed, this equation delivers characteristics that reveal information on reaction kinetics. The metal hydride considered for use throughout this study is that of $LaNi_5$ given its popularity with hydrogen sorption. Table 6.2 lists the characteristics of the material used in

the modelling work (sourced from Laurencelle & Goyette, 2007), with figure 6.6 displaying the characteristic PCT curves of absorption and desorption at 298K.

Table 6.2 – Parameters used in the van't Hoff equation in plotting a PCT for $LaNi_5$ at 298 K. Data Source: Laurencelle & Goyette (2007).

Parameter	**Value**
ΔH (absorption)	-31.4 kJ mol^{-1}
ΔS (absorption)	-111.7 J mol^{-1} K^{-1}
ϕ	0.038
ϕ_0	0
α_1	1
α_2	0.5
β	0.137
ρ_s^0	8400 kg m^{-3}
ρ_s^s	8517 kg m^{-3}

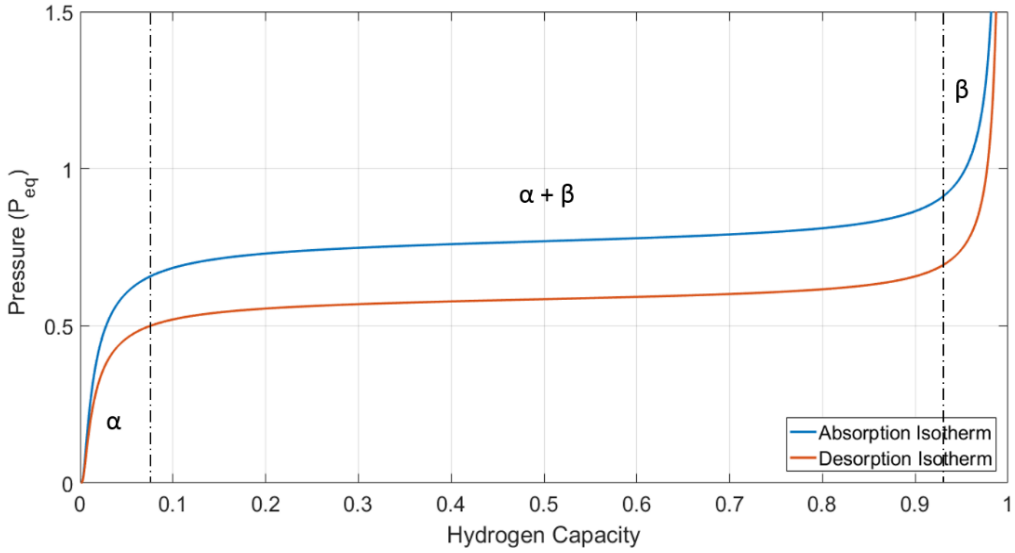

Figure 6.6 – Absorption and Desorption PCT plot for $LaNi_5$ at 298K.

6.3.1 Absorption Modelling

The relationship between pressure and temperature can affect the behaviour of metal hydrides, where insufficient dissipation of heat from the exothermic hydrogenation of these hydrides can lead to performance inhibition. This section looks at how absorption and desorption kinetics can be modelled alongside a balance of mass and energy within the material to show a good representation of how the material might behave in a real-world scenario. The overall aim is to create a metal hydride energy storage model which can be integrated within the established domestic model under the applied conditions which have been chosen to reflect a broad selection of those found in the UK.

In the previous section the storage of hydrogen as a compressed gas was considered; with it came the energy penalty of using a mechanical compressor to achieve pressures required for an appropriate volumetric energy density, capable of satisfying a majority proportion of the

domestic electrical energy load. The storage of hydrogen within a metal hydride does not consider any mechanical compression and so does not incur this penalty, instead being absorbed into the material under relatively typical conditions. It is hoped that this may some way go towards not only providing an improved means of hydrogen energy storage over compression, but that the behaviour of the system itself may in some way benefit over that which was previously observed for battery and compressed gas alike.

$LaNi_5$ has been established throughout this work as a suitable material, which has been at the centre of many studies into its performance capabilities and into the adaptation of its materialistic properties to enhance them. While it is in no way a perfect material, its properties do make it suitable for the purpose of domestic energy storage, and from here on 'the hydride' will refer to $LaNi_5$ unless stated otherwise.

6.3.2 Heat and Energy Balance

A number of equations rest at the heart of this model, aside from the van't Hoff equation introduced earlier. These equations are incorporated within the balance of mass, heat and energy within the hydride throughout the absorption and desorption processes and can be found in many of the discussed literature in this chapter, however the main influential contributors to this knowledge are Askri et al. (2004), Laurencelle & Goyette (2007), Wang et al. (2009) and Cho et al. (2013), each of whom deal with the modelling of $LaNi_5$.

The equation used in calculating the rate at which hydrogen mass is absorbed or desorbed per unit volume can be interpreted at individual time steps as:

$$\frac{\partial \rho_s}{\partial t} = k \frac{\rho_s^s - \rho_s}{\rho_s^s - \rho_s^0}, \tag{6.29}$$

or

$$\frac{\partial \rho_s}{\partial t} = k \frac{\rho_s - \rho_s^0}{\rho_s^s - \rho_s^0}, \tag{6.30}$$

where k is a rate constant determined by the activation energy and associated temperature dependency and by the pressure gradient. This term is substituted into these equations, where the following are found for absorption and desorption:

$$\frac{\partial \rho_s}{\partial t} = \boldsymbol{C_a exp}\left(\frac{\boldsymbol{E_a}}{\boldsymbol{RT}}\right) \boldsymbol{ln}\left(\frac{\boldsymbol{P}}{\boldsymbol{P_{eq}}}\right) \left(\frac{\rho_s^s - \rho_s}{\rho_s^s - \rho_s^0}\right), \tag{6.31}$$

and

$$\frac{\partial \rho_s}{\partial t} = \boldsymbol{C_d exp}\left(\frac{\boldsymbol{E_d}}{\boldsymbol{RT}}\right) \boldsymbol{ln}\left(\frac{\boldsymbol{P - P_{eq}}}{\boldsymbol{P_{eq}}}\right) \left(\frac{\rho_s - \rho_s^0}{\rho_s^s - \rho_s^0}\right), \tag{6.32}$$

where

$C_{a,d}$ are material specific rate constants for absorption and desorption,

$E_{a,d}$ are activation energies for absorption and desorption,

P is the input pressure of the gas.

With this absorption or desorption of hydrogen comes an imbalance in energy due to the (typically) exothermic and endothermic nature of each process, thus the system tends to equilibrate itself and restore balance. The overall balance of energy is given as:

$$\frac{\partial \rho c_p^e T}{\partial t} + \nabla \cdot \left(\rho_g c_p^g \vec{u} T\right) = \nabla \cdot \left(k^{eff} \nabla T\right) + \frac{\partial \rho_s}{\partial t}\left[\Delta H - \left(c_p^g - c_p^s\right)\right], \tag{6.33}$$

where

$c_p^{s,g}$ is the specific heat for the gas and solid,

ρc_p^e is the effective density and specific heat of the gas and solid,

u is the gaseous velocity vector,

k^{eff} is the effective thermal conductivity of the gas and solid.

As discussed earlier and as deliberated by Askri et al. (2004), the rate determining factor of the overall process is likely to be due to the dissipation of heat through the material over the rate of hydrogen diffusion. This is particularly true of the application at hand, given the hourly iteration of simulated results in the domestic model. As such, the second term of this equation is considered to have negligible effect on the overall balance of energy and is then negated.

6.3.3 Finite Element Method

The finite element (or volume) method has been used in a good number of studies regarding the modelling of hydride behaviour (see Askri et al., 2009; Førde et al., 2009; Freni et al., 2009; and the earlier references to Askri and Wang). Note that although similar, the previously referenced Laurencelle and Goyette use a finite difference technique. The finite element technique involves representing the hydride material as a 2D mesh of finite elements. The differential equations introduced earlier in this section, along with the van't Hoff equation visited earlier (6.3) are discretised in each of these elements which together form the bulk behaviour of the material. Figure 6.7 shows a schematic of this 2D mesh of finite elements.

Two assumptions are made to simplify this method to better allow integration within the time constraints of the main energy simulations. As discussed previously, diffusion of hydrogen

through the material is considered instantaneous relative to heat flow within the material; solid and gas temperatures are also considered to be in equilibrium.

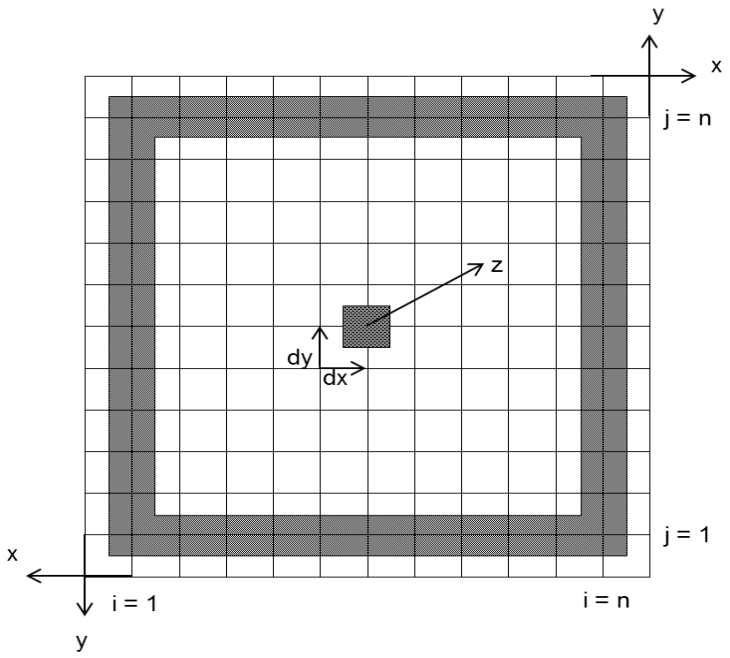

Figure 6.7 – Schematic representing the arrangement of finite elements in a 2D mesh.

With each iteration of the simulation, equations are approached in the following order: effective density / specific heat, pressures, absorbed mass per unit volume, energy balance. The mesh assumes a peripheral cooling system along three edges (with the final edge positioned at the centre of the material), which maintains a specific fluid temperature; thus, boundary conditions are given as:

$$-k^{eff}\frac{\partial T}{\partial x} = h\left(T - T_f\right), \tag{6.34}$$

where

h is the conductance between the hydride element and the cooling fluid,

T_f is the temperature of the cooling fluid.

Data obtained in the modelling of the 2D mesh of finite elements of volume ∂V is extrapolated to satisfy a fuller 3D material of volume V.

6.3.4 Model Testing

The Matlab model for hydrogen absorption in $LaNi_5$ was verified by comparing the results of absorption and desorption found in the study by Askri et al. (2003). Table 6.3 lists the parameters used in the simulation, as stated in their work. While these parameters reflect the simulation used in that work, note that the Matlab model developed for this work considers a 2D plane of square elements; Askri et al. consider a polar coordinate system for their work.

Table 6.3 – List of parameters for absorption and desorption of hydrogen in 30mm x 50mm $LaNi_5$. Source: Askri et al. (2003).

Parameter	Absorption Value	Desorption Value
c_p^g	14890 J/kg K	14890 J/kg K
c_p^s	335 J/kg K	335 J/kg K
k^g	0.1897 W/m K	0.1897 W/m K
k^s	1.000 W/m K	1.000 W/m K
E_a	21170 J/mol	-
E_d	-	16420 J/mol
C_a	59.187 s^{-1}	-
C_d	-	9.57 s^{-1}
Fluid Temperature	273 K	343 K
Initial Hydride Temperature	273 K	243 K
Hydride Porosity	0.5	0.5
Gas Inlet / Outlet Pressure	8 bar	0.8 bar

Figures 6.8 and 6.9 show a comparison of the results from the Matlab simulation and those delivered by Askri et al., for both absorption and desorption.

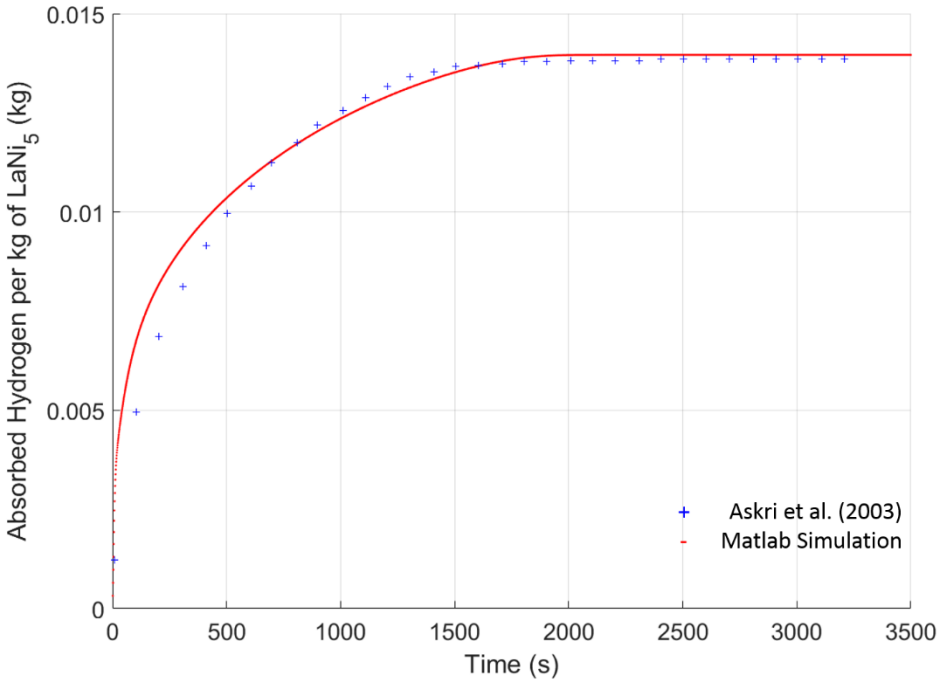

Figure 6.8 – Comparison of simulated absorption of Hydrogen in $LaNi_5$.

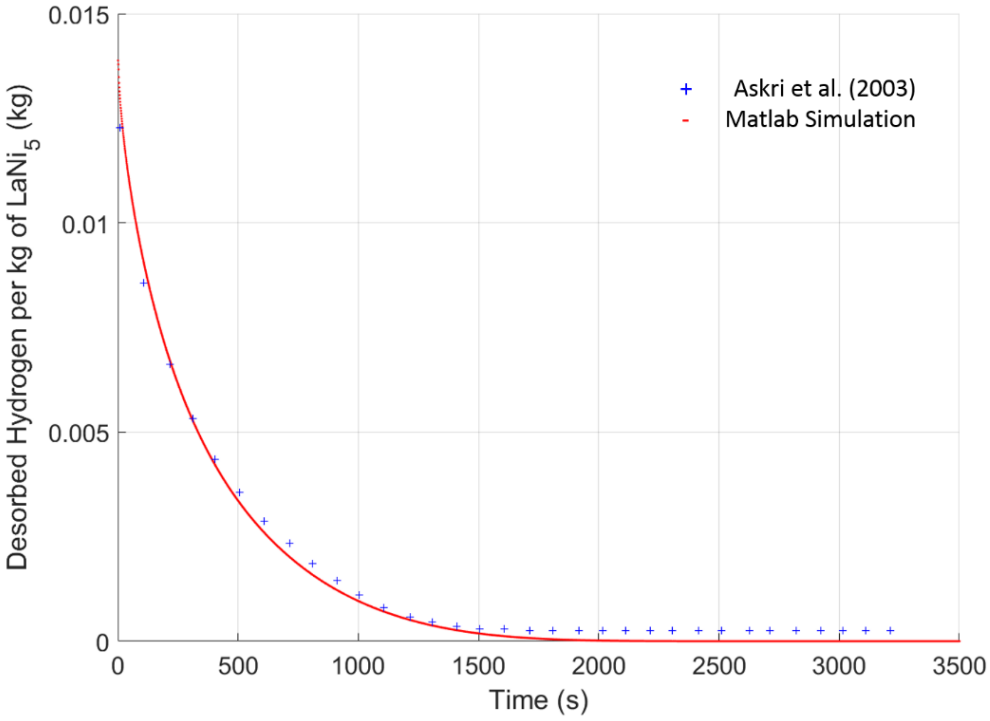

Figure 6.9 – Comparison of simulated desorption of hydrogen in $LaNi_5$.

Both figures 6.8 and 6.9 show a good agreement between the results simulated using the Matlab model, and those delivered by Askri at al. (2003). Subtle discrepancies in the absorption and desorption curves are assumed to arise because of the shape of the material modelled. Absorption and desorption of hydrogen in $LaNi_5$ was explored more fully, with a review of each process in terms of time series plots and time lapses for temperature and hydrogen capacity.

Absorption

Figure 6.10 shows the time series plot of temperature for absorption as produced by the Matlab model. This is followed by figures 6.11a to 6.11f which show a time lapse of the hydride's temperature profile at intervals of 100s, 500s, 1000s, 1500s, 2500s and 3500s.

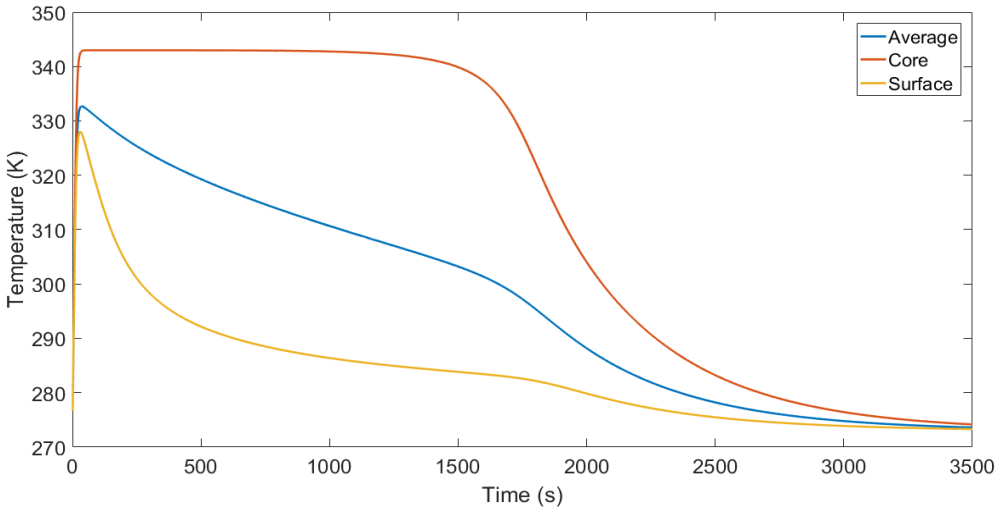

Figure 6.10 – Time series plot for average, core and surface temperatures of $LaNi_5$ during absorption.

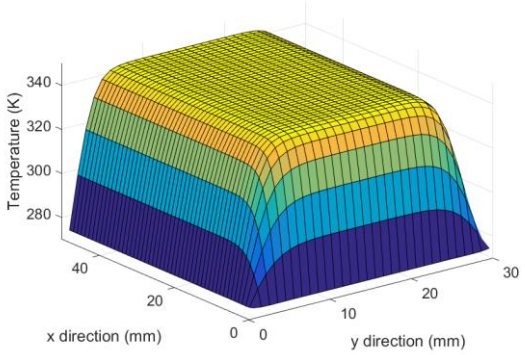

Figure 6.11a – $LaNi_5$ temperature mesh plot 100s into absorption.

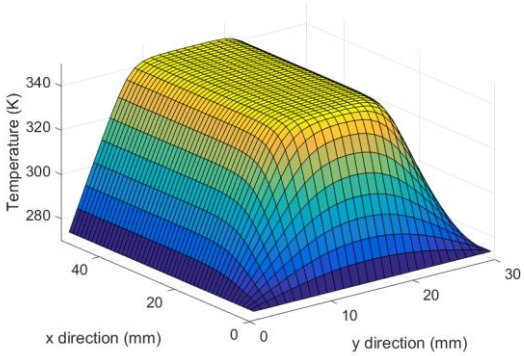

Figure 6.11b – $LaNi_5$ temperature mesh plot 500s into absorption.

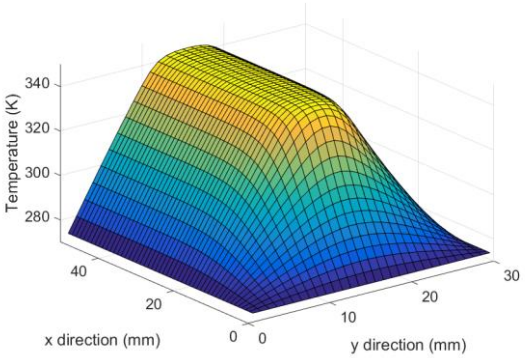

Figure 6.11c – $LaNi_5$ temperature mesh plot 1000s into absorption.

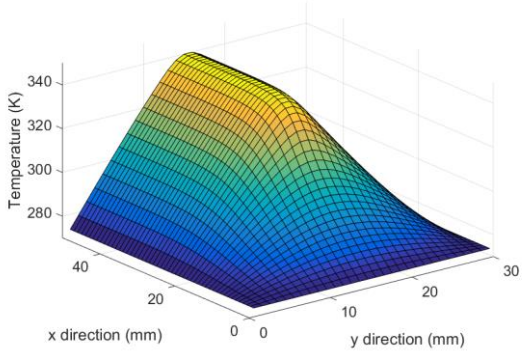

Figure 6.11d – $LaNi_5$ temperature mesh plot 1500s into absorption.

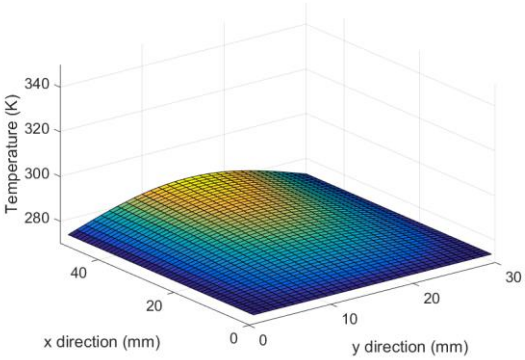

Figure 6.11e – $LaNi_5$ temperature mesh plot 2500s into absorption.

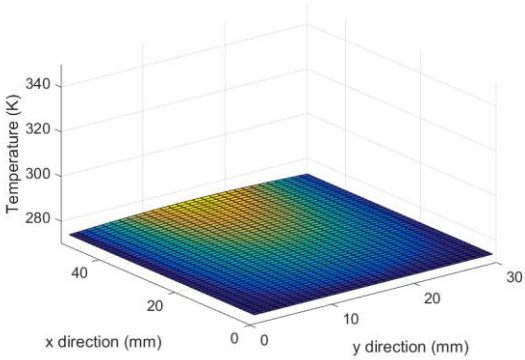

Figure 6.11f – $LaNi_5$ temperature mesh plot 3500s into absorption.

The time series plot, supported by the time lapse mesh plots tell the story of temperature evolution through metal hydrides during absorption. Initial hydride formation causes a rapid increase in temperature throughout the material, as can be seen in the first ~50s. Temperatures around the periphery of the material in contact with the cooling fluid begin to fall, dissipating heat from within the material. For the remainder of the simulation temperatures are seen to fall at a greater rate closer to this material periphery; temperature at the centre of the material though appears to remain almost constant until ~1500s. As seen in the mesh plots, temperature is gradually reduced from the outside in due to cooling. From the initial heat input of hydride formation, the centre is observed to remain at this high temperature until much later in the absorption process.

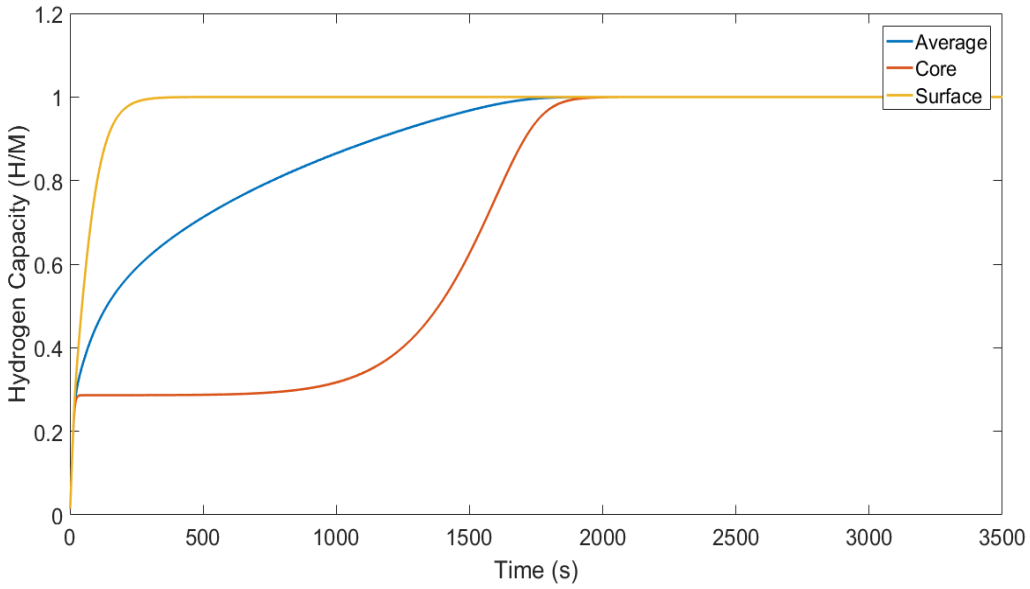

Figure 6.12 - Time series plot for average, core and surface hydrogen capacities of $LaNi_5$ during absorption.

The time series for hydrogen capacity during absorption shows an initial uniform uptake of hydrogen within ~10s, after which the hydrogen capacities through the hydride become divided. Observing the large difference between the uptake of hydrogen at the surface and that at the centre of the material, effects of initial rise of temperature and pressure can be realised. Both high temperatures and a low-pressure gradient contribute to the harsh reduction in hydride formation seen at the centre of the material, seen to last over the first ~1500s. Heat dissipation and the restoration of lower temperatures and pressures through the material would see the rate of central hydride formation increase towards the end of the absorption process. Conversely at the periphery, a lesser effect of the initial temperature and pressure rise is felt, with temperatures remaining low due to close proximity to the cooling edges. The evolution of hydride formation would then appear to follow an outside in behaviour, forming faster at the periphery and much slower at the heated centre. The time lapse mesh plots for hydride formation as hydrogen capacity during absorption are shown in figures 6.13a to 6.13f, showing support for this evolutionary trend.

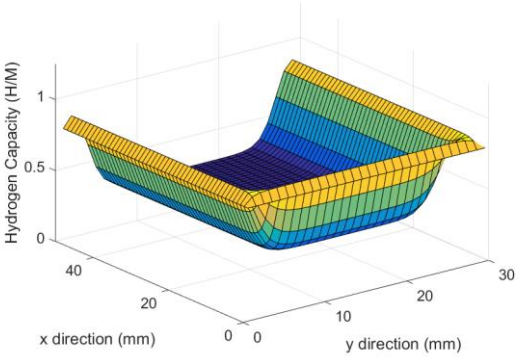

Figure 6.13a – $LaNi_5$ pressure mesh plot 100s into absorption.

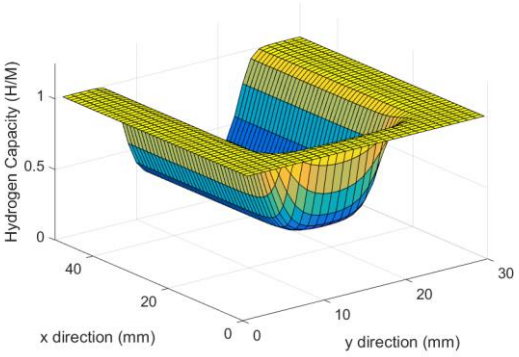

Figure 6.13b – $LaNi_5$ pressure mesh plot 500s into absorption.

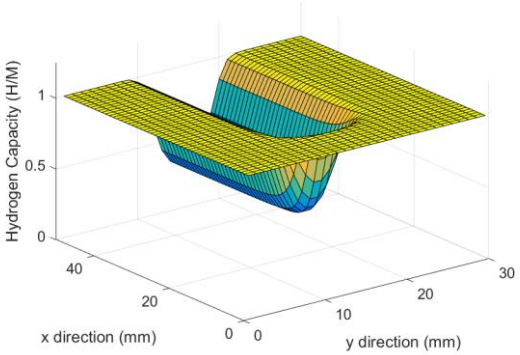

Figure 6.13c – $LaNi_5$ pressure mesh plot 1000s into absorption.

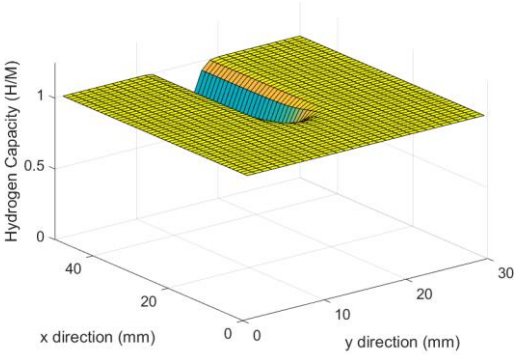

Figure 6.13d – $LaNi_5$ pressure mesh plot 1500s into absorption.

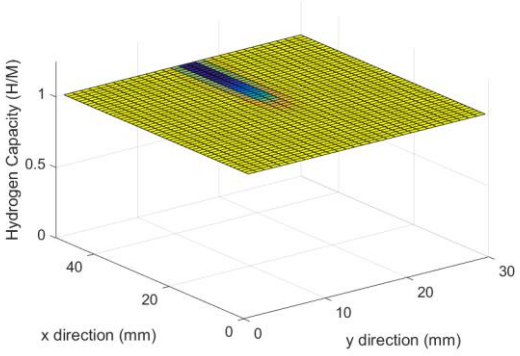

Figure 6.13e – $LaNi_5$ pressure mesh plot 2500s into absorption.

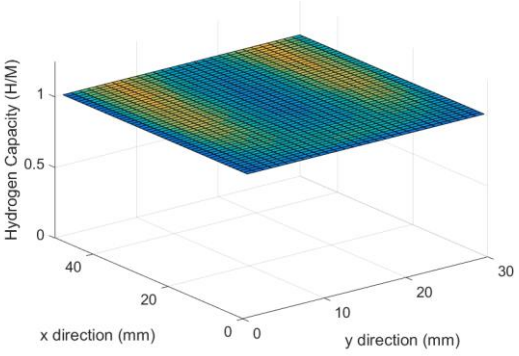

Figure 6.13f – $LaNi_5$ pressure mesh plot 3500s into absorption.

Desorption

The same approach is used in demonstrating the behaviours of temperature and hydride formation for desorption from $LaNi_5$. Note that the simulation material is initialised at full capacity and at the peripheral fluid's higher temperature of 343 K. Figure 6.14 shows the time series plot for the temperature of the hydride, taking an average and two points at the centre and surface of the material as a reference.

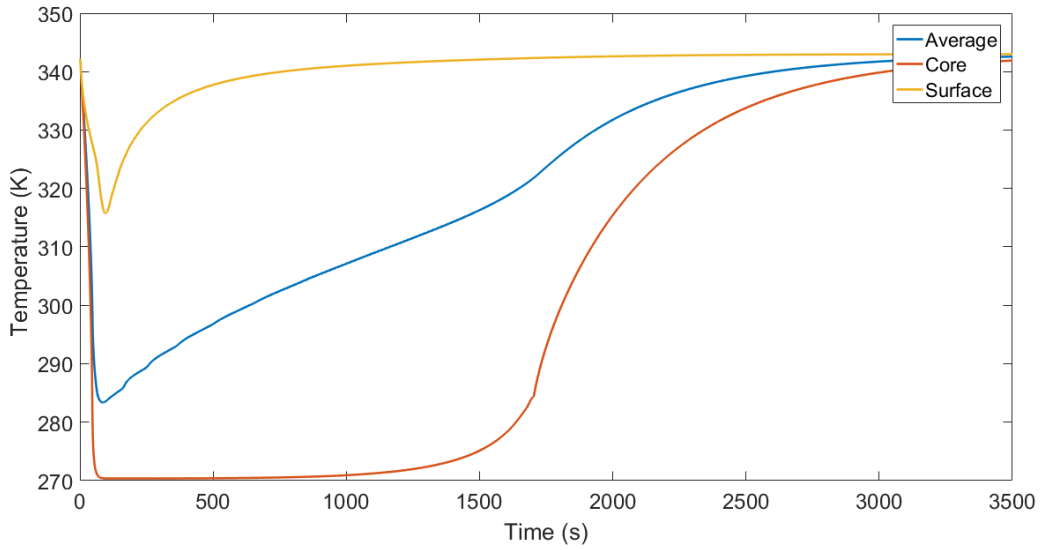

Figure 6.14 - Time series plot for average, core and surface temperatures of $LaNi_5$ during desorption.

The time series shows that during the initial stage of desorption ~50s there is a sudden drop in temperature, detected with increased impact towards the core of the material. This is due to the endothermic properties of the desorption process. At the periphery of the material, fluid at 343 K prevent the material in proximity from dropping to temperatures seen at the

core. The drop at all points is seen to recover back towards the initial temperature over the remainder of the process, however the rate of this recovery is different depending on location; slower recovery is seen at the centre of the material, where the heating effects are lowest. In contrast, material near the surface is seen to reach original temperatures at ~1000s, whereas this is not seen in the core of the material until ~3000s. The observed trend is similar in nature to that seen for absorption, however the decrease in temperature is not as harsh as the initial rise in temperature given hydride formation. Figures 6.15a to 6.15f now show the time lapse mesh plots for temperature throughout the desorption process at the defined time intervals.

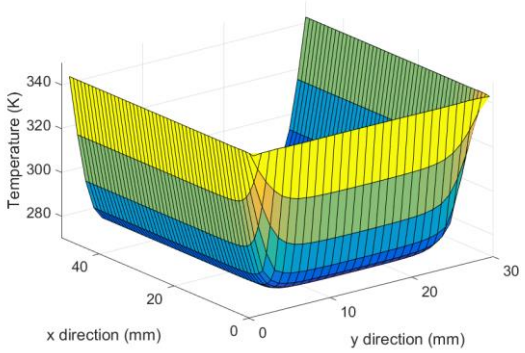

Figure 6.15a – $LaNi_5$ temperature mesh plot 100s into desorption.

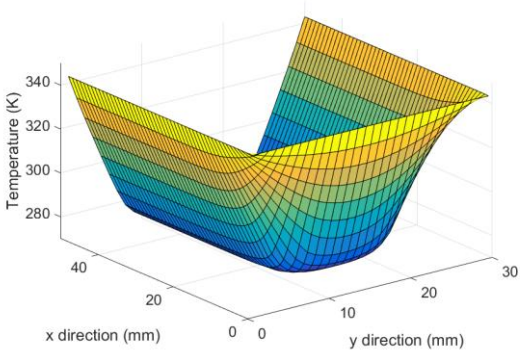

Figure 6.15b – $LaNi_5$ temperature mesh plot 500s into desorption.

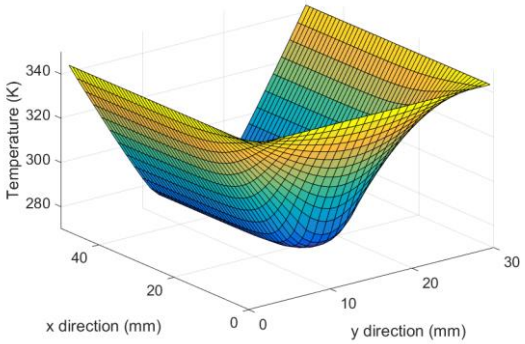

Figure 6.15c – $LaNi_5$ temperature mesh plot 1000s into desorption.

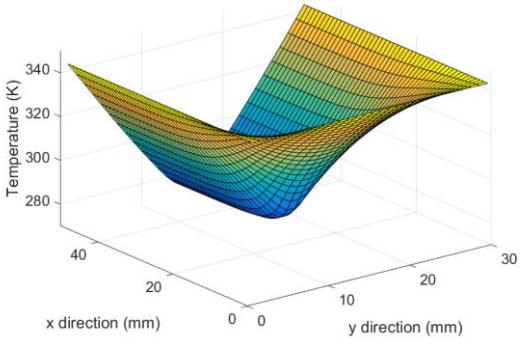

Figure 6.15d – $LaNi_5$ temperature mesh plot 1500s into desorption.

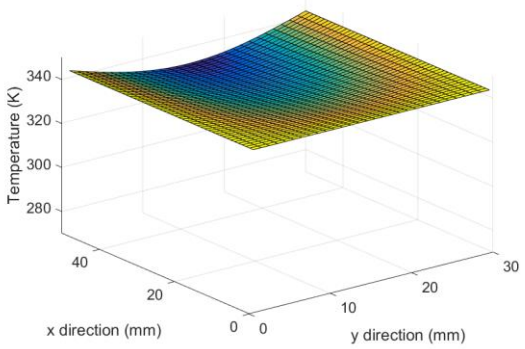

Figure 6.15e – $LaNi_5$ temperature mesh plot 2500s into desorption.

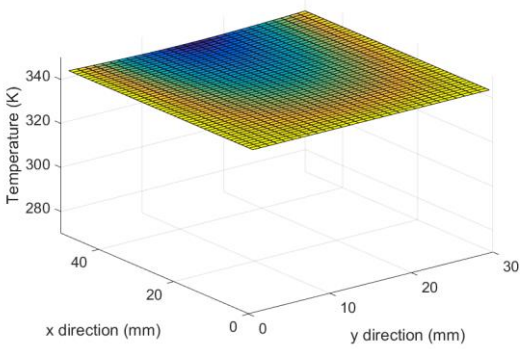

Figure 6.15f – $LaNi_5$ temperature mesh plot 3500s into desorption.

Temperature during desorption is the reverse of temperature during absorption; however, with desorption, as noted in the time series plot, the temperature stability is realised earlier. Figure 6.16 shows hydrogen capacity during desorption.

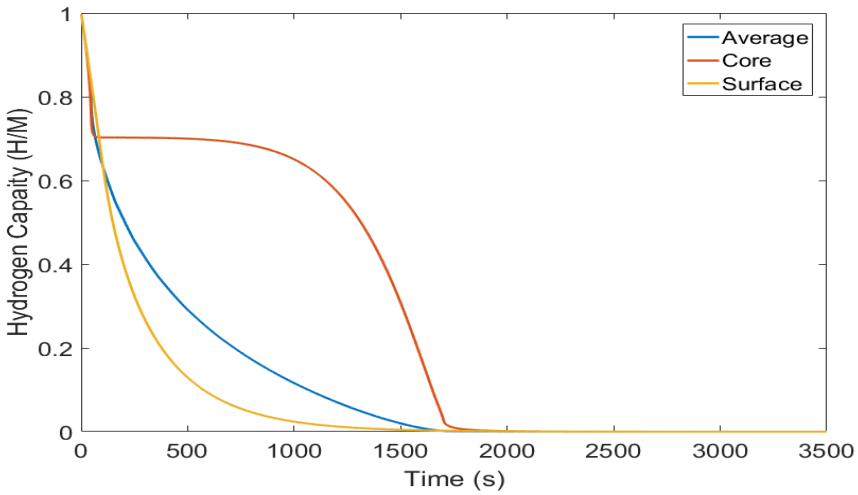

Figure 6.16 - Time series plot for average, core and surface hydrogen capacities of $LaNi_5$ during desorption.

Figure 6.16 shows an initial decrease in the capacity of hydrogen in the material until ~50s. The effect of the corresponding decreases in temperature within the material is noticed immediately afterwards, in that desorption stops at the core of the material. Temperature has less of an impact at the surface, where a higher temperature is maintained to allow desorption to continue. The rate of hydride deformation at the centre of the material increases shortly after ~1000s, while at other locations within the material, deformation occurs with an exponential decay. Total deformation occurs by ~1900s, meaning temperatures continue to equilibrate. $LaNi_5$ has an observably longer absorption time than desorption time; this is reflected in the time lapse mesh plots shown in figures 6.17a to 6.17f.

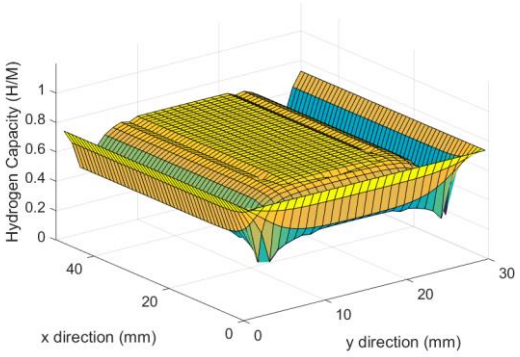

Figure 6.17a – $LaNi_5$ hydrogen capacity mesh plot 100s into desorption.

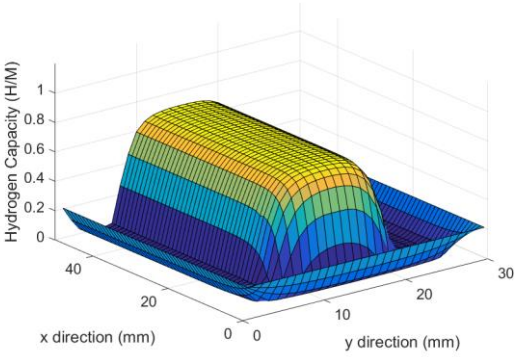

Figure 6.17b – $LaNi_5$ hydrogen capacity mesh plot 500s into desorption.

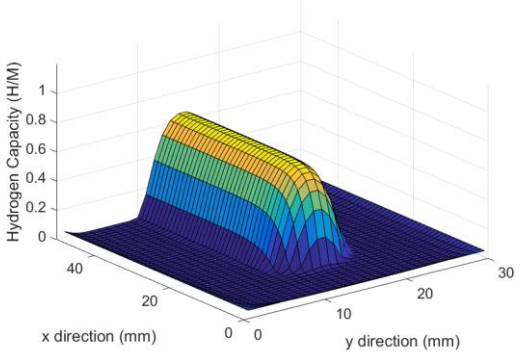

Figure 6.17c – $LaNi_5$ hydrogen capacity mesh plot 1000s into desorption.

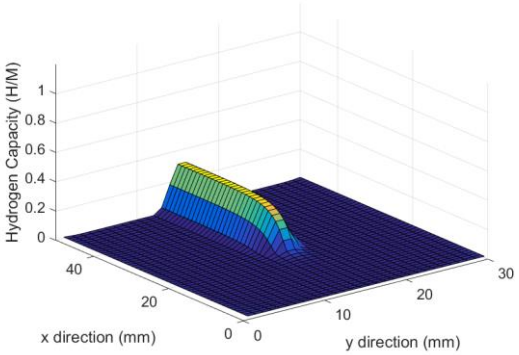

Figure 6.17d – $LaNi_5$ hydrogen capacity mesh plot 1500s into desorption.

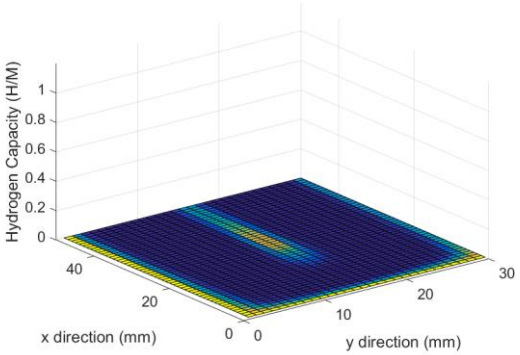

Figure 6.17e – $LaNi_5$ hydrogen capacity mesh plot 2500s into desorption.

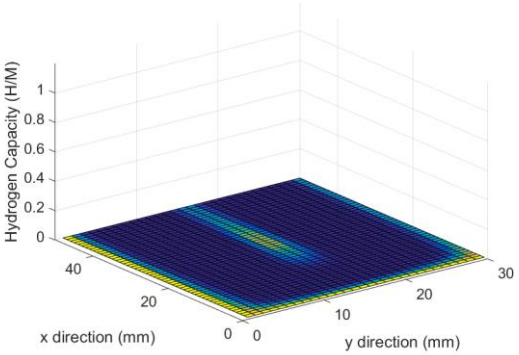

Figure 6.17f – $LaNi_5$ hydrogen capacity mesh plot 3500s into desorption.

The Matlab simulations explored for this section demonstrate the evolution of temperatures and hydride formation in $LaNi_5$ during the processes of absorption and desorption. The findings of both time series plots and time lapse mesh grid plots of the material have been shown for each of these evolutions and follow a logical behavioural trend throughout.

The results of Matlab simulations demonstrated a good fit when compared to those given by Askri et al. (figures 6.8 and 6.9). The propagation of activity within the mesh also cohered to the expected characteristics of a hydride material. During absorption, a rapid increase in temperature was observed, followed by a sharp decrease in the rate of absorption; as heat dissipated from the material, the rate of absorption increased. During desorption, a rapid decrease in temperature was observed, which slowed the rate of desorption from the material. With the dissipation of heat into the material, this rate began to increase.

Given the agreement in results between these Matlab simulations and those by Askri et al., and the logical progression of the simulated material properties throughout, the model is presumed to be suitable for the simulation of absorption and desorption of hydrogen in $LaNi_5$ within the core storage modelling of this work.

6.4 Activated Carbon Storage

To understand the stages involved in adsorption of hydrogen, be it physical adherence, thermal variations or differences in pressure, the fundamentals of the adsorption isotherm and the limitations which lie therein must initially be grasped. Before going into the mechanics of layered isotherm models and their background, a brief introduction to the variation in isotherm is given. Note that a sizeable proportion of knowledge obtained in

understanding the mechanisms of adsorption stems from the remarkable collection of information arranged by Do (1998), and is supported by numerous studies into the applications of activated carbon in particular.

Sing et al. (1985) propose six classifications of isotherm to explain adsorption behaviour in porous media. Preceding a brief explanation of each is a diagram of these classifications, figure 6.18.

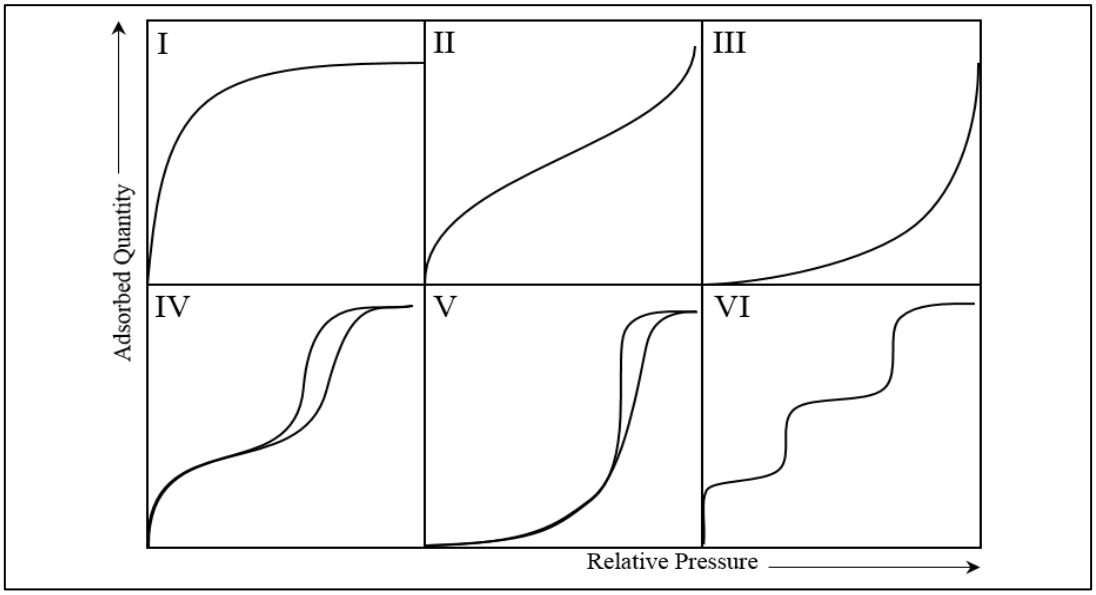

Figure 6.18 – Adsorption isotherms. Adapted from Sing et al. (1985).

Each isotherm represents a particular type of adsorption mechanic, identified as unique to particular permutations of a porous medium. This work, however, only looks at the type I isotherm, which is suggestive of monolayer adsorption and the adsorption of hydrogen in micropores. The remaining types of adsorption reflect multilayer adsorption and adsorption with effects of hysteresis / capillary condensation.

The most fundamental understanding of the relationship between adsorbed quantities of gases and the relative pressure which is found at these quantities is delivered by Henry's Law (Henry, 1803), which proposes some proportionality between the two measures:

$$X = KP, \tag{6.35}$$

where

X is the ratio of absorbed quantity,

K is some constant value,

P is the partial pressure of the adsorbate.

With the application of the Henry constant, K, the relationship states that as adsorbed quantities of gases on the adsorbent increases, so too does the partial pressure within the adsorbent. At this preliminary stage of knowledge, application of this relationship for isotherm interpretation was reserved for monolayer adsorption such as the type I isotherm with a maximum adsorption, representative of a single layer of absorbed gas. Further limitations existed in the isotherm's ability to accurately represent adsorption outside of a particular temperature and pressure range.

This fundamental knowledge was expanded upon in 1909 when Freundlich adapted Henry's law, proposing his own empirical equation for adsorption:

$$X = \alpha P^{\frac{1}{n}}, \tag{6.36}$$

where

X is the ratio of adsorbed quantity,

α is some constant value,

P is the partial pressure of the adsorbate,

n is a constant value greater than unity.

The equation was produced to allow the log plots of both adsorbed quantity and partial pressure gaving a gradient of 1/n. The expression was limited by this value of n however, by enforcing the saturation plateau regardless of pressure. This meant the isotherm was impractical for much higher pressures. Later works sought to develop models which could be used at higher pressures and under a range of temperatures (see Langmuir, 1918; Sips, 1950; Honig & Reyerson, 1952; Brunauer et al., 1938; Anderson, 1946; and Aranovich, 1988, 1989, 1990 & 1992), though a final development was explored for the adsorption model used in this work.

6.4.1 Adsorption Model

The adsorption model used for the simulation of hydrogen storage in activated carbon was motivated by a number of works, which use the finite element method to model uptake kinetics. Common to all is the Dubinin-Astakhov (DA) isotherm, used as a core equation, along with equations that balance mass, energy and momentum. The DA equation is:

$$a = a_0 \, exp\left[-\left(\frac{\varepsilon}{E}\right)^n\right], \tag{6.37}$$

where

- a is the total adsorbed quantity (mol/kg),
- a_0 is the saturation capacity (mol/kg),
- ε is the adsorption potential onto a surface (J/mol K),
- E is the characteristic energy (J/mol K).

The equation itself is a variation on the Dubinin-Radushkevich (DR) expression (Dubinin & Radushkevich, 1947; Dubinin et al., 1947). When n = 2, the DR equation, of which the DA is an extension, is recovered.

The DR equation took original influence from Polanyi's theory of adsorption (Polanyi, 1914), in which it is stated that the adsorption potential can be given by:

$$\varepsilon = RT\ ln\left(\frac{P_0}{P}\right), \tag{6.38}$$

with each parameter retaining earlier definitions. Dubinin's work, upon deliberating the DR equation based upon Polanyi's adsorption potential, considered a quantity of filling degree: simply a ratio of the adsorbed quantity to the maximum adsorption capacity (or filled pores). This filling degree in turn was considered to be a function of the adsorption potential and the characteristic energy of adsorption, E, which can be shown as:

$$\frac{a}{a_0} = f\left(\frac{\varepsilon}{E}\right). \tag{6.39}$$

A final proposal was made to form the DR equation, which was to suggest that the pore size distribution, and hence the distribution of energies, followed a Gaussian trend, thus producing the much-revered equation:

$$\frac{a}{a_0} = exp\left(-\left(\frac{\varepsilon}{E}\right)^n\right). \tag{6.40}$$

Works using the standard and modified DA equations for the purpose of modelling hydrogen adsorption in activated carbon are listed below in table 6.4, alongside the works in which the DA equations are modified for use.

Table 6.4 – Works containing modified Dubinin-Astakhov equations for modelling uptake of hydrogen in activated carbon and the works that modified the equations.

Source of modelling work with DA / modified DA equation	**Source of modified DA equation**	**DA Equation Form Used**
Hermosilla-Lara et al. (2007)	Dubinin (1975)	$\boldsymbol{a = a_0 exp\left[-\left(\frac{A}{E}\right)^2\right]}$ (6.41)
Momen et al. (2009) Momen et al. (2010)	Zhan et al. (2004)	$\boldsymbol{a = a_0 exp\left[-\left(\frac{RT}{E_a} ln\left(\frac{P_{lim}}{P}\right)\right)^2\right]}$ (6.42)
Xiao et al. (2010) Xiao et al. (2012) Xiao et al. (2013)	Richard et al. (2009)	$\boldsymbol{a_a = a_0 exp\left[-\left(\frac{RT}{\alpha+\beta T}\right)^m ln^m\left(\frac{P_0}{P}\right)\right]}$ (6.43)

In time, the modified DA equation was simply expanded upon by successive studies (Zhan et al. & Richard et al.) in terms of defining characteristic energies and the heterogeneity of the system. The characteristic energy is expanded from E and E_a to α + βT, to incorporate temperature dependency in the value. The parameters α and β represent the enthalpic and entropic factors of adsorption. The parameter m is analogous to the values of n and b seen previously which signify the surface heterogeneity. In all works noted above, the value assigned to the parameter is 2, and is seen to fit when considering adsorption of hydrogen in activated carbon. Figure 6.19 shows the form of these modified isotherms, where E_a is taken to be α + βT and m is taken as 2. The shape of the isotherms produced are in solid agreement

with those observed in the work by Momen et al. and demonstrates the temperature dependency of adsorption.

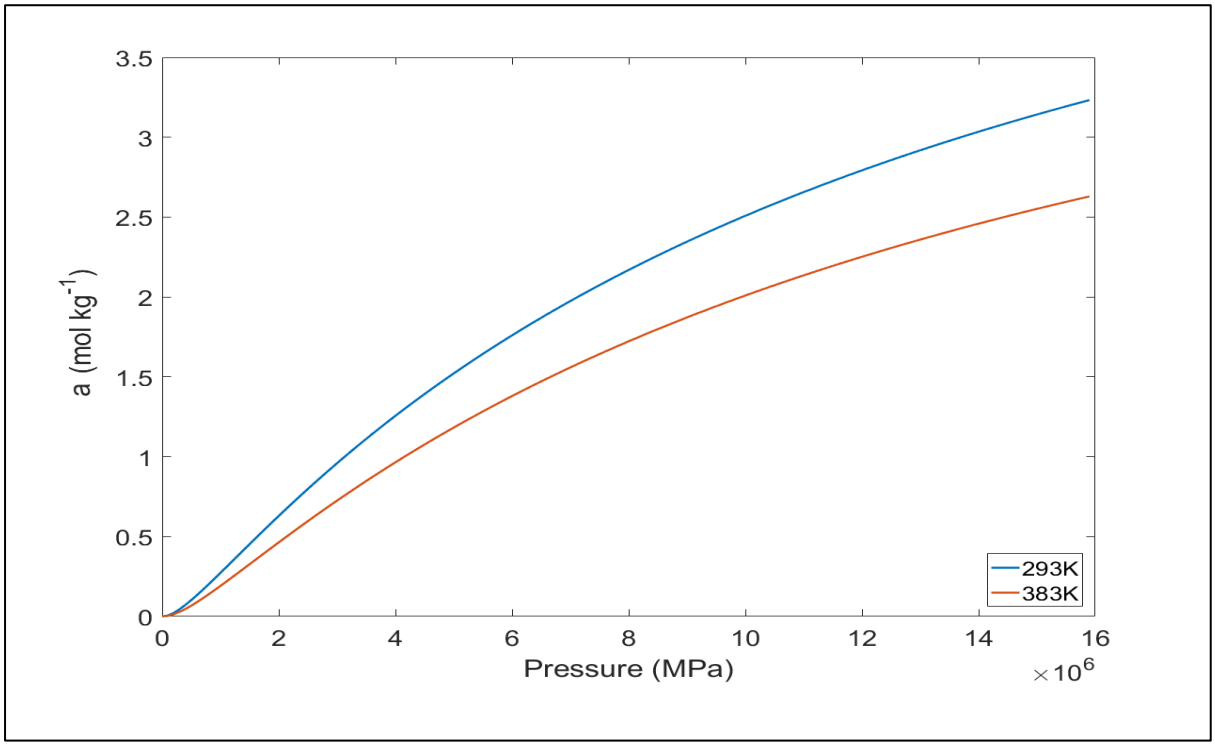

Figure 6.19 – Adsorption isotherms of hydrogen in activated carbon at 293K and 383K, modelled using the modified Dubinin-Astakhov equation provided by Richard et al. (2009).

Mass is introduced into the bulk of the system with a simple flowrate, however the mass of hydrogen added into the adsorbed phase is governed by the mass / momentum balance equation, given as follows:

$$\frac{\partial(\varepsilon_b \rho_g)}{dt} + \nabla \cdot \left(\rho_g \vec{v}\right) = -(1-\varepsilon_b)\rho_s M_{H_2} \frac{da}{dt}, \tag{6.44}$$

where

ε_b is the bed porosity,

ρ_g is the density of hydrogen (kg/m^3),

ρ_s is the density of activated carbon (kg/m^3),

$\vec{v}$ is the Darcy velocity (m/s),

M_{H_2} is the molecular mass of hydrogen (kg/mol),

$\frac{da}{dt}$ is the change in adsorbed quantity per time step (mol/s).

The balance of energy is also key in the previous modelling work, as is in the modelling for metal hydride absorption. The equation is given as:

$$\delta_{ts}\left(C_p\rho\right)_g \frac{\partial T}{\partial t} + \left(C_p\rho\right)_g \vec{v}\cdot\nabla T = \nabla\cdot\left(k_{eff}\nabla T\right) + Q, \tag{6.45}$$

where

$$\delta_{ts} = \frac{\varepsilon_b\left(C_p\rho\right)_g + \rho_s a M_{H_2} C_{pg} + \rho_s C_{ps}}{\left(C_p\rho\right)_g},$$

$$k_{eff} = \varepsilon_b k_g + (1-\varepsilon_b)k_s,$$

$$Q = (1-\varepsilon_b)\rho_s \frac{\partial n}{\partial t}\Delta H + \gamma T\left[\varepsilon_b \frac{\partial P}{\partial t} + (\vec{v}\cdot\nabla)P\right],$$

$$\Delta H = \alpha\sqrt{ln\left(\frac{a_0}{a}\right)},$$

and

$C_{pg,s}$ is the specific heat capacity of the gas and solid (J/kg K),

$\rho_{g,s}$ is the density of the gas and solid (kg/m^3),

$k_{g,s}$ is the thermal conductivity of the gas and solid (W/m K),

γ is the volume expansion coefficient.

The modelling to be used for adsorption in activated carbon follows loosely the modelling performed for the compressed hydrogen gas, in that it follows a similar operational logic (which will be explored in detail in the next chapter) with regards to the steps taken in each simulation. Two key factors contribute to the infeasibility of using finite element to simulate a mesh grid for activated carbon. 1) The size of the mesh grid required and 2) The finer resolution of the simulation which are required for stability; this results in the process being too computationally intensive for the purpose. Instead, analysis of the bulk material was used as in the approach taken to model the storage of compressed hydrogen. Each iteration of the simulation calculates the adsorbed quantity and the bulk pressure from the flow rate of hydrogen into the material.

To incorporate this model into an integrated energy system, the following simplifications are made: 1) Both gas phases (adsorbed and desorbed) are homogeneous with regards to pressure and temperature; 2) The pressure and temperature throughout the storage vessel is uniform; 3) The porosity of the activated carbon bed is assumed to be uniform. The material properties that are to be used in the simulations are listed in table 6.5.

Table 6.5 – Material properties of activated carbon as used in the simulation for adsorption of hydrogen in activated carbon. Source: Xiao et al., 2013.

Parameter	Value
a_0	71.6 mol kg^{-1}
P_0	1470 MPa
α	3080 J mol^{-1}
β	18.9 J mol^{-1} K^{-1}
ε_b	0.5
ρ_s	517.6 kg m^{-3}
ρ_g	Bender EoS
C_{ps}	825 J kg^{-1} K^{-1}
C_{pg}	14700 J kg^{-1} K^{-1}
k_s	0.646 W m^{-1} K^{-1}
k_g	0.206 W m^{-1} K^{-1}

6.5 Hydrogen Components

Within the storage models, electrolysers and fuel cells are used for the generation and consumption of hydrogen. Two equations govern the behaviour of each as used by Zini et al. (2010) in their work on simulated hydrogen energy systems. The equations give the relationship between the applied or drawn current of the electrolyser and fuel cell, and the mass of hydrogen either generated or consumed respectively. The equations are given as:

$$\dot{n}_{H2} = \eta_F \frac{N_C I_E}{ZF}, \tag{6.46}$$

$$\dot{n}_{H2} = \frac{N_C I_{FC}}{\eta_F ZF}, \tag{6.47}$$

where

η_F is the Faraday efficiency,

N_C is the number of cells in the series,

$\dot{n}_{H2}$ is the molar flow rate of hydrogen (mol/s),

$I_{E,FC}$ is the current of the electrolyser or fuel cell (A),

Z is the electron number for hydrogen (2),

F is the Faraday constant (A mol/g).

These equations are applied to each of the models, while taking into consideration the efficiency of both processes of electrolysis and consumption using a fuel cell.

The logic used within each of the Matlab models follows a particular structure. Four possible outcomes at each stage of the simulation are possible, given the energy system has some integrated energy storage. Figure 6.20 shows the flow of logic used to determine whether or not, out of these four scenarios, storage is considered. Further logic from the cases where

energy is either stored, or drawn from storage is expanded upon for each of the hydrogen storage methods in figures 6.21, 6.22 and 6.33. Relevant equations are highlighted for each.

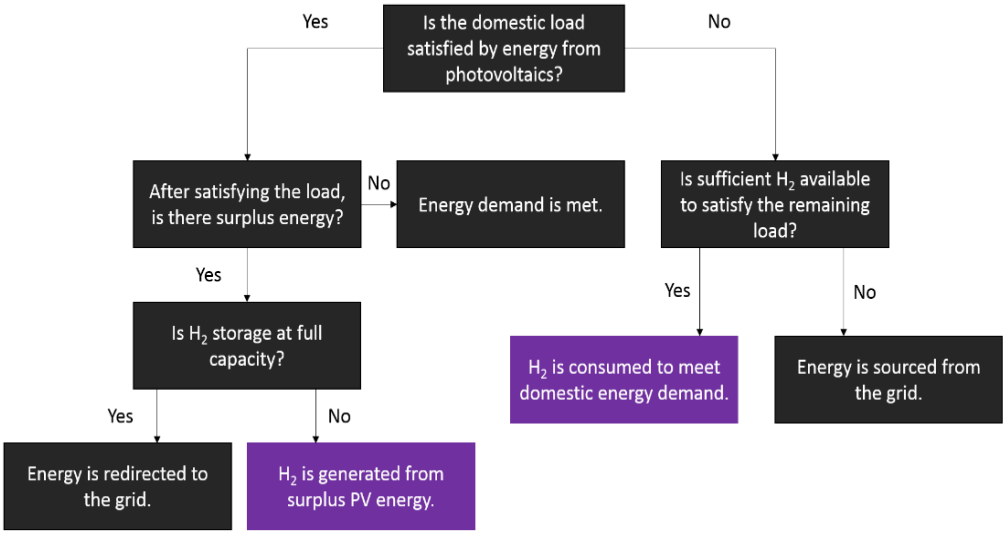

Figure 6.20 – Flow of logic used to determine domestic load satisfaction from photovoltaics and the resultant dependencies on stored and grid energies.

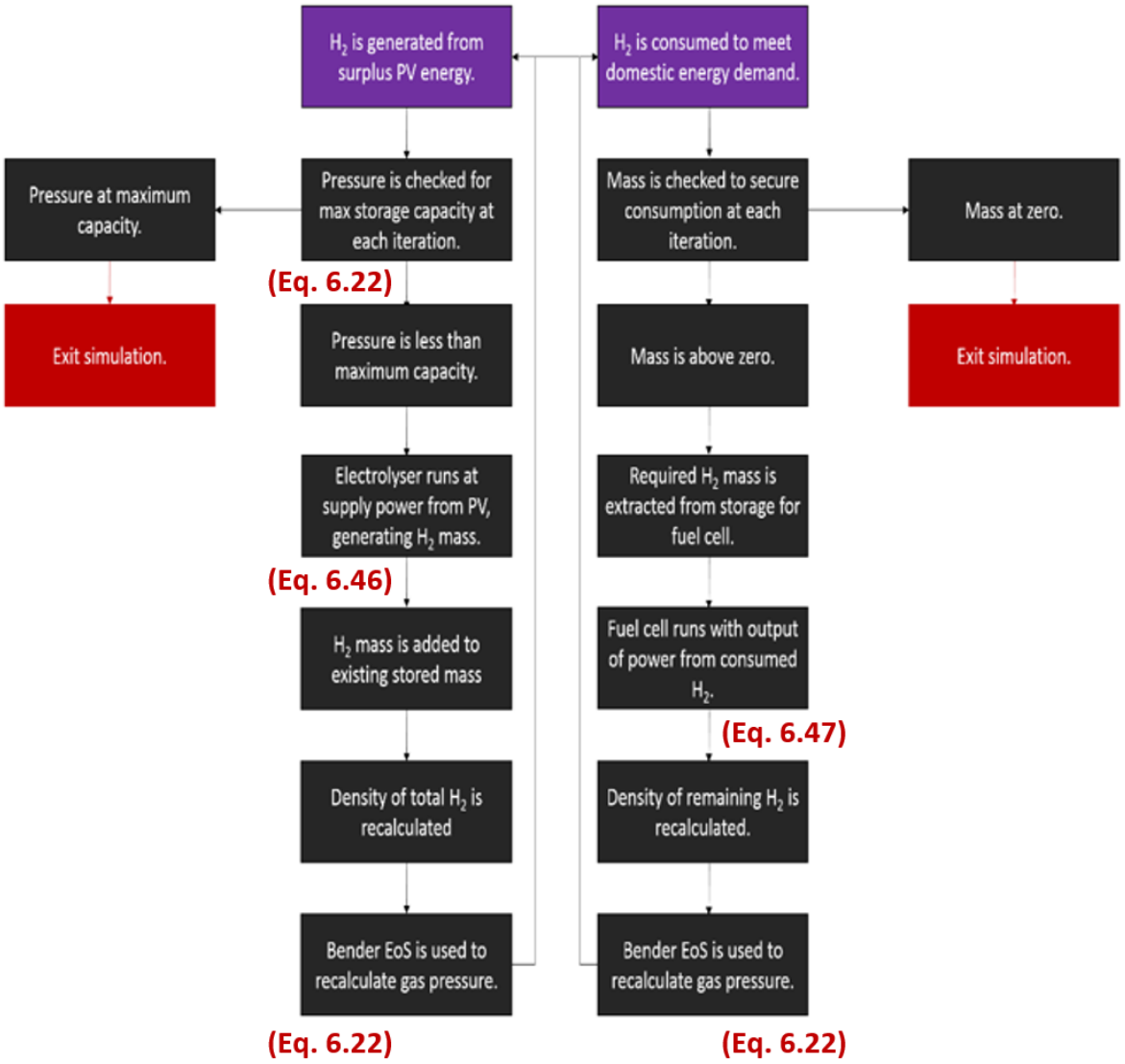

Figure 6.21 – Operational flow of hydrogen storage logic as a result of surplus or deficit in photovoltaic energy supply.

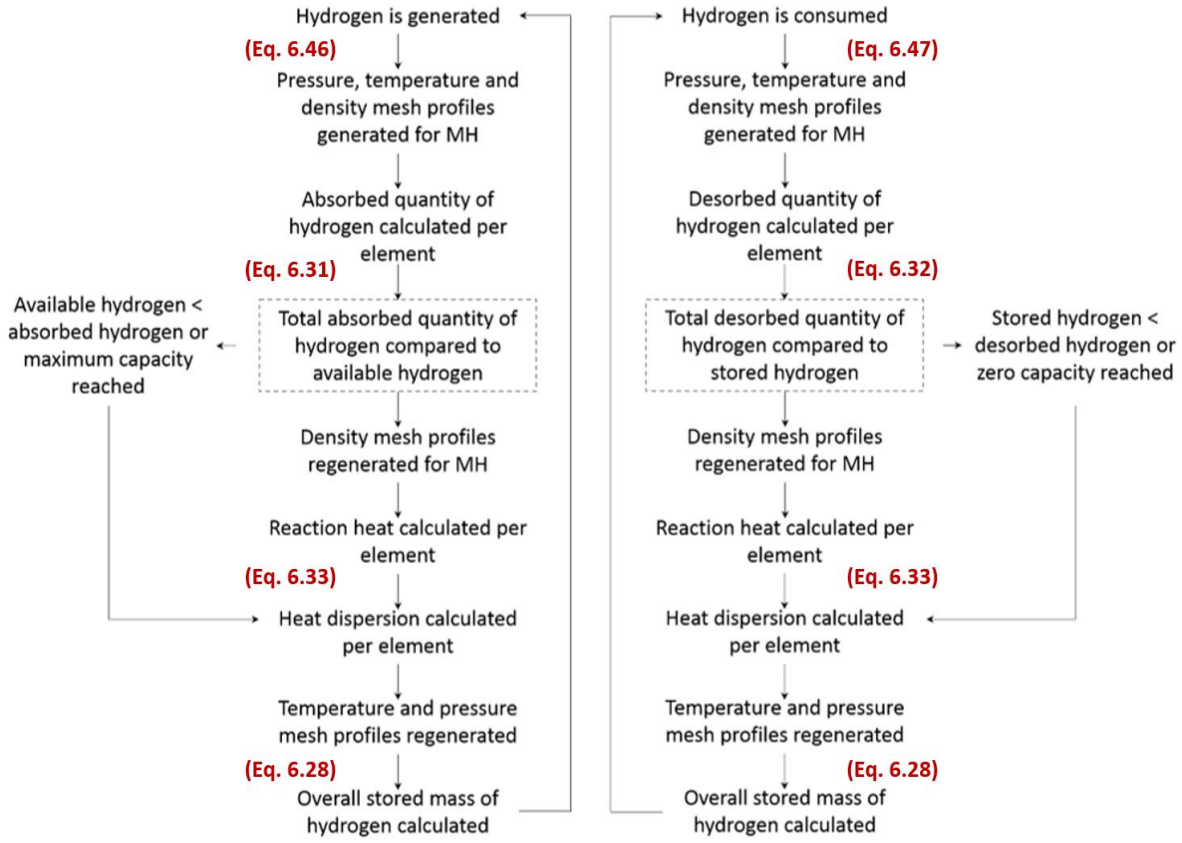

Figure 6.22 – Operational flow of logical steps for the simulation of absorption in $LaNi_5$.

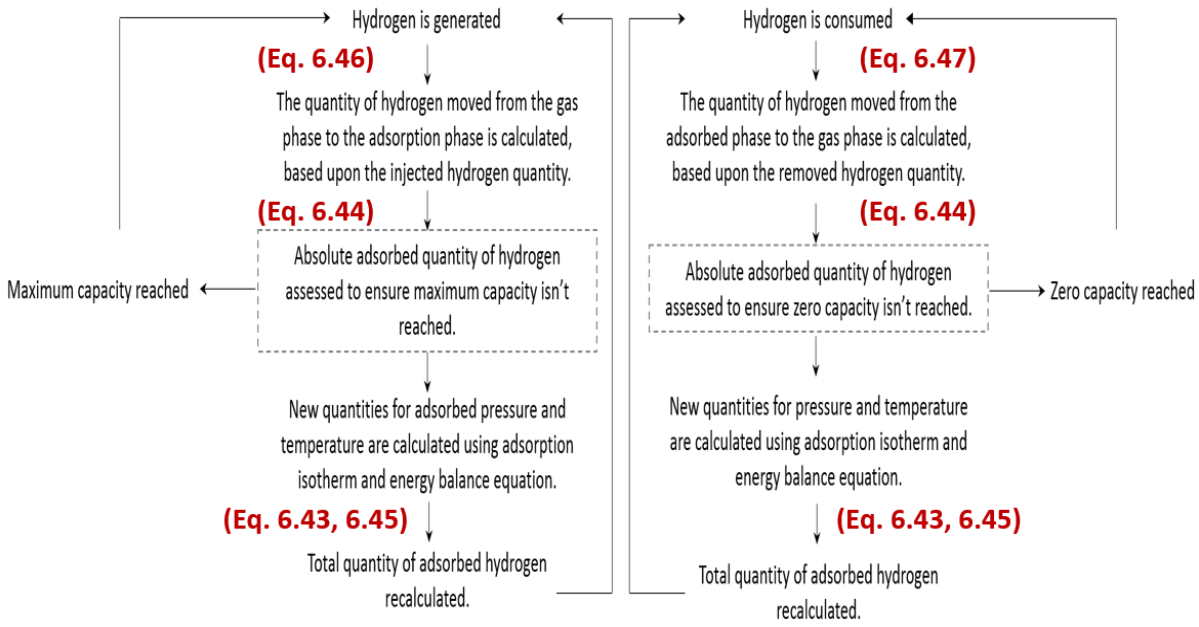

Figure 6.23 – Operation flow of logical steps for the simulation of adsorption of hydrogen in activated carbon.

The models behind each of the storage methods have been discussed in this chapter, along with the modelling behind the generation and consumption of hydrogen, and the logic behind each of the Matlab simulations. Each of the storage methods require a final sizing before moving onto the modelling exercise for storage. The energy capacity (or equivalent hydrogen storage capacity) of each of the storage methods are designed to be the same. This allows for a fair comparison against equivalent energy storage systems in order to identify variance in the behaviour of each. Maximum storage capacity is based upon the established technology of the home battery, which in this study is considered to be the Tesla Powerwall 2, with a storage capacity of 14 kWh. From the simulation results of the baseline model analysed in the previous chapter, this maximum storage capacity can support 2 days of electric energy consumption.

The equivalent mass of hydrogen required, allowing for the inefficiency of the fuel cell, is 0.6 kg. The storage conditions which facilitate this for each of the hydrogen storage methods are:

- 0.037 m^3 tank for compressed H_2 at 175 bar.
- 0.005 m^3 or 45 kg of $LaNi_5$ stored without compression.
- 0.034 m^3 or 17 kg of activated carbon stored using 175 bar.

These conditions are used to govern the maximum stored hydrogen within each of the storage models.

The main Matlab scripts used to model the storage of hydrogen in each scenario are given in Appendix A.

6.5.1 System Efficiency

Inefficiencies are inherent in each of the storage systems; figure 6.24 maps the efficiencies within a battery-based energy storage system; figure 6.25 maps efficiencies for compressed gas and activated carbon-based energy storage systems; and figure 6.26 finally maps those for the metal hydride-based energy storage system. Each figure displays an efficiency range per energy system.

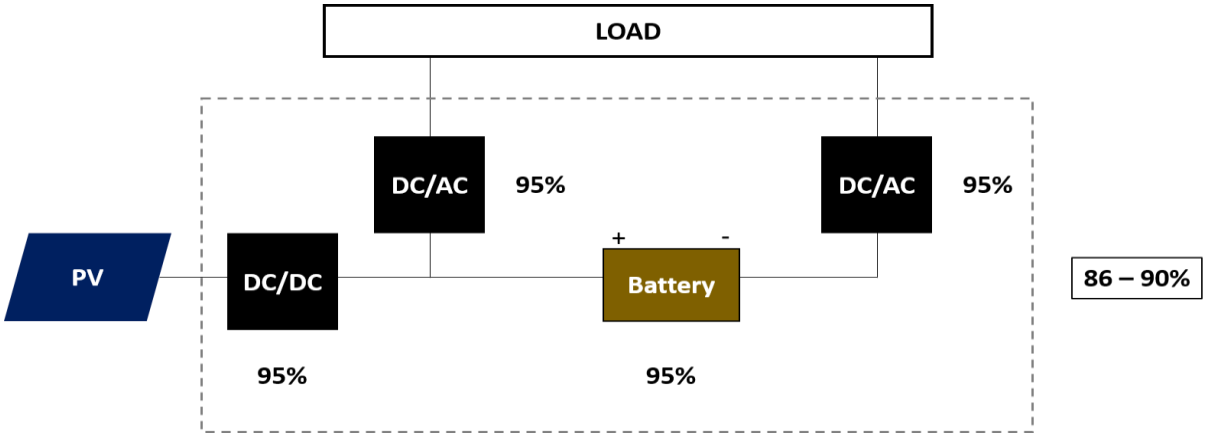

Figure 6.24 – Efficiency range for battery-based energy storage system.

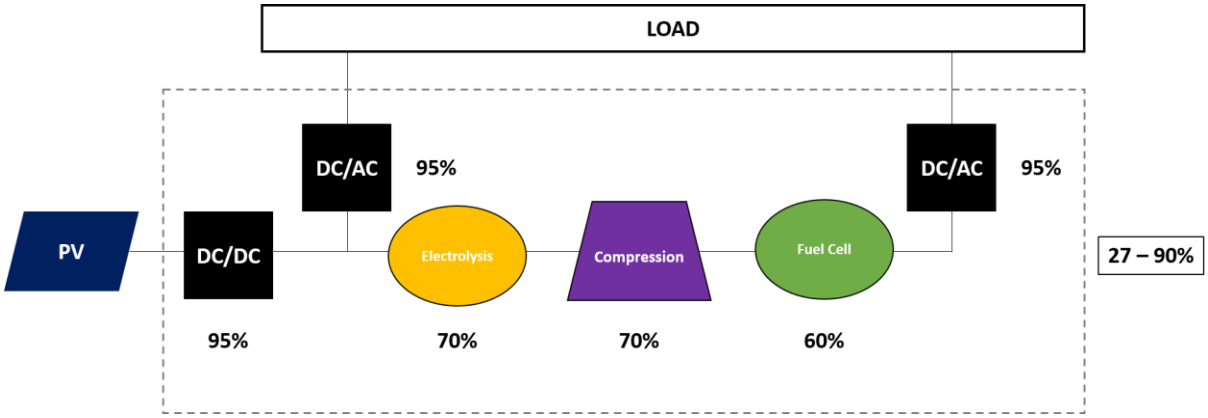

Figure 6.25 – Efficiency range for compressed gas and activated carbon-based energy storage systems.

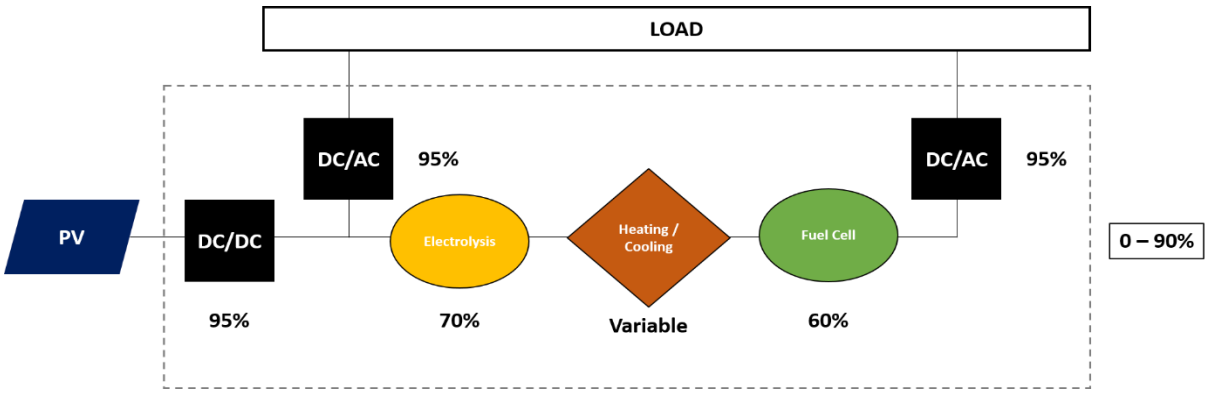

Figure 6.26 – Efficiency range for metal hydride-based energy storage systems.

For each of the figures 6.24, 6.25 and 6.26, the efficiencies of the DC/DC transformers and AC/DC transformers are taken from the Designbuilder software. The efficiency of the battery is determined from the data available from Designbuilder on the average daily self-discharge. Compression efficiency is taken from the DoE's H2A project (H2A Group, 2006). The efficiency of the metal hydride-based system is variable, given the energy required to heat or cool the metal hydride during sorption changes with each scenario. The logic of the Matlab model restricts the metal hydride energy system from having negative efficiency, so the minimum possibility is then 0%.

Though the battery-based energy storage system demonstrates the highest efficiency range, understanding the dynamicity of each storage method and its ability to respond to energy surplus and demand is key to determining the benefits. The next chapter analyses the results of annual energy simulations with the integration of these storage methods, reviewing the impact of this integration on the combined grid energy demand for each of the sensitivity factors and investigating any further tendency towards energy autonomy.

The development of these models concludes the fourth objective of this thesis. The next chapter uses these energy storage models with the outputs found using the models considered in chapter 4 and as discussed in chapter 5, addressing the fifth and penultimate objective of this thesis.

Chapter 7

Dynamic Energy Simulations:

Results of Modelling with Storage

The results presented in this chapter and the discussion surrounding those results address the final two objectives of this work. Models for energy storage presented in Chapter 6 have been used to process the output data from Designbuilder models of the Energy House under scenarios reflecting factors of sensitivity, which impact on the performance of the domestic energy system. The overall aim of the work, is understanding the role of energy storage methods with a view to achieve energy autonomy for a decentralised domestic energy regime, is investigated using the results explored in this chapter.

So far, the ranges of overall grid dependent energy consumptions have been simulated for factors of building archetype, occupancy profiles, building location, impact of future climate scenarios and applied retrofit. Scenarios within each category have demonstrated best and worst cases. Certain factors such as northern locations and exposed facades of detached buildings have shown a decrease in overall energy system performance; alternatively, factors such as deep retrofit, electric heating and reduced occupancy density have shown to greatly improve the energy performance of dwellings. Furthermore, a combination of the 'best case scenarios' from each sensitivity factor has shown that grid dependent energy consumption can be reduced by up to 86%.

Results from the simulations carried out in Chapter 5 demonstrated that significant quantities of energy generated using photovoltaics is redirected to the grid due to a mismatch in the supply and demand of energy in the home. This established a considerable need for some form of energy storage. Also revealed in Chapter 5 was the fact that in most cases, the amount of surplus energy, from solar generation, being sent to the grid was much higher than the remaining energy demand from the Energy House models. This offered the notion that in these cases, with some form of energy storage method in place, a self-sustaining autonomous energy system could be achieved.

This chapter now analyses the results from simulations with integrated energy storage. The baseline model's energy storage profiles are first analysed, before moving onto each of the sensitivity categories. A comparison is first made between the baseline, best and worst-case scenarios for each category to investigate the difference in annual energy storage trends. Heat maps are used to visualise the state of charge throughout the year in each case. Reduced annual profiles for each of the methods of storage within those categories are then explored, before a summary of the overall storage impact is made.

7.1 Baseline Model

The impact of using energy storage is first reviewed for the baseline model, before moving on to compare the impact within specific sensitivity categories. This is to familiarise with the heat maps and annual energy storage profiles, and to examine trends in storage for each of the energy storage methods. Figure 7.1 begins by simulating the heat map of battery state of charge for the baseline model.

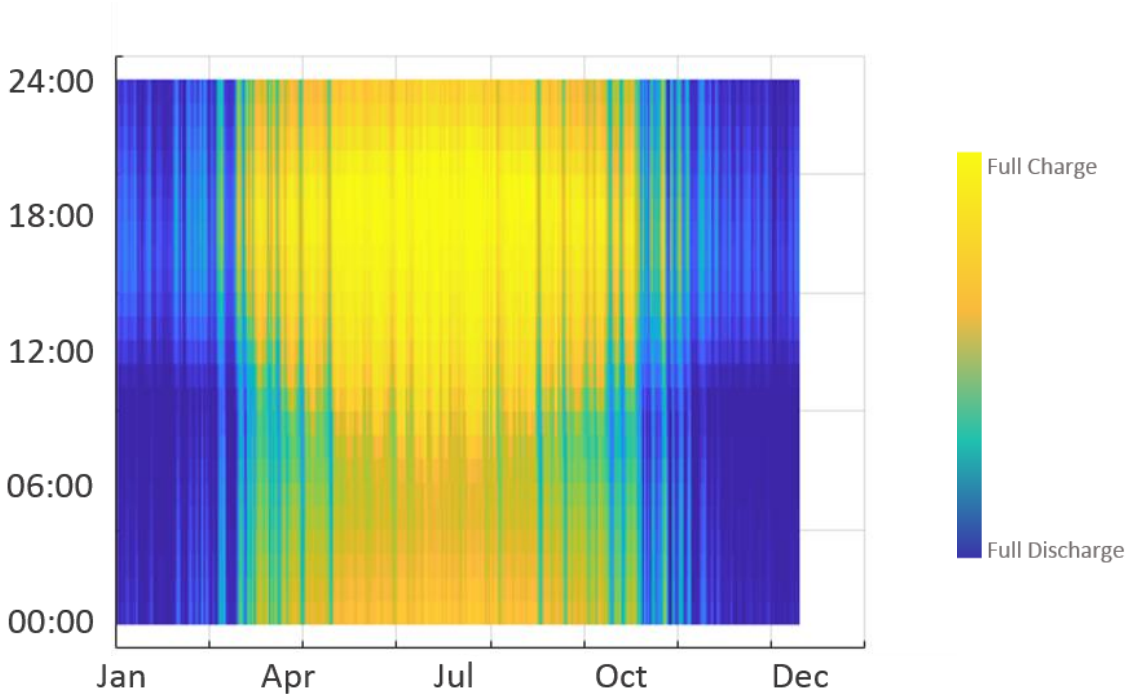

Figure 7.1 – Heat map of battery state of charge for the baseline scenario.

Figure 7.1 plots the quantity of energy stored in the battery of the baseline scenario at each hour, throughout the year. In this layout, trends can be spotted on a daily, weekly and annual basis. Darker regions show low energy storage, while lighter regions show higher levels of energy storage.

The daily trends shown in figure 7.1 indicate that energy storage occurs between mid-morning and early evening in most cases, while energy is consumed the rest of the time. This is synonymous with the energy generation of the solar panels. Variation of daily charging throughout the year shows that the energy storage period is extended across the summer months, resulting in an 'egg-timer' shape. The overall trend demonstrates a summer charging period, between the months of April and October, where the battery remains relatively fully charged throughout.

As different sensitivity categories are explored in this chapter, the baseline heat map in figure 7.1 will be compared with those of the individual sensitivity scenarios to review how those factors impact on these trends in energy storage.

Table 7.1 lists the overall (combined) grid energy consumption for the baseline model without energy storage, and with storage using the home battery, compressed hydrogen, metal hydride, and activated carbon. The table also lists the reduction in consumption given the integration of those energy storage methods.

Table 7.1 – Combined grid consumption for the baseline model with and without energy storage.

Storage Method	**None**	**Home Battery**	**Compressed H_2**	**Metal Hydride**	**Activated Carbon**
Combined Grid Consumption	7314 kWh	6011 kWh	5964 kWh	6207 kWh	6263 kWh
Consumption Reduction	n/a	18%	19%	15%	14%

Noting that each energy storage method has the same capacity, it is not unusual that the reduction in grid energy consumption is similar. There exists however, dissimilarities between the methods; minutiae which inform the responsiveness of each method to the storage and release of energy at the domestic scale. The results shown in table 7.1 show that battery and compressed hydrogen storage offer the highest reduction in grid energy consumption, with metal hydride and activated carbon storage slightly lower. The reasons for this can be investigated within the energy storage profiles themselves.

Annual energy storage profiles for each sensitivity category have been simulated and display the state of charge of each method of storage on an hourly basis. These data have been modified to give the daily average state of charge, to clearly define storage profiles in each case. The first example of this is given in figure 7.2, where the daily averaged – annual energy storage profiles for the baseline model are displayed. Each storage method is shown within this figure.

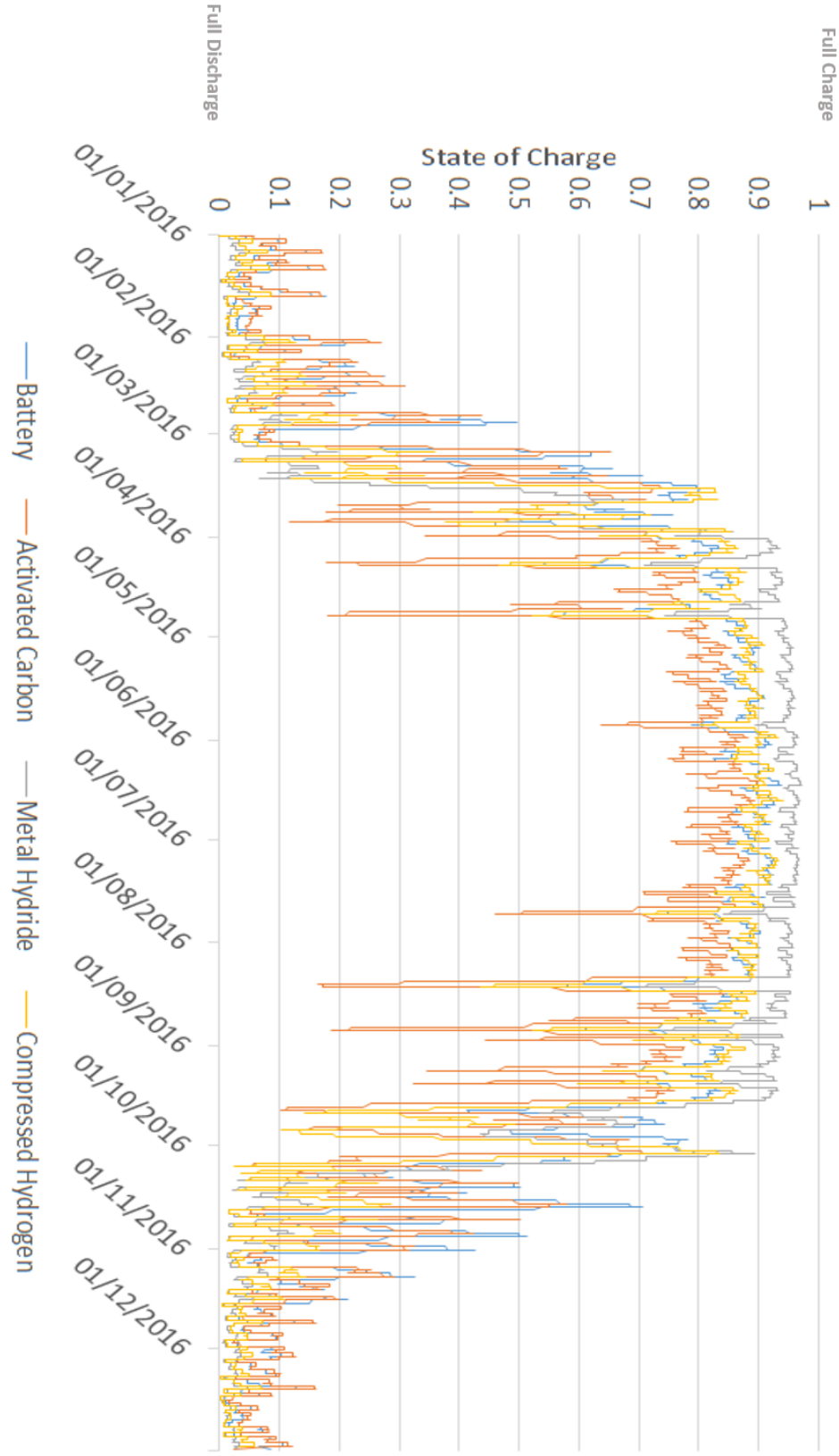

Figure 7.2 – Daily averaged annual energy storage profiles for the baseline model.

Recalling to figure 5.3 of Chapter 5, where the generation of energy throughout the summer months largely outweighed the demand during that same period, it is unsurprising to see that the storage of energy is indeed focused between April to October. All of the storage methods demonstrate this trend, revealing that a seasonal storage of energy is achieved while integrating storage into PV-based energy systems.

The states of charge reach a quasi-plateau over the summer months; however, this stored energy is often consumed, presumably over night while there is no PV available to power the base load of the building. Figure 7.3 shows non-averaged storage data for the battery over a week in June to investigate this.

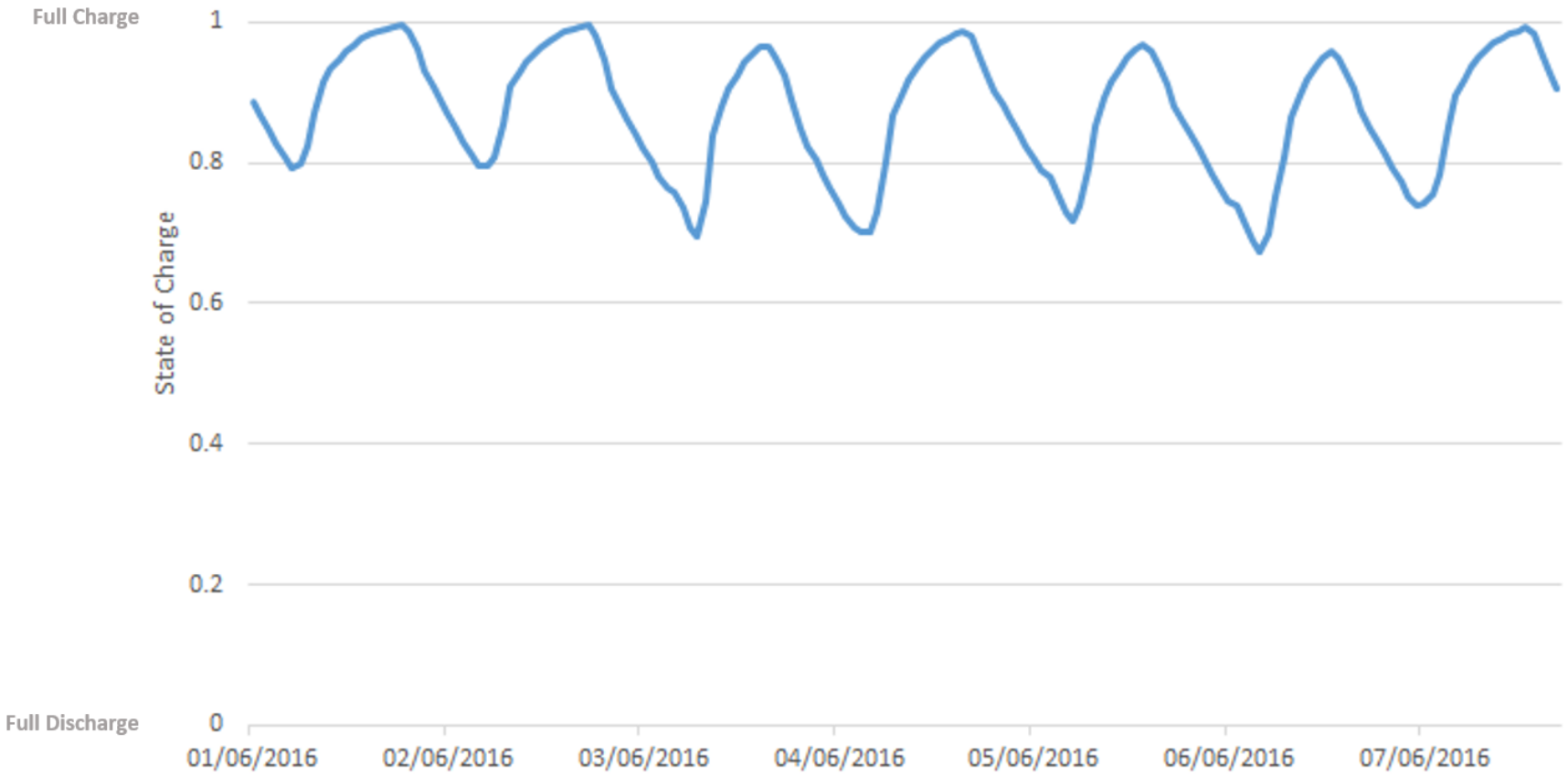

Figure 7.3 – Battery energy storage profile for the baseline model, representing a week in June.

The data in figure 7.3 shows that storage peaks during the day, while energy is consumed overnight. Figure 7.4 further compares this data to the states of charge of all storage methods for a comparison throughout the same period.

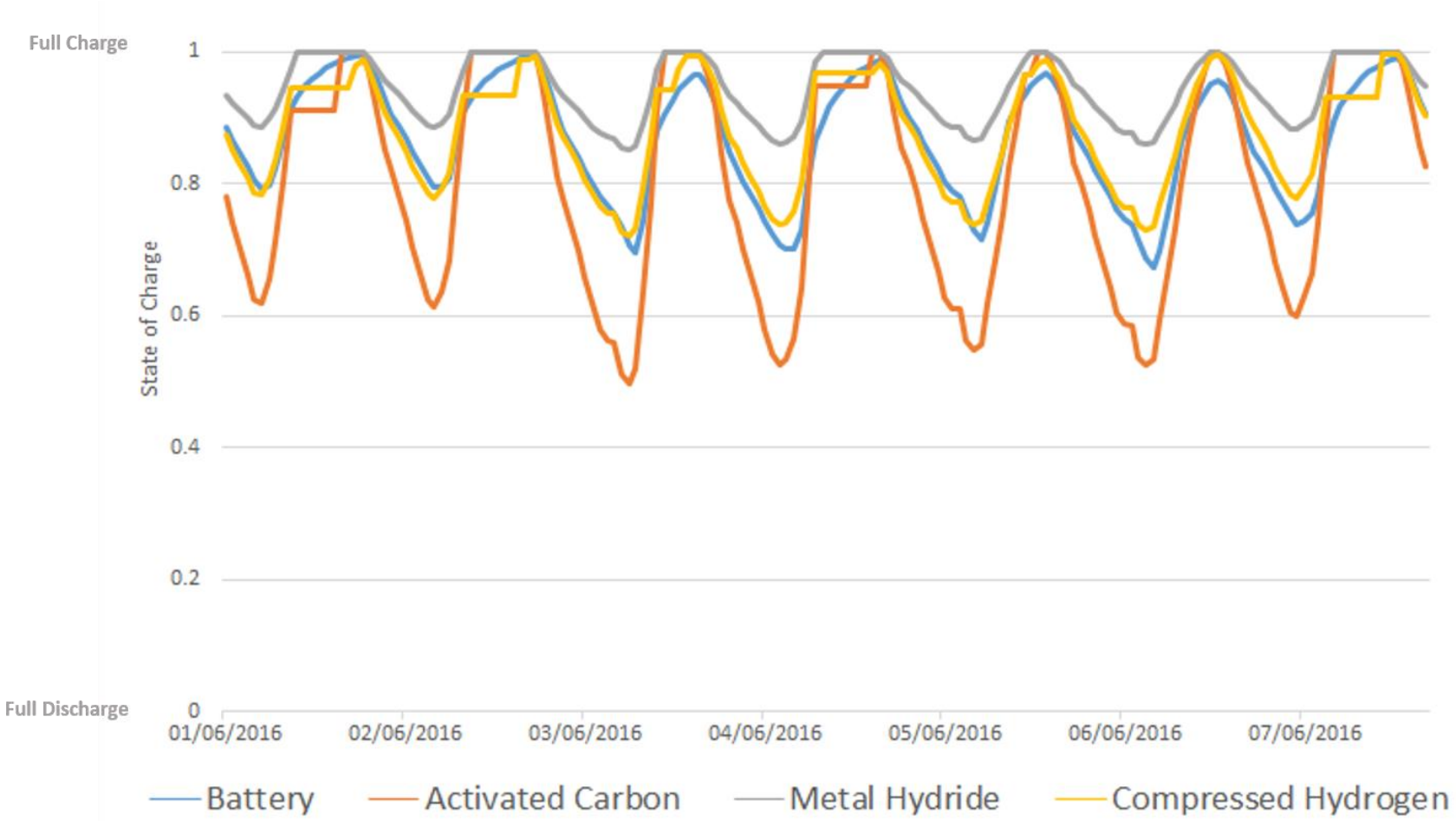

Figure 7.4 –Energy storage profile for the baseline model for all storage methods, representing a week in June.

Figure 7.4 identifies dissimilarity in the charging and discharging that occurs with each storage method. While compressed hydrogen generally mirrors the performance of the home battery, storage using activated carbon shows a poorer performance, with metal hydrides generally maintaining a higher state of charge. This gives some insight into the performance of each of the storage methods.

Both the home battery and compressed hydrogen demonstrated a similar reduction in grid energy consumption, which is supported in figure 7.4. Activated carbon is observed to consume more energy for the same demand; this suggests some system inefficiency greater than that found in the battery or with compressed hydrogen – possibly within the compression of hydrogen (i.e. long periods of compression at higher pressures). Alternatively, metal hydride storage demonstrates relatively slower charge and discharge of hydrogen, suggesting that the supply of energy may not be fast enough to meet the demand, thus introducing system inefficiencies in this way.

The identification of these inefficiencies is important in understanding how each method of storage behaves within the coming simulation scenarios.

Energy storage profiles for the battery were initially investigated for a comparison between the best and worst-case scenarios of each sensitivity category. The profiles for each energy storage method of that category were then compared for the worst and best-case scenarios to investigate the varying minutiae in storage performance at the extremes of that sensitivity.

As discussed earlier, the basic energy storage profile does not change for archetype, however occupancy, location and future climate changes were explored.

5.2 Occupancy

Earlier simulations revealed that the worst-case scenario for occupancy was for a home with 2 retired adults, whereas the best-case scenario was reserved for a home with 1 working adult. Figures 7.5, 7.6 and 7.7 compare the heat maps of energy storage for the baseline model, two retired adult model and the single working adult model.

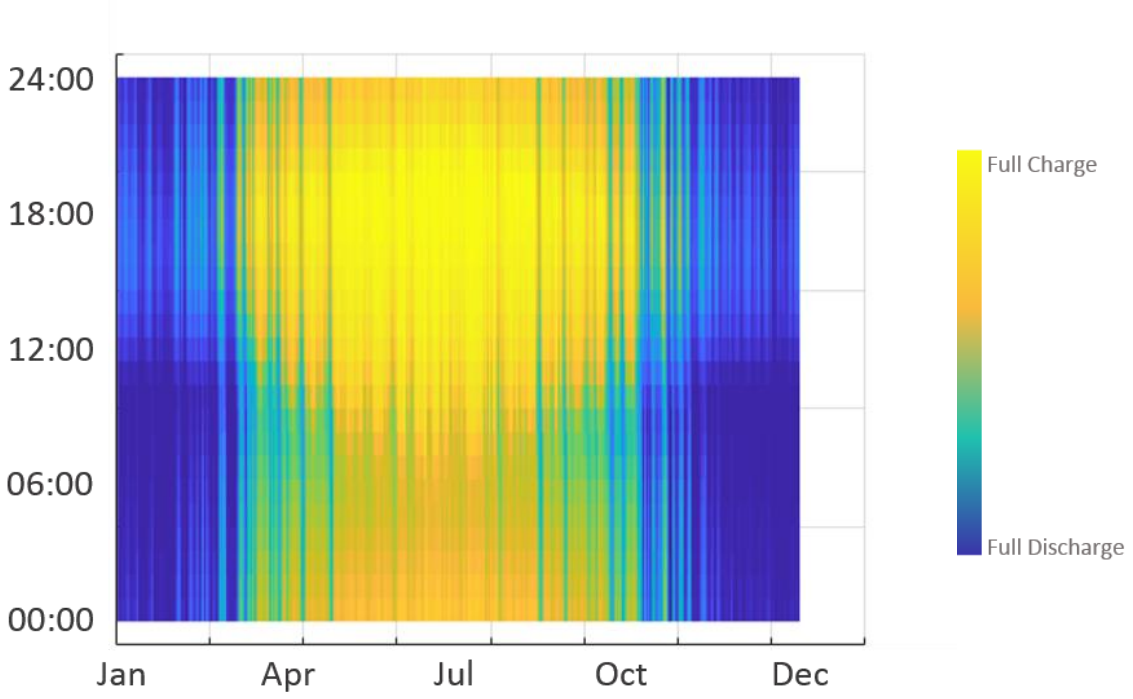

Figure 7.5 – Baseline model energy storage heatmap.

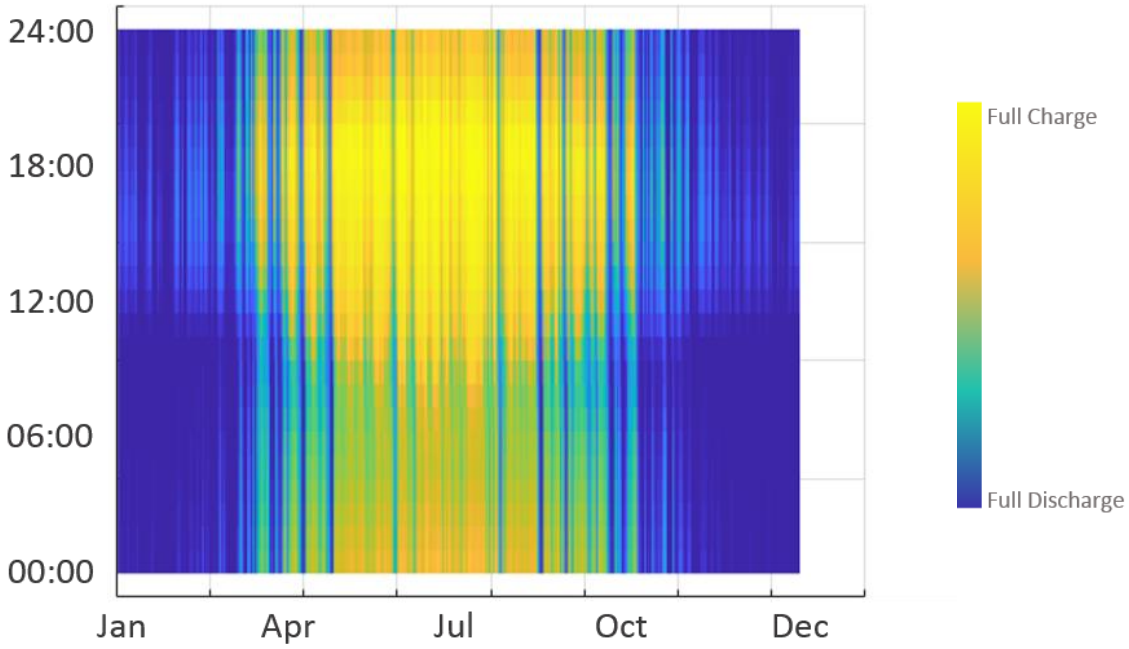

Figure 7.6 – Two retired adults model energy storage heatmap.

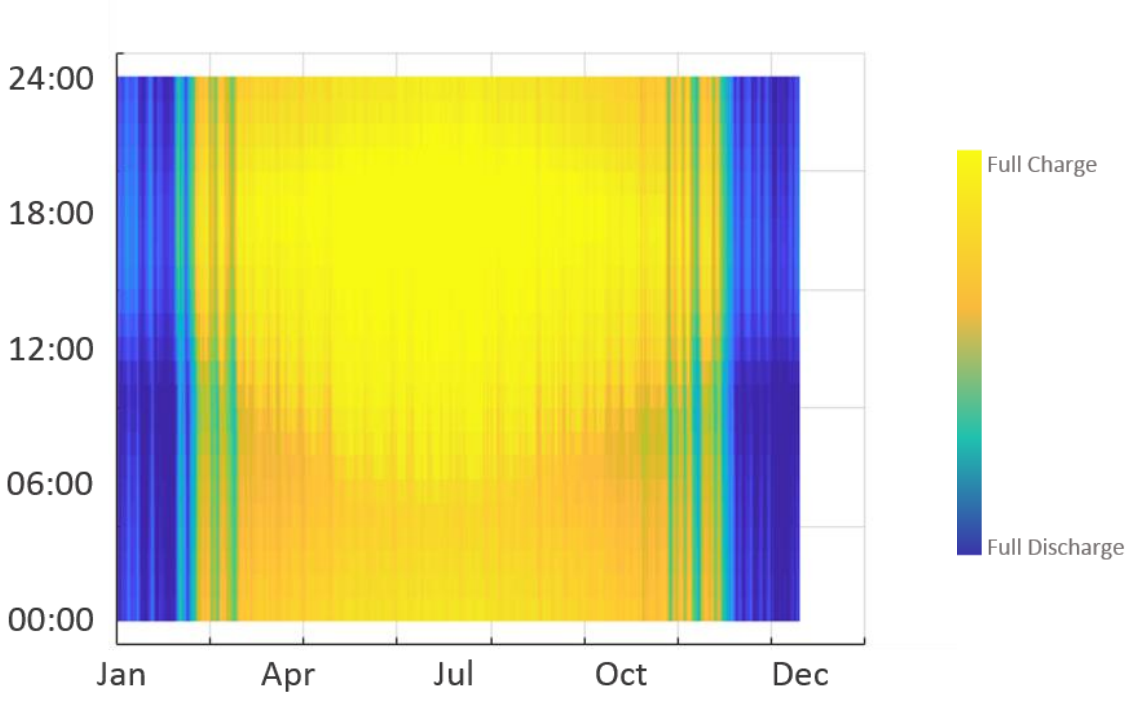

Figure 7.7 – Single working adult model energy storage heatmap

Data in figures 7.6 and 7.6 give stark contrasts to the data in 7.5. For the model with two retired occupants, an obviously reduced overall energy storage is observed throughout the year. Gaps in energy storage also occur periodically. The impact of occupancy on the energy storage profile is the development of the 'egg-timer' shape, given that the occupancy frequency is higher for two retired adults than two working adults, as used in the baseline model.

A different impact is observed for the single working adult occupancy profile, where energy storage is much higher throughout the year. Gaps in storage nightly consumptions as observed in the baseline model become infrequent due to the reduced occupancy density, and so reduced energy demand.

Table 7.2 gives a summary of the combined grid energy consumption with and without energy storage integration for a comparison of these scenarios.

Table 7.2 – Combined grid energy consumptions with consideration for battery energy storage, for the occupancy category.

Scenario	**Baseline**	**2 Retired Adults**	**1 Working Adult**
Consumption without Storage	7314	7681	7157
Consumption with Storage	6011	6501	6428
Reduction	18%	15%	10%

Energy storage profiles are now analysed for occupancy for each of the storage methods considered. These annual profiles are again given for models with 2 retired adults (figure 7.8) and with 1 working adult (figure 7.9).

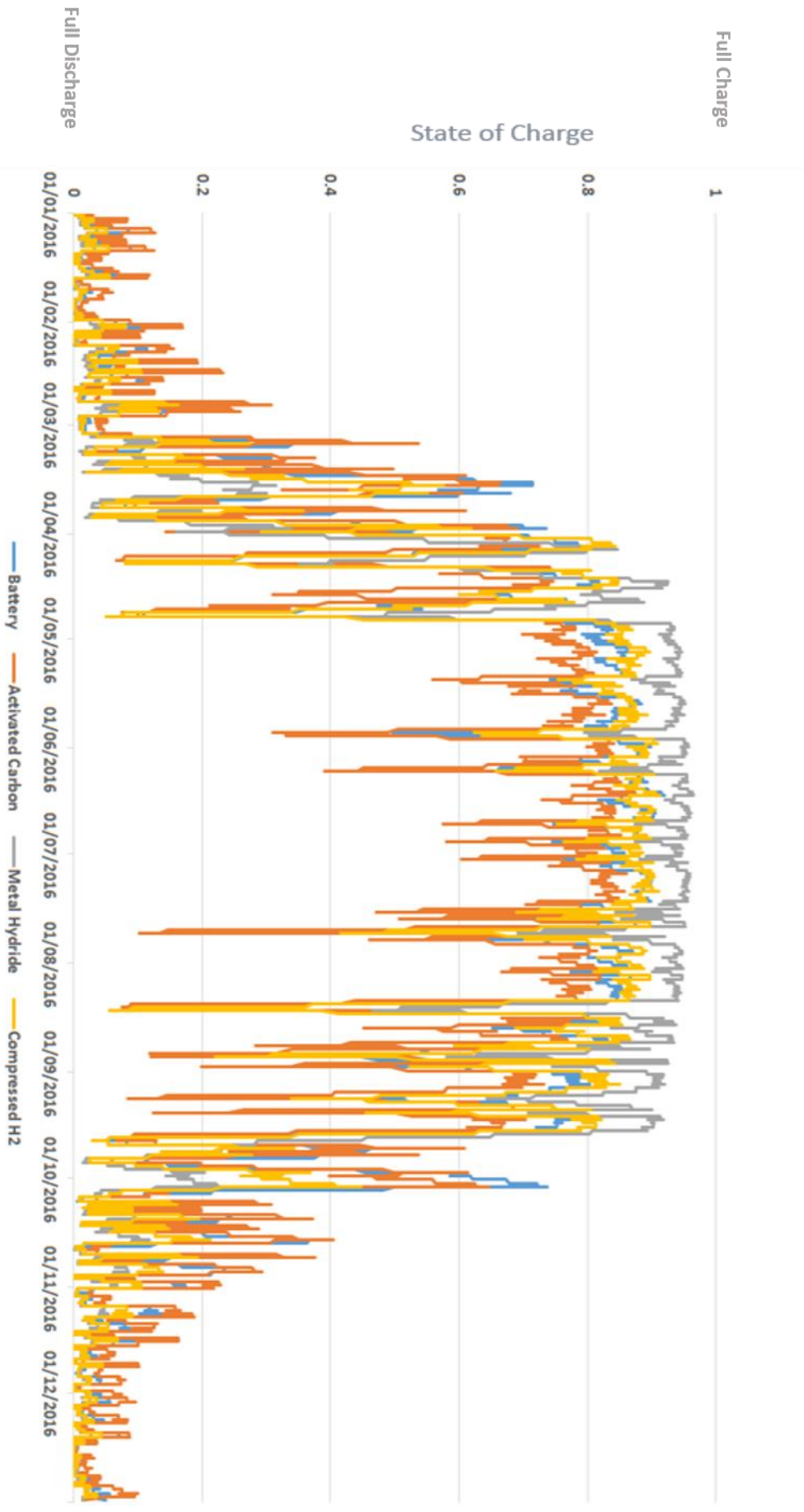

Figure 7.8 – Occupancy: Annual energy storage profiles for each storage method. Two Retired Adults.

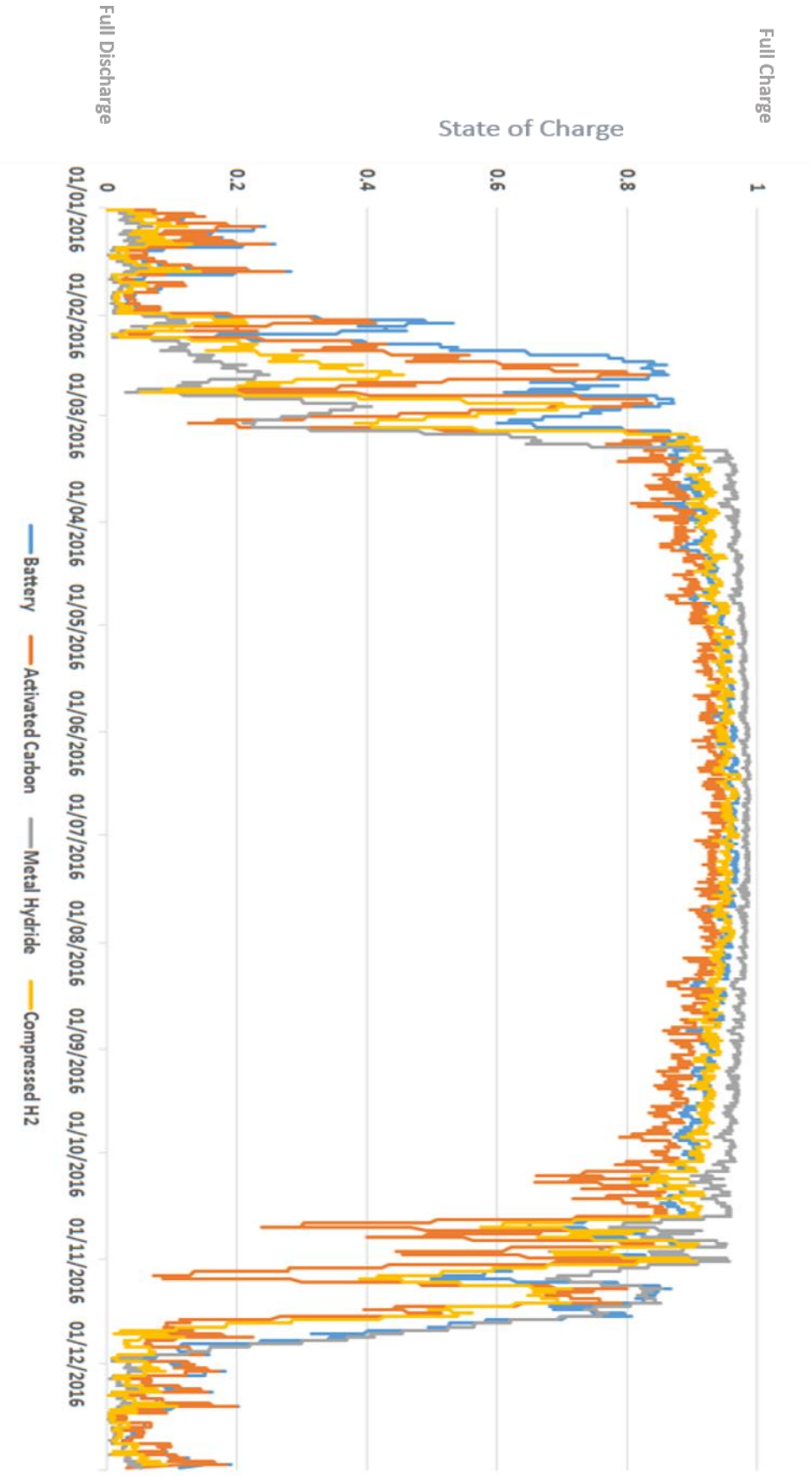

Figure 7.9 – Occupancy: Annual energy storage profiles for each storage method. Single Working Adult.

The same trends are seen in figures 7.8 for each of the storage methods: throughout the summer 'storage season' metal hydrides have a noticeably higher average state of charge than other storage methods, while activated carbon has a comparably lower average state of charge. Battery and compressed hydrogen storage remain quantitatively similar.

The data in figure 7.9 reveal – particularly in the lead up to and for the immediate period following the summer storage season – that for the same quantity of surplus solar energy, each storage method has a markedly different behaviour as storage reaches the plateau. Table 7.3 summarises the rates at which each method of storage reaches and leave the SOC plateau. While being an indicator of seasonal storage performance, this is indicative of the response of each storage method to the short-term conditions of storage (i.e. surplus energy and deficit demand).

Table 7.3 – Rates of approach and departure from the energy storage plateau for each method of energy storage.

	Approach to Plateau	**Departure from Plateau**
Battery	Fast	Delayed
Compressed H_2	Delayed	Fast
Metal Hydride	Delayed	Delayed
Activated Carbon	Fast	Fast

The battery demonstrates a fast response to surplus energy; this fast response could then be responsible for a quick replenishment of energy post-plateau, resulting in a delay to the average SOC reduction.

The opposite appears to be true for compressed hydrogen, where the build up to the energy plateau is delayed and the consumption post-plateau is faster than for the battery. The delayed build up can be explained by the consumption of additional energy to compress the gas. This delay then impacts on the consumption post-plateau, with a reduced replenishment of energy, the decay is much quicker than in the case of the battery.

With delayed uptake and release of energy either side of the storage season, metal hydride storage exhibits slow sorption behaviour. To improve on this, greater energy consumption is required to provide increased cooling and heating of the metal hydride for faster storage response times. This would impact on the overall system performance and reduce the already low performance of metal hydride storage.

Both storage and release of energy is higher for activated carbon than for the other storage methods. This is visible in the sharp peaks and troughs of the annual storage profile and in the overall lower SOC plateau, indicating that the response to additional energy demands are much larger than necessary. This means that the modelled system as a whole demonstrates a lower efficiency than the other storage methods, potentially due to an energy deficit incurred during compression.

The ideal scenario here would be a storage method with a fast response leading up to the storage season, and a delayed departure from that storage season. The battery is the method of storage that matches that description the closest.

Table 7.4 and 7.5 summarise energy storage for the two retired and the single working occupancy profiles, for all methods of storage, listing the combined grid demand with and without each storage type for a final comparison in this sensitivity category.

Table 7.4 – Occupancy: Energy summary for household with two retired adults.

Energy Storage Method	**Battery**	**Compressed H_2**	**Metal Hydride**	**Activated Carbon**
Combined Grid Demand [Without Storage]	7681 kWh			
Combined Grid Demand [With Storage]	6501 kWh	6199 kWh	6433 kWh	6690 kWh
Difference	15%	19%	16%	13%

Table 7.5 – Occupancy: Energy summary for household with one working adult.

Energy Storage Method	**Battery**	**Compressed H_2**	**Metal Hydride**	**Activated Carbon**
Combined Grid Demand [Without Storage]	7157 kWh			
Combined Grid Demand [With Storage]	6428 kWh	6411 kWh	6430 kWh	6472 kWh
Difference	10%	10%	10%	10%

Following the observation made earlier alluding to the benefit of storage for these occupancy profiles, energy storage does appear to be more beneficial for households with greater initial energy demand. Each of the storage methods perform similarly for the household with a single working adult, while greater variation is observed for the household with two retired

adults. With higher periods of occupancy and greater overall demand, storage is accessed more frequently under this occupancy profile, and therefore the dynamicity of the storage procedure plays a larger role in defining benefit to the overall energy system. The compressed hydrogen storage method performs the best given this scenario.

For the occupancy sensitivity category, profiles with higher energy demand have demonstrated greater sensitivity and greater benefit from energy storage, with the compressed hydrogen storage system delivering the highest reduction in combined grid demand. For profiles with lower energy demand, energy systems benefit equally from all storage methods, which deliver similar reductions in combined grid demand, but with less of an impact than for those with higher demand.

7.3 Location

The simulations from Chapter 5 revealed that the best and worst-case locations for combined grid energy consumption were Ebbw Vale – due to its exposure – and Plymouth – due to its increased solar incidence and higher average annual temperature. Figure 7.10, 7.11 and 7.12 compare the energy storage heat maps for the baseline model and each of the location scenarios.

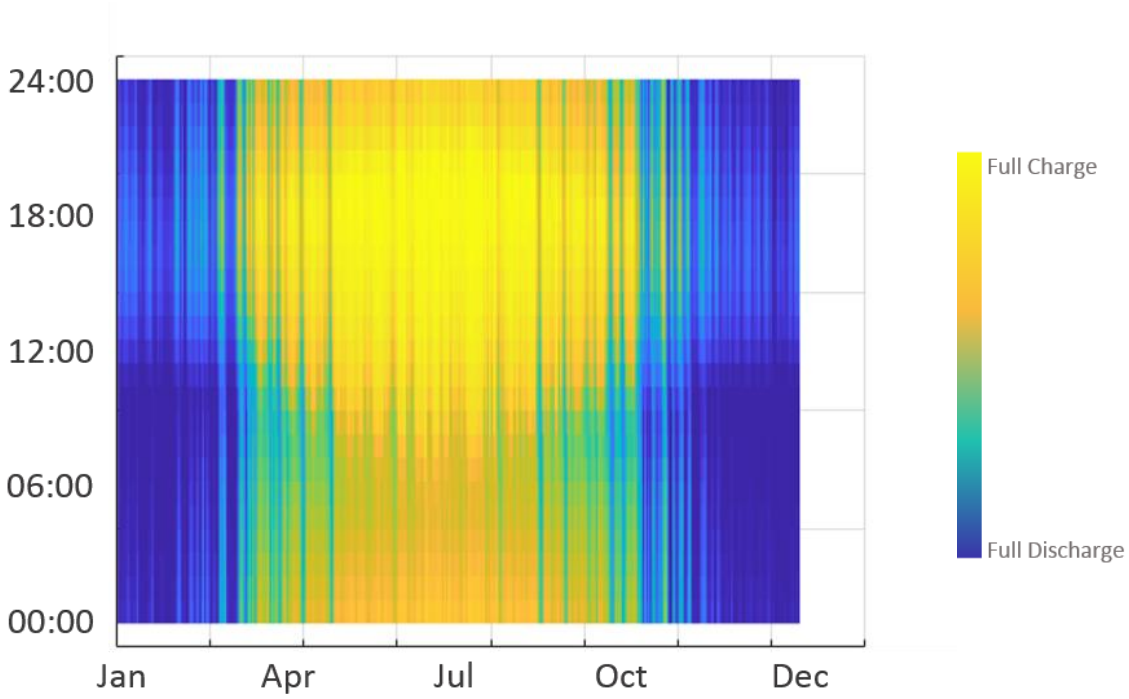

Figure 7.10 – Baseline model energy storage heatmap.

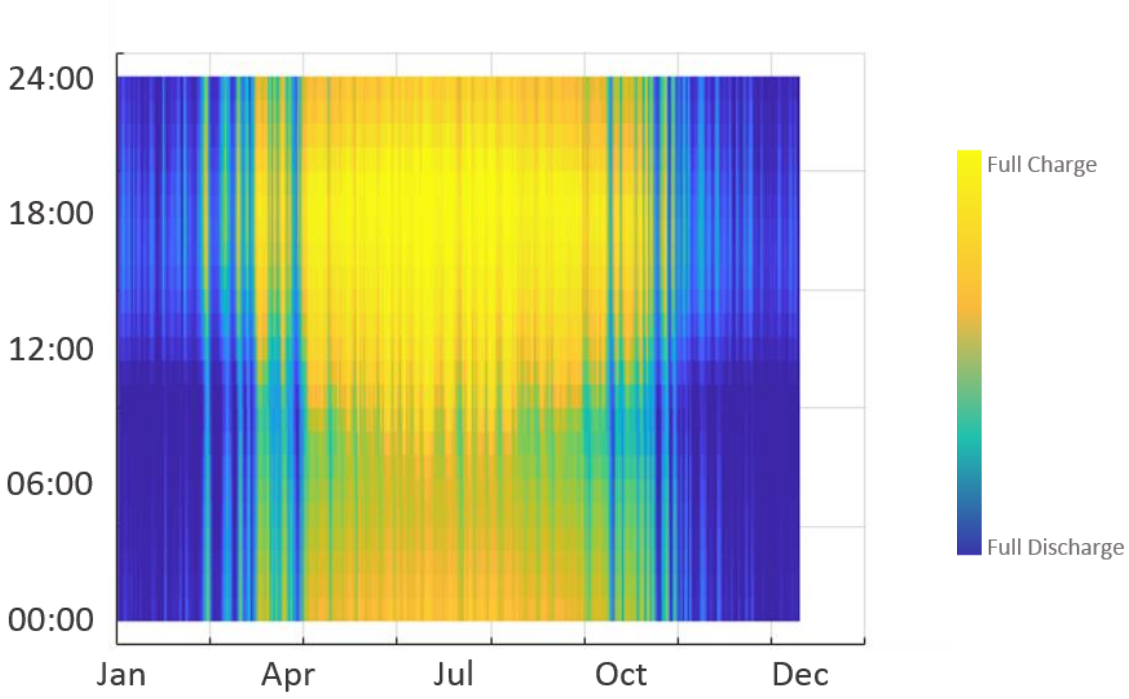

Figure 7.11 – Ebbw Vale model energy storage heatmap.

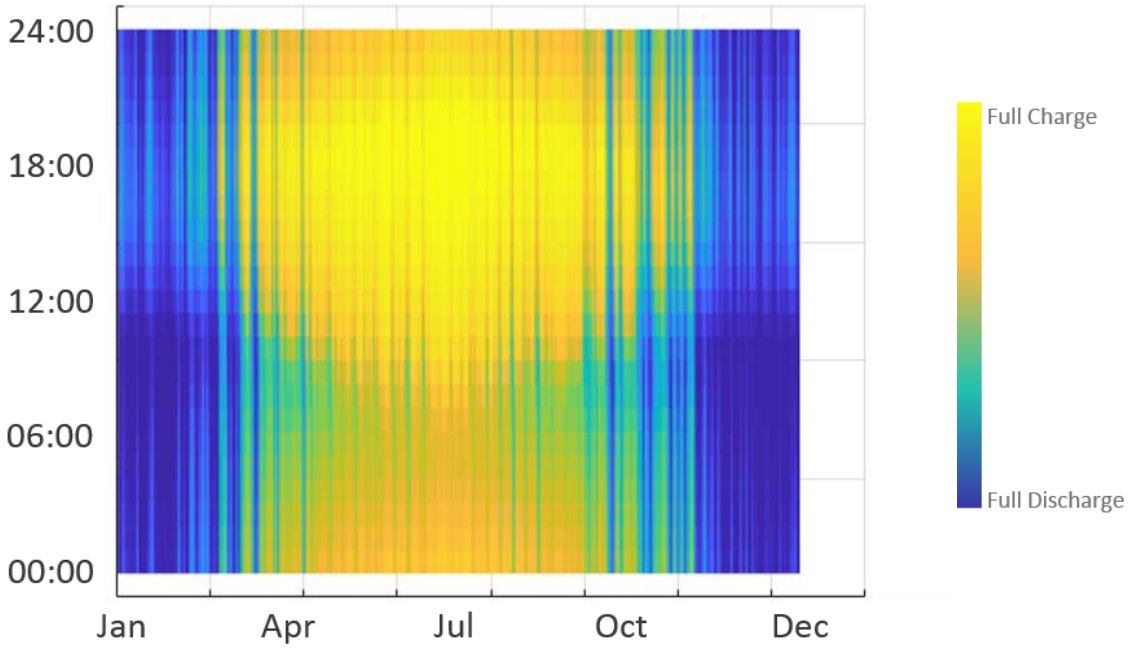

Figure7.12 – Plymouth model energy storage heatmap.

Aside from a limited number of obvious discrepancies, each storage heat map shows the same general trend throughout the year. The major impact on domestic energy demand observed for location scenarios is the consumption of gas due to temperature variation (see section 5.6). As in this case energy storage is only inclusive of electricity demand, there is no effect on the performance of energy storage.

Some variation is discernible upon closer inspection, this is due to the discrepancy between solar incidence at the two locations. The Ebbw vale heat map contains a greater number of gaps in energy storage, while the heat map for Plymouth demonstrates the filling of gaps originally observed in the baseline model. To better understand the impact of storage under these scenarios, table 7.6 gives a comparison of energy consumption with and without storage.

Table 7.6 – Location: Combined grid energy consumptions with consideration for battery energy storage, for the location category.

Scenario	Baseline	Ebbw Vale	Plymouth
Consumption without Storage	7314	8814	5758
Consumption with Storage	6011	7512	4385
Reduction	18%	15%	24%

Variation in the combined grid energy demand is brought about for location scenarios due to a combination of effects; both temperature and solar incidence at each of the locations. The higher demand is attributed to Ebbw Vale, while Plymouth has a reduced overall demand. The data in table 7.6 shows that storage using the battery would benefit Plymouth over Ebbw Vale, despite having a reduced demand. This suggests that increased surplus energy from solar is being taken advantage of at the southern location.

Figures 7.13 and 7.14 show the daily averaged annual energy storage profiles for each location to analyse variation between the storage methods themselves.

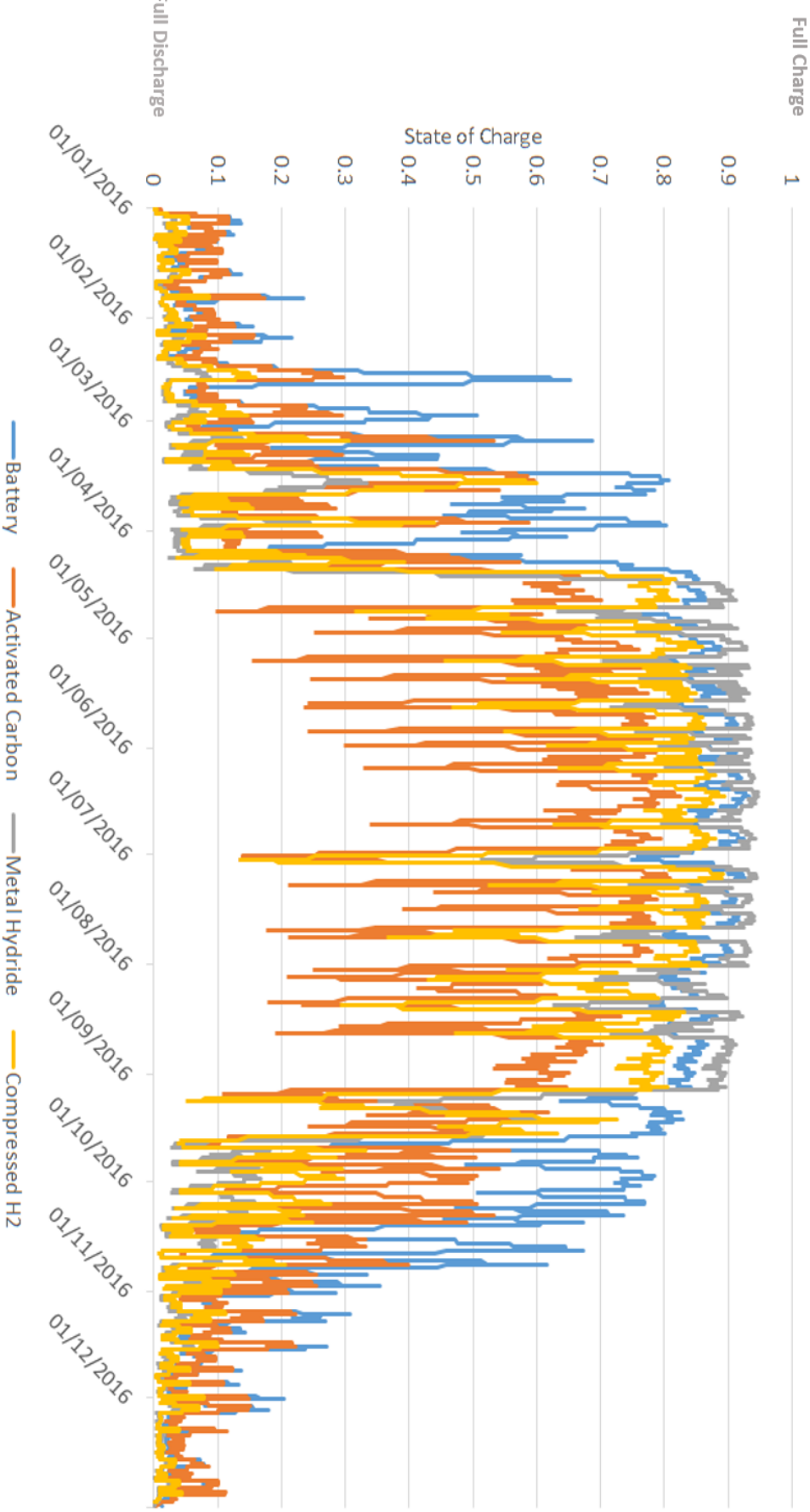

Figure 7.13 – Location: Annual energy storage profiles for each storage method at Ebbw Vale.

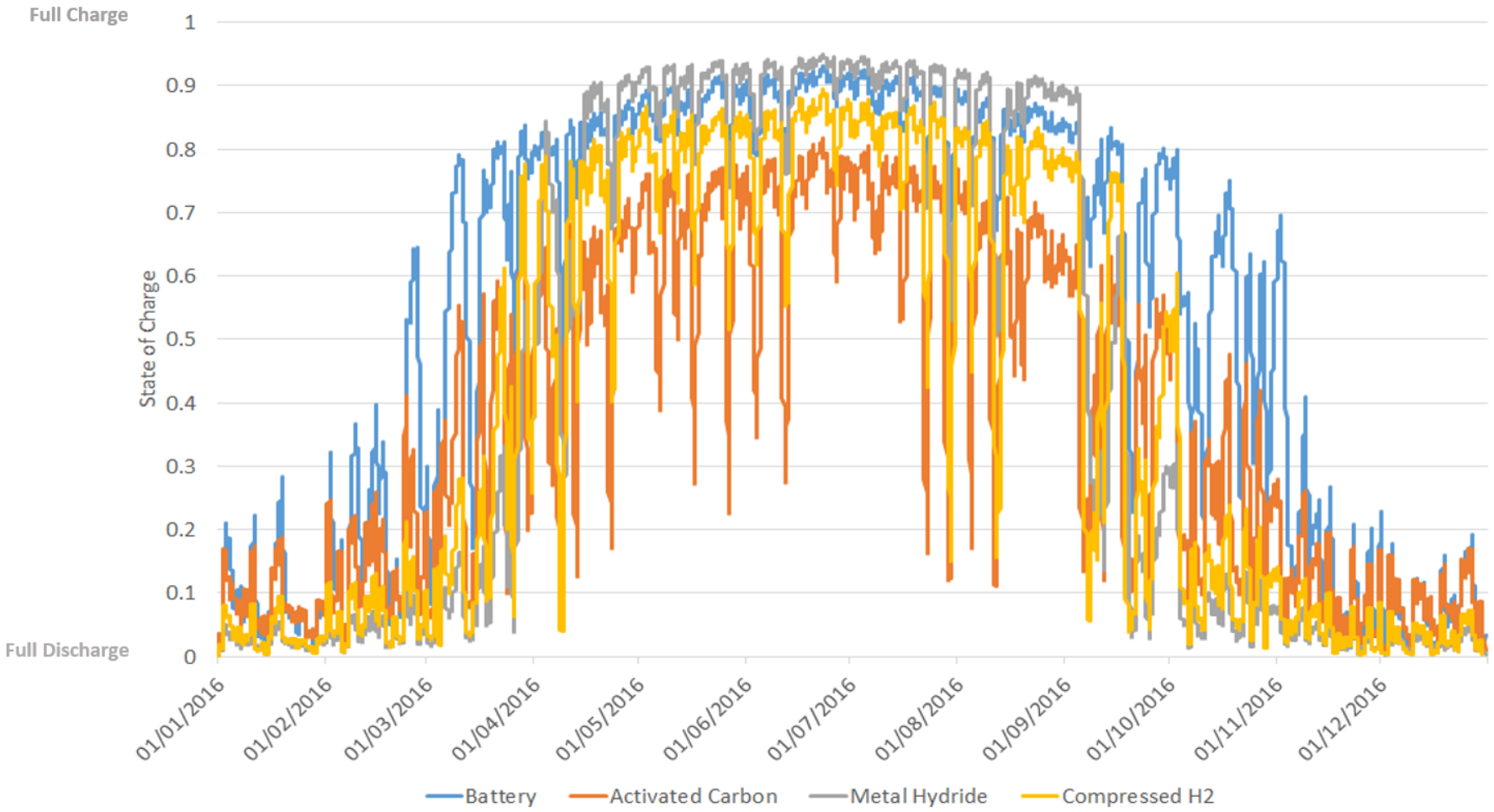

Figure 7.14 – Location: Annual energy storage profiles for each storage method at Plymouth.

Data from both figures 7.13 and 7.14 demonstrate similar trends in the build-up and departure from the storage plateau as observed in figures 7.8 and 7.9. The plateau itself offers this same similarity, in that metal hydride storage maintains a higher charge throughout the charging period, followed by the battery and compressed hydrogen methods, and finally activated carbon. The key difference is observed for the Ebbw Vale scenario, where a reduced solar incidence causes increased delays to the energy storage profile build-up. This is caused by a reduced ability to maintain and recharge storage levels. Because of this, the overall impact of energy storage at this location, despite the benefit observed for occupancy for the scenario with a higher demand, is lower than expected.

Conversely for the Plymouth location scenario, an increase in the overall rate of storage is observed. This means storage methods with fast charge or discharge become more responsive, and those with delayed charge or discharge are better maintained. In the case of the home battery, as indicated by the results in table 7.7, overall charging is delayed and overall discharging becomes faster. This takes the battery away from the ideal operation of fast charging and delayed discharging as discussed earlier.

To show exactly how the impact of location on rate of storage affects the overall domestic energy system, tables 7.7 and 7.8 now summarises combined grid energy storage for each location.

Table 7.7 – Location: Energy summary for household in Ebbw Vale.

Energy Storage Method	**Battery**	**Compressed H_2**	**Metal Hydride**	**Activated Carbon**
Combined Grid Demand [Without Storage]	8814 kWh			
Combined Grid Demand [With Storage]	7512 kWh	7853 kWh	8147 kWh	8462 kWh
Difference	15%	11%	8%	4%

Table 7.8 – Location: Energy summary for household in Plymouth.

Energy Storage Method	**Battery**	**Compressed H_2**	**Metal Hydride**	**Activated Carbon**
Combined Grid Demand [Without Storage]	5758 kWh			
Combined Grid Demand [With Storage]	4385 kWh	4742 kWh	4976 kWh	5297 kWh
Difference	24%	18%	14%	8%

The previous sensitivity category of occupancy revealed that while one scenario (two retired adults) gave considerable variation in the benefit of energy storage, the other (single working adult) did not. For the sensitivity category of location, both best and worst-case scenarios exhibit similar variance, with the battery outperforming the other storage methods in its capacity to reduce grid demand the most.

All methods of energy storage have greater benefit in the Plymouth location due to the increased solar incidence. Similar trends in both locations are observed given the occupancy profile for two working adults. It stands to reason from this comparison of results, that energy

storage has greater sensitivity to multiple occupancy over single occupancy, producing greater variation to the benefits of using energy storage.

For the location sensitivity category, profiles at either location have demonstrated similarity in sensitivity for all storage methods. The battery offers the greatest reduction in grid demand, followed by compressed hydrogen and metal hydride storage, and finally activated carbon. The greater tendency towards autonomy, particularly with the battery, for southern locations is due to the improved response of energy storage to surplus energy, given that greater quantities of energy are available for initial storage, and subsequent maintenance of the state of charge. Essentially, the charging rates for storage at southerly locations is increased, while the discharging rates are prolonged.

7.4 Future Climate

The future climate profile of 2080 demonstrated the greatest benefit for energy consumption and energy storage, given a slight increase to the overall photovoltaic output and higher annual temperatures. This had a combined impact on both gas and electricity consumption. Figures 7.15 and 7.16 compare the energy storage heat maps for the baseline model and 2080 future climate model.

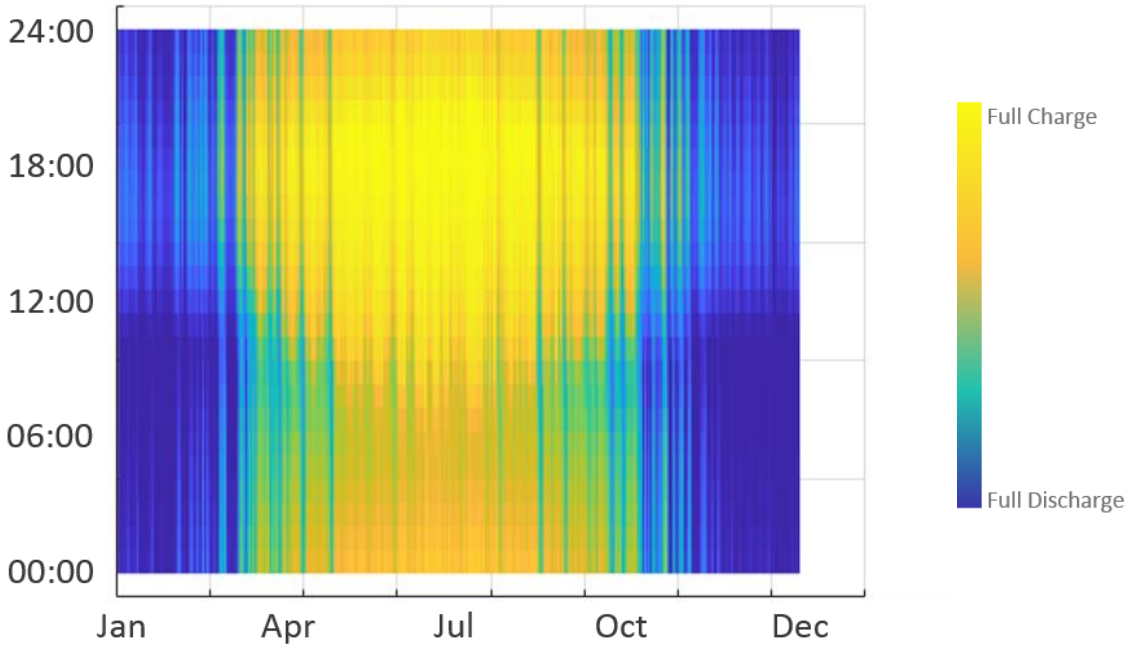

Figure 7.15 – Baseline model energy storage heatmap.

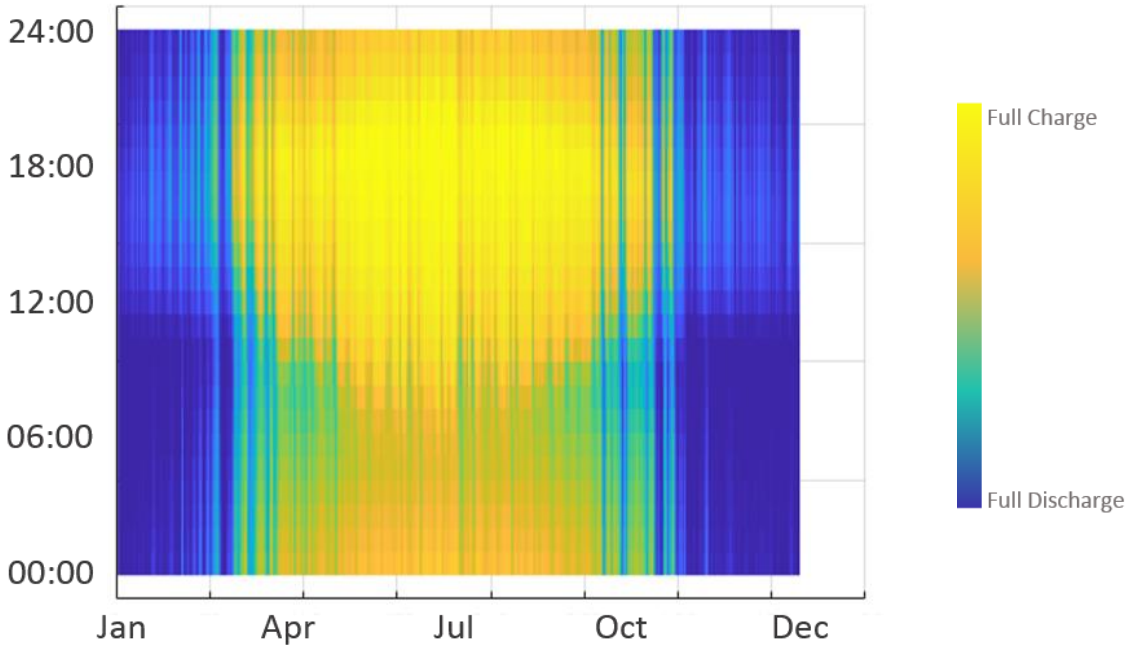

Figure 7.16 – 2080 future scenario model energy storage heatmap.

As with the heat maps shown for the location category, the data represented by figure 7.16 shares considerable similarity with the baseline model. Temperature variation is a common factor, which impacts only on gas consumption, and so limitations on the impact of climate change on storage performance exist. Similar to the location category, a secondary impact factor of increased solar incidence occurs. This causes an increase in the overall energy storage, reducing the number of gaps in figure 7.16, though close inspection of the figure is required to observe this impact. Table 7.9 gives the comparison of baseline to 2080 models' consumption with and without storage.

Table 7.9 – Future Climate: Combined grid energy consumptions with consideration for battery energy storage, for the future climate category.

Scenario	Baseline	2080
Consumption without Storage	7314 kWh	4867 kWh
Consumption with Storage	6011 kWh	3585 kWh
Reduction	18%	26%

The data suggests that energy storage has a much larger impact with future climates, given the observed changes to solar and temperature. Since temperature varies much more than solar radiation in those future climate profiles, temperature can be considered as having the main impact on reducing combined grid demand. While tending to move the energy system towards autonomy, the projected effect of future climates on the performance of energy storage integration should be deemed similar to the baseline model. Because of this, expectations of variation in the behaviour of energy storage methods are realised as being

synonymous to the conclusions drawn in the discussion surrounding table 7.3. For completeness, figure 7.17 displays the daily averaged annual energy storage profiles for each method, while the data in table 7.10 gives the energy summary for all storage methods.

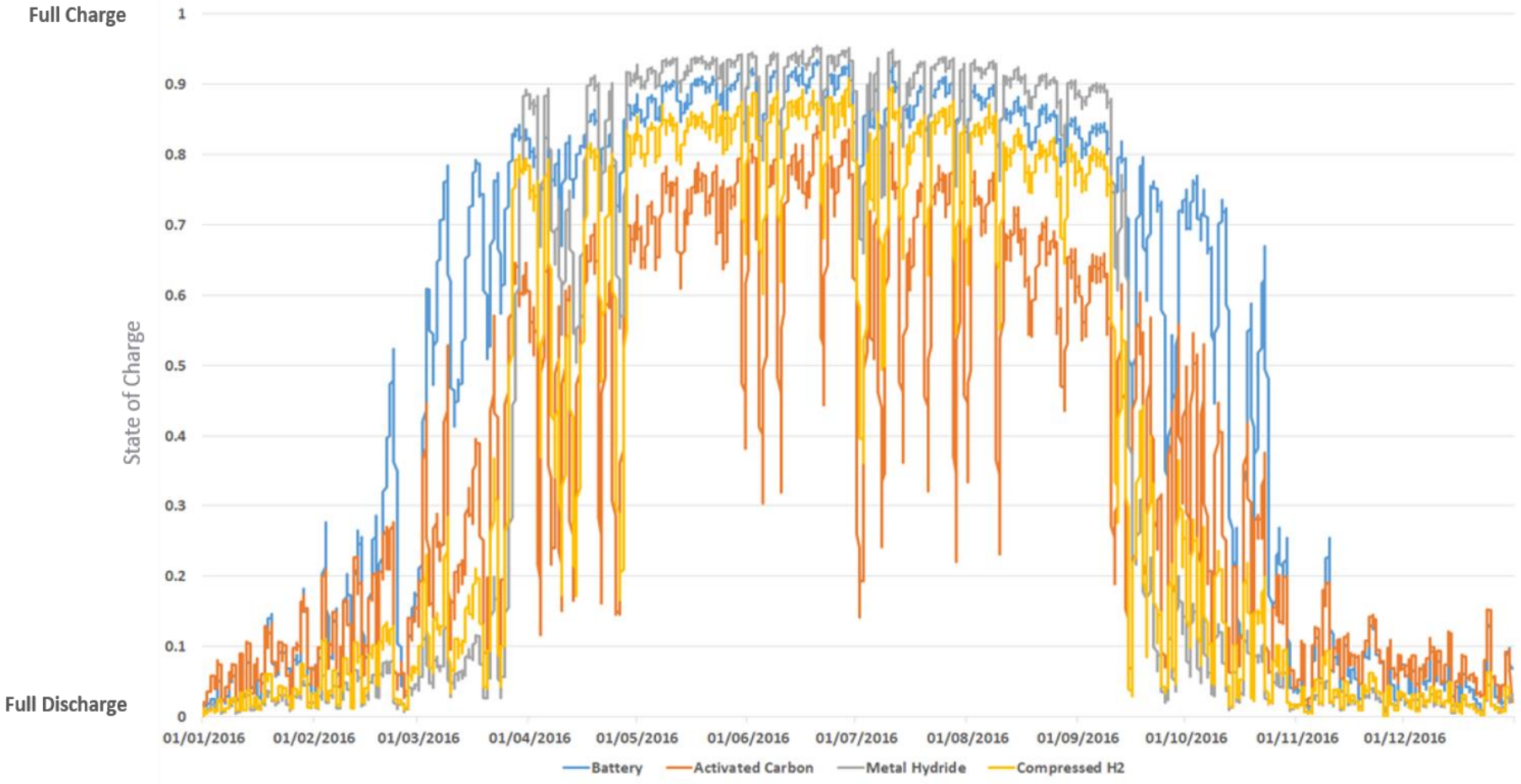

Figure 7.17 – Future Climates: Annual energy storage profiles for each storage method in 2080.

Table 7.10 – Future Climate: Energy summary for household in 2080.

Energy Storage Method	**Battery**	**Compressed H_2**	**Metal Hydride**	**Activated Carbon**
Combined Grid Demand [Without Storage]	4867 kWh			
Combined Grid Demand [With Storage]	3585 kWh	3914 kWh	4364 kWh	4472 kWh
Difference	26%	20%	10%	8%

The data shown in table 7.10 and the variation of that data shares a resemblance with the Plymouth location scenario data given in table 7.8. This says that similar results are achieved when temperature variation is a key factor, however these results are mostly reflective of the impact on gas consumption, and not on the performance of energy storage in itself. The slight deviation between the results of tables 7.8 and this table 7.10 is an indication of the variation caused by the change in solar incidence given this future climate profile. This shows an additional 2% reduction in the case of battery and compressed hydrogen, a 4% reduction in the case of metal hydride storage, and no change for activated carbon storage.

Results of the impact of future climates on energy storage have shown that for scenarios where temperature variation is a key factor, energy storage plays a minor role and does not offer any significant benefit over the baseline scenario. This sensitivity category, and that of location, would play an important role were electric heating considered as well. The impact of these combined categories is investigated later as the combined best-case scenarios are analysed, however the inclusion of electric heating with deep retrofit must first be considered.

7.5 Retrofit

Deep retrofit and the inclusion of electric heating resulted in a significant reduction to the overall energy consumption, as shown in chapter 5. The impact on consumption of energy for space heating is no longer limited to gas use, and so the performance of energy storage within the energy system can be considered to be of greater significance. This is contrary to the categories of location and future climate, where little improvement is observed given the core impact of those categories is on gas use alone. Figures 7.18 and 7.19 compare the energy storage heat maps for the baseline and retrofit models.

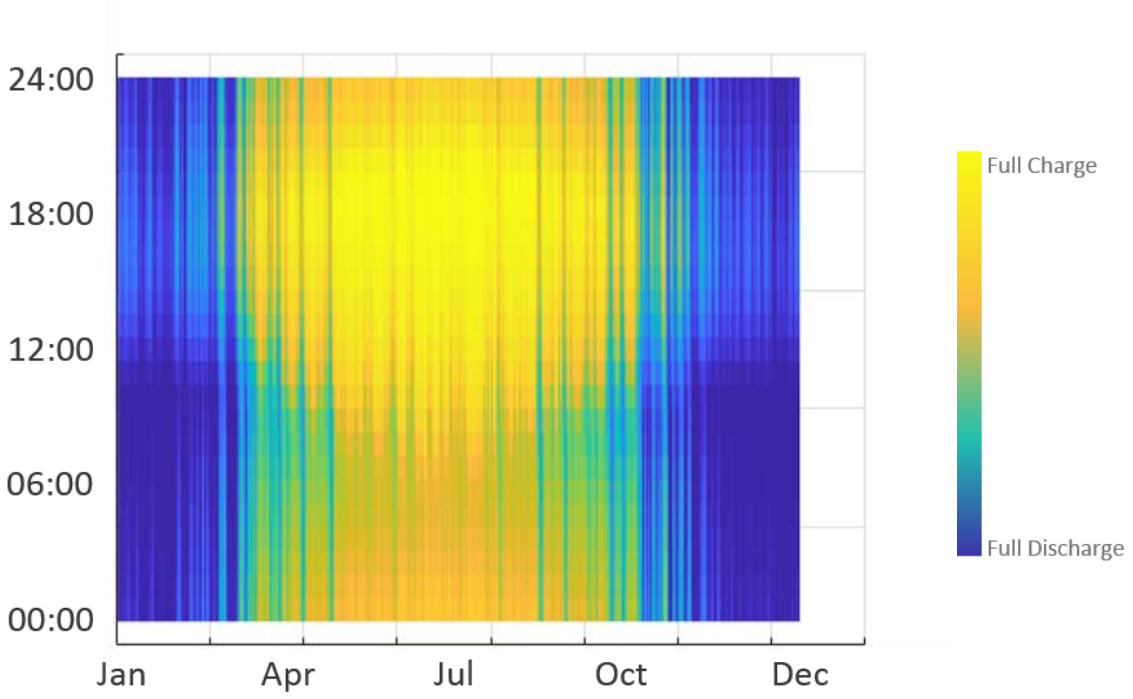

Figure 7.18 Basline model energy storage heatmap.

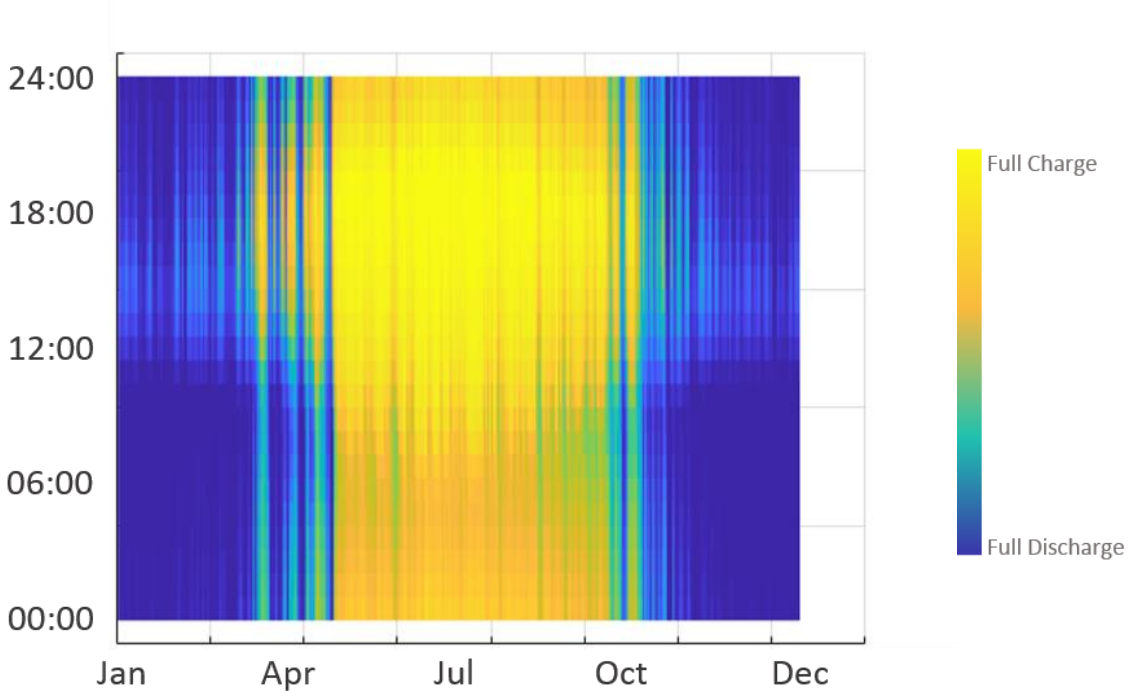

Figure 7.19 - Retrofit model energy storage heatmap.

The heat map shown in figure 7.19 shows considerable difference between the baseline and retrofit annual energy storage profiles. The key observation is that the retrofit model exhibits a much-reduced energy storage over the baseline model, particularly in the run-up to the summer storage season. As electric heating provides an additional load for the energy storage system to handle, it is not unexpected that this would cause a reduction in the overall storage. Table 7.11 gives a breakdown of the consumptions with and without storage between the two models.

Table 7.11 – Retrofit: Combined grid energy consumptions with consideration for battery energy storage, for the retrofit category.

Scenario	Baseline	Deep Retrofit, Electric Heating
Consumption without Storage	7314	3127
Consumption with Storage	6011	1089
Reduction	18%	50%

The data in table 7.11 reveals that deep retrofit has the largest impact on domestic energy storage, by providing a 50% reduction in the combined grid demand and thus taking the home half way to energy autonomy. This conclusion is simply due to the impact on an electric only domestic energy system. Figure 7.20 shows the variation in the performance of each storage method given this application of retrofit and electric heating.

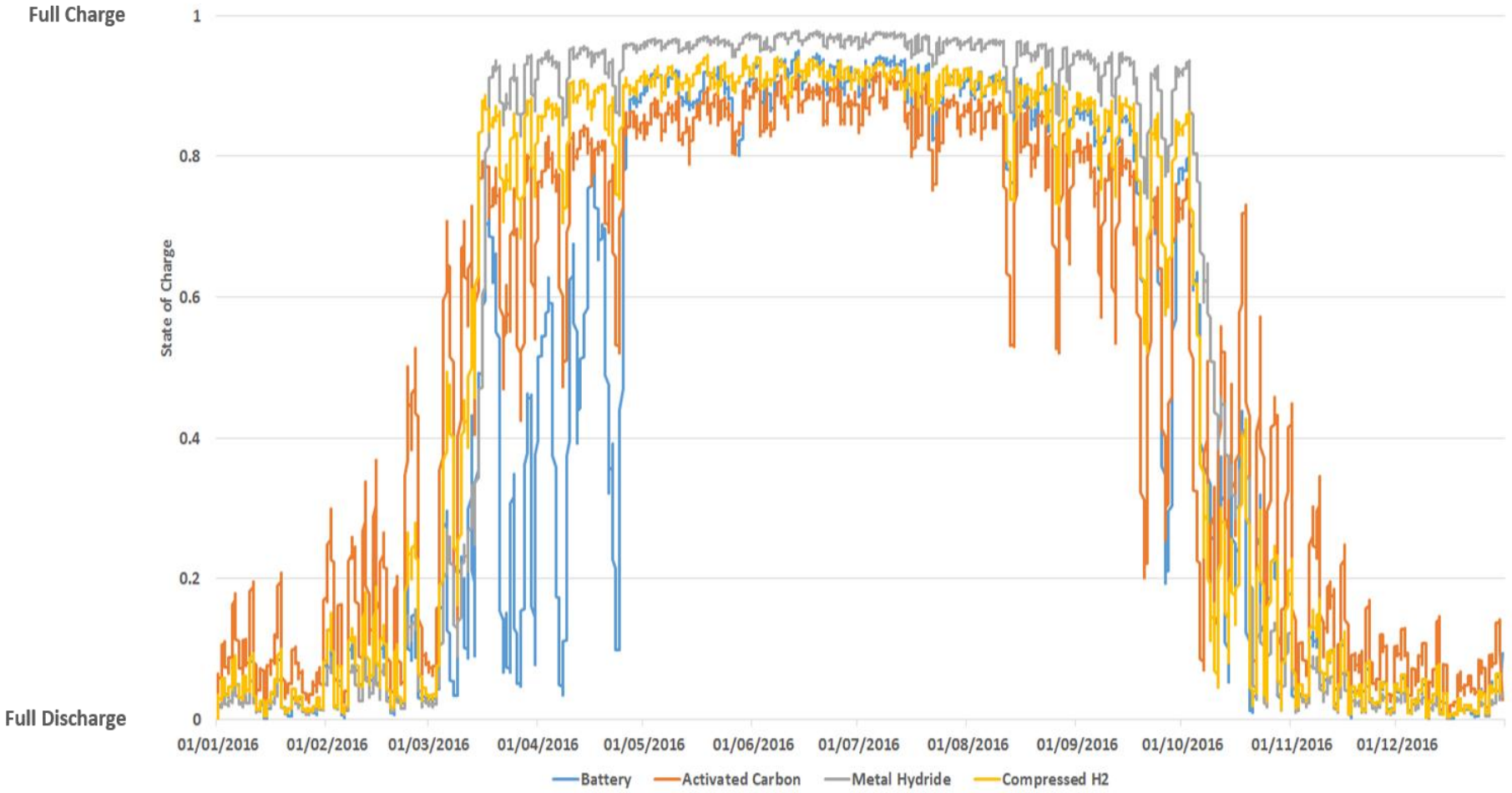

Figure 7.20 – Retrofit and electric heating: Annual energy storage profiles for each storage method using retrofit and electric heating.

The remaining methods of storage, compressed hydrogen, metal hydride and activated carbon, show a discrepancy in their annual energy storage profiles against that of battery storage. The delay in the build-up to the summer storage season as observed for the battery is not observed for any of the other methods of storage.

Throughout this period of discrepancy, the same demand for electricity is present. The additional storage seen at the start of the summer heating season has to be due to the response of hydrogen storage to the surplus energy generated, which provides a faster rate for the overall charging. Given this, the benefit of using hydrogen-based energy storage for homes with retrofit and electric heating would appear to be greater than when using the home battery. This is confirmed in the data provided in table 7.12.

Table 7.12 – Retrofit: Energy summary for households with retrofit and electric heating.

Energy Storage Method	**Battery**	**Compressed H_2**	**Metal Hydride**	**Activated Carbon**
Combined Grid Demand [Without Storage]	3127 kWh			
Combined Grid Demand [With Storage]	1089 kWh	314 kWh	408 kWh	508 kWh
Difference	50%	86%	81%	77%

Table 7.12 shows that hydrogen energy storage methods vastly outperform the battery in handling surplus energy outside of managing loads for electrical appliances and space heating. This reactivity, and given the fact that it is representative of the entire domestic load, puts hydrogen-based storage at the forefront of the search for energy autonomy. The most

prominent option in this case is the compressed hydrogen system, with metal hydride and activated carbon providing similar but lower reductions in the combined grid demand.

Within each sensitivity category, a different impact on the performance of energy storage has been observed. The next question to ask therefore, is how that impact changes with a combination of the best-case scenarios.

7.6 Best Cases

Figures 7.21 and 7.22 show the last heat map comparison for this chapter, for the baseline model and the best-case scenarios model.

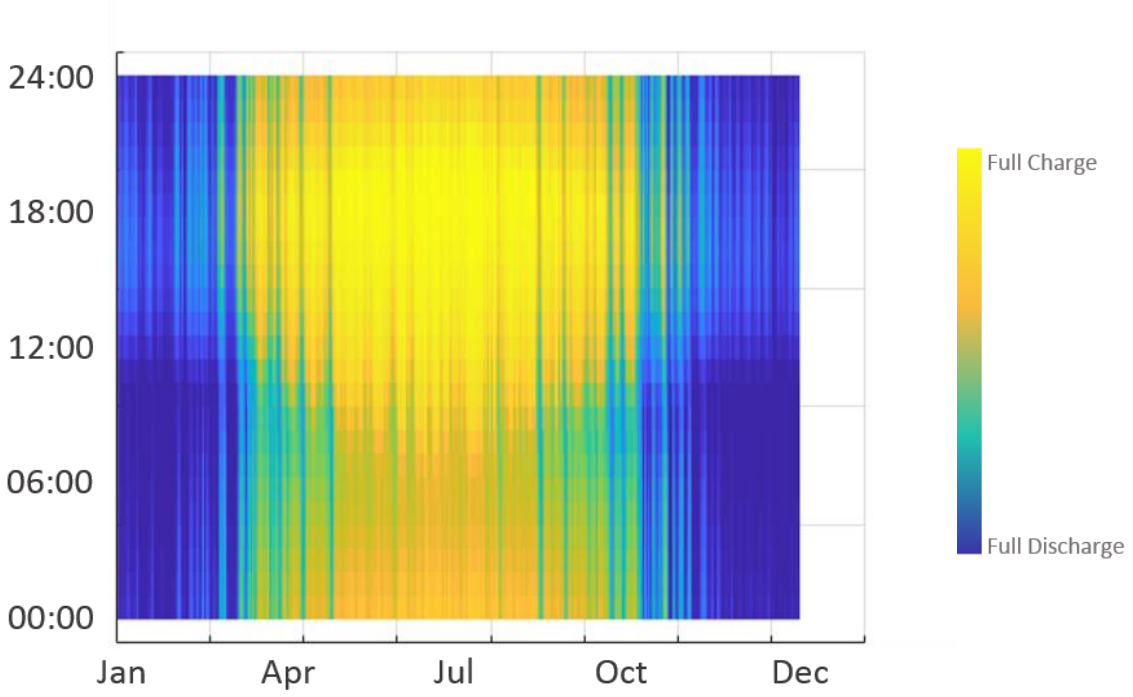

Figure 7.21 – Baseline model energy storage heatmap.

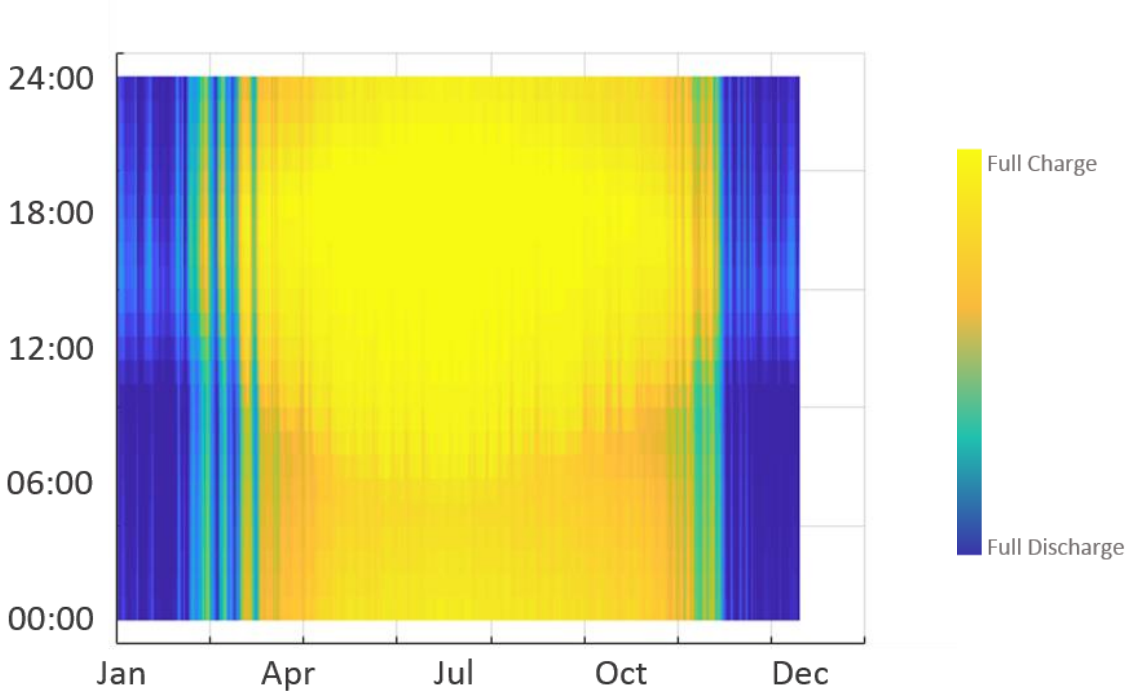

Figure 7.22 – Best cases model energy storage heatmap.

Figure 7.22 shows that with a combination of the best-case scenarios, energy storage receives the greatest impact. Not only is the summer storage season extended in comparison to the baseline's storage season, but the daily storage patterns exhibit considerably fewer gaps in storage. With this combination, only a small proportion of this heat map indicates little to no available stored energy.

Table 7.13 gives a final summary of energy storage performance for the combined best cases scenario. As a reminder, these scenarios are based on a mid-terrace archetype, single working adult occupancy, southern location of Plymouth, future climate scenario of 2080 and deep retrofit with electric heating.

Table 7.13 – Best Cases: Energy summary for households with a combination of best case scenarios.

Energy Storage Method	**Battery**	**Compressed H_2**	**Metal Hydride**	**Activated Carbon**
Combined Grid Demand [Without Storage]	1431 kWh			
Combined Grid Demand [With Storage]	242 kWh	30 kWh	28 kWh	53 kWh
Difference	83%	98%	98%	96%

The differences in combined grid consumption displayed in table 7.13 show that autonomy is almost achievable with the remaining demand in the range of tens of kWh in the case of hydrogen-based energy storage. When comparing the lowest figure of 28 kWh to the original baseline combined grid demand of 7314 kWh, a demand of just 0.4% remains. The prominence of the hydrogen-based energy storage methods is evident in these results, however the combination of best case sensitivity factors improves the battery's performance in approaching autonomy itself, with 3% of the baseline load remaining. Using a combination of these scenarios, autonomy appears relatively achievable.

These results reveal homes with energy storage are sensitive to different factors in various ways and that no one factor delivers enough of a benefit to favour full energy autonomy. Only a combination of energy saving measures and conditional favourability at their most extreme bring the home to the border of autonomy. This suggests that autonomy can only be predicted for a certain proportion of the UK's housing stock under these combined scenarios, and that further energy saving measures are required for the remaining stock if autonomy is to be sought. Figure 7.23 revisits those sensitivity ranges of chapter 5 depicting the range of

combined grid energy consumptions for each sensitivity category, and reveals how the application of energy storage changes those ranges.

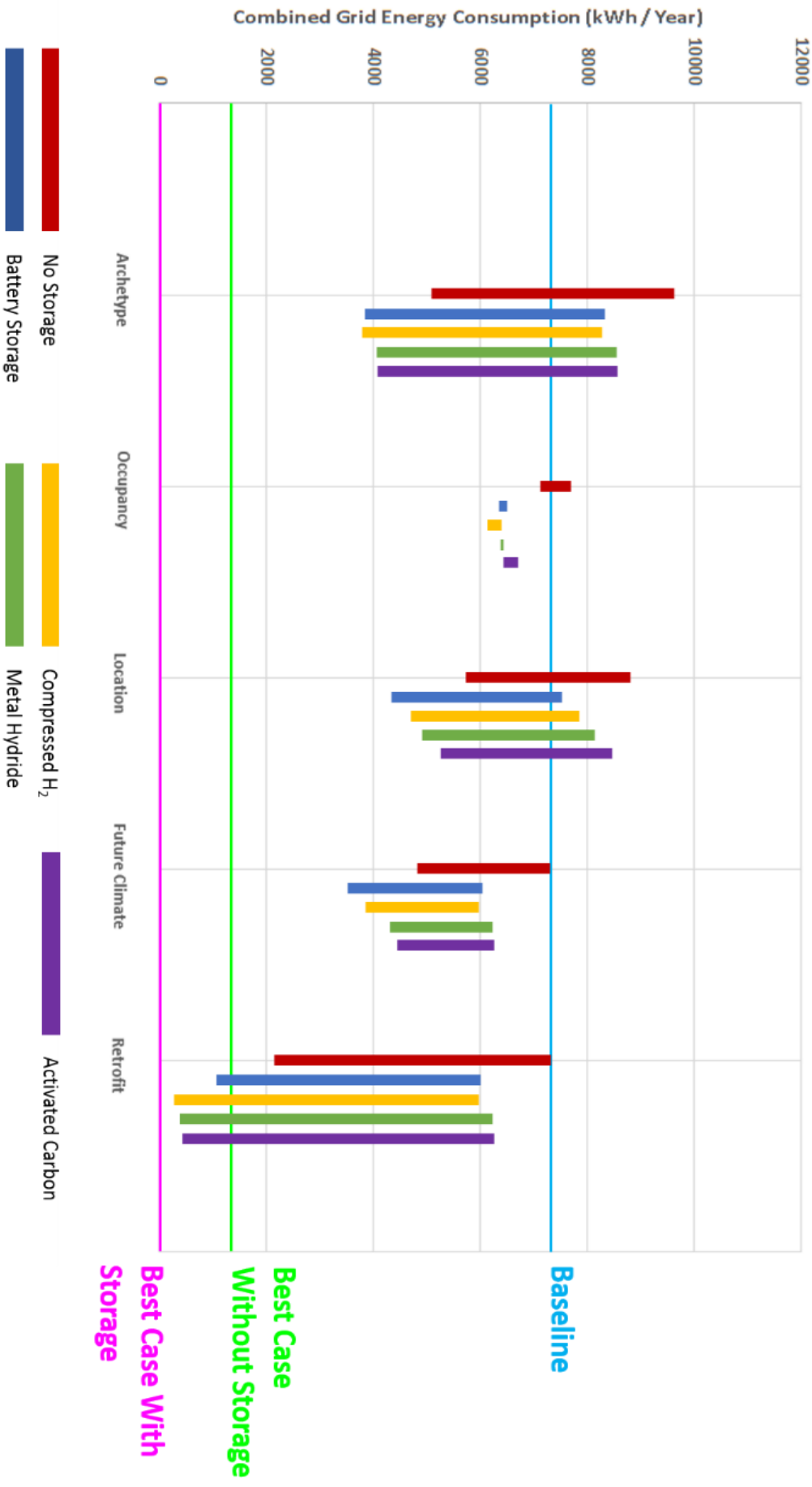

Figure 7.23 – Impact on combined grid energy consumption for each sensitivity category.

It is clear that the battery is dominant as the energy storage method that reduces the overall consumption range throughout each of the categories, with the exception of retrofit. As shown recently, the response of the hydrogen-based storage methods to surplus energy with the additional load of electric heating has reversed this trend, with the battery failing to reduce the best-case scenario for retrofit to a similar level of that using hydrogen-storage. Table 7.14 depicts the favourability of energy storage methods for each of the sensitivity factors, including a combination of best case scenarios, rated from 1 to 4 with 1 being the most favourable. This is to identify the most beneficial form of storage to use in each case, while reviewing a final combination of best case factors.

Table 7.14 – Depiction of the favourability of each method of storage for each of the sensitivity factors explored in modelling.

	Battery	Compressed Hydrogen	Metal Hydride	Activated Carbon
Baseline	**2**	**1**	**3**	**4**
Archetype	**2**	**1**	**3**	**4**
Occupancy	**3**	**1**	**2**	**4**
Location	**1**	**2**	**3**	**4**
Future Climate	**1**	**2**	**3**	**4**
Retrofit	**4**	**1**	**2**	**3**
Combined Best Cases	**4**	**2**	**1**	**3**

Table 7.14 reveals that compressed hydrogen is the most dominant and so the most beneficial method of energy storage for the majority of cases. The battery surpasses compressed hydrogen when differences in location and future climate profile are taken into consideration. When considering the impact of retrofit and electric heating on energy storage however, the battery becomes the least suitable solution, while activated carbon has shown throughout the majority of cases to be the least favourable of the hydrogen-based energy storage methods.

For the retrofit scenario and a final combination of all best-case scenarios, the battery's unsuitability was replaced with compressed hydrogen and metal hydrogen as the most suitable energy storage solutions for reducing overall grid energy demand. This reduction tends greatly towards energy autonomy, however limitations are imposed on the achievement of autonomy by this combination of scenarios.

The results given in this suggest that both the battery and compressed hydrogen energy storage methods share a similar platform as the most effective forms of storage. Only when additional complexity is introduced into the models, in the form of a combination of factors coupled with fully electric loads, do hydrogen-based storage methods benefit the domestic energy system. This demonstrates that traditional hydrogen storage methods over novel hydrogen storage methods are the best available option with regards to performance. Therefore, in some cases, with development, these technologies could prove to be useful.

As the results of modelling with integrated energy storage have been displayed and analysed, and the role of that storage understood in terms of impact on the domestic energy system under a variety of scenarios, all objectives of this research have been completed. A final conclusion and discussion can then be drawn to review these findings under the scope of the

aim of the thesis, on whether or not energy autonomy is achievable at this scale through the modelling of energy storage methods, and what limitations if any are imposed.

Chapter 8

Conclusion and Final Discussion

In response to the challenges facing the future of the UK's energy infrastructure, an alternative to the current centralised regime was proposed. The aim of this research was to investigate the feasibility of a decentralised domestic energy infrastructure in the UK, addressing energy consumption by one of the nation's larger sectors. The proposed alternative considered an application of photovoltaics with integrated energy storage systems, replacing the grid supply of main fuels with local generation, storage and consumption of energy, and thus reducing the national energy demand. By introducing local energy management, the concept of energy autonomy is proposed. Four emerging and novel technologies were considered for this study, the storage of energy using the home battery, and the storage of energy using hydrogen as an energy vector by means of storage using compression, metal hydride absorption and activated carbon adsorption. It was decided that the UK home should be modelled with the integration of these means of energy storage, under a range of scenarios befitting the UK.

The initial work identified the terrace house as the most populous in the UK. The Energy House at the University of Salford is a research facility that specialises in the energy performance of this building type. The end-terrace structure housed in a climate controlled chamber at this facility formed the basis for the modelling work carried out. Designbuilder was chosen as the software in which to undertake the modelling exercises, and as such a model of the Energy House facility was built from a measured specification.

The performance gap is a commonly reported phenomenon in the literature concerning the modelling and dynamic simulation of buildings (see Doran, 2001; Doran, 2008; Rye and Scott, 2010; Baker, 2011; and de Wilde, 2014). Discrepancies appear in this modelling work largely due to an assumption of parameters governing the determination of a building's energy consumption. The performance gap was quantified for the Energy House model as a discrepancy of 18.5% when compared to the true performance of the building (Marshall et al., 2017). A review of modelled building parameters revealed the source of this discrepancy in the predicted performance of building fabric and permeability. Building parameters – U-values and air permeability – were subsequently measured in-situ under controlled conditions, and used to replace the assumed values in the Energy House model. With the application of this calibration method, the performance gap was reduced to 2.5%.

A baseline model was conditioned to reflect realistic habitation of the building in its home city of Salford. Several of these conditions were then identified as having key influences on the overall energy demand of the home, these were building archetype, type of occupancy, building location, climate condition and level of retrofit. Variations to the baseline model under these categories were explored to investigate the sensitivity of each, and the subsequent impact on the domestic energy system with integrated storage.

A model for the home battery was used in Designbuilder to integrate energy storage into the home. Successive models for hydrogen storage using compression, metal hydrides and activated carbon were scripted using Matlab. These models encompassed the bulk storage of high pressure hydrogen in tanks and in activated carbon, and a finite element solution to the absorption of hydrogen in $LaNi_5$. Outputs from the best and worst-case scenarios from the

earlier modelling exercise were used to identify the overall impact of energy storage, and the effects of various sensitivity categories on this impact.

Simulations were conducted over a wide range of scenarios reflecting those typically found in the UK. The greatest impact on grid demand was seen in the cases where the building envelope underwent modification. Changes to the building's archetype and application of retrofit with electric heating produced a range of grid consumptions spanning 68% of the baseline consumption. Variation to the external weather conditions found at different locations and for future weather climates revealed less of an impact on grid energy consumption, with ranges spanning 37% of the baseline consumption. Occupancy variation was found to have the least impact on overall energy consumption, with a range of consumptions spanning just 12% of the baseline consumption.

This simulation exercise revealed that thermal performance of the home is a primary factor in overall energy consumption, and that for scenarios where improvements to that thermal performance were made, a tendency towards energy autonomy is observed. The maximum reduction of grid energy consumption was observed with the application of retrofit and electric heating; a predicted 70% reduction to grid energy consumption was found under this category. A final modelling exercise was conducted to combine all of the best-case scenarios under current conditions, these being a mid-terrace home, occupied by a single working adult, located in a southern location (Plymouth), with deep retrofit and electric heating. This gave a further reduction in the prediction of grid energy consumption to 86%.

Throughout the modelling work a common trend was identified, energy generated using photovoltaics was largely redirected to the grid due to a misalignment of supply and demand. In most cases a significant energy surplus was 'lost' compared to the residual domestic

demand. This supported the proposal of using energy storage in the home as a medium in closing the gap between residual grid demand and energy autonomy.

Further simulations revealed that scenarios exhibiting variations in external temperature (location and climate change) offered little to no impact on home energy systems with integrated storage. The home battery was found to be the most suitable in these cases, offering the greatest reduction in grid demand by 24 and 26% respectively. This suggests that few limitations, relating to location and climate change, exist in the application of domestic energy storage.

In all other cases, compressed hydrogen was shown to be the best candidate for energy storage, showing suitability in scenarios with a modified building envelope, and in particular where retrofit and electric heating was considered. A reduction of grid energy consumption of up to 86% was found in this case.

Throughout the previous modelling exercise, favourability, as determined in the best-cases of each sensitivity category, fell upon homes with high thermal performance, low occupancy density and lower latitudes. In combining these best cases for modelling with energy storage, this favourability was re-established. For the proportion of UK homes exhibiting these characteristics it has been found that domestic energy autonomy is feasible, with a reduction from the baseline model's overall grid energy consumption of 99.6%. Both compression and absorption of hydrogen in metal hydrides share preferentiality as the method of energy storage for domestic autonomy, given this combination of scenarios.

While energy autonomy has been shown to be achievable in the most extreme of cases, with a combination of preferential scenarios, the remaining housing stock would be exposed to residuals of energy demand. Key contributory factors to energy inefficiency were the

penalties from gas compression, material heating and cooling, and the conversion between AC and DC electricity; all of these factors were included within the modelling of this study, and require attention in future work. Additional measures are recommended to mitigate these factors, such as increased storage capacity, improvements to storage methods, further improvements to the home's energy efficiency, distribution of energy using the existing infrastructure, and the use of homes as a national 'storage network' for existing and planned renewable sources such as vehicle to grid/home programs. These measures could be used to facilitate supplementary energy in the home and are all recommended as the subjects for further study.

For domestic energy autonomy to be realised in the UK, considerable work is required to improve the energy efficiency of the current housing stock. Despite this, the work conducted has realised the importance of energy storage in the future of the UK's energy regime and that maintaining the drive towards energy efficient homes is crucial in realising decentralised energy as a solution to the challenges faced in the future of the UK's energy infrastructure.

Problems inherent in building energy modelling, stemming from the performance gap, have been a key feature of this work. In tackling the issue, a need to review current modelling tools has been highlighted, and the benefit of modelling and storage communities working closer on the issue of energy storage has been identified. The combination of building energy and energy storage modelling carried out in this work actively demonstrates the importance of accurate modelling software that could provide a platform to incorporate, adapt and build upon future integrated energy storage design.

Chapter 9

References

Ahern, C., Norton, B., & Enright, B. (2016). The Statistical Relevance and Effect of Assuming Pessimistic Default Overall Thermal Transmittance Coefficients on Dwelling Energy Performance Certification Quality in Ireland. Energy and Buildings, 268-278.

Alder, B.J., Young, D.A. and Mark, M.A., 1972. Studies in molecular dynamics. X. Corrections to the augmented van der Waals theory for the square well fluid. The Journal of Chemical Physics, 56(6), pp. 3013-3029.

Anderson, R.B., 1946. Modifications of the Brunauer, Emmett, and Teller equation. J. Am. Chem. Soc. (United States), 68.

Aranovich, G.L., 1988. Correction of the Multimolecular Adsorption Isotherm. Zhurnal Fizideskoi Khimii, 62, pp.3000-3008.

Aranovich, G.L., 1989. Thermodynamic Analysis of the Structure of Polymolecular Adsorption Layers in Multicomponent. Zhurnal Fizicheskoi Khimii, 63(6), pp.1527-1534.

Aranovich, G.L., 1990. Determination of Adsorption Heat under Extremely Low Filling on Adsorption-Isotherm. Zhurnal Fizicheskoi Khimii, 64(1), pp.161-165.

Aranovich, G.L., 1992. The theory of polymolecular adsorption. Langmuir, 8(2), pp.736-739.

ASHRAE, 2014. Standard 140-2014: Standard Method of Test for the Evaluation of Building Energy Analysis Computer Programs (ANSI Approved), the American Society of Heating, Refrigerating and Air Conditioning Engineers.

Askri, F., Jemni, A. and Nasrallah, S.B., 2003. Study of two-dimensional and dynamic heat and mass transfer in a metal–hydrogen reactor. International Journal of Hydrogen Energy, 28(5), pp.537-557.

Askri, F., Jemni, A. and Nasrallah, S.B., 2004. Prediction of transient heat and mass transfer in a closed metal–hydrogen reactor. International Journal of Hydrogen Energy, 29(2), pp.195-208.

Askri, F., Salah, M.B., Jemni, A. and Nasrallah, S.B., 2009. Optimization of hydrogen storage in metal-hydride tanks. International journal of hydrogen Energy, 34(2), pp.897-905.

ATTMA (2010) ATTMA Technical Standard L1. Measuring the Air Permeability of Building Envelopes (Dwellings). October 2010 Issue. Northampton, UK, Air Tightness Testing and Measurement Association.

Baker, P. (2011). U-values and Traditional Buildings. Glasgow: Historic Scotland Conservation Group.

Beattie, J.A. and Bridgeman, O.C., 1928, December. A new equation of state for fluids. In Proceedings of the American Academy of Arts and Sciences (Vol. 63, No. 5, pp. 229-308). American Academy of Arts & Sciences.

BEIS, 2017. Energy Consumption in the UK. Department for Business, Energy and Industrial Strategy. Crown, London.

Bender, E., 1971. Zur Aufstellung von Zustandsgleichungen, aus denen sich die Sättigungsgrößen exakt berechnen lassen—gezeigt am Beispiel des Methans. Kältetechnik, 23, p. 258.

Benedict, M., Webb, G.B. and Rubin, L.C., 1940. An empirical equation for thermodynamic properties of light hydrocarbons and their mixtures I. Methane, ethane, propane and n-butane. The Journal of Chemical Physics, 8(4), pp. 334-345.

Boser, O., 1976. Hydrogen sorption in LaNi5. *Journal of the Less Common Metals*, *46*(1), pp.91-99.

Boublík, T., 2005. Geometrical characteristics of the enlarged fused hard sphere models of simple molecules. The Journal of Physical Chemistry B, 109(41), pp. 19437-19442.

Boublik, T., 1975. Two-dimensional convex particle liquid. Molecular Physics, 29(2), pp. 421-428.

Box, G.E. and Draper, N.R., 1987. *Empirical model-building and response surfaces* (Vol. 424). New York: Wiley.

BP, 2016. Statistical Review of World Energy, bp.com/statisticalreview, accessed 14th December 2016.

BRE, 2008. A Study of Hard to Treat Homes Using the English House Condition Survey. Defra and Energy Saving Trust, London.

BRE, 2016. Conventions on U-value Calculations. BRE.

BRE, 2016. Standard Assessment Procedure, Building Research Establishment.

Brown, P., Swan, W. and Chahal, S., 2014. Retrofitting social housing: reflections by tenants on adopting and living with retrofit technology. *Energy Efficiency*, *7*(4), pp.641-653.

Brunauer, S., Emmett, P.H. and Teller, E., 1938. Adsorption of gases in multimolecular layers. *Journal of the American chemical society*, *60*(2), pp.309-319.

Bunn, R. and Burman, E., 2015, April. S-curves to model and visualise the energy performance gap between design and reality–first steps to a practical tool. Chartered Institution of Building Services Engineers (CIBSE).

CEN, 2007. EN 15265 Energy Performance of Buildings – Calculation of Energy Needs for Space Heating and Cooling using Dynamic Methods. European Committee for Standardization.

Chahal, S., Swan, W. and Brown, P., 2012, January. Tenant perceptions and experiences of retrofit. In *Proceedings of Retrofit 2012 Conference. University of Salford, Salford* (pp. 24-26).

Chen, H., Chou, P., Duri, S., Lei, H. and Reason, J., 2009, October. The design and implementation of a smart building control system. In *e-Business Engineering, 2009. ICEBE'09. IEEE International Conference on* (pp. 255-262). IEEE.

Chen, S.S. and Kreglewski, A., 1977. Applications of the Augmented van der Waals Theory of Fluids.: I. Pure Fluids.*Berichte der Bunsengesellschaft für physikalische Chemie*,*81*(10), pp.1048-1052.

Cho, J.H., Yu, S.S., Kim, M.Y., Kang, S.G., Lee, Y.D., Ahn, K.Y. and Ji, H.J., 2013. Dynamic modeling and simulation of hydrogen supply capacity from a metal hydride tank. *International journal of hydrogen energy*, *38*(21), pp.8813-8828.

Chong, A., Lam, K.P., Pozzi, M. and Yang, J., 2017. Bayesian calibration of building energy models with large datasets. *Energy and Buildings*, *154*, pp.343-355.

Chou, K.C., Li, Q., Lin, Q., Jiang, L.J. and Xu, K.D., 2005. Kinetics of absorption and desorption of hydrogen in alloy powder. *International Journal of Hydrogen Energy*, *30*(3), pp.301-309.

CIBSE, 2006. Guide A: Environmental Design. London, The Chartered Institute of Building Service Engineers.

CIBSE, 2000. Testing buildings for air leakage: CIBSE Technical Memoranda TM23: 2000. London, The Chartered Institute of Building Services Engineers.

Cibulka, I., Kováčiková, J., Hnědkovský, L. and Novák, J.P., 2001. A simple method for evaluation of parameters of the Bender equation of state from experimental data. Fluid Phase Equilibria, 1(180), pp. 27-40.

Coakley, D., Raftery, P. and Keane, M., 2014. A review of methods to match building energy simulation models to measured data. *Renewable and sustainable energy reviews*,*37*, pp.123-141.

Crawley DB, Pedersen CO, Lawrie LK, Winkelmann FC. EnergyPlus: Energy Simulation Program. ASHRAE Journal 2000; 42: 49–56

Crawley, D.B., Lawrie, L.K., Pedersen, C.O., Winkelmann, F.C., Witte, M.J., Strand, R.K., Liesen, R.J., Buhl, W.F., Huang, Y.J., Henninger, R.H. and Glazer, J., 2004. EnergyPlus: an update. *IBPSA-USA Journal*, *1*(1).

Crawley, D.B., Hand, J.W., Kummert, M. and Griffith, B.T., 2008. Contrasting the capabilities of building energy performance simulation programs. *Building and environment*,*43*(4), pp.661-673.

De Wilde, P., 2014. The gap between predicted and measured energy performance of buildings: A framework for investigation. *Automation in Construction*, *41*, pp.40-49.

DECC, 2010a. Annual Energy Statement. London: HM Government.

DECC, 2011. The Carbon Plan: Delivering our Low Carbon Future. London: HM Government.

DECC, 2012. Smart Metering Implementation Programme. First Annual Progress Report on the Roll-out of Smart Meters. London: HM Government.

Do, D.D., 1998. Adsorption Analysis: Equilibria and Kinetics: (With CD Containing Computer Matlab Programs) (Vol. 2). World Scientific.

Doran, S., 2001. DETR Framework Project Report: Field investigations of the thermal performance of construction elements as built,

Doran S and Carr B (2008) Thermal Transmittance of Walls of Dwellings Before and After Application of Cavity Wall Insulation. A Report Prepared by BRE Scotland for the Energy Saving Trust, Report Number 222077, East Kilbride, UK, BRE Scotland.

Dornheim, M., 2011. Thermodynamics of metal hydrides: tailoring reaction enthalpies of hydrogen storage materials. In *Thermodynamics-Interaction Studies-Solids, Liquids and Gases*. InTech.

van Dronkelaar, C., Dowson, M., Spataru, C. and Mumovic, D., 2016. A review of the regulatory energy performance gap and its underlying causes in non-domestic buildings. *Frontiers in Mechanical Engineering*, *1*, p.17.

Dubinin, M.M., 1975. Progress in Surface and Membrane, vol. 9. Academic, New York.

Dubinin, M.M. and Radushkevich, L.V., 1947. Equation of the characteristic curve of activated charcoal. Chem. Zentr, 1(1), p.875.

Dubinin, M.M., Zaverina, E.D. and Radushkevich, L.V., 1947. Sorption and structure of active carbons. I. Adsorption of organic vapors. Zhurnal Fizicheskoi Khimii, 21(3), pp.151-162.

Eames, M., Kershaw, T. and Coley, D., 2011. On the creation of future probabilistic design weather years from UKCP09.*Building Services Engineering Research and Technology*,*32*(2), pp.127-142.

Elliott Jr, J.R., Suresh, S.J. and Donohue, M.D., 1990. A simple equation of state for non-spherical and associating molecules. Industrial & engineering chemistry research, 29(7), pp. 1476-1485.

Evangelisti, L., Guattari, C., Gori, P. and Vollaro, R.D.L., 2015. In situ thermal transmittance measurements for investigating differences between wall models and actual building performance. *Sustainability*, *7*(8), pp.10388-10398.

Facinelli, W.A., 1983. Modeling and simulation of lead-acid batteries for photovoltaic systems.

Farmer, D., Gorse, C., Swan, W., Fitton, R., Brooke-Peat, M., Miles-Shenton, D. and Johnston, D., 2017. Measuring thermal performance in steady-state conditions at each stage of a full fabric retrofit to a solid wall dwelling. *Energy and Buildings*.

Førde, T., Næss, E. and Yartys, V.A., 2009. Modelling and experimental results of heat transfer in a metal hydride store during hydrogen charge and discharge. *international journal of hydrogen energy*, *34*(12), pp.5121-5130.

Foxon, T. J., Hammond, G. P., Pearson, P. J. G., 2010. Developing transition pathways for a low carbon electricity system in the UK. Technological Forecasting & Social Change, 77, pp. 1203-1213.

Foxon, T.J., 2011. A coevolutionary framework for analysing a transition to a sustainable low carbon economy. *Ecological Economics*, *70*(12), pp.2258-2267.

Foxon, T. J., 2013. Transition pathways for a UK low carbon electricity future. Energy Policy, 52, pp. 10-24.

Foxon, T.J., Reed, M.S. and Stringer, L.C., 2009. Governing long-term social–ecological change: what can the adaptive management and transition management approaches learn from each other?. *Environmental Policy and Governance*,*19*(1), pp.3-20.

Foxon, T.J., Hammond, G.P. and Pearson, P.J., 2008, September. Transition pathways for a low carbon energy system in the UK: assessing the compatibility of large-scale and small-scale options. In *7th BIEE Academic Conference, St Johns College, Oxford, 24-25 September*.

Freni, A., Cipiti, F. and Cacciola, G., 2009. Finite element-based simulation of a metal hydride-based hydrogen storage tank. International Journal of Hydrogen Energy, 34(20), pp.8574-8582.

Freundlich, H., 1909. The theory of adsorption. Z. Chem. Ind. Kolloide, 3, pp.212-220.

Gershuny, J., Sullivan, O. (2017). *United Kingdom Time Use Survey, 2014-2015*. [data collection]. UK Data Service. SN: 8128, http://doi.org/10.5255/UKDA-SN-8128-1

Ghazouani, J., Chouaieb, O. and Bellagi, A., 2005. Evaluation of the parameters of the Bender equation of state for low acentric factor fluids and carbon dioxide. Thermochimica acta, 432(1), pp. 10-19.

Goetzberger, A., Stahl, W., Bopp, G., Heinzel, A. and Voss, K., 1994. The self-sufficient solar house Freiburg. *Advances in Solar Energy*, *9*.

Grießhaber, W. and Sick, F., 1991. Simulation of hydrogen-oxygen systems with PV for the self-sufficient solar house. FhG-ISE, Freiburg im Breisgau.

H2A Group, 2006. H2A Delivery Components Model Version 1.1: Users Guide.

Harvey, R., Abouatallah, R. and Cargnelli, J., 2016. Large-scale water electrolysis for power-to-gas. *PEM Electrolysis for Hydrogen Production: Principles and Applications*, p.303.

Henninger, R.H. and Witte, M.J., 2013. EnergyPlus testing with building thermal envelope and fabric load tests from ANSI. *ASHRAE standard*, *140*, p.2011.

Henninger, R.H., Witte, M.J. and Crawley, D.B., 2003, August. Experience testing EnergyPlus with the IEA HVAC BESTEST E100-E200 series. In *Proceedings of Building Simulation*.

Henry, W., 1803. Experiments on the quantity of gases absorbed by water, at different temperatures, and under different pressures. Philosophical Transactions of the Royal Society of London, 93, pp.29-276.

Heo, Y., Choudhary, R., & Augenbroe, G. A. (2012). Calibration of Building Energy Models for Retrofit Analysis under Uncertainty. Energy and Buildings, 550-560.

Hermosilla-Lara, G., Momen, G., Marty, P.H., Le Neindre, B. and Hassouni, K., 2007. Hydrogen storage by adsorption on activated carbon: investigation of the thermal effects during the charging process. International Journal of Hydrogen Energy, 32(10), pp.1542-1553.

Hollmuller, P., Joubert, J.M., Lachal, B. and Yvon, K., 2000. Evaluation of a 5 kW p photovoltaic hydrogen production and storage installation for a residential home in Switzerland. International Journal of Hydrogen Energy, 25(2), pp.97-109.

Hong, T. and Lin, H.W., 2013. *Occupant behavior: impact on energy use of private offices* (No. LBNL-6128E). Ernest Orlando Lawrence Berkeley National Laboratory, Berkeley, CA (US).

Honig, J.M. and Reyerson, L.H., 1952. Adsorption of nitrogen, oxygen and argon on rutile at low temperatures; applicability of the concept of surface heterogeneity. *The Journal of Physical Chemistry*, *56*(1), pp.140-144.

Hyman, E., 1986. Modeling and computerized characterization of lead-acid battery discharges. *BEST Facility Topical Report, RD*, pp.83-1.

ISO, 1994. ISO 9869: Thermal insulation – Building elements - In situ measurement of thermal resistance and thermal transmittance. Geneva, Switzerland, International Organization for Standardisation.

ISO, 2007. ISO 10456:2007. Building Materials and Products, Hygrothermal Properties, Tabulated Design Values and Procedures for Determining Declared and Design Thermal Values. Geneva, Switzerland: International Organization for Standardisation.

ISO, 2007. ISO 6946:2007. Building components and building elements – Thermal resistance and thermal transmittance – Calculation method. Geneva, Switzerland: International Organization for Standardisation.

ISO, 2008. ISO 13790: 2008. Energy Performance of Buildings - Calculation of Energy Use for Space Heating and Cooling. Geneva, Switzerland: International Organization for Standardization.

ISO, 2015. ISO 6781: Performance of buildings -- Detection of heat, air and moisture irregularities in buildings by infrared methods -- Part 3: Qualifications of equipment operators, data analysts and report writers. Geneva, Switzerland, International Organization for Standardisation.

Ji, Y., Fitton, R., Swan, W., & Webster, P. (2014). Assessing Overheating of the UK Existing Dwellings - A Case Study of Replica Victorian End Terrace House. Building and Environment, 1-11.

Johnston, D. Miles-Shenton, D. Farmer, D. and Wingfield, J. (2013) Whole House Heat Loss Test Method (Coheating). June 2013 [Internet] Leeds, Leeds Metropolitan University. Available from: <www.leedsbeckett.ac.uk/as/cebe/projects/cebe_coheating_test_method_june2013.pdf > [Accessed 22nd September 2016].

Jordá-Beneyto, M., Suárez-García, F., Lozano-Castelló, D., Cazorla-Amorós, D. and Linares-Solano, A., 2007. Hydrogen storage on chemically activated carbons and carbon nanomaterials at high pressures. *Carbon*, *45*(2), pp.293-303.

Karvonen, A., 2013. Towards systemic domestic retrofit: a social practices approach. *Building Research & Information*,*41*(5), pp.563-574.

Kennedy, D., 2007. New nuclear power generation in the UK: Cost benefit analysis. *Energy Policy*, *35*(7), pp.3701-3716.

Kennedy, M.C. and O'Hagan, A., 2001. Bayesian calibration of computer models. *Journal of the Royal Statistical Society: Series B (Statistical Methodology)*, *63*(3), pp.425-464.

Klein, S.A., Beckman, W.A., Mitchell, J.W., Duffie, J.A., Duffie, N.A., Freeman, T.L., Mitchell, J.C., Braun, J.E., Evans, B.L., Kummer, J.P. and Urban, R.E., 2004. TRNSYS 16–A TRaNsient system simulation program, user manual. *Solar Energy Laboratory. Madison: University of Wisconsin-Madison*.

Krajačić, G., Martins, R., Busuttil, A., Duić, N. and da Graça Carvalho, M., 2008. Hydrogen as an energy vector in the islands' energy supply. *International Journal of Hydrogen Energy*, *33*(4), pp.1091-1103.

Langmuir, I., 1918. The adsorption of gases on plane surfaces of glass, mica and platinum. *Journal of the American Chemical society*, *40*(9), pp.1361-1403.

Laurencelle, F. and Goyette, J., 2007. Simulation of heat transfer in a metal hydride reactor with aluminium foam. *International Journal of Hydrogen Energy*, *32*(14), pp.2957-2964.

Lemmon, E.W., Huber, M.L. and Leachman, J.W., 2008. Revised standardized equation for hydrogen gas densities for fuel consumption applications. *Journal of research of the National Institute of Standards and Technology*, *113*(6), p.341.

Li, Q., Augenbroe, G. and Brown, J., 2016. Assessment of linear emulators in lightweight Bayesian calibration of dynamic building energy models for parameter estimation and performance prediction. *Energy and Buildings*, *124*, pp.194-202.

Lototskyy, M.V., Yartys, V.A., Pollet, B.G. and Bowman, R.C., 2014. Metal hydride hydrogen compressors: a review. International journal of hydrogen energy, 39(11), pp.5818-5851.

Manfren, M., Aste, N., & Moshksar, R. (2013). Calibration and Uncertainty Analysis for Computer Models - A Meta-Model based Approach for Integrated Building Energy Simulation. Applied Energy, 627-641.

Manwell, J.F. and McGowan, J.G., 1991, September. A new battery storage model for wind/diesel systems. In*Proceedings of the AWEA Annual Conference, Palm Springs, CA*.

Manwell, J.F. and McGowan, J.G., 1993. Lead acid battery storage model for hybrid energy systems. *Solar Energy*,*50*(5), pp.399-405.

Manwell, J.F., McGowan, J.G., Baring-Gould, I. and Stein, W., 1995. *Recent progress in battery models for hybrid wind power systems* (No. CONF-950309--). American Wind Energy Association, Washington, DC (United States).

Marini, D., Buswell, R., and Hopfe, C. 2015a. A critical software review- how is hot water modelled in current building simulation? BS15, India.

Marini, D., Buswell, R., and Hopfe, C. 2015b. Estimating heat from domestic hot water systems in uk dwellings. BS15, India.

Marini, D., He, M., Buswell, R.A., Hopfe, C.J. and Crawley, D., 2016. Modelling and calibration of a domestic building using high-resolution monitoring data.

Marshall, A., Fitton, R., Swan, W., Farmer, D., Johnston, D., Benjaber, M. and Ji, Y., 2017. Domestic building fabric performance: Closing the gap between the in situ measured and modelled performance. *Energy and Buildings*.

Martani, C., Lee, D., Robinson, P., Britter, R. and Ratti, C., 2012. ENERNET: Studying the dynamic relationship between building occupancy and energy consumption. *Energy and Buildings*, *47*, pp.584-591.

Martin, M., Gommel, C., Borkhart, C. and Fromm, E., 1996. Absorption and desorption kinetics of hydrogen storage alloys. *Journal of Alloys and Compounds*, *238*(1-2), pp.193-201.

Momen, G., Hermosilla, G., Michau, A., Pons, M., Firdaouss, M. and Hassouni, K., 2009. Hydrogen storage in an activated carbon bed: effect of energ y release on storage capacity of the tank. *international journal of hydrogen energy*, *34*(9), pp.3799-3809.

Momen, G., Jafari, R. and Hassouni, K., 2010. On the effect of process temperature on the performance of activated carbon bed hydrogen storage tank. *International Journal of Thermal Sciences*, *49*(8), pp.1468-1476.

Müller, A., Winkelmann, J. and Fischer, J., 1996. Backone family of equations of state: 1. Nonpolar and polar pure fluids. AIChE Journal, 42(4), pp. 1116-1126.

Muthukumar, P., Satheesh, A., Linder, M., Mertz, R. and Groll, M., 2009. Studies on hydriding kinetics of some La-based metal hydride alloys. *International Journal of Hydrogen Energy*, *34*(17), pp.7253-7262.

Mylona, A., 2012. The use of UKCP09 to produce weather files for building simulation. *Building Services Engineering Research and Technology*, *33*(1), pp.51-62.

Nagy, B. and Simándi, B., 2008. Effects of particle size distribution, moisture content, and initial oil content on the supercritical fluid extraction of paprika. The Journal of Supercritical Fluids, 46(3), pp. 293-298.

NCM, 2008. National Calculation Methodology (NCM) modelling guide. Department for Communities and Local Government, 2008, London.

NIHE, 2009. Northern Ireland House Condition Survey 2009. Northern Ireland Housing Executive.

Nishizaki, T., Miyamoto, K. and Yoshida, K., 1983. Coefficients of performance of hydride heat pumps. *Journal of the Less Common Metals*, *89*(2), pp.559-566.

NIST Standard Reference Database 69: NIST Chemistry WebBook. webbook.NIST.gov/cgi/fluid.cgi" accessed September 2016.

Ofgem, 2015. Electricity security of supply: A commentary on National Grid's Future Energy Scenarios for the next three winters, Ofgem.

Ofgem 2016. Future Energy Insights. London: Ofgem, UK.

Ofgem 2017. Future Energy Insights. London: Ofgem, UK.

ONS, 2016. Housing: Social Trends. London: Office for National Statistics.

ONS, 2017. Housing Statistics for Scotland. Office for National Statistics.

Orecchini, F., 2006. The era of energy vectors. *International journal of hydrogen energy*, *31*(14), pp.1951-1954.

Pan, Y., Huang, Z. and Wu, G., 2007. Calibrated building energy simulation and its application in a high-rise commercial building in Shanghai. *Energy and Buildings*, *39*(6), pp.651-657.

Patil, N., Marshall, A., Fitton, R. and Waddington, D., 2017. COMBINED IMAGING TECHNOLOGIES FOR MEASURING THE IN-SITU THERMAL AND ACOUSTIC ENERGY EFFICIENCY OF RETROFIT BUILDING ELEMENTS.*WELCOME TO DELEGATES IRC 2017*, p.966.

Pedrazzi, S., Zini, G. and Tartarini, P., 2010. Complete modeling and software implementation of a virtual solar hydrogen hybrid system. *Energy Conversion and Management*, *51*(1), pp.122-129.

Pelsmakers, S., Croxford, B. and Elwell, C.A., 2017. Suspended timber ground floors: measured heat loss compared with models. *Building Research & Information*, pp.1-14.

Peng, D.Y. and Robinson, D.B., 1976. A new two-constant equation of state. Industrial & Engineering Chemistry Fundamentals, 15(1), pp. 59-64.

Polanyi, M., 1914. Adsorption from the point of view of the Third Law of Thermodynamics. Verh. Deut. Phys. Ges, 16, pp.1012-1016.

Raftery, P., Keane, M. and O'Donnell, J., 2011. Calibrating whole building energy models: An evidence-based methodology. *Energy and Buildings*, *43*(9), pp.2356-2364.

Rohani, G. and Nour, M., 2014. Techno-economical analysis of stand-alone hybrid renewable power system for Ras Musherib in United Arab Emirates. *Energy*, *64*, pp.828-841.

RIBA, 2013. Plan of Work 2013 overview. *London: Royal Institute of British Architects*.

Richard, M.A., Bénard, P. and Chahine, R., 2009. Gas adsorption process in activated carbon over a wide temperature range above the critical point. Part 1: modified Dubinin-Astakhov model. Adsorption, 15(1), pp.43-51.

Rodrigues, S., Faria, F., Ivaki, A.R., Cafôfo, N., Chen, X., Mata-Lima, H. and Morgado-Dias, F., 2016. Tesla powerwall: analysis of its use in Portugal and United States. *International Journal of Power and Energy Systems*, *36*(1), pp.37-43.

Roels, S., Bacher, P., Bauwens, G., Castaño, S., Jiménez, M.J. and Madsen, H., 2017. On site characterisation of the overall heat loss coefficient: Comparison of different assessment methods by a blind validation exercise on a round robin test box. *Energy and Buildings*, *153*, pp.179-189.

Rye, C., & Scott, C. (2010). The SPAB Research Report 1. U-value Report. Society for the Protection of Ancient Buildings.

SBEM, 2017. SBEM: Simplified Building Energy Model. BRE.

Schinder, P.J., Flasar, F.M., Marouf, E.A., French, R.G., McGhee, C.A., Kliore, A.J., Rappaport, N.J., Barbinis, E., Fleischman, D. and Anabtawi, A., 2011. The structure of Titan's atmosphere from Cassini radio occultations. Icarus, 215(2), pp. 460-474.

SDC. (2006). 'Stock Take': Delivering Improvements in Existing Housing. Sustainable Development Commission.

SEAI, 2012. Sustainable Energy Authority of Ireland, Irish Official Method for Calculating and Rating Energy Performance of Dwellings.

Shabani, B. and Andrews, J., 2011. An experimental investigation of a PEM fuel cell to supply both heat and power in a solar-hydrogen RAPS system. *International journal of hydrogen energy*, *36*(9), pp.5442-5452.

Shrestha, S.S. and Maxwell, D.G., 2011. *Empirical validation of building energy simulation software: EnergyPlus*. Oak Ridge National Laboratory (ORNL); Building Technologies Research and Integration Center.

Sing, K.S., 1985. Reporting physisorption data for gas/solid systems with special reference to the determination of surface area and porosity (Recommendations 1984). *Pure and applied chemistry*, *57*(4), pp.603-619.

Sips, R., 1950. On the structure of a catalyst surface. II. *The Journal of Chemical Physics*, *18*(8), pp.1024-1026.

Sovacool, B.K., 2006. *The power production paradox: Revealing the socio-technical impediments to distributed generation technologies* (Doctoral dissertation).

Stahl, W., Voss, K. and Goetzberger, A., 1994. The self-sufficient solar house in Freiburg. *Solar Energy*, *52*(1), pp.111-125.

Suganthi, L. and Samuel, A.A., 2012. Energy models for demand forecasting—A review. *Renewable and sustainable energy reviews*, *16*(2), pp.1223-1240.

Sun, J. and Reddy, T.A., 2006. Calibration of building energy simulation programs using the analytic optimization approach (RP-1051). *HVAC&R Research*, *12*(1), pp.177-196.

Swan, W., Ruddock, L., Smith, L. and Fitton, R., 2013. Adoption of sustainable retrofit in UK social housing. *Structural Survey*, *31*(3), pp.181-193.

Swan, W., Fitton, R., Gorse, C., Farmer, D. and Benjaber, M., 2017. The staged retrofit of a solid wall property under controlled conditions. *Energy and Buildings*, *156*, pp.250-257.

Tham, Y., Muneer, T., Levermore, G.J. and Chow, D., 2011. An examination of UKCIP02 and UKCP09 solar radiation data sets for the UK climate related to their use in building design. *Building Services Engineering Research and Technology*, *32*(3), pp.207-228.

Tian, W., Yang, S., Li, Z., Wei, S., Pan, W. and Liu, Y., 2016. Identifying informative energy data in Bayesian calibration of building energy models. *Energy and Buildings*, *119*, pp.363-376.

UK Government, 2008. Climate Change Act 2008. London: UK Parliament.

Ulleberg, Ø. and Mørner, S.O., 1997. TRNSYS simulation models for solar-hydrogen systems. Solar Energy, 59(4-6), pp.271-279.

Ustinov, E.A., Do, D.D., Herbst, A., Staudt, R. and Harting, P., 2002. Modeling of gas adsorption equilibrium over a wide range of pressure: A thermodynamic approach based on equation of state. Journal of colloid and interface science, 250(1), pp. 49-62.

Vale, B. and Vale, R.J.D., 2000. *The new autonomous house: Design and planning for sustainability*. Thames & Hudson.

Van der Waals, J.D., 1873. Over de Continuiteit van den Gas-en Vloeistoftoestand (Vol. 1). Sijthoff.

Voss, K., Goetzberger, A., Bopp, G., Häberle, A., Heinzel, A. and Lehmberg, H., 1996. The self-sufficient solar house in Freiburg—Results of 3 years of operation. Solar Energy, 58(1-3), pp. 17-23.

Wang, Y., Adroher, X.C., Chen, J., Yang, X.G. and Miller, T., 2009. Three-dimensional modeling of hydrogen sorption in metal hydride hydrogen storage beds. Journal of Power Sources, 194(2), pp.997-1006.

Warren, P., 2014. A review of demand-side management policy in the UK. *Renewable and Sustainable Energy Reviews*, *29*, pp.941-951.

WEC, 2016. World Energy Trilemma Index: Benchmarking the Sustainability of National Energy Systems. World Energy Council.

Wendland, M., Saleh, B. and Fischer, J., 2004. Accurate thermodynamic properties from the BACKONE equation for the processing of natural gas. Energy & fuels, 18(4), pp.938-951.

Witte, M.J., Henninger, R.H., Glazer, J. and Crawley, D.B., 2001. Testing and validation of a new building energy simulation program. *Proceedings of Building Simulation 2001*, pp.353-360.

Xiao, J., Tong, L., Deng, C., Bénard, P. and Chahine, R., 2010. Simulation of heat and mass transfer in activated carbon tank for hydrogen storage. International journal of hydrogen energy, 35(15), pp.8106-8116.

Xiao, J., Wang, J., Cossement, D., Bénard, P. and Chahine, R., 2012. Finite element model for charge and discharge cycle of activated carbon hydrogen storage. International journal of hydrogen energy, 37(1), pp.802-810.

Xiao, J., Peng, R., Cossement, D., Bénard, P. and Chahine, R., 2013. CFD model for charge and discharge cycle of adsorptive hydrogen storage on activated carbon. International journal of hydrogen energy, 38(3), pp.1450-1459.

Zero Carbon Hub, 2013. Zero carbon strategies for tomorrow's new homes. *Zero Carbon Hub, Milton Keynes*.

Zero Carbon Hub, 2014. Closing the gap between design and as-built performance. *End of term report*.

Zhan, L., Li, K.X., Zhang, R., Liu, Q.F., Lü, C.X. and Ling, L.C., 2004. Improvements of the DA equation for application in hydrogen adsorption at supercritical conditions. The Journal of supercritical fluids, 28(1), pp.37-45.

Zini, G., Marazzi, R., Pedrazzi, S. and Tartarini, P., 2010. A solar hydrogen hybrid system with activated carbon storage. *International journal of hydrogen energy*, *35*(10), pp.4909-4917

Zini, G. and Tartarini, P., 2010. Wind-hydrogen energy stand-alone system with carbon storage: modeling and simulation. *Renewable Energy*, *35*(11), pp.2461-2467.

Appendix A – Main Matlab Scripts for Storage Models

Compressed Hydrogen

```
%Get File%
fname=uigetfile({'*.csv'},'File Selector');
sheet = fname(1:end-4);
xlsread(fname,sheet);
data=xlsread(fname,sheet);

%Analyse File Data
Demand_E = data(:,1);
Demand_G = data(:,2);
Demand_T = Demand_E + Demand_G;
Temp_Ex = 294;%(data(:,3)+273);
Energy_Gen = -data(:,3);
Surplus = Energy_Gen - Demand_E;
max = numel(Demand_E);

%Initialisations
HREQ = zeros(max,1);
rho = zeros(max,1);
P = zeros(max,1);
H2_Gen = zeros(max,1);
Deficit = 0;
M_H = zeros(max,1);
V_H = 0;
Stored = 0;
P(1) = 0.1;
Ireq = zeros(max,1);
PFC = zeros(max,1);
%Constants
eff = 0.533;
nc = 60;
F = 96485;
Vely = 60;
PMAX = 17.5;
V = 0.03;
Grid = 0;
status = zeros(max,1);

for i = 2:max


    if Surplus(i)>0
%If +ve surplus, convert energy to hydrogen
        H2_Gen(i) = (nc*(Surplus(i)*1000/Vely))*eff*2E-3*3600/(2*F);
%Calculated amount to be generated
        M_H(i) = M_H(i-1) + H2_Gen(i);
%Accumulative mass of hydrogen
        rho(i) = M_H(i)/V;
%Calculate volumetric density
        P(i) = BENDER_PFUNC(Temp_Ex,rho(i));
%Calculate internal pressure, check to see if it has passed the max.
        status(i) = 1;
        if P(i)>PMAX
%Condition if max exceeded
```

```
            status(i) = 2;
            H2_Gen(i) = 0;
            M_H(i) = M_H(i-1);                                          %Reduce
generated mass by 1 iteration
            rho(i) = M_H(i)/V;
%Recalculate rho
            P(i) = BENDER_PFUNC(Temp_Ex,rho(i));
            Grid = Grid + Surplus(i);
        end
        HREQ(i) = 0;
%Counter to below, none required
        Stored = Stored + H2_Gen(i);
    else
%If -ive surplus, convert hydrogen to energy
        HREQ(i) = -Surplus(i)*3600000/(0.6*141000000);

        if HREQ(i) < M_H(i-1)
            Ireq(i) = (HREQ(i)/0.07)*35;
            if Ireq(i)<35
                PFC(i) = FC(Temp_Ex,Ireq(i));
                M_H(i) = M_H(i-1) - HREQ(i);
                status(i) = 5;
            else
                Deficit = Deficit + Surplus(i);
                status(i) = 6;
            end
        else
            Deficit = Deficit + Surplus(i);
            status(i) = 6;
        end
    end
end
aa = gradient(M_H);
bb = aa > 0;
cc = aa(bb);
Stored_Total = sum(cc);
Equivalent_kWh = Stored*0.7*141000000/3600000;
```

Metal Hydride

```
%Get File%
fname=uigetfile({'*.csv'},'File Selector');
%sheet = fname(1:end-4);
xlsread(fname);
data=xlsread(fname);

%Analyse File Data
Demand_E = data(:,1);
Demand_G = data(:,2);
Demand_T = Demand_E + Demand_G;
Temp_Ex = 294;%(data(:,3)+273);
Energy_Gen = -data(:,3);
Surplus = Energy_Gen - Demand_E;
max = numel(Demand_E);

%Initialisations
HREQ = zeros(max,1);
rho = zeros(max,1);
P = zeros(max,1);
H2_Gen = zeros(max,1);
Deficit = 0;
M_H = zeros(max,1);
V_H = 0;
Stored = 0;
P(1) = 0.1;
Ireq = zeros(max,1);
PFC = zeros(max,1);
MOUT = zeros(max,1);

%Constants
eff = 0.533;
nc = 60;
F = 96485;
Vely = 60;
PMAX = 17.5;
x = 62;
y = 62;
T0 = Temp_Ex;
Tint = zeros(x,y);
Tint = Tint + T0;
rhos0 = 8400;
rhos = zeros(x,y);
rhos = rhos + rhos0;
deftot = 0;
TIN = Tint;
rhosIN = rhos;
dens = zeros(max,1);
dens(1) = rhos0;
MH_MH2 = zeros(max,1);

for i = 2:8760
    tic
    complete = i
    Te = Temp_Ex;
    def = 0;
```

```
    if Surplus(i)>0 % if there is surplus
%If +ive surplus, convert energy to hydrogen
        H2_Gen(i) = (nc*(Surplus(i)*1000/Vely))*eff*2E-3*3600/(2*F);
%Calculated amount to be generated
        H2IN = H2_Gen(i)/3600;
        [ rhosOUT,TOUT,MOUT ] = MH_red( Te,TIN,x,y,rhosIN,H2IN );
        %absorb the hydrogen
status(i) = 1;
        TIN = TOUT;
    rhosIN = rhosOUT;
    MH_MH2(i) = MOUT;
    dens(i) = mean(mean(rhosOUT));
    else       %    if there isn't surplus
%If -ive surplus, convert hydrogen to energy
        HREQ(i) = -Surplus(i)*3600000/(0.6*141000000);
        if MH_MH2(i-1)>HREQ(i) % if there's hydrogen available
         H2REQ = HREQ(i)/3600;
         def = 0;
         status(i) = 2;
        else % if there isn't hydrogen available
           H2REQ = 0;
           def = HREQ(i);
           status(i) = 3;
        end
         [ rhosOUT,TOUT,MOUT ] = MHD_red( Te,TIN,x,y,rhosIN,H2REQ );
         deftot = deftot + def;
         TIN = TOUT;
         rhosIN = rhosOUT;
         MH_MH2(i) = MOUT;
         dens(i) = mean(mean(rhosOUT));
    end
    toc
end
aa = gradient(MH_MH2);
bb = aa > 0;
cc = aa(bb);
H2_Storage = sum(cc);
```

Absorption

```
function [ rhosOUT,TOUT,MOUT ] = MH33( Te,TIN,x,y,rhosIN,H2IN )
%LANI5

format long g

M = 2.016;
timestep = 1; %time step for simulation
M = 2.02; %hydrogen mmass
Cpg = 14890; %specific heat capacity for hydrogen
phi = 0.038; %constant
phi0 = 0; %constant
a1 = 1; %constant
a2 = 0.5; %constant
b = 0.137; %constant
kg = 0.1897; %hydrogen thermal conductivity
he = 1000; %edge loss
x = 62; %number of mesh points in x direction
y = 62; %number of mesh points in y direction
```

```
z = 400; %number of layers - z-2 for 3d internal processes
dx = 1E-3; %individual mesh measurement
dy = 1E-3;
dz = 1E-3; %all equal to give V = 1E-9 each mesh cube
dV = dx*dy*dz; %individual volumes
V = x*(2*y)*(2*z)*dV
rhos0 = 8400; %initial density
MS0 = rhos0*V %initial mass of metal
T0 = 293; %initial temperature
TF = 293;
Pg = 200; %gas pressure in
Pgout = 0.5; %gas pressure desorption
S = -110;
H = -31800;
e = 0.5;
Cps = 335;
ks = 1.0;
rhoss = 8517;
Ea = 21170;
Cainit = 59.187;
MAX = 1.28;


%Initialise
R =8.314;
Tint = zeros(x,y);
rhos = zeros(x,y);
rhos = rhos + rhos0;
rhoCpeabs = zeros(x,y);
Peq = zeros(x,y);
HHM = zeros(x,y);
Tint = Tint + T0;
dTdt = zeros(x,y);
tdiff = zeros(x,y);
wtpc = zeros(x,y);
keff = 1;
rhog = zeros(x,y);
rhoCpe = zeros(x,y);
drhosdt = zeros(x,y);
Cpe = ((0.5*Cps)+(0.5*Cpg));
tmax = 3600;

%From Prev
Tint = TIN;
rhos = rhosIN;

%H2IN is mass for absorption per second.
abs_max = H2IN/V;
h2inn = H2IN
absss_maxx = abs_max

for t = 1:timestep:tmax
    t;

    Tint(:,y) = TF;
    Tint(1,:) = TF;
    Tint(x,:) = TF;

    del2T = del2(Tint);
```

```
    rhog = (Pg*M)./(R*Tint*1E-3);
    rhoCpe = (e.*rhog*Cpg)+((1-e).*rhos*Cps);
    Peq = exp((H./(R*Tint)-(S/R))); %pressure calculation
    drhosdt = Cainit*exp(-Ea./(R.*Tint)).*log(Pg./Peq).*(-rhos+rhoss);
%absorption calculation
    if sum(sum(drhosdt))>abs_max
        drhosdt = drhosdt.*0;
        drhosdt = drhosdt + (abs_max);
    end
    rhos = rhos + (timestep.*drhosdt);
    dT1 = -H.*drhosdt/(2*Cpe);
    dT2 = keff.*del2T*dy*dx./(rhoCpe*dV*dx);
    Tint = Tint + (timestep.*(dT2 + dT1));
    HHM = MAX.*(rhos-rhos0)/(rhoss-rhos0);
    mass_tot = (mean(mean(rhos))-rhos0)*V;
    MASS = (mean(mean(rhos)))*V;
    H2_MASS = MASS - MS0;
    diff = rhos - rhos0;
    rhosOUT = rhos;
    TOUT = Tint;
    MOUT = H2_MASS;

end

end
```

Desorption

```
function [ rhosOUT,TOUT,MOUT] = MH( Te,TIN,x,y,rhosIN,H2REQ )
%LANI5

format long g

timestep = 1; %time step for simulation
M = 2.02; %hydrogen mmass
Cpg = 14890; %specific heat capacity for hydrogen
phi = 0.038; %constant
phi0 = 0; %constant
a1 = 1; %constant
a2 = 0.5; %constant
b = 0.137; %constant
kg = 0.1897; %hydrogen thermal conductivity
he = 1000; %edge loss
x = 62; %number of mesh points in x direction
y = 62; %number of mesh points in y direction
z = 400; %number of layers - z-2 for 3d internal processes
dx = 1E-3; %individual mesh measurement
dy = 1E-3;
dz = 1E-3; %all equal to give V = 1E-9 each mesh cube
dV = dx*dy*dz; %individual volumes
V = x*(2*y)*(2*z)*dV
rhos0 = 8400; %initial density
MS0 = rhos0*V %initial mass of metal
T0 = 293; %initial temperature
TF = 353;
Pg = 200; %gas pressure in
Pgout = 0.5; %gas pressure desorption
```

```
S = -110;
H = -31800;
e = 0.5;
Cps = 335;
ks = 1.0;
rhoss = 8517;
Ea = 21170;
Cainit = 59.187;
MAX = 1.28;

%Initialise
R =8.314;
Tint = zeros(x,y);
rhos = zeros(x,y);
rhos = rhos + rhos0;
rhoCpeabs = zeros(x,y);
Peq = zeros(x,y);
HHM = zeros(x,y);
Tint = Tint + T0;
dTdt = zeros(x,y);
tdiff = zeros(x,y);
wtpc = zeros(x,y);
keff = 1;
rhog = zeros(x,y);
rhoCpe = zeros(x,y);
drhosdt = zeros(x,y);
Cpe = ((0.5*Cps)+(0.5*Cpg));
Ed = 16420;
Cd = 9.57;
def = 0;
tmax = 3600;

%From Prev
Tint = TIN;
rhos = rhosIN;

%H2IN is mass for absorption per second.
d_max = H2REQ/V;

for t = 1:timestep:tmax
    t;
    Tint(:,y) = TF;
    Tint(1,:) = TF;
    Tint(x,:) = TF;
    del2T = del2(Tint);
    rhog = (Pg*M)./(R*Tint*1E-3);
    rhoCpe = (e.*rhog*Cpg)+((1-e).*rhos*Cps);
    Peq = exp((H./(R*Tint)-(S/R))); %pressure calculation
    drhosdt = real(Cd*exp(-Ed./(R.*Tint)).*log((Peq-Pgout)./Peq).*(rhos-
rhos0)); %absorption calculation
    if -sum(sum(drhosdt))>d_max
        drhosdt = drhosdt.*0;
        drhosdt = drhosdt - (d_max);
    end
    rhos = rhos + (timestep.*drhosdt);
    dT1 = -H.*drhosdt/(2*Cpe);
    dT2 = keff.*del2T*dy*dx./(rhoCpe*dV*dx);
    Tint = Tint + (timestep.*(dT2 - dT1));
    HHM = MAX.*(rhos-rhos0)/(rhoss-rhos0);
    mass_tot = (mean(mean(rhos))-rhos0)*V;
```

```
    MASS = (mean(mean(rhos)))*V;
    H2_MASS = MASS - MS0;
    rhosOUT = rhos;
    TOUT = Tint;
    MOUT = H2_MASS;
end

end
```

Activated Carbon

```
format long g
%Get File%
fname=uigetfile({'*.csv'},'File Selector');
%sheet = fname(1:end-4);
xlsread(fname);
data=xlsread(fname);

%Analyse File Data
Demand_E = data(:,1);
Demand_G = data(:,2);
Demand_T = Demand_E + Demand_G;
Temp_Ex = 294;
Energy_Gen = -data(:,3);
Surplus = Energy_Gen - Demand_E;
max = numel(Demand_E);

%Initialisations
HREQ = zeros(max,1);
rho = zeros(max,1);
P = zeros(max,1);
H2_Gen = zeros(max,1);
Deficit = 0;
M_H = zeros(max,1);
V_H = 0;
Stored = 0;
Ireq = zeros(max,1);
PFC = zeros(max,1);
MOUT = zeros(max,1);
m = zeros(max,1);

%Constants
x = 10;
y = 10;
eff = 0.7;
nc = 60;
F = 96485;
Vely = 60;
PMAX = 17.5;
%V = 7.21/(10*PMAX);
q = zeros(x,y);
q = q + 0;
POUT = zeros(x,y);
POUT = POUT + 1e5;
T0 = Temp_Ex(1);
Tint = zeros(x,y);
Tint = Tint + T0;
TOUT = zeros(x,y);
TOUT = TOUT + T0;
deftot = 0;
TIN = Tint;
qIN = q;
MH_MH2 = zeros(max,1);
PAV = zeros(max,1);
PAV(1) = 1;
TAV = zeros(max,1);
TAV(1) = T0;
nIN = 0;
status = zeros(max,1);
```

```
MMAX = 0.6;
Waste = 0;
nn = zeros(max,1);

for i = 2:max
    tic
    complete = i/8760*100
    Te = Temp_Ex;
    def = 0;
    if Surplus(i)>0
%If +ive surplus, convert energy to hydrogen
        H2_Gen(i) = (nc*(Surplus(i)*1000/Vely))*eff*2E-3*3600/(2*F);
%Calculated amount to be generated
        if MH_MH2(i-1)<(MMAX-(H2_Gen(i)))
            H2IN = H2_Gen(i)/3600;
            status(i) = 1;
            [ nOUT,MH,POUT,MMAX ] = ACRED( Te,nIN,H2IN,i,status(i) );
            nIN = nOUT;
            MH_MH2(i) = MH;
            PAV(i) = POUT;
            nn(i) = nOUT;
        else
            H2IN = 0;
            Waste = Waste + H2_Gen(i)
            MH_MH2(i) = MH_MH2(i-1);
            PAV(i)=  PAV(i-1);
            status(i) = 2;
        end
    else
%If -ive surplus, convert hydrogen to energy
        HREQ(i) = Surplus(i)*3600000/(0.6*141000000);

        if MH_MH2(i-1)>abs(HREQ(i)*2)

            H2REQ = HREQ(i)/3600;
            def = 0;
            status(i) = 5;
            [ nOUT,MH,POUT,MMAX ] = ACRED( Te,nIN,H2REQ,i,status(i) );
            nIN = nOUT;
            MH_MH2(i) = MH;
            PAV(i) = POUT;
            nn(i) = nOUT;
            if MH_MH2(i)<0
                pause();
            end
        else
            H2REQ = 0;
            def = HREQ(i);
            PAV(i) = PAV(i-1);
            MH_MH2(i) = MH_MH2(i-1);
            status(i) = 6;
        end
        deftot = deftot + def;
    end
    toc

end

Equivalent_kWh = Stored*0.7*141000000/3600000;
aa = gradient(MH_MH2);
```

```
bb = aa > 0;
cc = aa(bb);
Stored_Total = sum(cc);
deficit = deftot*141000000/3600000;
```